

University of Southampton Research Repository

Copyright © and Moral Rights for this thesis and, where applicable, any accompanying data are retained by the author and/or other copyright owners. A copy can be downloaded for personal non-commercial research or study, without prior permission or charge. This thesis and the accompanying data cannot be reproduced or quoted extensively from without first obtaining permission in writing from the copyright holder/s. The content of the thesis and accompanying research data (where applicable) must not be changed in any way or sold commercially in any format or medium without the formal permission of the copyright holder/s.

When referring to this thesis and any accompanying data, full bibliographic details must be given, e.g.

Thesis: Author (Year of Submission) "Full thesis title", University of Southampton, name of the University Faculty or School or Department, PhD Thesis, pagination.

Data: Author (Year) Title. URI [dataset]

UNIVERSITY OF SOUTHAMPTON

Faculty of Engineering and Physical Sciences School of Physics and Astronomy

Dissecting the origin of obscuration in AGN via comprehensive semi-analytic and semi-empirical orientation and evolutionary models

DOI: asdf Volume 1 of 1

by

Alba Vega Alonso Tetilla

MSc in Astrophysics

ORCiD: 0000-0002-6916-9133

A thesis for the degree of Doctor of Philosophy

February 2025

University of Southampton

Abstract

Faculty of Engineering and Physical Sciences School of Physics and Astronomy

Doctor of Philosophy

Dissecting the origin of obscuration in AGN via comprehensive semi-analytic and semi-empirical orientation and evolutionary models

by Alba Vega Alonso Tetilla

The origin of obscuration in Active Galactic Nuclei (AGN) remains a topic of debate, particularly regarding the relative contributions from galaxy-scale and torus-linked obscuration. While torus-linked obscuration is central to Orientation models, galaxy-scale obscuration is considered relevant in both Orientation and Evolutionary models. However, it remains unclear whether AGN obscuration is primarily driven by line-of-sight effects, a temporary dust-enshrouded phase in galaxy evolution, or a combination of both. This thesis investigates the effects of Orientation and Evolutionary models on AGN obscuration, using cosmological semi-analytic models, semi-empirical prescriptions, and hydrodynamical simulations. By modelling AGN evolution at the object level, considering different light curves, gas density profiles, and AGN feedback, I explore how factors such as host galaxy properties, torus-like components, gas fractions, mergers, starbursts, and clustering influence AGN obscuration. Both unobscured and obscured AGN, including Compton-thick sources, are analysed to assess the role of environment and galaxy characteristics.

Irrespective of the assumptions on specific AGN light curve (accretion rate or bolometric luminosity evolution with time) or galaxy gas fractions, I find that, on the strict assumption of an exponential profile for the gas component, galaxy-scale obscuration alone can hardly reproduce the fraction of $\log (N_{\rm H}/{\rm cm}^{-2}) > 24$ sources at least at $z \le 3$. This requires an additional torus component with a thickness that decreases with luminosity to match the data. The torus should be present in all evolutionary stages of a visible AGN to be effective, although galaxy-scale gas obscuration may be sufficient to reproduce the obscured fraction with $22 < \log(N_{\rm H}/{\rm cm}^{-2}) < 24$ (Compton-thin, CTN) if I assume extremely compact gas disc components. The claimed drop of CTN fractions with increasing luminosity does not appear to be a consequence of AGN feedback, but rather of gas reservoirs becoming more compact. Traditional (pure) Evolutionary models with obscuration pre-peak and optically/UV visible post-peak struggle to reproduce the AGN obscured fractions at $z \lesssim 3$ inferred from X-ray surveys. However, incorporating a central source with Comptonthick (CTK) column densities between $24 < \log(N_{\rm H}/{\rm cm}^{-2}) < 26$, such as a torus-like component, or a fine-tuned luminosity dependency, successfully reproduces observations. My results indicate that traditional Evolutionary models are less effective at reproducing the high fractions of obscured AGN observed at $z \leq 3$, while models with sharp post-peak declines or persistent or multiple obscuration phases are more successful. Incorporating a torus component, particularly one that decreases in thickness with increasing AGN power, effectively aligns with observed luminosity-dependent obscuration fractions, suggesting that orientation effects may still represent a key component even in Evolutionary models. In addition, I explore the clustering properties of AGN using the two-point correlation function, showing that stellar mass and obscuration have minimal influence on clustering strength. Environmental effects, however, introduce significant variability. These findings provide new insights into the complex relation between orientation, evolution, and environmental factors in AGN obscuration.

Contents

Li	st of	Figures	;	ix
Li	st of	Tables		xvi
De	eclara	ition of	f Authorship	xix
A	cknov	wledge	ments	xx
De	efinit	ions an	nd Abbreviations	xxv
1	Intr	oductio	on	1
	1.1	Motiv	ration and scientific background	2
	1.2	Quest	ions I seek to answer	3
	1.3	Thesis	s outline	4
	1.4	Origin	nal sources	5
2	Acti	ve Gal	actic Nuclei	7
	2.1	Histor	rical Overview	7
	2.2	AGN	structure	8
		2.2.1	Super-massive Black Hole (SMBH)	ç
		2.2.2	Accretion disc	10
		2.2.3	Corona	11
		2.2.4	Obscuring material	11
		2.2.5	Emission lines	11
		2.2.6	Jets	12
		2.2.7	Other AGN characteristics	12
	2.3	AGN	classification	14
	2.4	AGN	emission mechanisms	16
		2.4.1	UV/optical emission	18
		2.4.2	X-ray emission	
	2.5	AGN	obscuration	
		2.5.1	Unified Model	20
			2.5.1.1 Torus	
		2.5.2	Evolutionary model	22
		2.5.3	Orientation and Evolutionary as complementary models	23
		2.5.4	Merger and starburst galaxies	
	2.6	X-ray	observational data	
		_	Tologgongo laboratorios and currores	25

vi CONTENTS

		2.6.2	Relevant observations	26
		2.6.3	Observational data used	26
			2.6.3.1 Obscuration over X-ray luminosity	26
			2.6.3.2 Obscuration over Eddington rate	28
	2.7	Galax	y clustering	29
3	The	oretical	l model simulations	31
	3.1	Physic	cal theoretical models of galaxy formation	31
		3.1.1	Magneticum and the Gadget catalogue	32
	3.2	Semi-a	analytic models	32
		3.2.1	GAEA	33
		3.2.2	Other semi-analytic models	35
	3.3	Semi-e	empirical models	35
4	Met	hodolo	gy	37
	4.1	Obscu	ration of semi-analytic galaxies	37
	4.2	Metho	odology of the orientation model	38
		4.2.1	Column density distribution: contribution from the galaxy	39
		4.2.2	Column density distribution: contribution from the <i>torus</i>	43
	4.3	Metho	odology of the Evolutionary models	47
		4.3.1	Analytically integrated light curve	47
		4.3.2	Pure evolutionary models	52
			4.3.2.1 Fine-tuned luminosity models	54
			4.3.2.2 Contribution from a torus-like component	55
		4.3.3	Orientation and evolution <i>hybrid</i> model	56
		4.3.4	High star-forming galaxies and major mergers as CTK sources	56
	4.4		ration in Eddington ratio distributions of semi-analytic galaxies .	57
		4.4.1	Column density calculation	57
		4.4.2	Eddington ratio calculation	58
	4.5	Cluste	ering analysis with semi-analytic galaxies	59
5			e roles of the orientation, and multi-scale gas distributions in shap-	
	_		curation of Active Galactic Nuclei through cosmic time	61
	5.1		ole of galaxy size and AGN feedback in shaping the obscured AGN	- 4
	- 0		on with L_{X}	61
	5.2	-	ndence on gas disc scale thickness	66
	5.3		ontribution of the torus to the AGN obscured fraction	67
	5.4		ndence on light curve	71
		5.4.1	Dependence on time-varying HI column density	72 74
		5.4.2	Effect of the short-lived torus	74
	5.5	-	adence of the AGN obscured fractions on the gas fractions in the alaxies	75
	5.6	U	ssion on the limitations of an orientation model and the inclusion	
		of a to	rus model	77
6	Prol	oing the	e roles of evolution in shaping the obscuration of Active Galactic	
		_	ough cosmic time	79
	6.1	The ro	ble of evolution in shaping the obscured AGN fraction with $L_{\rm X}$	80

CONTENTS vii

	6.2	The impact of a torus component within an Evolutionary model	83
	6.3	Hybrid model	86
	6.4	Redshift evolution	88
	6.5	Can starburst alone explain the fraction of obscured AGN at $z>1$?	90
	6.6	The contribution of mergers to the fraction of obscured AGN	92
	6.7	Dependence of the predicted AGN number densities on the input pa-	
		rameters/assumptions	94
	6.8	Assessing the definition of starburst in relation to the Main Sequence and	
		SFR	95
	6.9	Breaking degeneracies via AGN clustering	96
	6.10	Orientation vs Evolutionary models	96
		The effect of alternative density profiles and their relation with gas com-	
		pactness	97
	6.12	The implications of Little Red Dots and other AGN populations	98
		Comparison with previous works	99
7		nplementary model predictions: Eddington ratio distributions and spatial	
		ribution	101
	7.1	O	101
		7.1.1 The <i>forbidden</i> region	
		7.1.2 Eddington ratio distributions in Orientation and Evolutionary mod-	
		els	108
		7.1.3 The role of Orientation and the torus and its connection with Evo-	
		S .	108
	7.2	Studying the obscuration using Clustering	109
		7.2.1 Clustering in the Orientation model	110
		7.2.2 Clustering in the Evolutionary model	112
8	Con	clusions	115
U	8.1		115
	8.2	The role of the Evolutionary model	
	8.3	The Eddington ratio distribution effect	
	8.4	The role of clustering	
	8.5	Future work	119
	8.6	Take-home messages	121
	0.0	Take-nome messages	141
Αı	pend	dix A Study of molecular gas in a semi-analytical context	125
•	_	endix A.1 Updated gas model implementation in GAEA SAM model	125
		endix A.2 Molecular gas fraction, total gas fraction, and depletion time.	126
		endix A.3 Redshift evolution of the molecular gas fraction and depletion	
		time	131
	Арр	endix A.4 Discussion and conclusions	134
	11		
Ap	_	dix B Studying the roles of density profiles and gas distribution in shap-	
	_	the obscuration of hydrosimulated Active Galactic Nuclei though cosmic	
	time		135
		endix B.1 Fiducial galaxy	136
	App	endix B.2 HI column density in hydrodynamic simulated galaxies	137

Appendix B.2.1 HI column density calculation	138	
Appendix C Industrial secondment in OLT		
References	145	

List of Figures

2.1	Ricci	9
2.2	Figure from Harrison [2014]. Schematic representation of an unobscured AGN SED. The black solid curve is the total SED, and the coloured curves are divided by the main physical components. In gray, an example of	
2.3	starburst (Section 2.5.2 and Chapter 6) galaxy radio-UV SED Figure and caption from Beckmann and Shrader [2012]. Schematic representation of our understanding of the AGN phenomenon in the unified scheme [1]. The type of object I see depends on the viewing angle, whether or not the AGN produces a significant jet emission, and how powerful the central engine is. Note that radio loud objects are generally thought to display symmetric jet emission. Graphic courtesy of Marie-Luise Menzel (MPE)	17 21
4.1	Diagram depicting a typical galaxy in the mock sample characterised by an exponential gas density profile and a disc geometry. In this Figure, R traces the line-of-sight, R_d is the gas scale length, h is the thickness of the disc, θ is the angle between the vertical and R , α is the random angle for the random line-of-sight, R_{max} marks the end point of the galaxy edges along R , R_b is the radius of the Blast Wave, and θ_{op} is the opening angle	
4.2	of the Blast Wave (central white sphere in the Figure) Diagram of the <i>fiducial</i> torus model where I implement both the radiation-driven outflows described by Wada, where θ_{crit} is the critical angle of the radiation-accelerated gas (right side), and the RA&R constant limit angles (left side). α is the random line-of-sight angle. The diagram is separated in two for clarity	39 45
4.3	Diagrams of the Evolutionary models 1, 2, 3, and 4, and the work of the optically/UV visible window. Obscuration in Models 1 and 2 constitutes column densities between 10 ²² and 10 ²⁴ cm ⁻² (CTN), in Model 3 the prepeak obscured phase is divided in two with column densities between 10 ²² and 10 ²⁴ cm ⁻² (CTN) and between 10 ²⁴ and 10 ²⁶ cm ⁻² (CTK), and in Model 4 the pre-peak obscured phase has column densities between 10 ²⁴ and 10 ²⁶ cm ⁻² (CTK) and the post-peak obscured phase has column densities between 10 ²² and 10 ²⁴ cm ⁻² (CTN). In all cases, dark shadow corresponds to CTK obscuration, light shadow represents the CTN obscured phase, and uncoloured area corresponds with the optically/UV visible phase. We include the effect of each model specification to the	1
	CTN obscured fractions	48

x LIST OF FIGURES

5.1	Mean column density distribution and obscured fractions at $z = 2.4$ depending on the X-ray luminosity. Green dashed lines correspond to the	
	model using the (gas) scale length from GAEA and without BW. Blue	
	solid and red dotted lines are calculated with the scale length fit from van	
	der Wel et al. [2014] no-BW and BW models respectively. All three lines	
	assume $R_{\rm d,gas} = 0.3 \cdot R_{\rm d,\star}$. Left panel: Column density distributions pre-	
	dicted by each model, as labelled. Lines correspond to the mean values	
	of the column density at fixed AGN X-ray luminosity, and the coloured	
	areas mark the predicted σ region around the mean. Middle panel: CTN	
	obscured fractions. Grey areas correspond to the observations by U14,	
	B15, and A19 as labelled. Right panel: CTK obscured fractions. Obser-	
	vations with the same format as in the middle panel	64
5.2	Predicted fraction of CTN obscuration as a function of X-ray luminosity	
	and without a BW for different values of the relation between gas disc	
	radius $R_{d,gas}$ and stellar disc radius $R_{d,\star}$, $R_{d,gas} = N \cdot R_{d,\star}$, as labelled,	
	with a fixed thickness of $h = R_d/8$ at redshift $z = 2.4$. I explore $N = 0.2$,	
	N = 0.3, $N = 0.5$, and $N = 1.0$. Fiducial model refers to the model using	
	van der Wel et al. [2014] fit and $N=0.3$ (see text). The observational	
	data is shown as in Figure 5.1	64
5.3	Obscured fractions of galaxies between $L_X = 10^{43}$ erg/s and $L_X = 10^{45}$	
	erg/s (left panel) and between $L_X = 10^{44}$ erg/s and $L_X = 10^{45}$ erg/s	
	(right panel) as a function of the column density for the fiducial host	
	model with (dotted red line) and without (blue solid line) BW at redshift	
	z = 2.4. Observational data correspond to U14 and A19, as labelled	66
5.4	Host galaxy CTN obscured sources for the fiducial host galaxy model	
	without BW modifying the prescription of the scale height at redshift	
	$z = 2.4$. I compare the disc heights $h = R_d/6$, $h = R_d/8$ and $h = R_d/15$.	6
	Observations as in Figure 5.1.	67
5.5	Column density distribution and obscured fractions depending on the	
	X-ray luminosity for different types of torus models at redshift $z = 2.4$.	
	Fiducial model (blue solid line) refers to a combination of Wada and	
	RA&R torus models (see text), red dotted line shows the Wada torus	
	model, and green dashed line is the RA&R model. Observations shown as in Figure 5.1. Left panel: Mean column density distribution along	
	with its σ (coloured area). Middle panel: CTN obscured fractions. Right	
	panel: CTK obscured fractions	69
5.6	Compton-thin and thick obscured AGN fractions depending on the X-	0)
5.0	ray luminosity for galaxies including BW (dashed red) or without the	
	BW (solid blue line) and the fiducial torus model. Each panel corre-	
	sponds with a different redshift as labelled. Observations shown as in	
	Figure 5.1.	69
5.7	Obscured fractions of galaxies between $L_{\rm X}=10^{43}$ erg/s and $L_{\rm X}=10^{45}$	0,
0.7	erg/s (left panel) and between $L_X = 10^{44}$ er/s and $L_X = 10^{45}$ erg/s (right	
	panel) as function of the column density for the fiducial galaxy model	
	(host and torus) with (dotted red line) and without (blue solid line) BW	
	at redshift $z = 2.4$. Observational data correspond with U14 and A19, as	
	labelled.	70

LIST OF FIGURES xi

5.8	CTN (left panel) and CTK (right panel) obscured fractions for the fiducial model without BW (solid blue line), fiducial model with the BW (dashed red line), no BW model but using the randomly picked X-ray luminosity	
	(dotted black line), and the BW model using the randomly picked X-ray	17 1
- 0	luminosity (dash-dotted grey line). Observations as in Figure 5.1	71
5.9	AGN obscured fractions depending on the X-ray luminosity randomly	
	selected within the LC assuming the model from Section 4.3, for both with and without the BW at redshift $z = 2.4$. Observations as in Figure	
	5.1. Left panel: CTN obscured fractions. Right panel: CTK obscured	
	fractions	72
5 10	Host galaxy CTN obscured fractions for the fiducial model without BW	12
5.10	(solid blue line), fiducial model with the BW (dotted red line), no BW	
	model but using the randomly picked X-ray luminosity with a time de-	
	pendent column density (dashed cyan line), and the BW model by using	
	the randomly picked X-ray luminosity with a time dependent column	
	density (dash-dotted pink line) at redshift $z = 2.4$. Observations as in	
	Figure 5.1	73
5.11	AGN obscured fractions depending on the X-ray luminosity of the fidu-	
	cial galaxy model compared against the random X-ray luminosity within	
	the <i>modified</i> light curve, for both BW and no-BW, assuming that the fidu-	
	cial torus model only appears in the pre-peak phase at redshift $z = 2.4$.	
	Observations as in Figure 5.1. Left panel: CTN obscured fractions. Right	
	panel: CTK obscured fractions	74
5.12	AGN obscured fractions depending on the X-ray luminosity of the fidu-	
	cial galaxy model compared against the random X-ray luminosity within	
	the <i>modified</i> light curve, for both BW and no-BW model, assuming that	
	the Wada torus model only appears in the pre-peak phase at redshift	
	z = 2.4. Observations as in Figure 5.1. Left panel: CTN obscured fractions. Right panel: CTK obscured fractions	75
5 12	CTN obscured fractions of the host galaxy using the empirical relation	75
5.15	from Santini et al. [2014] to estimate cold gas fractions at redshift $z = 2.4$.	
	I compare with the original GAEA cold gas fractions as in the fiducial	
	host model. Observations as in Figure 5.1	76
	8	
6.1	CTN obscured fractions depending on the X-ray luminosity and assum-	
	ing Model 1 and 2 LCs. The column density of the host galaxy is assigned	
	depending on the LC without a fine-tuned luminosity dependency (solid	
	line) or with a fine-tuned luminosity dependency (dashed line, read text	
	for more information). The observations correspond with U14, A19 and	
	B15. A luminosity dependent visibility window model with a post-peak	
	LC phase that decreases with luminosity reproduces better the U14, A19	01
()	CTN fractions than models without a luminosity dependency	81
6.2	Visibility window time distributions for Models 1-4 with and without luminosity dependency, as labelled. For Model 3 I also include the model	
	without a post-peak and bigger fraction of the pre-peak as CTK phase	
	(2/3 instead of 1/3, yellow dash-dotted line). In Model 4 I also include	
	the effect of making a bigger constant window in 10^8 yr	81
		-

xii LIST OF FIGURES

6.3	CTN and CTK obscured fractions depending on the X-ray luminosity	
	and assuming Model 3 and 4 LCs. The optically/UV visibility window of Model 3 corresponds with the complete post-peak phase of the LC for the 'with post peak' solid line, and just the peak luminosity of the LC.	
	the 'with post-peak' solid line, and just the peak luminosity of the LC for the 'without post-peak' dashed and dotted lines. The fraction of the	
	LC assigned to the obscured phase is the first 1/3 for the dashed line and 2/3 for the dotted line. The observations are the same as in Figure	
	6.1. A luminosity dependent visibility window model with a post-peak LC phase that decreases with luminosity improves Models 3 and 4 when	
	compared to U14, A19 CTN fractions than models without a luminosity dependency.	83
6.4	CTN and CTK obscured fractions depending on the X-ray luminosity including the fiducial torus within Evolutionary Models 1 and 2. The torus can be long-lived (alive during the whole LC) or short-lived (alive	0.5
	during the obscured phases of the LC. The observations are the same as in Figure 6.1. A torus component can help to reproduce the CTK AGN	
	obscured fractions under Models 1 and 2	84
6.5	CTN and CTK obscured fractions depending on the X-ray luminosity	
	including the fiducial torus within Evolutionary Models 3 and 4. The	
	torus can be long-lived or short-lived. In Model 3, the LC can have a long post-peak (solid blue and dashed red lines) or short post-peak (dot-	
	ted yellow and dashed green lines). In Model 4, the LC can have a short	
	optically/UV visibility window ($\Delta \tau_{\rm QSO} \sim 10^7$ yr, solid blue and dashed	
	red lines) or a long one ($\Delta au_{QSO} \sim 10^8$ yr, dotted yellow and dashed green	
	lines). The observations are the same as in Figure 6.1. The relation be-	0=
	tween the torus model and the visibility window is degenerate	85
6.6	CTN and CTK obscured fractions depending on the X-ray luminosity assuming the mixed model (using Evolutionary Models 3 and 4 together	
	with the Orientation model from Section 4.2). Here, the torus model	
	is always long-lived. The optically/UV visible window of Model 4 is	
	$\Delta \tau_{\rm QSO} \sim 10^7$ yr, while Model 3 uses all the post-peak phase as win-	
	dow. The observations are the same as in Figure 6.1. Under a model that	
	includes both Orientation and Evolutionary models, orientation domi-	
	nates over the evolution at redshift $z = 2.4.$	87
6.7	Redshift evolution of Model 3 fine-tuned (solid line) and Model 3 with	
	the long-lived torus (dotted line) for redshifts $z=0.99,2.42$, and 3.31. The observations are the same as in Figure 6.1. The luminosity depen-	
	dency and the torus model are affected by a z-dependency, especially at	
	lower redshifts.	89
6.8	AGN distribution at redshift z=2.4 with contours at 100%, 95%, 75%,	
	50%, and 25% with the MS (black line). Left panel: empirical MS for the	
	total population and for the starburst from Carraro et al. [2020]. Right	
	panel: CTK obscuration limit on the assumptions that these sources are	
	residing in host galaxies with SFRs above 100 M _☉ /yr (solid, blue lines),	
	and 4 times the GAEA predicted MS (dotted red line), at the MS (dot-	89
	dashed green line)	07

LIST OF FIGURES xiii

6.9	CTK obscured fractions depending on the X-ray luminosity of the starburst obscuration models. In each model, I assume as CTK obscured galaxies those above the limit indicated either in SFR, or MS (Main Sequence). The observations are the same as in Figure 6.1. The SFR limit of best model to reproduce the CTK obscured fractions is related to the	90
6.10	Main Sequence	90
6.11	random column density. The observations are the same as in Figure 6.1. The merger ratio of the best model to reproduce the CTK obscured fractions is constant and the model must include a torus-like component that produces CTK obscuration	93
	cuts provide different results depending on the Evolutionary model used.	94
7.1	Accretion-rate function using Orientation and Evolutionary models as labelled for the total column density distribution (solid line), and AGN with $N_{\rm H} < 10^{24}$ cm ⁻² (dotted line). The observational data are from Georgakakis et al. [2017a] at redshift $z \sim 2.75$	102
7.2	Normalized specific accretion-rate function using Orientation and Evolutionary models as labelled for unobscured column density distribution ($N_{\rm H} < 10^{22}~{\rm cm}^{-2}$, solid line), and CTN obscured with $10^{22} < N_{\rm H} < 10^{24}~{\rm cm}^{-2}$ (dotted line). The plotted SARDs are normalized to unity for each obscuration bin following Equation 4.19. The observational data are	
7.3	from Laloux et al. [2024] from redshift bin $z \sim 2-2.5$ CTN obscured fractions using Evolutionary models from Chapter 6 and the Orientation models from Chapter 5 at redshift $z=2.42$. The grey areas correspond with the observational data to Laloux et al. [2024] at	103
	z = 2	104

xiv LIST OF FIGURES

7.4	Column density using Evolutionary Models 3 and 4 from Chapter 6 and the Orientation model from Chapter 5. The lines correspond to 2σ and the coloured areas to $1-2\sigma$ at redshift $z=2.4$. Grey (long-lived absorption from clouds near the centre of the galaxy, upper left region) and yellow (outer dust lanes that can obscure over much of the plane at low column densities) areas and the black limit (effective Eddington limit	
	with a standard ISM grain abundance) come from Fabian et al. [2008, 2009] at redshift $z=0$. The upper right region is called "the forbidden region" (here in white) as the Fabian et al. [2008] sample avoided that region	105
7.5	CTN and CTK obscured fractions for the studied models assuming that galaxies with a host column density above $\log N_{\rm H} = 23~{\rm cm}^{-2}$ and below the limit defined by Laloux et al. [2024] at redshift $z=2.5$ quickly move to a value below $\log N_{\rm H}=22~{\rm cm}^{-2}$. Thus, the torus is the solely creator of CTK column density. The blue lines correspond with the original models described in previous Chapters, while the orange lines refer to	105
7.6	the models including Laloux et al. [2024] limit	107
7.7	tation model for the host galaxy and fiducial torus model Projected 2-point correlation function at different bins of stellar mass (as labelled). Each line corresponds to a different column density bin. Grey area corresponds to the total column density bin of redshift $1.1 < z < 3$ from Viitanen et al. [2023]. Upper panels: column density calculated using the Evolutionary Model 3 including the long-lived fiducial torus model. Bottom panels: column density calculated using the Evolutionary Model 4 including the long-lived fiducial torus model	110
Арр	endix A.1 Molecular gas fraction of galaxies (grey area) with a stellar mass above $10^9~\rm M_{\odot}$ and AGN (contours) with luminosities above $L_{\rm bol}\sim 10^{42}~\rm erg/s$ at redshift $z=0$. Points correspond to Andreani et al. [2018], Groves et al. [2015], Lisenfeld et al. [2017], Koss et al. [2021] (AGN samples), Tacconi et al. [2018] and Liu et al. [2021]. Contours define the 5%,	
A 1010	10%, 20% and 40% of the total AGN distribution	127
Арр	pendix A.2 Depletion time of galaxies (grey area) with a stellar mass above $10^9~{\rm M}_{\odot}$ and AGN (contours) with luminosities above $L_{\rm bol}\sim10^{42}~{\rm erg/s}$	
	at redshift $z=0$. Points correspond to Andreani et al. [2018], Groves et al. [2015], Koss et al. [2021], Lisenfeld et al. [2017], Koss et al. [2021], Tacconi et al. [2018] and Liu et al. [2021]. Contours define the 5%, 10%, 20% and 40% of the total AGN distribution	128
Арр	pendix A.3 Molecular and atomic gas fraction of galaxies (grey area) with	120
TT	a stellar mass above $10^9\mathrm{M}_\odot$ and AGN (contours) with luminosities above $L_\mathrm{bol}\sim 10^{42}\mathrm{erg/s}$ at redshift $z=0$. Points correspond to Andreani et al. [2018], Groves et al. [2015]. Contours define the 5%, 10%, 20% and 40%	
	of the total AGN distribution	130

LIST OF FIGURES xv

Appendix A.4 Molecular gas fraction of galaxies (grey area) with a stellar mass above $10^9 \rm M_{\odot}$ and AGN (contours) with luminosities above $L_{\rm bol} \sim 10^{42} \rm erg/s$ at redshift $z=2.42$. Points correspond to Tacconi et al. [2018],	
Kaasinen et al. [2019] and Liu et al. [2021]. Contours define the 5%, 10%, 20% and 40% of the total AGN distribution	131
Appendix A.5 Depletion time of galaxies (grey area) with a stellar mass above $10^9~{\rm M}_{\odot}$ and AGN (contours) with luminosities above ${\rm L_{bol}} \sim 10^{42}~{\rm erg/s}$ at redshift $z=2.42$. Points correspond to Tacconi et al. [2018], Kaasinen et al. [2019] and Liu et al. [2021]. Contours define the 5%, 10%, 20% and	
40% of the total AGN distribution	132
Appendix A.6 Molecular gas, SFR and stellar mass distributions of GAEA-merged galaxies over redshift for a stellar mass selection of $M_{\star} \sim 10^{10-11}$ M	I⊙.
Observational points correspond to Groves et al. [2015], Kakkad et al. [2017], Andreani et al. [2018], Tacconi et al. [2018], Kaasinen et al. [2019], Koss et al. [2021], Suzuki et al. [2021], Liu et al. [2021]	132
Appendix A.7 Molecular gas fraction, depletion time and gas fraction evolution on redshift of GAEA-merged galaxies for a stellar mass selection of $M_{\star} \sim 10^{10-11} \ \mathrm{M}_{\odot}$. Observational points correspond to Groves et al. [2015], Kakkad et al. [2017], Andreani et al. [2018], Tacconi et al. [2018], Kaasinen et al. [2019], Koss et al. [2021], Suzuki et al. [2021], Liu et al. [2021]	133
Appendix B.1 Spatial distribution of cold gas particles (black) in the galaxy at redshift $z = 0.0$. The left panel displays the projection in the xy plane, while the right panel shows the xz plane. In green are the particles selected from a cylindrical region defined by a radius of 0.002 Mpc and a	
height of 0.2 Mpc	139
Appendix B.2 Spatial distribution of cold gas particles (black) in the galaxy at redshift $z = 2.39$. The left panel displays the projection in the xy plane, while the right panel shows the xz plane. In green are the particles selected from a cylindrical region defined by a radius of 0.002 Mpc and	
a height of 0.2 Mpc	139

List of Tables

2.1	Data limits and parameters in the selected studies	29
4.1	Summary of the different models studied in the paper. They are separated by their area of appliance (host galaxy, torus or both) and by model (no-BW/BW, RA&R/Wada/Fiducial, or a combination)	46
4.2	j i i i i i i i i i i i i i i i i i i i	
	rated by their area of appliance (host galaxy, torus or both) and by model.	50
Арр	endix B.1 Basic variables of the Fiducial galaxy from Valentini et al. [2020] calculated in this Appendix. The differences between the paper and this Table come from the definition of the constant $h_{100} = 0.73$, which has been selected to follow Fontanot et al. [2020] and I decide to keep it	
	consistent within the thesis.	140

Declaration of Authorship

I declare that this thesis and the work presented in it is my own and has been generated by me as the result of my own original research.

I confirm that:

- 1. This work was done wholly or mainly while in candidature for a research degree at this University;
- 2. Where any part of this thesis has previously been submitted for a degree or any other qualification at this University or any other institution, this has been clearly stated;
- 3. Where I have consulted the published work of others, this is always clearly attributed;
- 4. Where I have quoted from the work of others, the source is always given. With the exception of such quotations, this thesis is entirely my own work;
- 5. I have acknowledged all main sources of help;
- 6. Where the thesis is based on work done by myself jointly with others, I have made clear exactly what was done by others and what I have contributed myself;
- 7. Parts of this work have been published as: Alonso-Tetilla et al. [2024], Alonso-Tetilla et al. (submitted), Alonso-Tetilla et al. (in prep).

Signed:	Date:

Acknowledgements

This PhD received funding from the European Union's Horizon 2020 research and innovation programme under the Marie Skłodowska-Curie grant agreement No. 860744 for the BiD4BESt project (Coordinator: F. Shankar).

I have to thank so many people for helping along my PhD journey. First, I would like to thank my supervisor, Prof. Francesco Shankar. His support, guidance, feedback, patience, and encouragement have been instrumental in shaping this work. I am truly grateful for the countless hours he devoted to reviewing my drafts, challenging my ideas, and pushing me to reach my full potential. I would also like to thanks my co-supervisor, Dr. Fabio Fontanot, for his supervision and help along the 4 years of PhD, and for welcoming in Trieste two times to closely collaborate. I am also very grateful to have worked with Prof. Nicola Menci and Prof. Andrea Lapi during the different projects, improving my work in interesting discussions. Also thanks to Imogen Gingell and Roberto Gilli for their deep analysis of my thesis and their comments, which improved the thesis to what it is now. And special thanks to Dr. Sandra de Jesus Raimundo and Dr. Anna Puglisi for the useful discussion on my work, my papers and my thesis.

Also, a big thank you to the people from the BiD4BESt project, who made me enjoy my PhD both scientifically and socially. This experience would not have been the same without you.

Working at the Astronomy group at Southampton has been a pleasure. The warm welcome, especially during the first year of the PhD and in the middle of a pandemic, made me aware that I am part of something bigger, part of the scientific community, and not just someone coding in their living room. Also, a special thanks to INAF-OATs all PhD students, in particular to Jacopo, Marta, Vieri, Jasbir, Arianna and Roberta, who welcomed me from the beginning. Thank so much to all my friends from the University, particularly people from the music societies. Thanks to you I could have my mind out of the PhD for a few hours. I will always treasure the rehearsals, concerts and socials we did together.

Special thanks to the friends that had to deal with my complaints and desperation: Victor, David, Marianna, George, Jack and Lucille. Sin nuestras noches de cine, los paseos, le chiamate settimanali, or monthly calls, dog pictures, e les concerts joués ensemble, life would be less interesting. Also thanks to my friends from Bristol, Will, Callum, Vi and Liam, for being always there when I needed them.

Gracias a mis padres, Eladio y Carmina. Sin vosotros nunca hubiera llegado hasta aquí. Sois todo lo que una hija puede soñar y espero que estéis tan orgullosos de mi trabajo como yo lo estoy. Gracias por una vida maravillosa.

To my family and friends

Definitions and Abbreviations

AEGIS All Wavelength Extended Groth Strip International Survey

AGN Active Galactic Nucleus/Nuclei

ASCA Advanced Satellite for Cosmology and Astrophysics

ASPECS ALMA Spectroscopic Survey in the Hubble Ultra Deep Field

BH Black Hole

BLR Broad Line Region

BW Blast Wave

CANDELS Cosmic Assembly Near-infrared Deep Extragalactic Legacy Survey

CF Covering factor

COSMOS Cosmological Evolution Survey

CTN Compton-thin CTK Compton-thick

CXB Cosmic X-ray Background ENLR Extended Narrow Line Region

F06-GAEA GAEA run with characteristics from Fontanot et al. [2006]

 F_{e} Iron

FIR Far-infrarred

 f_{aw} Fraction of the cold gas ejected [from Menci et al., 2019, BW model]

GAEA GAlaxy Evolution and Assembly

GOODS Great Observatories Origins Deep Survey

H Hydrogen h Scale height

 H_e Helio

HI Neutral atomic hydrogen

HQ11-GAEA GAEA run with the light curve from?

 $H2 \text{ or } H_2$ Molecular hydrogen

IR Infrarred

ISM Interestellar medium

JWST James Webb Space Telescope

kpc Kiloparsecs L Luminosity

L_{bol} Bolometric luminosity

LC Light Curve LRDs Little Red Dots

 $\begin{array}{lll} LF & & Luminosity Function \\ LSS & & Large\text{-scale structure} \\ L_X & & X\text{-ray luminosity} \\ M_{cold} & & Cold gas mass \\ \end{array}$

 M_{gas} Gas mass M_{hot} Hot gas mass M_{\star} Stellar mass MIR or mid-IF Mid-infrarred Mpc Megaparsecs

N Relation between the scale length of the gas and stellar component of the galactic disc

N_H Hydrogen column density

NLR Narrow Line Region

O Oxigen

OVV Optically violent variable

pc Parsecs

QSO Quasi-stellar object, or quasar

 $R_{\rm b}$ Radius of the BW $R_{\rm d}$ Scale length

 $R_{\rm d,gas}$ Scale length of the gas component of the galactic disc $R_{\rm d,\star}$ Scale length of the stellar component of the galactic disc

 $R_{\rm d.Wel}$ Scale length using van der Wel et al. [2014]

 $R_{\rm eff}$ Effective radius

*R*_{max} Maximum galactic radius

ROSAT ROentgen SATellite SAM Semi-analytic model SAR Specific accretion rate

SARD Specific accretion rate distribution

SED Spectral energy distribution SMBH Supermassive black hole

UV Ultraviolet

XLF X-ray luminosity function

XRB X-ray background

z Redshift

α Line-of-sight angle

 θ_{crit} Critical angle in the Wada torus model

2pcf 2-point correlation function

Chapter 1

Introduction

For as long as humans have walked the Earth, we have looked to the skies with wonder, curiosity, and a profound sense of admiration. The mysteries of the Universe have captivated our imagination, driving not only scientific discovery but also deeply influencing literature, music, and culture throughout history. Our fascination with the stars and planets transcends mere observation; it is a lasting theme that impregnate every aspect of human creativity, from the ancient myths and legends told around campfires to the groundbreaking achievements of modern astrophysics. The sky, with all its complexity, invites us to explore, to learn, and to seek answers to the questions that have haunted us for millennia.

Music has long been a powerful medium through which this cosmic curiosity has been expressed. Gustav Holst's *The Planets*, composed in the early 20th century, remains one of the most evocative orchestral works, each movement capturing the essence of a different planet as seen through the eyes of mythology. Other composers have similarly drawn inspiration from the mysteries of the Universe: John Williams with *Star Wars*, Jerry Goldsmith with *Star Trek*, or even Muse and their song *Supermassive Black Hole*, show our eager of adventure and space exploration, blending space phenomena with human emotion and existential themes.

Literature is equally submerged in astronomical themes. From Isaac Asimov's works, where robots and space travel become metaphors for human struggles and evolution, to the cultural phenomenon of *Star Trek*, which envisioned a future where humanity ventures beyond Earth to explore strange new worlds, space has always been more than just a backdrop: it is a character in its own right. *Star Trek*, in particular, captures the essence of human curiosity and our yearning for discovery. Its motto, "to boldly go where no one has gone before," encapsulates a spirit that is as old as humanity itself. The vastness of space becomes a reflection of our own desire to learn, adapt, and solve the mysteries of existence, much like detectives unravelling the details of a case. Pretty much like Agents Fox Mulder and Dr Dana Scully, seeking the answers to

extraterrestrial phenomena while they try to find their own stories, who they are in this vast universe.

In this sense, we are all cosmic detectives. Our pursuit of knowledge, much like Sherlock Holmes' steady quest for truth, drives us to understand the universe in all its dimensions. We ask questions, we search for clues, and we follow leads—whether through a telescope or through mathematical equations. We ponder the great questions of life, the universe, and everything. As Douglas Adams so hilariously framed in *The Hitchhiker's Guide to the Galaxy*, we seek answers, only to discover that the Universe *might just disappear and be replaced by an even more bizarre and inexplicable* Universe if ever anyone discovers exactly what the Universe is for and why it is here, or that *this might have already happened*.

Astronomy, astrophysics, and space exploration are not merely scientific disciplines: they are essential elements of what it means to be human. They reflect our intrinsic need to explore, to question, and to seek out meaning. Just as music, literature, and art have channelled our cosmic wonder, science gives us the tools to probe deeper, to understand the forces that govern the stars, and to piece together the puzzle of our existence. And, perhaps, at the end of it all, we might indeed find that the answer to life, the universe, and everything is, quite simply, 42. But until then, our journey of discovery continues, with the Universe as our greatest and most enigmatic frontier.

1.1 Motivation and scientific background

In Peterson [1997], an active galactic nucleus (AGN) is defined as a galaxy with "the existence of energetic phenomena in the nuclei, or central regions, of galaxies which cannot be attributed clearly and directly to stars." In a more recent review by Hickox and Alexander [2018], an AGN is described as "the observed manifestation of gas accretion onto a supermassive black hole (SMBH)." Over the past 20 years, the definition of AGN has significantly evolved, driven by increasingly detailed observations, which have highlighted AGN as key sources for studying the co-evolution of galaxies and black holes. However, AGN remain relatively rare objects, existing at the boundaries of our current understanding, and present intriguing characteristics that are not yet fully understood.

One such characteristic, which motivates this thesis project, is the phenomenon of AGN obscuration. An AGN is considered obscured when the emission from its accretion disc, particularly in the ultraviolet (UV) and optical wavelengths, is blocked by intervening material along the line of sight between the accretion disc and the observer [see Alonso-Tetilla et al., 2024, and references therein]. This obscuration is typically caused by material in the form of gas or dust in the interstellar medium (ISM) of the host galaxy, which absorbs or scatters a significant fraction of the accretion disc emission [e.g., Lapi et al.,

2005, Buchner et al., 2017, Hickox and Alexander, 2018, Gilli et al., 2022]. Alternatively, the obscuration can also result from a dusty inner torus within a few parsecs of the central SMBH [e.g., Packham et al., 2005, Radomski et al., 2008, Burtscher et al., 2013, Gallimore et al., 2016, Imanishi et al., 2016, García-Burillo et al., 2016, 2019, 2021, Hönig and Kishimoto, 2017, Hönig et al., 2018, Hönig, 2019]. At X-ray wavelengths, gas is the dominant source of obscuration, primarily affecting the regions near the accretion disc under the gravitational influence of the SMBH. The nature of obscuration, both its behaviour and its influence within the host galaxy, is typically explained by two primary models: the Evolutionary model and the Orientation model.

The Evolutionary model, first proposed by Sanders et al. [1988], describes galaxy evolution as driven by mergers that trigger intense star formation, followed by a phase of AGN obscuration and SMBH growth. This phase concludes as the gas is consumed or expelled by stellar or quasar feedback, leading to an unobscured AGN phase [see also Granato et al., 2004, Di Matteo et al., 2005, Hopkins et al., 2008]. Obscuration in this model is primarily attributed to gas within the host galaxy, and some studies suggest it is more prominent in inclined or edge-on galaxies, as well as in galaxies undergoing gas-rich mergers [e.g., Goulding et al., 2012, Buchner and Bauer, 2017]. In contrast, the Orientation model, commonly referred to as the *Unified model* of AGN [Antonucci, 1993], explains obscuration as the result of the observer's viewing angle relative to the accretion disc, which is surrounded by a thick, dusty, molecular torus [see also Urry and Padovani, 1995, Netzer, 2015]. Despite the fact that many studies favour one of these two models, it is likely that both play a role, with obscuration resulting from a combination of galaxy evolution processes and orientation effects.

1.2 Questions I seek to answer

It is clear that there is a lot missing in the study of AGN obscuration, **especially** between the two major theories: Orientation model and Evolutionary model. Most studies focus on one of the models while not accounting for the findings of the other, missing that the most likely situation comes from a mix of the two effects in each AGN. From the perspective of finding the limitations of each theory and a middle ground solution to all the observational evidence pointing out to different parts of both theories, in this thesis I study separately the two models using the same cosmological, semi-analytic catalogue GAEA.

In this scientific context, the primary goal of this thesis is to understand the relative roles of Orientation, Evolution, and other galactic characteristics such as multi-scale gas distributions, in shaping the obscuration of Active Galactic Nuclei through cosmic time. The main scientific questions that I aim to address in this thesis can be summarized as follows:

- What is the effect of the host galaxy **on** shaping the AGN obscuration?
- What is the effect of the torus in shaping the AGN obscuration under an Orientation model and Evolutionary models?
- What is the effect of the gas fractions in shaping the AGN obscuration?
- What is the effect of the light curve (accretion rate and AGN luminosity with time) in shaping the AGN obscuration under Orientation and Evolutionary models?
- Is there any other variables that could substantially affect the AGN obscuration?
- Do I find differences in the clustering of AGN with different obscuration with the same stellar mass?
- What is the predicted redshift evolution of AGN obscuration?

The answer to these questions will improve our understanding of the mechanisms of AGN obscuration and how they fit within the broader context of AGN evolution. Ultimately, this is connected to galaxy evolution and the growth of supermassive black holes, facilitating our understanding of the Universe. To address these questions, I analyse the galaxy catalogue of the semi-analytic model GAEA, which includes state-of-the-art analytic prescriptions for AGN feedback and black hole growth, making it an ideal, self-consistent and flexible model to study the obscuration and evolution of AGN galaxies. I also include analytic models throughout the thesis that complement GAEA catalogues, such as analytic light curves, or empirical models from direct observations.

1.3 Thesis outline

In this thesis I present the analysis of AGN galaxies making use of the GAEA catalogue from the perspective of Orientation and Evolutionary models. This thesis is organised as follows.

First, the introduction and background **of** this study are found in Chapter 1, followed by **a** summary of the scientific background of AGN in Chapter 2 and of the adopted cosmological models in Chapter 3. In particular, I will describe the characteristics of what is considered an AGN, how they are classified, where and how obscuration affects the galaxy, and finally comment **on** the state-of-the-art X-ray observations and models relevant for this thesis.

In Chapter 4 I will describe the methodology followed to model obscuration in AGN. I will provide details on how to calculate the column density distribution, the Eddington ratio distribution, and how to include a torus model.

Chapter 5 includes the results and discussion of the Orientation model, the effect of multi-scale gas distributions, and the contribution of the torus in the AGN obscured fractions.

In Chapter 6 I will show the implications of several Evolutionary models described by different underlying light curves and distinct phases of obscuration in the host galaxy. I will also study the effect of a mixed model with Evolution and Orientation elements and the possible contributions of starbursts and mergers to the CTK population of AGN.

Chapter 7 covers the analysis of additional key predictions from the reference Orientation and Evolutionary models, namely Eddington ratio distributions and clustering.

Finally, in Chapter 8 I will discuss the main results of this thesis, draw my conclusions, and provide ideas for future directions.

As part of the thesis project, other minor studies have been carried out in parallel to the main findings. Despite those projects not being a key part of the main research, they have been useful to either produce some of the results or to increase the statistical analysis of data in general. This work, not directly related to the thesis objectives but still relevant, has been included in the Appendixes.

The project described in Appendix A was aimed to help with the production of the next major update of the GAEA model, now starting to be published as De Lucia et al. [2024], Fontanot et al. [2024]. That project was focused on using the model to reproduce results from previous papers, and give a first test of the new implementations, helping the main developers to find incompatibility, numerical or output problems.

In Appendix B, I dive in alternative approaches to probe AGN obscuration by calculating the column density on a hydro-simulated AGN galaxy.

Finally, and a bit outside of the scope of this work, a project based on the analysis of maritime transportation and trajectories was developed as part of an internship in Data Science with the company OmegaLambdaTec in Munich (Germany), which is mentioned in Appendix C.

1.4 Original sources

Most of the original work presented in this thesis has been published or submitted for publication. The original journal articles are listed below:

 Alonso-Tetilla et al., "Probing the roles of the orientation, and multi-scale gas distributions in shaping the obscuration of Active Galactic Nuclei through cosmic time", 2024, MNRAS, 527, 10878.

- Alonso-Tetilla et al., "Probing the roles of the evolution in shaping the obscuration of Active Galactic Nuclei through cosmic time", 2024, submitted to MNRAS.
- Alonso-Tetilla et al., "Probing the roles of Eddington ratio distribution in shaping the obscuration of Active Galactic Nuclei", 2025, to be submitted.

Additional papers to which I have contributing during my PhD are listed below:

- Andonie et al., "Obscuration beyond the nucleus: infrared quasars can be buried in extreme compact starbursts", 2024, MNRAS, 527, L144.
- Fu et al., "Unveiling the (in)consistencies among the galaxy stellar mass function, star formation histories, satellite abundances, and intracluster light from a semi-empirical perspective", 2024, MNRAS, 532, 177.
- Laloux et al., "Accretion properties of X-ray AGN: evidence for radiation-regulated obscuration with redshift-dependent host galaxy contribution", 2024, MNRAS, 532, 3459.
- Lopez et al., "IRX-CIGALE: a tailored module for Low-Luminosity AGN", 2024, submitted to A&A.
- Euclid Collaboration et al., "Euclid. I. Overview of the Euclid mission", 2024, submitted to A&A special issue 'Euclid on Sky'.
- Shankar et al., "Revealing AGN feedback from the residuals of SMBH scaling relations: dominance of stellar velocity dispersion and host halo mass", submitted to MNRAS.

An introduction to GAEA, a list of their recent work, as well as datafile containing published model predictions, can be found at https://sites.google.com/inaf.it/gaea/home.

Chapter 2

Active Galactic Nuclei

2.1 Historical Overview

The history¹ of active galactic nuclei (AGN) can be traced back to the first optical spectrum of an active galaxy, which revealed strong emission lines in the nebula NGC 1068 [Fath, 1909]. However, it was Seyfert [1943] who first identified a distinct class of galaxies with similar characteristics. These galaxies, which exhibited high central surface brightness, were distinguished by optical spectra dominated by high-excitation nuclear emission lines. Following this discovery, Woltjer [1959] tried to understand the underlying physics of the Seyfert [1943] galaxies, arriving at several key conclusions:

- The nuclei of these galaxies were unresolved, implying a nuclear region with a size smaller than 100 parsecs.
- These types of (spiral) galaxies could either represent a constant state or a phase in galaxy evolution. In the latter case, if the Universe is approximately 10^{10} years old and 1 out of 100 galaxies is a spiral, the duration of this phase would be $10^{10}/100 = 10^8$ years.
- Assuming that the material surrounding the nucleus is gravitationally bound, the mass of the nucleus must be substantial, as indicated by virial theorem arguments. If the galaxy has a large radius and the nucleus is less than 100 pc, then the mass contained in the central region must be on the order of 10% of the total galaxy mass. If the galaxy radius is small, it suggests that the galaxy is generating an extraordinary amount of energy within a very small volume.

The first radio surveys with sufficient angular resolution, conducted in the late 1950s, revealed the existence of *quasars*. These surveys [e.g., Edge et al., 1959, Pilkington and

¹See Peterson [1997].

Scott, 1965, Gower et al., 1967, Ekers, 1969, Ehman et al., 1970] identified most radio sources as resolved galaxies. However, some sources were associated with star-like optical objects, leading to their classification as "quasi-stellar radio sources," later shortened to *quasars*. The emission lines in these quasi-stellar objects were redshifted, which showed that they are not actually stars but extragalactic objects [Schmidt, 1963]. Although the physical nature of these sources was not fully understood at the time, the term "quasar" persists, and it is often used interchangeably with "quasi-stellar objects" (QSOs) in recent literature, including in this thesis. However, some studies distinguish between the two, using "quasar" to refer specifically to radio-loud sources and "QSO" for radio-quiet sources.

AGN were initially divided into two major subclasses: Seyfert galaxies, as characterized by Seyfert [1943], and quasars. The primary distinction between these subclasses lies in the luminosity of the central source. In Seyfert galaxies, the energy emitted by the central source at optical wavelengths is comparable to the total energy emitted by all the stars in the galaxy, typically around $10^{11}L_{\odot}$. In contrast, quasars are significantly brighter, emitting more than 100 times the luminosity of the stars in their host galaxies.

These objects, characterized by their extreme luminosities, were quickly recognized as critical to our understanding of galaxy formation and evolution. Two major theoretical connections were made early on: Burbidge et al. [1963] linked active galactic nuclei to galaxy formation and evolution, while Zel'dovich and Novikov [1964] proposed that supermassive black holes (SMBHs) might play a central role in powering these luminous sources.

2.2 AGN structure

The most widely accepted structure of AGN is closely associated with the *Unified* model of AGN [Antonucci, 1993, Urry and Padovani, 1995], which is often used for illustrative purposes despite some limitations (Figure 2.1). While further discussion of the Unified model and its relevance to this work, as well as characteristics beyond its framework, will be presented in Section 2.5, the key features proposed by this model remain foundational in our understanding of AGN structure.

As depicted in Figure 2.1², the AGN structure, extending from the innermost to the outer regions of the host galaxy, comprises several key components. At the centre lies the SMBH, surrounded by an accretion disc, with the *broad line region* (BLR) and *narrow line region* (NLR) situated at increasing distances from the nucleus, and an obscuring torus encompassing these regions. This configuration exists within a few kiloparsecs (kpc) of the SMBH and is influenced by its gravitational forces and the galaxy gravitational potential, depending on the broad line region or narrow line region (see Section

²https://www.isdc.unige.ch/~ricci/Website/Active_Galactic_Nuclei.html

2.2. AGN structure 9

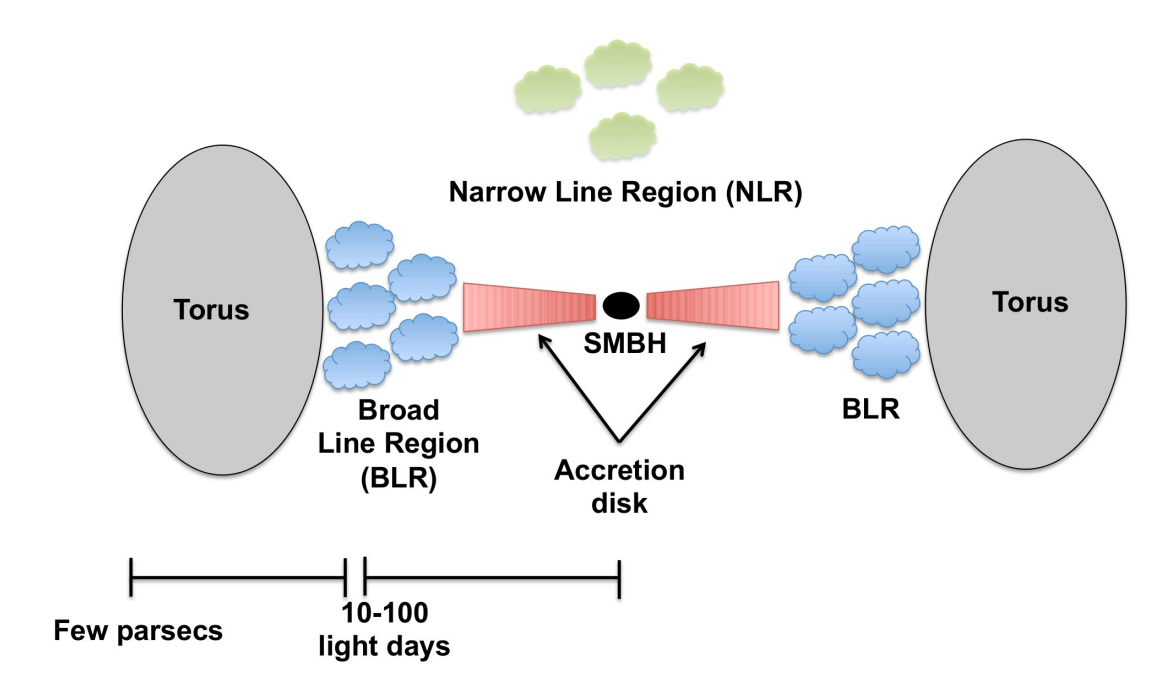


FIGURE 2.1: Schematic diagram of the inner parts of the AGN. Image credit: Claudio Ricci.

2.2.5. Additionally, other galactic components, such as the stellar disc, gas disc, and star formation processes, can also impact the AGN and its evolution.

2.2.1 Super-massive Black Hole (SMBH)

In the AGN model, the galaxy hosts a central SMBH with a mass range of approximately 10^6 to $10^9 M_{\odot}$ [Kormendy and Richstone, 1995], which grows through mass accretion. The existence of black holes was first predicted by Einstein [1916], with direct observational evidence following in Bolton [1972], Webster and Murdin [1972], Event Horizon Telescope Collaboration et al. [2019]. The presence of SMBHs at the centres of AGN was initially proposed by Zel'dovich and Novikov [1964] and Lynden-Bell [1969] and later confirmed through various observations. SMBHs play a crucial role in AGN structure, as their accretion processes provide a natural explanation for the extreme luminosities observed in AGN.

However, accretion is not continuous throughout the life of the SMBH but occurs in intermittent, relatively short phases of active growth, blended with longer periods of quiescence (inactivity). The ratio of actively accreting SMBHs to non-accreting ones (e.g., the Milky Way and Sagittarius A*) remains unknown. Investigating AGN obscuration may shed light on this aspect of AGN evolution, potentially offering insights into the fraction of time SMBHs spend in their active phases.

2.2.2 Accretion disc

The accretion disc is a structure that forms around the SMBH (circumnuclear region) when diffuse material, including gas and dust, migrates from galactic scales to sub-kiloparsec distances with a certain amount of angular momentum. As this material infalls, it heats up, producing electromagnetic radiation that peaks in the ultraviolet (UV) wavelength range. The properties of the accretion disc, such as its thickness, size, and column density, can vary significantly [Netzer, 2013].

Shakura and Sunyaev [1973] provides a model to explain the spectra observed from accreting stellar black holes, defining the bolometric luminosity of the accretion disc as:

$$L_{\text{bol}} = \mu \dot{M}_{\text{BH}} c^2, \tag{2.1}$$

where $\dot{M}_{\rm BH}$ is the accretion rate, c is the speed of light, μ represents the radiative efficiency, and $L_{\rm bol}$ is the bolometric luminosity, representing the total luminosity emitted by the accretion disc across the entire electromagnetic spectrum. As discussed in Chapter 3, I adopt a radiative efficiency parameter μ given by:

$$\mu = \frac{\epsilon_{\rm rad}}{1 - \epsilon_{\rm rad}} \sim 0.18, \ \epsilon_{\rm rad} \sim 0.15, \tag{2.2}$$

where $\epsilon_{\rm rad}$ is the parameter historically adopted by SAMs, and particularly used in GAEA.

Accretion onto the SMBH is constrained by radiation pressure. When radiation pressure balances the gravitational force of the SMBH, the AGN reaches a luminosity known as the Eddington luminosity, which is defined by:

$$L_{\rm Edd} = \frac{4\pi G M_{\rm BH} m_p c}{\sigma_{\rm T}} \sim 1.3 \cdot 10^{38} \frac{M_{\rm BH}}{M_{\odot}} \, \rm erg/s, \tag{2.3}$$

assuming a purely ionized medium and spherically symmetric geometry. Here, $M_{\rm BH}$ denotes the mass of the black hole, G is the gravitational constant, m_p is the proton mass, and $\sigma_{\rm T}$ is the Thomson scattering cross-section.

Furthermore, the Eddington luminosity can be expressed in terms of the accretion rate using the relation $L_{\rm Edd} = \mu \dot{M}_{\rm Edd} c^2$ from Equation (2.1) when the accretion luminosity is equal to the Eddington luminosity. Consequently, the ratio of the bolometric luminosity to the Eddington luminosity (or *Eddington limit*), known as the *Eddington ratio*, is given by:

$$\lambda_{\rm Edd} = \frac{L_{\rm bol}}{L_{\rm Edd}}. (2.4)$$

The Eddington ratio classifies sources into two regimes: sub-Eddington ($\lambda_{Edd} < 1$) and super-Eddington ($\lambda_{Edd} > 1$).

Alternative accretion scenarios have been proposed over the years [e.g., Bondi, 1952], but these models are not considered in the present study and fall outside the scope of this thesis.

2.2.3 Corona

Katz [1976] suggested that, in order to explain the X-ray spectrum observed in AGN, there is a corona of hot electron gas, which undergoes Comptonization of optical-UV photons near or within the accretion disc. This corona exhibits a power-law decline in its emission, resulting from inverse Compton scattering. The X-ray spectrum, characterized by variability on timescales of days or shorter [McHardy, 1989], supports the accretion disc-corona model [Ghisellini, 1993]. However, the mechanisms sustaining the corona and its interactions with the accretion disc remain poorly understood [see Section 1.2.5 of Ricci, 2011, for a comprehensive review]. A more detailed discussion of X-ray emission in AGN galaxies will be provided in Section 2.4.

2.2.4 Obscuring material

The X-ray power-law of the corona has been observed to change due to the presence of cold material along the line of sight [Mushotzky, 1982, Turner et al., 1998, Risaliti et al., 1999]. Some studies have sought to explain the differences between AGN that exhibit clear X-ray emission and those obscured by material preventing the detection of a clear spectrum. The exact nature of the obscuring material and the number of heavily obscured AGN remain uncertain. However, it is well established that obscured sources exist, as the X-ray background cannot be fully explained without accounting for them [Fabian and Iwasawa, 1999, Gilli et al., 2007, 2010, 2011, 2022, Hickox and Alexander, 2018]. Among the two most popular explanations for this obscuration are the orientation-based model, commonly referred to as the *Unified model* [Antonucci, 1993], and the evolutionary-based model [e.g., Sanders et al., 1988, Hopkins et al., 2008, and references therein]. These models will be further explored in Section 2.5. The Unified model proposes a torus-like structure, characterized by its compact and dusty nature, as the source of the required obscuration, which is absent from the ISM but consistent with observations [Gilli et al., 2022, Alonso-Tetilla et al., 2024]. This structure will also be discussed in detail in Section 2.5.

2.2.5 Emission lines

Spectral observations have shown a division between broad and narrow emission lines, which originate from different regions of the AGN nucleus. This division is crucial for modelling AGN types, as clear evidence for a continuous transition between these two

types of emission has not yet been observed, suggesting the existence of two distinct classes of AGN (see Section 2.3).

Broad emission lines. The strong, broad emission lines characteristic of AGN are prominent in the UV-optical spectra of quasars. While most quasars display these lines, some may be obscured from detection due to redshift effects or limitations in the spectral window of the detector [Peterson, 1997]. The region responsible for broad emission, known as the Broad Line Region (BLR), is composed of dense clouds of ionized gas [approximately 10^{10} cm⁻³ Netzer, 2013]. Variability studies of these broad lines have shown that the BLR extends over a range of distances from the supermassive black hole (SMBH), from 10 to 100 light-days in Seyfert Type 1 AGN (see Section 2.3) to several light-years in brighter quasars [e.g., Netzer, 1990]. This region is located very close to the SMBH, typically at sub-parsec or parsec-scale distances [Netzer, 2013].

Narrow emission lines. In contrast, the Narrow Line Region (NLR) is significantly larger than the BLR and produces narrower emission lines [Netzer, 2013, 2015]. The NLR exhibits low variability in its emission lines [Netzer, 1990] and is characterized by a lower gas density [approximately 10^4 cm⁻³ Netzer, 2013], with a typical spatial extent of 100-300 pc. In more luminous quasars, the NLR can be even larger, spanning several kiloparsecs in diameter. When this region extends beyond several kiloparsecs, it is referred to as the extended narrow line region (ENLR). The narrow emission lines are produced as ionized gas clouds are excited by the radiation field of the AGN from the **inner** regions of the AGN.

2.2.6 Jets

Jets are highly collimated structures, ranging in size from parsecs to hundreds of kiloparsecs, that are ejected from the central regions of galaxies and extend to distances often exceeding the total size of the host galaxy [Jennison and Das Gupta, 1953]. These jets, characterized by tightly collimated magnetic fields, propagate at relativistic velocities and can be detected across multiple wavelengths.

2.2.7 Other AGN characteristics

Radio Properties of Quasars. The radio morphology of quasars and radio galaxies can be divided into two main components: *extended* and *compact*. In both cases, the emission is believed to be powered by the synchrotron mechanism [for more information on synchrotron radiation, see Walker, 1994]. The extended component, which is "spatially resolved", typically exhibits a double-lobed structure, with two radio emission lobes located on either side of the quasar or galactic centre. These lobes can be symmetric or

2.2. AGN structure 13

asymmetric and span distances on the order of Mpc. In contrast, the compact component is unresolved at approximately $\sim 1''$ resolution, and quasars are often associated with these compact radio sources. The amount of radio emission produced by an AGN is a key factor in its classification, particularly in distinguishing between radio-loud and radio-quiet quasars.

Variability. AGNs have been found to be variable at all wavelengths at which they have been observed, and those variations appear to be aperiodic and have variable amplitude [Peterson, 1997]. This characteristic is one of the earliest studied properties of quasars [Smith and Hoffleit, 1963], and the quasar light variability can occur on timescales ranging from a few months [e.g., Soldi et al., 2014] to just a few days [e.g., Pica and Smith, 1983, Smith et al., 2018]. This variability is a fundamental characteristic in the evolutionary model of AGN, which attributes differences in AGN classifications to the evolutionary stages of the AGN.

Scaling Relations. Scaling relations represent correlations between various parameters that describe the physical properties of galaxies [D'Onofrio et al., 2021], and they are crucial for understanding the co-evolution of SMBH and their host galaxies [e.g., Kormendy and Richstone, 1995, Volonteri and Natarajan, 2009]. Notable examples relevant for AGN include scaling relations between SMBH mass and their host galaxy properties like the SMBH mass and stellar mass relation, $M_{\rm BH}-M_{\star}$, or the SMBH mass and velocity dispersion relation, $M_{\rm BH}-\sigma$ [e.g., Gebhardt et al., 2000, Menci et al., 2023]. There are currently many sources for the study of AGN scaling relations, however sometimes they present significant systematic offsets with respect to the local relations [Reines and Volonteri, 2015, Shankar et al., 2019, Farrah et al., 2023]. For a comprehensive review on scaling relations of galaxies, AGN, and associated models, see D'Onofrio et al. [2021].

AGN Feedback. AGN feedback refers to the self-regulating process by which energy released by the AGN influences its surroundings and host galaxy [Morganti, 2017]. This feedback can impact several aspects, such as limiting SMBH growth, triggering quenching, affecting cooling mechanisms, influencing nuclear activity, and regulating the AGN duty cycle, which is the ratio of the time intervals during which the AGN is active and inactive. AGN feedback is typically classified into two modes: *QSO-mode* and *Radio-mode*. The QSO-mode is associated with high-luminosity AGN emitting near the Eddington limit, where the feedback manifests as radiation or wind from the accretion disc, and sometimes through jets. This mode is responsible for driving gas out of the host galaxy. In contrast, the Radio-mode is linked to lower-luminosity AGN and involves kinetic energy transfer, primarily via jets. Distinguishing between these two feedback modes often requires multi-wavelength observations [Fabian, 2012], and I will examine some of their effects, like a Blast Wave, in Chapter 5. Both models are included in GAEA and in this thesis I will be mostly focusing on the QSO-mode.

Demography. The different AGN characteristics described previously underscore the importance of developing a comprehensive AGN demography [Bianchi et al., 2022], which involves consistent definitions across wavelengths of what constitutes an AGN, as opposed to AGN *candidates*, and establishing clear boundaries for various AGN characteristics and parameters (e.g., stellar mass M_{\star} , star formation rate (SFR), etc.). Recent studies suggest that the James Webb Space Telescope (JWST) may play a pivotal role in advancing AGN demographic research [Lyu et al., 2023]. However, a complete census of AGN, including their evolution and relationship with non-AGN galaxies, remains ambiguous. My study of obscuration pretends to contribute to this goal.

Host Galaxy. While the AGN represents the high-energy environment surrounding the SMBH, the host galaxy also plays a significant role and is affected by AGN activity. Kormendy and Ho [2013] provide a detailed review of the relationship between SMBHs and their host galaxies, which can also be applied to AGN-hosting galaxies. Early work by Sanders et al. [1988] proposed a connection between galaxy mergers, gas inflow, star formation, and AGN fueling, suggesting that AGN triggering may be linked to the environment of the host galaxy. In this scenario, the host galaxy would become increasingly luminous, evolving from infrared levels to bright quasar-like luminosities. Hopkins et al. [2005] similarly predicted that galaxy mergers could trigger a short, luminous AGN phase. AGN activity also exerts feedback on the host galaxy, influencing processes such as star formation quenching [Cattaneo et al., 2009]. Thus, it is essential to understand the properties, structure, and formation of AGN host galaxies, particularly in relation to obscuration and the associated material, to gain a comprehensive understanding of the intricate co-evolution of SMBHs and their hosts.

2.3 AGN classification

The defining characteristic of all AGN is their emission in the X-ray regime [Elvis et al., 1978]. However, AGN classification began earlier, when Schmidt [1969] outlined the properties of quasars. These objects were initially identified as star-like sources with radio emission, time-variable continuum flux, significant UV flux, broad emission lines, and large redshifts. Today, we know of AGN and quasars at redshifts as high as $z\sim 12$, thanks to the JWST [Juodžbalis et al., 2023], but in the 1960s, following the first observations [Schmidt, 1963], redshifts of z<1 were considered already large redshifts, and even into the 1990s, quasars at $z\sim 5$ were noteworthy.

The evolving understanding of AGN physics has led to a classification system that has been continuously adapted over time. Initially based on a very basic framework, the classification has been modified to incorporate new characteristics of galaxies. Below, I summarize the primary AGN categories without attempting to propose new classifications.

Seyfert Galaxies. First described by Seyfert [1943], Seyfert galaxies are characterized by bright nuclear regions and unusual emission-line features in their spectra. These galaxies appear as distant spirals with a bright central nucleus resembling a star. Khachikian and Weedman [1974] introduced the distinction between two types of Seyfert galaxies: *Type 1* Seyfert galaxies exhibit both narrow and broad emission lines, with narrow lines corresponding to low-density ionized gas and velocities of several hundred km s⁻¹, and broad lines with widths up to 10⁴ km s⁻¹. In contrast, *Type 2* Seyfert galaxies only display narrow lines in their spectra. The origin of this difference remains unclear, and it led to the development of the Unified Model of AGN (see Section 2.5).

Quasars. Schmidt and Green [1983] established the distinction between Seyfert galaxies and quasars based on the lower luminosity of Seyfert AGN. While the spectra of quasars and Seyfert galaxies are quite similar, quasars show two notable differences: (a) weaker narrow emission lines compared to Seyferts, and (b) weak stellar absorption features. Although radio emission originally defined quasars, only a small fraction of the quasars detected are radio-loud, with radio galaxies forming a distinct class.

Radio Galaxies. Historically, radio galaxies were considered a separate class of AGN until the broader classification of AGN into radio-loud and radio-quiet subtypes was established. Radio galaxies are further divided into broad-line radio galaxies (BLRGs) and narrow-line radio galaxies (NLRGs), corresponding to the radio-loud analogues of Seyfert Type 1 and Type 2 galaxies, respectively [Peterson, 1997]. An early approach to AGN classification distinguished between radio-loud and radio-quiet objects, based on initial observations of radio sources. By examining the *U*-excess³, quasars could be identified by comparing the same region of sky through *B* and *U* filters [Ryle and Sandage, 1964]. This method yielded a significant population of quasar-like objects, enabling the optical selection of quasars [Sandage, 1965]. Optically selected quasars have distinct spectral energy distributions (SEDs, see Figure 2.2) compared to radio-selected quasars, with radio-quiet quasars exhibiting radio emissions about 100 times weaker relative to their UV-optical-infrared emission. It soon became evident that radio-loud quasars represent only a small subset of the AGN population, while radio-quiet quasars are far more common [Peterson, 1997].

LINERs. Low-Ionization Nuclear Emission-line Region (LINER) galaxies are distinguished by their spectra, which exhibit stronger emission from weakly ionized or neutral atoms compared to strongly ionized atoms, in contrast to more luminous AGN [Heckman, 1980].

 $^{^{3}}$ Referring to Johnson UBV photometry, where the U-B colour index is small (i.e., negative) in quasars, indicative of an ultraviolet excess. Quasars also occupy a region of colour-colour diagrams that is not densely populated by stars [Hewitt and Burbidge, 1993].

Blazars. Blazars are highly variable galaxies characterized by relativistic jets aligned with the observer's line of sight, causing them to appear much brighter than jets pointing in other directions. This category includes BL LAac objects [Blandford and Rees, 1978], intrinsically low-power radio galaxies, and optically violently variable (OVV) quasars, which are intrinsically powerful radio-loud quasars.

Little Red Dots. In the last observations of the JWST, some galaxies appeared with massive black holes just a few million years after the origin of the Universe. These galaxies, seen as *Little Red Dots* in the long exposure images of the early Universe, are believed to be compact galaxies with obscured AGN [e.g., Labbe et al., 2023, Xiao et al., 2023, Killi et al., 2023, Baggen et al., 2024], which could be the reason why they appear with a red colour and why they are easily observed in the infrared, but seems to have intrinsically weak X-ray [e.g., Maiolino et al., 2024]. Since this thesis is focused on X-ray data, I will not be including these sources in my sample, despite mentioning briefly how they can affect to the results.

Given these findings, comparisons across different wavelengths are essential. Optically selected samples tend to be dominated by radio-quiet quasars but may still contain some radio-loud sources. The distinction between radio-loud and radio-quiet quasars remains challenging. For instance, Kellermann et al. [1989] proposed using the radio-to-optical flux ratio as a criterion, though ambiguities persist due to the limitations of radio emission data. Recent studies advocate for an alternative classification system, distinguishing AGN based on the presence or absence of jets [i.e., jetted vs. non-jetted galaxies Padovani et al., 2017], as over 90% of AGN are radio-quiet [Padovani et al., 2011, and references therein].

While the radio-loud versus radio-quiet classification remains widely used, it largely derives from early optical observations. In this study, I adopt a classification scheme based on bolometric and X-ray luminosities, as well as obscuration properties, which are further detailed in Section 2.5.

2.4 AGN emission mechanisms

Due to the wide range of temperatures within the gas of the accretion disc⁴, the emission from AGN spans across various wavelengths, generating an extremely extended SED. Most of the accreted gas has temperatures around $T \sim 10^4 - 10^5$ K [van de Voort et al., 2011], corresponding to an emission in the $\sim 30 - 300$ nm range, which falls within the UV-optical region of the spectrum.

As previously discussed in the context of AGN history, the SED of an AGN accretion disc is distinct from other astrophysical sources, helping in its identification. Figure

⁴The temperature decreases with increasing distance from the SMBH [Hickox and Alexander, 2018].

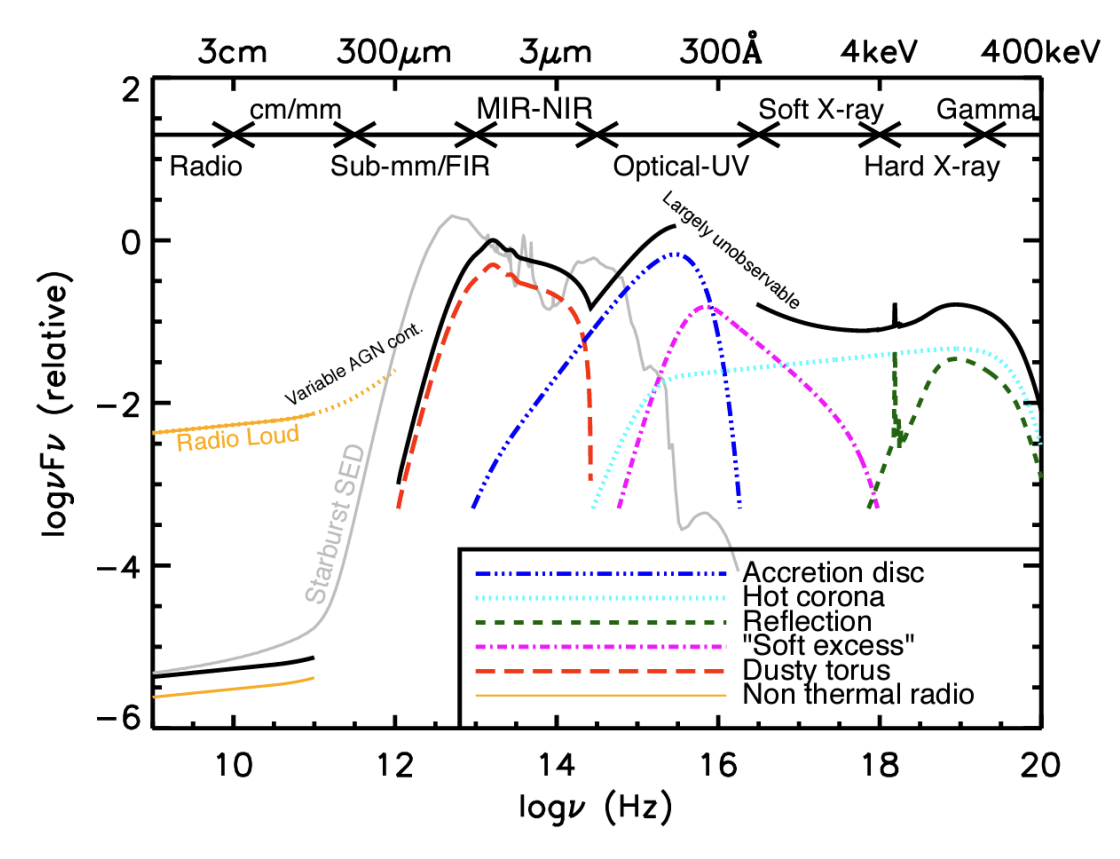


FIGURE 2.2: Figure from Harrison [2014]. Schematic representation of an unobscured AGN SED. The black solid curve is the total SED, and the coloured curves are divided by the main physical components. In gray, an example of starburst (Section 2.5.2 and Chapter 6) galaxy radio-UV SED.

2.2 presents a schematic example of an AGN SED, highlighting its relative contribution across different wavelengths. This Figure underscores the importance of multiwavelength observations for understanding the comprehensive behaviour of AGN and its impact on the host galaxy. Indeed, the SED suggest a continuum spectrum, and its different *bumps* would be result of different parts of the AGN at work. For example, a radio-loud AGN would present a higher SED at lower frequencies than a radio-quiet AGN, therefore their names. The torus emits in the sub-mm/infrarred wavelengths, while the accretion disc appears in the optical-UV wavelengths, known as *the big blue bump*. The hot corona is responsible for the X-rays that might also reflect off the accretion disc and/or the torus, producing the called *reflection* component in the X-ray region [George and Fabian, 1991]. As shown in Figure 2.2, a *soft excess* is often present over the emission of simple accretion disc models, however the origin of this soft excess emission is still a topic of debate [Done et al., 2012].

However, in this study, I focus primarily on X-ray emissions, as they provide one of the most reliable and complete methods for identifying obscured AGN [Hickox and Alexander, 2018]. Other wavelengths are also considered, particularly in relation to their comparison with X-ray luminosities and their role in obscuration classification.

2.4.1 UV/optical emission

The total AGN spectrum, as shown in Figure 2.2 [Harrison, 2014], reveals that the peak emission predominantly lies within the optical-UV regime, primarily due to the Rayleigh-Jeans tail of the accretion disc emission. This behaviour is consistent with the black-body radiation effect of the accretion disc [Page and Thorne, 1974, Thorne, 1974]. In addition, emission lines from both the BLR and NLR are prominent in this regime, originating from the classical torus structure postulated by the Unified Model [see Section 2.5, and also, e.g., Baldwin et al., 1981, Risaliti et al., 1999, Zakamska et al., 2003]. As a result, it is not surprising that the UV/optical regime remains the most frequently observed and studied portion of the AGN spectrum. This is further supported by the availability of extensive imaging and spectroscopic data, as well as the numerous telescopes dedicated to AGN observations, despite the challenges posed by potential contamination from other sources, such as stars, which can be mistaken for AGN if no emission lines are visible.

A significant limitation of UV/optical observations is their bias toward detecting *unobscured* AGN, as these sources have visible broad lines and accretion discs that are not absorbed by the dust in their host galaxies. This issue is especially pronounced when observing NLR emission lines, which are easier to detect than BLR lines but can also arise in star-forming regions, making the presence of narrow lines alone insufficient for conclusively identifying AGN. Furthermore, optical spectroscopic selection is biased against sources with attenuated NLRs, potentially overlooking obscured AGN.

Nevertheless, optical emission remains valuable for studying AGN variability, particularly in low-luminosity AGN [e.g., Villforth et al., 2010].

2.4.2 X-ray emission

Due to the presence of numerous bright non-AGN sources in the optical/UV regime, X-ray emission has often been the preferred energy range for AGN studies, as the majority of bright X-ray sources are likely to be AGN.

X-ray emission in AGN arises from high-energy electrons in the corona, found in the outer regions of the accretion disc, via inverse Compton scattering of UV seed photons. The X-ray spectrum can be divided into two components: soft X-rays (0.2–10 keV, $L_{\rm X} > 10^{42}~{\rm erg~s^{-1}}$) and hard X-rays (10–200 keV), bridging the gap between UV (below 0.2 keV) and γ -rays (above 200 keV, see Figure 2.2). This distinction between soft and hard X-rays roughly corresponds to the sensitivity of X-ray observatories and the absorption by intervening column density gas (Section 2.5). X-ray luminosities, both observed and intrinsic, are typically much higher in AGN compared to stellar processes, such as those

from hot gas or X-ray binaries, making X-ray wavebands a reliable criterion for AGN identification.

As mentioned, the hot corona is believed to be the primary source of X-ray emission in AGN [Hickox and Alexander, 2018, Beard, 2023], and a correlation between X-ray and UV-optical emission has been established for unobscured AGN [Steffen et al., 2006, Lusso and Risaliti, 2016].

2.5 AGN obscuration

In the X-ray regime, AGN can be further classified based on their level of obscuration, independent of their radio emission or luminosity. Obscuration refers to the presence of intervening material along the line-of-sight that blocks or attenuates the emission from the AGN accretion disc, making it difficult to detect the AGN in certain wavelengths [Hickox and Alexander, 2018]. The degree of obscuration is typically measured using the hydrogen column density, $N_{\rm H}$, along the line-of-sight, which quantifies the number of hydrogen atoms per square centimetre along the line of sight. This value helps describe the amount of material that lies between the observer and the central source, affecting how much radiation is absorbed or scattered before it reaches us.

The Compton *limit* is commonly defined as the point at which the obscuration becomes so high that the material around the AGN becomes Compton-thick, meaning X-rays with energies lower than 10 keV are absorbed by the material in the line of sight. At lower energies (below 10 keV), X-rays are primarily absorbed by the photoelectric effect, which depends on the atomic number of the absorbing medium. Hydrogen and helium, as the most abundant elements, dominate the absorption cross-section. The Compton limit occurs at column densities around $N_{\rm H} \sim 1.5 \cdot 10^{24} \ {\rm cm}^{-2}$ [Peterson, 1997]. The critical density related to the Compton limit is derived by calculating when the Thomson optical depth, which is the probability that a photon is scattered by an electron, reaches unity. At this limit, the material is so dense that even high-energy X-rays (>10 keV) are scattered or absorbed due to the large amount of gas. At high column densities, Compton scattering becomes significant. X-rays lose energy upon interacting with free or weakly bound electrons. For very high $N_{\rm H}$, the scattering cross-section becomes comparable to or greater than the absorption cross-section, leading to a large fraction of the X-rays being scattered out of the line of sight. The limit represents a critical threshold where the gas density is high enough to significantly scatter or absorb even high-energy X-rays, limiting the amount of observable radiation from the AGN. For a mathematical derivation of this limit see Peterson [1997], Longair [2011].

AGN can be categorized as *unobscured* if the column density is $log(N_H/cm^{-2}) < 22$, which allows the X-ray spectrum to appear similar to the optical one. These sources are also referred to as *UV/optically visible* AGN in this thesis. Conversely, if the column

density exceeds $log(N_H/cm^{-2}) > 22$, the spectrum becomes attenuated, classifying the galaxy as an *obscured* AGN.

Within the obscured category, a further distinction is often made based on Compton scattering. In this thesis, I use this Compton limit to divide the obscuration in Compton-thin (CTN, obscured AGN with column densities in the range $22 < \log(N_{\rm H}/{\rm cm}^{-2}) < 24$) or Compton-thick (CTK, those with $\log(N_{\rm H}/{\rm cm}^{-2}) > 24$) obscuration. Some studies introduce an additional subclass for *heavily* obscured AGN, referring to sources with $\log(N_{\rm H}/{\rm cm}^{-2}) > 23$.

While this classification is adopted in this study, alternative methods are also used in the literature, including measurements based on X-ray hardness ratios, the ratio of observed X-ray luminosity to intrinsic AGN luminosity (derived from infrared or optical data), or a high equivalent width of the Fe K α line, indicating strong reflection features [Greenwell, 2023].

2.5.1 Unified Model

As previously discussed, the classification of AGN has been a topic of extensive debate and study, aimed at understanding their characteristics, evolution within galaxies, and cosmological context. A significant milestone in this effort was the development of the *Unified Model*, originally proposed by Antonucci [1993]. According to this model, all AGN types are fundamentally the same but appear different due to the angle at which they are observed relative to the line-of-sight. The goal of this model was to provide a framework that required the fewest assumptions to explain the observed diversity of AGN types (illustrated in Figure 2.3). For instance, the two Seyfert subtypes are explained by the presence of an obscuring structure within the galaxy, which, depending on the viewing angle, can block the BLR from view. This causes the galaxy to be classified as either Type 1 or Type 2, or as one of the intermediate types [Osterbrock, 1981].

The Unified Model envisions the AGN structure as follows. At the centre of the galaxy is a SMBH accreting matter via an accretion disc. Gas within the host galaxy, when close enough to the SMBH (at scales much less than a parsec), becomes ionized and is strongly influenced by the gravitational field of the black hole as it moves inward. The gravitational potential energy lost during this inward migration is radiated away, predominantly in the form of X-ray emission, broad emission lines, and accretion disc emission (optical/UV). This region, characterized by high-velocity gas close to the black hole, is referred to as the BLR. The accretion disc itself forms as a consequence of the angular momentum conservation of the inflowing material. Further out from the SMBH, there exists a region of lower-density gas that moves more slowly and is less

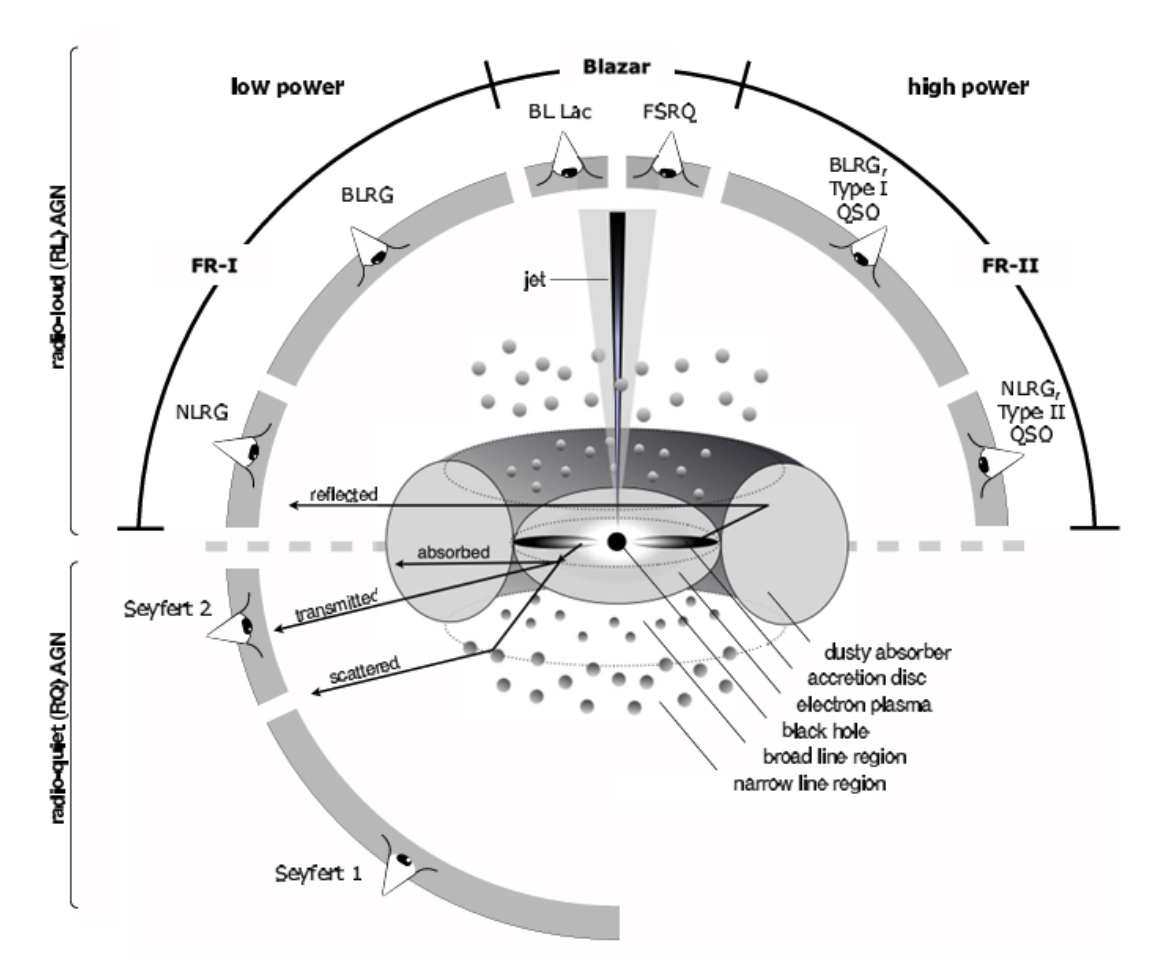


FIGURE 2.3: Figure and caption from Beckmann and Shrader [2012]. Schematic representation of our understanding of the AGN phenomenon in the unified scheme [1]. The type of object I see depends on the viewing angle, whether or not the AGN produces a significant jet emission, and how powerful the central engine is. Note that radio loud objects are generally thought to display symmetric jet emission. Graphic courtesy of Marie-Luise Menzel (MPE).

affected by the gravity of the black hole. This region produces narrow emission lines and is known as the narrow-line region (Section 2.2).

2.5.1.1 Torus

A torus-like structure, commonly referred to as *the torus*, is thought to surround the central region of AGN and plays a critical role in obscuring the BLR, allowing only the narrow emission lines to be visible.

The geometry of the torus has been a subject of considerable debate. Initially, it was modelled as a thick, *doughnut*-shaped structure by Antonucci [1993]. However, more recent models propose a thinner or variable-thickness torus [Ramos Almeida and Ricci, 2017], which may depend on galaxy properties such as luminosity [Wada, 2015] and could potentially evolve with redshift on cosmological scales.

Regardless of its specific geometry, there is substantial evidence supporting the existence of the torus in nearby galaxies [e.g., García-Burillo et al., 2016, 2019, 2021]. Therefore, research should shift from questioning the role of the torus role in obscuration to understanding *how* this obscuration occurs and determining its physical limits. This thesis focuses on analysing the fundamental characteristics required for a torus to match observational data (see Chapter 5). Additionally, it examines the constraints in terms of luminosity dependence and lifetime imposed by both the Orientation model (Chapter 5) and the Evolutionary model (Chapter 6).

2.5.2 Evolutionary model

AGN have been observed to evolve in tandem with their host galaxies, influenced by interactions with other galaxies and their environments (see Section 2.2). Understanding the co-evolution of AGN and their host galaxies is crucial for a comprehensive understanding of AGN and SMBHs.

While the Orientation model successfully explains many aspects of AGN that were previously unaccounted for, there are still observational phenomena that it does not address. Gas-rich mergers [e.g., Hopkins et al., 2005, 2008, and references therein] may trigger significant increases in SFR, leading to enhanced gas inflow into the central SMBH and potentially altering AGN activity, whilst inducing a dust-enshrouded phase in the host galaxy. Moreover, evolution in the level of obscuration has been suggested [e.g., Lapi et al., 2006, Hopkins et al., 2008, Lapi et al., 2014], which could also influence other galactic components such as the torus. Promoted by these theoretical frameworks, Chapter 6 will investigate the interplay between Orientation and Evolution models and their relative influences.

Additionally, studies on the AGN LF, which examine the distribution of AGN as a function of redshift and their comoving space density, provide insights into how AGN evolve over time [Peterson, 1997, Shen et al., 2020]. The bolometric AGN LF and AGN emissivity has been shown to peak around z=2, and then to steadily decrease since those epochs (although new measurements from JWST are finding evidence for a large population of AGN even at z>4, I will not discuss these new findings in detail in this thesis, as further discussed in Section 6.12). At the same time, a significant number of obscured galaxies, observed in the submm [Alexander and Hickox, 2012, Alexander et al., 2016] and FIR from Herschel [Lapi et al., 2017], have also been observed at $z\sim2-3$, which may be examples of dust-enshrouded, obscured AGN. This thesis will focus on this redshift range and will address the role of evolutionary processes, including mergers and starbursts [e.g., Ellison et al., 2008, Knapen et al., 2015, Silva et al., 2021, Horstman et al., 2021] in driving obscuration in AGN.

2.5.3 Orientation and Evolutionary as complementary models

Observations indicate that both orientation and evolutionary effects can play a role in obscuring the AGN [e.g., Polletta et al., 2008, 2011]. For example, *Type* 2 AGN (as mentioned in Section 2.3) lack broad emission lines. This characteristic is usually interpreted as an orientation effect since broad emission lines are believed to originate in the inner clouds orbiting the central black hole, which, assuming typical covering factors of $\sim 20-40\%$ [Khachikian and Weedman, 1974, Peterson, 1997, Kuhn et al., 2024], should remain invisible to edge-on lines of sight intersecting the torus aperture. On the other hand, galaxies hosting *Type* 1 AGN appear in several instances more massive than *Type* 2 AGN, at odds with expectations from basic Unification models [Ricci et al., 2022b]. In a similar vein, some studies suggest that AGN are ubiquitous in starburst and actively star-forming galaxies at different redshifts [e.g., Alexander et al., 2005, 2016, Rodighiero et al., 2015, Mullaney et al., 2015, Mountrichas and Shankar, 2023, Mountrichas et al., 2024, and references therein], in line with predictions from Evolutionary models.

An evolutionary connection between star formation, black hole accretion and fuelling [Granato et al., 2006, Shankar et al., 2004, 2012, 2016], and AGN obscuration is expected given their common dependence on the cold gas content of the host galaxy itself [e.g., Harrison, 2017]. In the context of Evolutionary models, in fact, many works have identified the presence of galaxies with high cold gas fractions and star formation rates (SFRs) in the obscured AGN population because of, e.g., high levels of dust [e.g., Afonso et al., 2003, Wijesinghe et al., 2011, Chen et al., 2015] as well as carrying the signatures of relatively recent mergers [e.g., Darg et al., 2010, Ricci et al., 2017a, Yutani et al., 2022, Pierce et al., 2023].

2.5.4 Merger and starburst galaxies

In the framework of Evolutionary models, numerous studies have highlighted the impact of high cold gas fractions and elevated SFRs [e.g., Afonso et al., 2003, Wijesinghe et al., 2011, Chen et al., 2015], as well as recent merger activity [e.g., Darg et al., 2010, Ricci et al., 2017a, Yutani et al., 2022], on AGN obscuration. Starbursts and enhanced SFRs are frequently driven by mergers and galaxy interactions, as supported by both observational studies [e.g., Armus et al., 1987, Kennicutt et al., 1987, Xu and Sulentic, 1991, Sanders and Mirabel, 1996, Ellison et al., 2008, 2013, Knapen et al., 2015, Silva et al., 2021, Horstman et al., 2021, Andonie et al., 2024] and simulations [e.g., Hernquist and Katz, 1989, Barnes and Hernquist, 1991, Springel and Hernquist, 2005, Di Matteo et al., 2008, Saitoh et al., 2009, Karl et al., 2010, Teyssier et al., 2010, Moreno et al., 2015, 2019, Renaud et al., 2014, 2018, 2022, Linden and Mihos, 2022], and can efficiently funnel gas towards the central regions further contributing to the formation of obscuring structures around the central SMBH as well as providing large-scale obscuration via

cold gas and dust. These findings reinforce the notion of a possible connection between mergers on AGN obscuration.

Observations find a significant fraction of AGN associated with high star formation activity, suggesting a potential direct relationship AGN activity and SFR levels [Peterson, 1997, Zewdie et al., 2020], indeed several groups in recent years have identified from X-ray data a (mean) correlation between X-ray luminosity and SFR for morphological types, although with a lower normalization for early-type galaxies [Yang et al., 2019, Carraro et al., 2020, 2022]. Starburst galaxies in particular, that seems to be characterized by elevated cold gas mass content [Zhou et al., 2018], lie above the Main Sequence exhibiting exceptionally high SFR relative to typical star-forming galaxies of similar stellar mass, and proportionally higher (mean) X-ray luminosities. These galaxies deplete their gas reservoirs rapidly and often show high column densities $(\log_{10}(N_{\rm H}/{\rm cm}^{-2}) > 23)$, which may be sufficient to account for at least some of the very obscured AGN [e.g., Lapi et al., 2014, Andonie et al., 2024].

2.6 X-ray observational data

A variety of methods are adopted to identify and characterize obscured AGN [for an extensive overview of the different methods depending on wavelength see Hickox and Alexander, 2018]. X-ray observations [e.g., Giacconi, 2009] are one of the best methods for selecting obscured AGN since they are directly associated with the accretion disc, and its hot corona. X-rays have more penetrating power through thick mediums, at least until the Compton-thin/thick limit of $N_{\rm H} \sim 10^{24}~{\rm cm}^{-2}$. A variety of observational studies have attempted to describe the demography and evolution of AGN as a function of their column densities [e.g., Ueda et al., 2014, Aird et al., 2015, Buchner et al., 2015, Ananna et al., 2019, Laloux et al., 2023]. It has been several times recognized that the Cosmic X-ray Background (CXB) of AGN can be reproduced by a collection of AGN with varying column densities ranging from $N_{\rm H} \sim 10^{20} - 10^{26}~{\rm cm}^{-2}$ [e.g., Gilli et al., 2007, Shen, 2009, Shankar et al., 2009, Ueda et al., 2014, Aird et al., 2015, Ananna et al., 2019, Gilli et al., 2022, and references therein].

Although this thesis primarily focuses on the study of galaxies within a semi-analytic framework, I will compare with X-ray data because they provide a comprehensive view of AGN demography at z < 3. This Section provides an overview of key X-ray telescopes, laboratories, and surveys that are instrumental in detecting significant X-ray sources. Additionally, it includes a summary of background analysis and relevant X-ray observational findings pertinent to this research.

2.6.1 Telescopes, laboratories and surveys

Below there is a concise, non-exhaustive list of significant X-ray observatories, laboratories, and surveys, presented chronologically, that have contributed to our understanding of X-ray emissions in general and AGN sources in particular.

ROSAT⁵: Launched in 1990, the ROSAT mission, a German/US/UK collaboration, operated for nearly nine years. It was dedicated to an all-sky survey as well as a pointed phase, succeeding the UHURU satellite.

XMM-Newton⁶: Launched in 1999, the European Space Agency's X-ray Multi-Mirror Mission Newton operates in a highly elliptical 48-hour orbit. Notable for its large effective area (1000 cm²), XMM-Newton excels in X-ray observations.

Chandra⁷: Also launched in 1999, NASA's Chandra X-ray Observatory observes X-ray wavelengths from a high-Earth orbit with a 48-hour period. Its high resolution and small point spread function (PSF) make it particularly effective for deep surveys of distant sources.

INTEGRAL⁸: Launched in 2002, the European Space Agency's INTErnational Gamma-Ray Astrophysics Laboratory (*INTEGRAL*) operates in a highly eccentric geosynchronous orbit. It is renowned for its simultaneous observations across gamma rays, X-rays, and visible light, focusing on phenomena such as explosions, element formation, black holes, and other exotic objects.

Suzaku⁹: Launched in 2005, the Japanese/NASA mission Suzaku specializes in highenergy X-ray sources. It features five soft X-ray telescopes and various instruments, including an X-ray spectroscope that enhances the measurement of individual X-ray photon energies.

Swift¹⁰: Launched in 2004, NASA's Swift satellite is a multi-wavelength observatory equipped with an X-ray telescope (XRT). It is designed to study gamma-ray bursts and includes capabilities for detecting UV/optical wavelengths and high-energy X-rays with its Burst Alert Telescope (BAT).

Surveys: Key surveys include the Advanced Large Sky Survey [ALSS Ueda et al., 1999, Akiyama et al., 2000], the Advanced Satellite for Cosmology and Astrophysics [ASCA, e.g., Medium Sensitivity Survey AMSS Ueda et al., 2001, Akiyama et al., 2003], the Chandra Deep Field South [CDFS Xue et al., 2011], the Cosmological Evolution Survey [COSMOS Scoville et al., 2007], the All Wavelength Extended Groth Strip International

⁵https://heasarc.gsfc.nasa.gov/docs/rosat/rosat.html
6https://www.cosmos.esa.int/web/xmm-newton
7https://chandra.harvard.edu/
8https://www.esa.int/Science_Exploration/Space_Science/Integral_overview
9https://science.nasa.gov/mission/suzaku/

¹⁰https://swift.gsfc.nasa.gov/

Survey [AEGIS Davis et al., 2007], the *Swift*/BAT [e.g., 9-month survey BAT9 Tueller et al., 2008], the Subaru/XMM-Newton Deep Survey [SXDS, a combination of short-visible/MIR/X-ray wavelengths Ueda et al., 2008, Akiyama et al., 2015], and MAXI [e.g., 7-month survey MAXI7 Hiroi et al., 2011, Ueda et al., 2011], among others.

2.6.2 Relevant observations

Point Sources. While this project emphasizes the study of large samples of AGN and their collective characteristics for their use as a statistical level, it is crucial to acknowledge the significant contributions of individual source studies. These studies help to refine important information regarding key AGN galactic features [Querejeta et al., 2017, 2021, Leist et al., 2023, Peralta de Arriba et al., 2023, López et al., 2023, García-Bernete et al., 2024, Speranza et al., 2024] such as what a torus really is, how it behaves and what is its relation to the rest of the galaxy [García-Burillo et al., 2016, 2019, 2021].

Cosmic X-ray Background. The Cosmic X-ray Background (CXB or XRB, depending on the literature) refers to the diffuse radiation that constitutes the energy density of the X-ray sky [Fabian and Barcons, 1992]. Although the precise origin of this radiation remains uncertain, the detection of numerous individual X-ray sources suggests that a significant portion, approximately 50% of the total intensity, is attributable to unresolved sources [Gilli et al., 2007]. This unresolved fraction is believed to have an extragalactic origin. Recent theories propose that this unresolved component may include a substantial number of Compton-thick AGN sources [Gilli et al., 2007, Ananna et al., 2019], which are challenging to detect due to their obscuration. Therefore, accurate calculations and constraints on the CXB are crucial for determining the fraction of Compton-thick obscured AGN.

2.6.3 Observational data used

2.6.3.1 Obscuration over X-ray luminosity

In this thesis, I compare the predicted mean N_H column densities and obscured AGN fractions as a function of AGN X-ray luminosity, with data from Ueda et al. [2014], Buchner et al. [2015], and Ananna et al. [2019] [U14, B15, A19, hereafter], which are among the most complete compilations in terms of AGN luminosity and redshift coverage, including data from deep surveys from observatories such as Swift/BAT, ASCA, XMM-Newton, Chandra, ROSAT, or AEGIS. The major differences between U14, B15, and A19 are described and deeply studied in A19, Sections 3.1 and 3.2, where they focus on the different methods to calculate the X-ray luminosity function. Specifically, I use two forms from A19, one which closely follows the analytic formula by U14 with updated parameters, and a new one derived from Machine Learning algorithms, which

I label as A19-ML throughout. It is interesting to note that the two A19 prescriptions are fits to the same data sets but with different prescriptions, and provide very different results.

I need to take into account that the obscured values from U14 are extrapolations for column densities $\log N_{\rm H} > 24 \, [{\rm cm}^{-2}]$ since they do not have heavy CTK AGN in their samples. U14 use a parametric model to fit the X-ray luminosity function (XLF), but could not directly constrain the CTK fraction, which is derived from matching the Xray background (XRB) with some assumptions on the spectra of AGN. U14 do not assume any specific constraints for the CTK, but each bin of CTK is the same as the CTN fraction. However, they still fit the XRB, implying a strong degeneracy with the CTK AGN obscured fractions. They also use data that do not have any galaxy detected over $\log N_{\rm H} \sim 25 \, [{\rm cm}^{-2}]$ (except in infrared, but not resolvable in X-ray, for an updated analysis of U14 see also Yamada et al. 2021). While B15 have galaxies with CTK obscuration, A19's analysis extrapolates for $\log N_{\rm H} > 25$ [cm⁻²]. The aim of A19 was to calculate new fractions where no assumptions on the CTK AGN fraction were given. Also, updating some B15 constraints, according to A19, does not help to match the observational data at the time. A19-ML replaces the absorption function from U14 with the one from Ricci et al. [2015], which includes corrections for the geometry of the torus and inherently predicts a higher fraction of CTK AGN sources, particularly in the local universe. The neural networks account better for the contribution of CTK sources than previous works due to the iteratively adjust of the XLF to fit the XRB, otherwise under-represented due to observational biases, according to A19. Also, the neural network adjusts space densities across different absorption bins, ensuring that CTK AGN contribute significantly to the observed XRB spectrum. Finally, note that the A19-ML data presents a very irregular CTK fractions trend, heavily deviating from all other measurements [e.g., Ueda et al., 2014, Buchner et al., 2015, Aird et al., 2015, Peca et al., 2023, Signorini et al., 2023]. B15 use two different approaches: one where they have high CTK at high luminosity, overestimating the XLF by 3 times [see appendixes of A19], which produces around 55%-65% CTK, and another one where they use a constant slope prior which generates a lower CTK obscuration, around 20%. In this thesis I use the 10%–90% quantiles of the posterior samples from both models as limits of the data. The major problem is that the uncertainty of the spectra distributions among the data available is not consistent with each other, and some of them never produce the cosmic XRB, which affects the conversion between number counts and flux, creating different obscured fractions.

In this thesis I do not address the origin of these discrepancies, but instead I use the total of the available observational results assumed to be CTK to bracket the current empirical constraints on the fraction of obscured AGN as a function of luminosity and redshift. Despite U14 and A19 not attempting to directly identify CTK AGN by, e.g.,

spectral fitting [see B15], this thesis aims to reproduce their results to validate the models and explore some caveats and limitations. My results therefore on, e.g., the need for a torus-like component to generate more CTK sources, rest on the future validation of the current observational constraints. I acknowledge, for example, other interesting works such as Akylas et al. [2012, see also Treister et al. 2009], who put forward models able to fit the XRB without any CTK AGN, but by modifying the X-ray spectrum of AGN, or Georgakakis et al. [2017b], who suggest lower fraction of CTN AGN with $L_X > 10^{44}$ erg/s using the wide-area XMM-XXL survey.

2.6.3.2 Obscuration over Eddington rate

Additional data will be used when I study the AGN obscuration and Eddington ratio in Chapter 7. Specifically, in this Chapter I will be discussing the observations from Georgakakis et al. [2017a] and Laloux et al. [2024], which particularly provide specific accretion rates distributions (SARD, see Section 4.4), where Laloux et al. [2024] also focus on the study of AGN CTN obscuration. The SARD provides the probability for a given galaxy to be active at a given redshift and at a given specific accretion rate, which can be related to the Eddington rates as I explain in Chapter 4. These data are important because they encapsulate information on the duty cycle and underlying Eddington ratio distributions, which then connects with the light curves that can be directly predicted by the models.

Georgakakis et al. [2017a], Laloux et al. [2024] employ multiwavelength surveys, primarily focused on X-ray data, to evaluate AGN activity, accretion rates, and stellar masses. Each study provides unique insights into how AGN influence galaxy formation and growth, but they differ in data range, methodology for SARD calculations, and the treatment of limitations like survey sensitivity and obscured AGN. Below, I provide detailed comparisons of the data, SARD calculations, and data limits across the studies.

The studies rely on X-ray observations, primarily from Chandra and XMM-Newton, alongside multiwavelength data from major surveys. Laloux et al. [2024] employs COS-MOS, AEGIS-XD, and CDFS, while Georgakakis et al. [2017a] use data from CANDELS, UltraVISTA, and additional deep Chandra fields [see also Aird et al., 2018]. The stellar mass selection in all studies ranges from $\sim 10^8 M_{\odot}$ to $\sim 10^{11.5} M_{\odot}$, focusing primarily on massive galaxies. This broad range captures both star-forming and quiescent galaxies. However, caveats arise due to survey depth and sensitivity limits, particularly at lower masses and higher redshifts. While other works like Aird et al. [2018] struggle with sample completeness for lower-mass galaxies at high redshift, potentially biasing their results towards higher-mass galaxies, Laloux et al. [2024] discuss that the effect of the stellar mass selection bias in their case is minimal.

Paper	Redshift	Stellar Mass	X-ray Lum	$\lambda_{ ext{Edd}}$
	Range	$\log(M_{\odot})$	log(erg/s)	Range
Laloux et al. [2024]	0.0 - 6.0	9.5 - 11.5	$\sim 10^{41}$ - 10^{45}	$-5 \le \log \lambda \le 2$
Georgakakis et al. [2017a]	0.0 - 3.0	8.5 - 11.5	$\sim 10^{42}$ - 10^{45}	$-4 \le \log \lambda \le 1.5$

TABLE 2.1: Data limits and parameters in the selected studies.

In each study, SARD calculations rely on integrating AGN accretion rates as a function of stellar mass and redshift. Laloux et al. [2024] [see also Aird et al., 2018] adopt Bayesian methods to model the distribution of specific black hole accretion rates (λ_{sBHAR}). Georgakakis et al. [2017a] use parametric and power-law models to explore these distributions, with corrections for biases like obscuration.

The studies note various limitations, particularly concerning sensitivity and sample size. Laloux et al. [2024] emphasize uncertainties in low-luminosity AGN and the challenges posed by small quiescent galaxy samples. Georgakakis et al. [2017a] highlight the difficulty in accounting for obscured AGN and redshift-dependent completeness issues.

2.7 Galaxy clustering

Clustering analysis, particularly the two-point correlation function (2pCF), plays a crucial role in understanding the large-scale structure (LSS) of the Universe, and is instrumental in the study of galaxy evolution in a dark matter dominated Universe, as galaxies are expected to closely follow the underlying spatial distribution of their host dark matter haloes. The 2pCF is a statistical tool that quantifies the excess probability of finding pairs of galaxies separated by a given distance, compared to a random distribution. By measuring the spatial clustering of galaxies, one can infer the nature of their environments and the dark matter halos (DMHs) they inhabit, making it a key method for exploring the link between galaxy formation, evolution, and their surroundings [see, e.g., Sánchez et al., 2006].

The importance of the 2pCF extends to the study of AGN. As described in Allevato et al. [2021], among others, clustering as a function of SMBH mass could reveal the underlying scaling between $M_{\rm BH}$ and $M_{\star}/M_{\rm halo}$, and the clustering as a function of Eddington ratio could provide clues to the underlying LC. In general terms, AGN clustering could also provide some hints towards unveiling the origin of obscuration in AGN, and in particular provide complementary means to distinguish between Orientation versus Evolutionary models [Koutoulidis et al., 2018]. For example, in pure Orientation models, where obscuration is predominantly dictated by the torus and inner clouds around the SMBHs, the large-scale clustering should appear to be largely independent of the level of obscuration within AGN. On the other hand, AGN clustering could be sensitive

to obscuration if, for example, AGN tend to reside in denser regions more susceptible to mergers, gas inflows, or starbursts. By applying the 2pCF to AGN classified by their level of obscuration, it is possible to examine how factors like hydrogen column density correlate with their large-scale spatial distribution and environment [Cole and Kaiser, 1989]. This approach has the potential to reveal whether obscured AGN are more likely to reside in dense environments, such as massive dark matter halos, compared to unobscured AGN.

The 2pCF distinguishes between clustering on small and large scales through the 1-halo and 2-halo terms, which reflect different galaxy pairings [see, e.g., Cooray and Sheth, 2002]. The 1-halo term accounts for pairs of galaxies residing within the same dark matter halo, while the 2-halo term represents pairs in separate halos. For obscured AGN, the clustering signal at small scales (1-halo term) can be particularly sensitive to the number of satellite galaxies within the host halos, where AGN activity might be triggered or sustained by interactions or mergers. On large scales (2-halo term), clustering can indicate whether obscured AGN preferentially form in denser regions of the LSS, potentially linking their obscuration to large-scale environment-driven processes like gas inflows or mergers [e.g, Gatti et al., 2016, Viitanen et al., 2023].

Observational studies have shown that obscured AGN, often identified by their high column densities ($N_H > 10^{22}\,\mathrm{cm}^{-2}$), tend to cluster more strongly than unobscured AGN at intermediate redshifts ($z \sim 1$) [Hickox et al., 2011, Elyiv et al., 2012, Donoso et al., 2014, DiPompeo et al., 2014, 2015, 2016, 2017, Koutoulidis et al., 2018], than at lower redshifts [Ebrero et al., 2009, Coil et al., 2009, Gilli et al., 2009, Mountrichas and Georgakakis, 2012, Krumpe et al., 2012, 2018, Geach et al., 2013, Jiang et al., 2016, Mendez et al., 2016, Powell et al., 2018]. This suggests that obscured AGN, especially in star-forming galaxies at higher redshifts, might inhabit more massive halos or denser environments, which supports the idea that environmental factors, such as galaxy interactions, may play a significant role in obscuration. However, this result is still open to debate and it is the objective of current studies.

By analysing the clustering of obscured and unobscured AGN, I could test various theoretical models of AGN evolution, especially those that posit different evolutionary phases for AGN activity driven by changes in gas supply or galaxy mergers. A preliminary exploration of the clustering properties within the semi-analytic GAEA model will be presented in Chapter 7. I will generate several predictions from GAEA of the 2pCF of AGN for different column densities and AGN luminosities at fixed redshift and stellar mass, and compare with some of the most recent clustering data on X-ray AGN. In conclusion, the 2pCF represents a powerful tool for investigating the clustering properties of AGN, and can provide valuable complementary constraints on their evolution and possibly origin behind their obscuration.

Chapter 3

Theoretical model simulations

Understanding galaxy formation and evolution is a complex task that requires the application of various theoretical models. These models attempt to simulate the processes that shape galaxies over cosmic time, from the early universe to the present day. Given the wide range of physical phenomena involved—including gravitational interactions, gas dynamics, star formation, and feedback from supernovae and active galactic nuclei—different modelling approaches have been developed, each with its own strengths and limitations. This Chapter provides an overview of the primary theoretical models adopted to study galaxy formation and evolution, with a focus on those most relevant to this thesis.

I start this Chapter by briefly describing hydrodynamic simulations. These simulations track both dark matter and baryonic matter (gas, stars, and dust), solving the equations of gravity and hydrodynamics to model galaxy formation in a cosmological context. In this thesis, I place a stronger emphasis on two alternative approaches that form the backbone of my theoretical framework: semi-analytic models (SAMs) and semi-empirical models (SEMs). These techniques offer a more computationally efficient way to explore large volumes of parameter space and the underlying physical mechanisms driving galaxy evolution.

3.1 Physical theoretical models of galaxy formation

Hydrodynamic simulations are sophisticated models that replicate the behaviour of baryons and dark matter within a defined volume, sampling fluids by means of particles (in the case of Lagrangian codes) representing dark matter, gas, and stars to simulate the universe across cosmic time. These simulations incorporate physical properties and interactions among particles, enabling their evolution under various forces and parameters. Similar to other simulation types, the output is written into snapshots to

facilitate analysis. However, these simulations are constrained by a resolution limit, which prevents detailed study of galactic effects. This limitation can be addressed by creating sub-grid models for individual sources, allowing for the study and connection of host galaxy properties with the surrounding volume and nearby galaxies.

In this thesis, I will show an example of a galaxy evolved in a zoom-in simulation in Appendix B, which employ the Gadget-3 code. I also comment on the most widely used version of the Gadget code, Magneticum. Other hydrodynamic simulation codes not addressed in this thesis but of common use to study AGN and galaxies include the IllustrisTNG Project [*Arepo* code Springel, 2010], Ramses with HorizonAGN [Teyssier, 2002], ChaNGA with Romulus [Menon et al., 2015], Gizmo with Mufasa, Simba, or FIRE [Hopkins, 2017], and Swift with FLAMINGO [Kegerreis et al., 2019].

3.1.1 Magneticum and the Gadget catalogue

The Magneticum simulation uses hydrodynamical prescriptions to trace the formation of cosmological structures across various redshifts and scales. Each volume is sampled with a very large number of particles ($\gtrsim 10^{10}$). The base code for these simulations, *Gadget*, has several versions. The most commonly used version, due to its free availability, is Gadget-2² [Springel, 2005]. However, the Magneticum simulation was run using Gadget-3, an updated, non-public version of Gadget-2, also employed by simulations like Eagle and MassiveBlack-II. Using the Gadget-3, Valentini et al. [2020] incorporated a sub-resolution model for star formation and stellar feedback, tailored for disc galaxies in the original introductory paper. In Appendix B I will briefly discuss the obscuration properties of a typical starforming galaxy generated by Valentini et al. [2020] as zoom-in simulations.

3.2 Semi-analytic models

Semi-analytic models (SAMs) are built on top dark matter merger trees [e.g., Menci et al., 2005] generated by N-body dark matter simulations [De Lucia and Blaizot, 2007], as well as analytical prescriptions inspired from theoretical arguments and numerical simulations, and aim to describe ab initio, via a sequence of physically motivated prescriptions, the formation and evolution of galaxies within their host DM potential wells [Cole et al., 2000]. By using analytical relations and best-fit parameters, SAMs provide a valuable complementary approach to hydrodynamic simulations, particularly in terms of flexibility, and computational efficiency. Their modular nature allows for specific processes to be easily switched on or off to assess their impact on observational data

¹http://www.magneticum.org/

²https://wwwmpa.mpa-garching.mpg.de/gadget/

[e.g., Menci et al., 2014]. In a comprehensive review, Somerville and Davé [2015] discuss the state-of-the-art in semi-analytic models. For a detailed overview of the general properties, history, and evolution of SAMs, I refer readers to that review. In this thesis, I will focus on the specific semi-analytic model: GAlaxy Evolution and Assembly (GAEA).

3.2.1 GAEA

In this thesis I present a study of orientation and evolutionary obscuration in AGN in a cosmological context taking advantage of the predictions of the semi-analytic model GAEA [Fontanot et al., 2020, F20 hereafter], which follows the evolution of galaxies and their central SMBHs from early times down to the present epoch. GAEA incorporates state-of-the-art recipes to describe the evolution of stars and gas in galaxies, as well as providing a detailed modelling of the growth of the central SMBHs. I hereby provide a brief overview of GAEA's modelling of SMBHs, while full details can be found in F20. In particular, in this thesis I focus on the so-called HQ11-GAEA realization, which includes Hopkins and Quataert [2011] and Hopkins et al. [2006a] prescriptions to estimate:

- The fraction of cold gas from the host galaxy expected to lose enough angular momentum to reach the central regions and gather into a low angular momentum gas reservoir. These events are triggered by mergers or disc instabilities, able to perturb the cold gas content of galaxy discs.
- 2. The accretion onto the SMBH of the material gathered into the reservoir. The accretion rate follows a light curve, with a shape inspired by the results of numerical hydrodynamic simulations.

The original model has been calibrated on Dark Matter Merger trees drawn from the Millennium Simulation [Springel et al., 2005, WMAP1 lambda cold dark matter concordance cosmology, i.e., $\Omega_{\Lambda}=0.75$, $\Omega_{\rm m}=0.25$, $\Omega_b=0.045$, n=1, $\sigma_8=0.9$, and $H_0=73~{\rm km~s^{-1}~Mpc^{-1}}$], which typically allows for a good description of galaxy properties down to a stellar mass scale of the order of $10^9~{\rm M}_{\odot}$. The simulation has evolved from the original first version [De Lucia and Blaizot, 2007] to include key improvements [described in F20]:

- A detailed treatment of chemical enrichment from De Lucia et al. [2014], following explicitly the differential enrichment associated with asymptotic giant branch (AGB) stars, Type II SNe, and Type Ia SNe.
- An updated modelling of stellar feedback [Hirschmann et al., 2016], including ejecting feedback in the form of stellar-driven outflows (inspired by results from

hydrodynamic simulations), combined with a time-scale of gas re-incorporation that depends on DMH mass [Henriques et al., 2013];

 An improved modelling of disc sizes [Xie et al., 2017] that traces the evolution of angular momentum following the mass and energy exchanges among different galaxy components.

SMBH seeding in GAEA is performed following Volonteri et al. [2011] and corresponds to seed masses of $\sim 10^4 {\rm M}_{\odot}$ (which is the resolution of the Millennium Simulation) on haloes/galaxies above a certain mass limit. The subsequent growth of these seeds is then followed via gas accretion (mostly following the Bondi-Hoyle approach) and mergers with other SMBHs. The accretion of gas onto the SMBH in GAEA is triggered by both galaxy mergers and disc instabilities, which contribute to the creation of a central gas reservoir of low angular momentum, which in turn gradually feeds the central SMBH. The accretion onto the central SMBH is then redistributed in time following an AGN LC, namely composed of an initial (super-)Eddington accretion phase, which lasts until the SMBH reaches the self-regulation limit, followed by a power-law decline, as also suggested by theoretical arguments and hydrodynamic simulations [e.g., Granato et al., 2004, Lapi et al., 2006, Hopkins et al., 2007, Shen, 2009]. GAEA, as well as radio-mode feedback, also includes OSO-mode feedback in the form of winds. AGN winds heat the cold gas eventually expelling it in the hot gas. Specifically, the model realization considered in this thesis, HQ11-GAEA, uses the outflow rate predictions as a function of cold gas mass, bolometric luminosity and black hole mass from Menci et al. [2019].

The HQ11-GAEA model is calibrated to reproduce the evolution of the AGN³ bolometric luminosity function without applying any obscuration correction to model predictions, while still reproducing all galaxy properties discussed in previous papers [e.g., Hirschmann et al., 2016], like mass-metallicity relations, quenched fractions and cold gas fractions. For a study of the evolution of galaxy stellar mass function and **cosmic** SFR to high redshift, I refer the reader to Fontanot et al. [2017], a deeper analysis on the chemical enrichment can be found in De Lucia et al. [2014], and for information on the fraction of passive galaxies as a function of stellar mass to De Lucia et al. [2019].

GAEA also includes prescriptions for the radio-mode accretion and feedback. The radio-mode is treated, by construction, as an (almost) continuous accretion process of hot gas from the halo [which gives rise to tensions with the observed distribution of radio galaxies - see e.g., Fontanot et al., 2011]. This SMBH accretion mode becomes relevant for massive galaxies residing in massive haloes at low-redshifts, as those are the environments where an efficient quenching of the cooling flows and late SFR is required. In observations, the radio-mode is often associated with low disc luminosity

 $^{^3}$ I define AGN as those galaxies shining above $L_{\rm bol}\sim 10^{42}$ erg/s at some point during their active phase.

[Narayan and Yi, 1994, 1995, Quataert and Narayan, 1999, Maoz, 2007], although other studies seem to find that there is no relation between radio mode and low luminosity [Panessa et al., 2007].

3.2.2 Other semi-analytic models

Roma SAM. In this project, I use outputs from the state-of-the-art Roma SAM [Menci et al., 2002, 2004, 2005, 2008, 2014, 2018, Lamastra et al., 2010]. This model includes a self-regulating AGN feedback mechanism from supernovae, which inhibits further star formation by the AGN. A detailed summary is provided in Zanisi [2021]. However, in this thesis, I specifically use the outflow results generated by the quasar mode feedback implemented as a blast wave, as detailed in Chapter 4, following the methodology of Lapi et al. [2005] and Menci et al. [2008].

L-Galaxies⁴. As the successor to the *Munich* model, this SAM builds upon the subhalo merger trees from the Millennium [Springel et al., 2005] and Millennium-II [Boylan-Kolchin et al., 2009] simulations. Since its inception in Henriques et al. [2015], the model has undergone several updates, such as the ability to spatially resolve phenomena in galactic discs [Henriques et al., 2020] and the inclusion of binary stellar evolution and dust studies [Yates et al., 2024].

SHARK. Presented by Lagos et al. [2018, 2019], SHARK is a SAM designed with software engineering best practices, emphasizing flexibility and open-source availability. One of its main advantages over other models is the ease with which modifications, such as adjustments to dust mass, can be incorporated.

Other popular SAMs are: GALFORM [Cole et al., 2000], Munich model [Croton et al., 2006], Sant-Cruz model [Somerville et al., 2008, Somerville and Davé, 2015], Morgana [Monaco et al., 2007], GALICS [Hatton et al., 2003], or SatGen [Jiang et al., 2021]. What I provide above is not an exhaustive list of SAMs, but it is mostly intended to give a brief overview on the richness and diversity of this type of models aimed at making a holistic view of galaxy formation and evolution.

3.3 Semi-empirical models

Semi-empirical models serve as a complementary tool to simulations like hydrodynamical simulations and semi-analytic models (see Section 3.2). Unlike first-principles models, semi-empirical models derive physical processes from observables, correlating properties to dark matter haloes via empirical recipes such as abundance matching between the stellar mass function and halo mass function [e.g., Kravtsov et al.,

⁴https://lgalaxiespublicrelease.github.io/

2004, Shankar et al., 2006, Kravtsov et al., 2018] or even star formation rate and halo accretion rate [Boco et al., 2023]. By applying additional parametrizations and assumptions, but always in a controlled and limited amount, semi-empirical models can create mock galaxies with greater predictive power and could also test some specific theory of galaxy evolution, such as galaxy quenching of the effect of mergers on SMBHs [e.g., Shankar et al., 2013].

Notable examples of state-of-the-art SEMs include UniverseMachine [Behroozi et al., 2019], Trinity [Zhang et al., 2023], STEEL [Grylls et al., 2020, Grylls, 2020], and DECODE [Fu et al., 2022].

Chapter 4

Methodology

The origin of obscuration in Active Galactic Nuclei (AGN) is still an open debate. In particular, it is unclear what drives the relative contributions to the line-of-sight column densities from galaxy-scale and torus-linked obscuration. The latter source is expected to play a significant role in Unification Models, while the former is thought to be relevant in both Unification and Evolutionary Models. In this Chapter, I make use of a combination of cosmological semi-analytic models and semi-empirical prescriptions for the properties of galaxies and AGN, to study AGN obscuration. I consider a detailed object-by-object modelling of AGN evolution, including different AGN light curves (LCs) composed of phases of varying levels of obscuration, gas density profiles, both Orientation and Evolutionary models and also AGN feedback-induced gas cavities.

4.1 Obscuration of semi-analytic galaxies

Throughout this thesis, I use the comprehensive semi-analytic model (SAM) for GAlaxy Evolution and Assembly [GAEA, Fontanot et al., 2020, F20 hereafter] as a self-consistent baseline for a realistic simulated population of galaxies and their central SMBHs, consistent with the present constraints on the galaxy stellar mass function and AGN luminosity function. Starting from GAEA predictions, I then assign to each model galaxy a line-of-sight Hydrogen column density $N_{\rm H}$, based on its gas mass, as well as a torus component based on its SMBH mass and AGN luminosity. However, I also check the robustness of my results by varying various key prescriptions of the GAEA model in a semi-empirical fashion, by adopting, for example, different AGN LCs, gas fractions, or gas disc sizes.

This Chapter outlines the methodologies employed in the thesis to investigate origin of obscuration in active galactic nuclei (AGN). The structure of the Chapter is as follows.

In Section 4.2, I describe the core predictions on the galaxy population generated by GAEA which I use as baseline for my calculations, the computation of column density from the large-scale gas distribution, the inclusion of an AGN-driven Blast Wave, and the modelling of a dusty torus-like central component. In Section 4.3 I describe my methodology in the framework of the GAEA SAM, and I provide the details of the AGN and host galaxy modelling under the Evolutionary model. Section 4.4 presents the calculations for studying the Eddington ratio distributions and Section 4.5 the clustering of semi-analytic galaxies.

4.2 Methodology of the orientation model

My methodology to study the statistical distribution of obscured and unobscured AGN in orientation models relies on the following steps:

- I start from a realistic mock of galaxies (GAEA galaxy catalogues) at a given redshift consistent with available data on the stellar mass function and AGN/quasar (QSO) luminosity functions.
- 2. I then assign to each galaxy a HI line-of-sight column density based on its gas content and geometry, and examine the effect of an AGN-driven Blast Wave in modulating the $N_{\rm H}$.
- 3. To each galaxy, I also assign a torus-like component based on its SMBH mass, and AGN luminosity.
- 4. I then repeat the steps above at different epochs to study the predicted evolution of AGN obscuration as a function of redshift.

As previously mentioned, I use as a reference the galaxies and SMBHs extracted from the GAEA SAM, which also yields cold gas fractions, disc sizes, and SMBH accretion rates (light curves). The advantage of using this SAM is that a state-of-the-art cosmological model provides inner self-consistency among the different variables and models used, for example retaining the AGN feedback-induced relation between gas fractions used in each accretion event and AGN luminosity before/after each accretion. Nevertheless, in a data-driven approach, I also explore the impact on the results by varying, in turn, galaxy gas fractions, AGN light curves, and galaxy radii as guided by observational results. I show that the main results are broadly invariant under these changes except for some notable examples which I discuss in detail in the next Sections.

The GAEA model was described in Section 3.2.1. I provide full details on how I compute galaxy-scale obscuration in Section 4.2.1, while in Section 4.2.2 I discuss how I assign a torus-like component to each active galaxy.

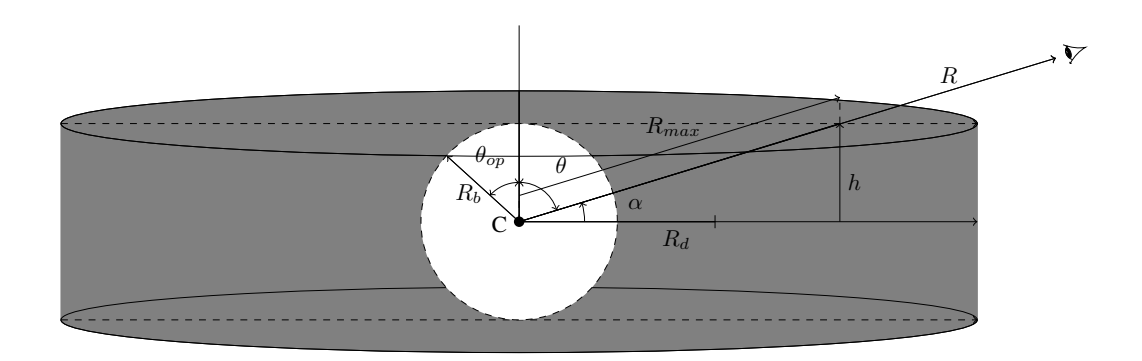


FIGURE 4.1: Diagram depicting a typical galaxy in the mock sample characterised by an exponential gas density profile and a disc geometry. In this Figure, R traces the line-of-sight, $R_{\rm d}$ is the gas scale length, h is the thickness of the disc, θ is the angle between the vertical and R, α is the random angle for the random line-of-sight, $R_{\rm max}$ marks the end point of the galaxy edges along R, $R_{\rm b}$ is the radius of the Blast Wave, and $\theta_{\rm op}$ is the opening angle of the Blast Wave (central white sphere in the Figure).

4.2.1 Column density distribution: contribution from the galaxy

Throughout this thesis I consistently assume that the gas density in star-forming discs follows an exponential density profile,

$$\rho(R,\theta) = \rho_0 \exp\left(-R/R_d\right),\tag{4.1}$$

where ρ_0 is the central gas volume density, R is the line-of-sight radius from the centre of the disc to the furthermost part of the galaxy, R_d is the gas disc scale length, and θ is the angle between the rotational vertical axis of the galaxy and the line of sight. The geometry is visualized in Figure 4.1.

Although possibly not all galaxies are characterized by exponential density profiles for their gas component [e.g., van der Kruit, 1979, Pohlen and Trujillo, 2006, Bigiel and Blitz, 2012, Wang et al., 2014], Eq. (4.1) still represents a good approximation to the gas mass distribution of many galaxies at different epochs and stellar masses, and becoming even a better approximation at higher redshifts [e.g., Patterson, 1940, Freeman, 1970, Hodge et al., 2019, Hunter et al., 2021, Ferreira et al., 2022, and references therein]. In some highly star-forming high-redshift galaxies, the gas disc profile may deviate from an exponential one, attaining a more compact and spherical geometry. I will anyhow continue adopting an exponential gas density profile, although I will also briefly discuss the impact of switching to, e.g., a Sérsic profile in Chapter 5, as well as in Chapter 6. Also, Eq 4.1 is consistent with the fact that GAEA, following common recipes in SAMs, assumes that the cold gas density settles in an exponential profile once in rotational equilibrium. This gas profile is consistent with surface brightness profiles observed in some galaxy samples [e.g., ASPECS, Aravena et al. 2020, and CANDELS,

Grogin et al. 2011, Koekemoer et al. 2011, or Hodge et al., 2019], as predicted by hydrodynamic simulations [Aumer et al., 2013], and used by previous semi-analytic models [Fu et al., 2009, 2010], but with a gas disc scale length that could be different from the stellar component, as discussed below.

The normalization ρ_0 in Eq. 4.1 is chosen in a way that the integral of the gas density over the full radial (R), vertical (θ) and azimuthal (ϕ) extent of the galaxy equals the gas mass of the host galaxy ($M_{\rm gas}$), i.e.,

$$\int_{0}^{2\pi} \int_{0}^{\pi} \int_{0}^{\infty} \rho(R,\theta) R^{2} \sin\theta dR d\theta d\phi = M_{\text{gas}}$$

$$\Rightarrow \rho_{0} = \frac{M_{\text{gas}}}{4\pi R_{d}^{2} I},$$
(4.2)

where

$$I = \int_0^\infty e^{-x} x^2 dx = 2, (4.3)$$

and $x = R/R_d$. For simplicity of visualization and computation, especially in models with a Blast Wave, I will always use cylindrical coordinates in all my calculations.

Throughout the chapter, I assume a disc thickness $h=R_{\rm d}/8$ [e.g., Nath Patra, 2020]. As a sanity check, I also consider other possible definitions [e.g., Ojha, 2001, $h=R_{\rm d}/15$] showing that the disc thickness plays a relatively minor role in AGN obscuration with respect to other input variables. This test is discussed in Section 5.2.

The line-of-sight HI column density is then calculated as

$$N_H = \int_0^{R_{\text{max}}} \rho(R, \theta) dR = \int_0^{\frac{h}{R_d \sin \alpha}} \rho_0 e^{-x} dx,$$
 (4.4)

where α is the angle between the plane of the galaxy and the line-of-sight, and R_{max} is maximum radius of the galaxy for a given line-of-sight (see Figure 4.1).

I am making two assumptions in this methodology:

- What X-ray observations measure is driven by hydrogen ($N_{\rm H}$ from X-ray spectra assume solar abundance of H/H_e/O/F_e).
- That $M_{\rm gas}$ consists of 100% hydrogen.

As mentioned before, GAEA includes the effects of AGN feedback on reducing the gas mass in the low angular momentum reservoir around the SMBH, as well as in the surrounding galaxy. However, GAEA does not include the dynamical effect of AGN feedback on the gas distribution in the host galaxy, which becomes relevant when calculating the line-of-sight $N_{\rm H}$ column density. To include this effect, I follow a model based on the AGN-driven outflows proposed by Menci et al. [2019] [see also Lapi et al.,

2005, Menci et al., 2008], which analytically follows the two-dimensional expansion of AGN-driven outflows as a function of the global properties of the host galaxy and of the luminosity of the central AGN. These AGN driven outflows are effectively winds [for a review see King and Pounds, 2015]. Different theoretical works [e.g., Silk and Rees, 1998, King, 2003, Granato et al., 2004, Lapi et al., 2005, Silk and Nusser, 2010, King et al., 2011, Faucher-Giguère and Quataert, 2012] have tried to capture the main features of the outflows using models based on shocks expanding into the interstellar medium (ISM). These models use power-law density profiles or exponential discs [Hartwig et al., 2018], and spherical approximation, consistent with AGN-driven outflows with luminosity, outflow rate, and shock velocity dependence. The Menci et al. [2019] treatment effectively follows the expansion velocity of the shock and the mass outflow rate out to large radii where the stellar/gas discs are the dominant components, creating a Blast Wave (BW). This BW creates a cavity in the gas, pushing the gas to the outskirts of the galaxy and creating a thin layer around the BW with heavily compressed gas. Menci et al. [2019] provide tabulated numerical solutions for the fraction of the cold gas ejected (f_{qw}) as a function of the properties of the AGN and host galaxy. These scaling have been included in the F06-GAEA SAM [F20], showing that AGN-driven winds help in reproducing the (low) levels of SFR in massive galaxies, removing some cold gas still in place in these galaxies since $z \sim 2$.

I compute the opening angle of the AGN BW for each galaxy which depends on the AGN bolometric luminosity, the cold gas mass $M_{\rm gas}$, and the virial velocity of the parent Dark Matter Halo $V_{\rm vir}$ following the tabulated values by Menci et al. [2019]. In this work, the virial velocity is used to predict the amount of reduction in gas mass in the centre of galaxies, and its impact on the line-of-sight column density. This model assumes that the opening angle corresponds to the maximum aperture of the BW, which occurs at the peak luminosity of the AGN. Therefore, the $N_{\rm H}$ corresponds to the one at the maximum value of the bolometric luminosity, although I also explore model variants where I relax this assumption.

Assuming gas mass conservation during the expansion of the BW [Lapi et al., 2005, Menci et al., 2008], the part of the total gas mass that is pushed away by the bubble creating a central cavity will all be compressed in a thin layer around the bubble. When $R_b > h$, the BW pushes the gas outside the disc galaxy and part of that gas is removed. In that scenario, a line-of-sight with $\alpha \sim 0$ will see the same $N_{\rm H}$ as without the BW. However, when $R_b > R_{\rm max}$, the BW removes the gas from the line-of-sight reducing $N_{\rm H}$. I can thus compute the total line-of-sight column density $N_{\rm H}$ as the sum of two components, the contribution from the shell and from the outer, still unperturbed gas disc

$$N_{\rm H} = \left(\frac{\theta_{\rm op}}{90}\right) N_{\rm H}^{\rm shell} + N_{\rm H}^{\rm out} \tag{4.5}$$

The column density of the outside, unperturbed disc is

$$N_{\rm H}^{\rm out} = \rho_0 \frac{Q_{\rm out}}{I} \tag{4.6}$$

where I is given in Eq 4.3 and Q_{out} is defined as

$$Q_{\text{out}} = \int_{R_{\text{b}}/R_{\text{d}}}^{R_{\text{max}}/R_{\text{d}}} x^2 e^{-x} dx, \ R_{\text{b}} < R_{\text{max}}$$
 (4.7)

with R_b the radius of the bubble calculated from θ_{op} . The column density contribution from the shell is instead given by

$$N_{\rm H}^{\rm shell} = \frac{M_{\rm gas}^{\rm shell}}{4\pi R_{\rm b}^2} \tag{4.8}$$

where the cold gas mass of the cavity is calculated by

$$M_{\rm gas}^{\rm shell} = M_{\rm gas} \frac{Q_{\rm shell}}{I}$$
 and $Q_{\rm shell} = \int_0^{R_{\rm b}/R_{\rm d}} e^{-x} x^2 dx$. (4.9)

In the reference model, I assume that the column density does not evolve during the lifetime of the AGN. However, AGN feedback models predict some evolution in the amount of gas content in the host galaxy already during the relatively brief lifetime of the AGN [see, e.g., Granato et al., 2004, Lapi et al., 2006, 2014, Santini et al., 2014]. Indeed, even in GAEA the gas mass is reduced by the AGN feedback. However, Eq 4.1 considers a single snapshot of $M_{\rm gas}$ when the AGN is at the beginning of its light curve. The gas mass reaches a maximum value at the start of the SMBH active phase, and then rapidly decreases around and after the peak of the light curve [see also Cavaliere et al., 2002, Lapi et al., 2005]. This evolution is explored in Chapter 6. In what follows, for convenience all my main results are plotted against the peak luminosity (luminosity at the peak accretion rate within the light curve), although I will show in Section 5.4 that this assumption plays a minor role on my results.

The bolometric luminosities are directly calculated from the gas accretion rates onto the central SMBHs. More specifically, the GAEA model includes both a QSO- and a radio-mode AGN feedback, each one characterized by its own independent values for QSO- and radio-mode radiative efficiency which sets the fraction of rest mass energy of the accretion flow onto the SMBH that is converted into radiative or kinetic luminosity, respectively. Note that the QSO- and radio-mode feedback are independently calculated in GAEA, which means that each galaxy could have luminosity from one model or both. The radio-mode feedback is generally less efficient, with a kinetic efficiency of just 2%, against the 15% assumed for the radiative-mode feedback. In Fontanot et al. [2020], both the contributions of the QSO- and Radio-mode accretion have been taken

into account to estimate the AGN/QSO luminosity function (LF). In general, for consistency, I follow the same approach. It is worth stressing that Radio-mode accretion becomes relevant only for massive galaxies residing in massive haloes at low-redshifts, as those are the environments where an efficient quenching of the cooling flows and late SFR is required. Radio-mode accretion, by construction, is treated as an (almost) continuous accretion process of hot gas from the halo (which gives rise to tensions with the observed distribution of radio galaxies [see e.g., Fontanot et al., 2011]). At low redshift, this implies that the radio-mode is dominant in galaxies devoid of their cold gas content. On the other end, in modelling the QSO-mode, GAEA is explicitly dealing with the flow of the cold gas from the host galaxy disc to the reservoir, and with the effects of feedback on the evolution of the total cold gas content. These considerations imply that the geometrical modelling of obscuration correlates better with the QSO-mode prescription, while the Radio-mode channel is typically underestimating the obscuration by construction. I will thus also present model predictions on the AGN obscured fractions removing the sources dominated by Radio-mode accretion and show that these are very similar to the full model outputs at $z \gtrsim 2$, but diverge somewhat at low z and low L, as further detailed below. The 2-10 keV intrinsic X-ray luminosities are calculated from bolometric luminosities via the bolometric correction by Duras et al. [2020]. Similar results would be retrieved adopting, for example, the Marconi et al. [2004] bolometric correction.

4.2.2 Column density distribution: contribution from the *torus*

It is now clear from direct and indirect (via, e.g., Spectral Energy Distribution (SED) fitting) observations that a torus-like component [Combes et al., 2019, García-Burillo et al., 2019, 2021] is an essential ingredient required to fully model the observational properties of AGN [see Netzer, 2015, Ramos Almeida and Ricci, 2017, Hickox and Alexander, 2018, for reviews], especially in their $\log_{10}(N_{\rm H}/{\rm cm}^{-2}) > 24$ phase [Risaliti et al., 1999, Marchesi et al., 2018]. The torus can be pictured as a compact reservoir of low-angular momentum dusty gaseous material, and/or part of a windy outflowing structure connected to the accretion disc [Hönig, 2019, and references therein]. Irrespective of its underlying nature, a torus around a SMBH significantly contributes to absorb UV light from the accretion disc and reprocess it in IR bands. As GAEA does not explicitly include the dynamical modelling of an accretion disc and a torus around the central SMBH, in what follows I include two torus models and also a combination of them: the model proposed by Wada [2015, Wada hereafter] ¹ and the model proposed by Ramos Almeida and Ricci [2017, RA&R hereafter]. The former model analytically connects the dependence of the torus size and thickness on AGN luminosity/accretion rate and SMBH mass, as detailed below, and assumes that in an AGN there is always enough

¹I adopt the version of the code provided by Johannes Buchner: https://github.com/ JohannesBuchner/agnviz

circumnuclear material to feed a torus. The latter assumes that the column density increases for larger inclination angles, with maximum CTK column densities for the centre of the torus, with no explicit dependence on SMBH accretion rate or mass. I give further details below.

RA&R is based on the model where the fraction of the optical/UV and X-ray radiation processed by the torus and observed in the mid-infrared is proportional to its covering factor [Ricci et al., 2015, 2017b]. Under this model, they assume that in the X-rays the covering factor of the gas and dust surrounding the SMBH can be estimated using a statistical argument and studying the absorption properties of large samples of AGN. Since a compact X-ray corona only gives information of that particular line-ofsight, a large sample study could provide further constrains on inclination angles and therefore other characteristics of the obscuring material. The intrinsic column density distribution of local hard X-ray selected AGN in the data of Ricci et al. [2015] shows an average roughly constant with luminosity covering factor (CF) of the obscuring material of 70%, implying a maximum opening angle of 45 degrees (CF = $\sin \theta$). Some other works, like Tanimoto et al. [2020, 2022], Ogawa et al. [2021], Yamada et al. [2021, 2023], propose torus opening angles somewhat larger between 60-90 degrees, corresponding to higher CF (CF \sim 90-100%) [see also Esparza-Arredondo et al., 2021, for CF>70% for Seyfer 2 galaxies in the X-ray and for Seyfer 1 & 2 in MIR]. In order to match the targeted Compton-thick AGN observed fractions [U14, A19], in what follows I will adopt the same baseline structure of the RA&R model but with a slightly larger value of the covering factor, CF~93%, which is more representative of the latest observational results and, I found, simultaneously provides a better match to the data on the fractions of Compton-thick AGN. Following the RA&R layout, the CF is then subdivided into three areas, the low Compton-thin (CTN, $N_{\rm H} \sim 10^{22}-10^{23}~{\rm cm}^{-2}$), high Compton-thin (CTN, $N_{\rm H} \sim 10^{23}-10^{24}~{\rm cm}^{-2}$) and low Compton-thick (CTK, $N_{\rm H} \sim 10^{24}-10^{26}~{\rm cm}^{-2}$), corresponding to 52-70 degree (CF \sim 93%), 27-52 degree (CF \sim 78%), and 0-27 degree (CF \sim 45%) angles, respectively (see Figure 4.2).

Wada suggests a kinematic model to describe the behaviour of the radiative feedback and the origin of the dependence of the obscured fractions on AGN luminosity. Their work proposes that the AGN produces a fountain of gas creating a radiation pressure on the dusty gas, with the accretion disc radiating most of its energy towards the direction of the rotational axis, not towards the plane of the disc. Besides, the radiative heating is isotropic affecting the surrounding gas through advection. They assume that the X-ray radiation from the AGN is spherically symmetric and heats the inner part of the thin gas disc, making it geometrically thick.

The way I include the Wada torus model in the host galaxies is by assuming a random value of α line-of-sight, which compared with the torus critical angle $\theta_{\rm crit}$ provides with a random column density, either $N_H \sim 10^{22}-10^{24}~{\rm cm}^{-2}$ (CTN obscuration) or $N_H \sim 10^{24}-10^{26}~{\rm cm}^{-2}$ (CTK obscuration). The selected values depend on the absence or

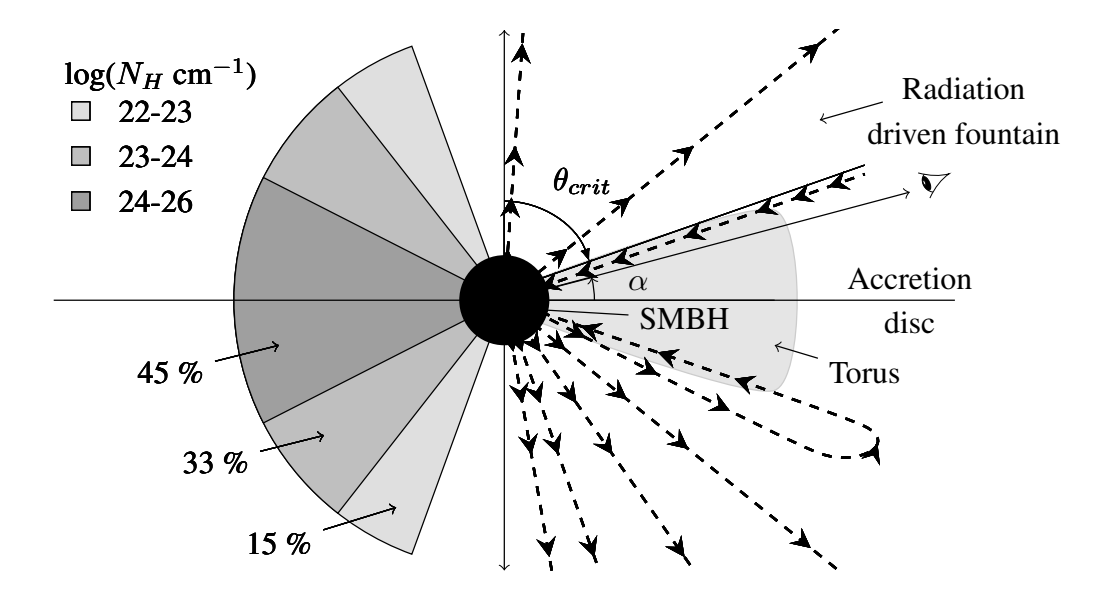


FIGURE 4.2: Diagram of the *fiducial* torus model where I implement both the radiation-driven outflows described by Wada, where θ_{crit} is the critical angle of the radiation-accelerated gas (right side), and the RA&R constant limit angles (left side). α is the random line-of-sight angle. The diagram is separated in two for clarity.

presence of the torus, which is in turn determined by the line-of-sight α for both the torus, and the host disc components (see Fig. 4.1 and 4.2) and its relation with θ_{crit} , the critical angle of the radiation-accelerated gas (see Fig. 4.2). If $\alpha < 90 - \theta$, the line-of-sight lies within the torus, and the source is assumed to be CTK, otherwise it is considered a CTN AGN.

The critical angle θ_{crit} originates from the balance between the radiation pressure on the gas and the gravitational potential of the SMBH. At any angle $\theta \leq \theta_{\text{crit}}$, the radiation force is large enough to allow the dusty gas to escape, and therefore I expect gas outflows forming without the presence of the torus. In the region defined by $\theta > \theta_{\text{crit}}$, the gas eventually falls back towards the equatorial plane, causing dusty gas to remain in the centre and forming a thick torus. The critical angle θ_{crit} depends on both the SMBH mass M_{BH} and the bolometric luminosity L_{X} . More specifically, following Eq. 6 from Wada [2015], the critical angle is defined as

$$\cos \theta_{\text{crit}} = \frac{GM_{\text{BH}}}{r_0} \frac{16\pi c}{\kappa \gamma_{\text{dust}} L_{\text{UV}}} \left(\frac{1}{r_{\text{dust}}} - \frac{2}{r_0} \right)^{-1}$$
(4.10)

where c is the velocity of light, $\kappa = 10^3$ cm² g⁻¹ is the opacity of the dusty gas, $\gamma_{\rm dust} = 1/100$ is the dust-to-gas ratio, r_0 is the radius within which the X-ray heating is effective, $r_{\rm dust}$ is the dust sublimation radius, and $L_{\rm UV}$ is the UV luminosity of the AGN [Marconi et al., 2004]. This UV luminosity is related to the X-ray luminosity of the AGN by $L_{\rm X} = (1/2) \cdot L_{\rm UV} |\cos(\theta)|$ where θ is the angle from the rotational axis. All fixed values are

Part	Model	Summary
	Fiducial host	Model using Eq. 4.4. Column density calcu-
	$(R_{\rm d.Wel}, \text{no BW})$	lated with a disc morphology using all the gas
	,,,,,,,,,,,,,,,,,,,,,,,,,,,,,,,,,,,,,,,	available.
Host	Fiducial host + BW	Model using Eq. 4.5. Column density calcu-
	$(R_{d,Wel}, BW)$	lated with a disc morphology from the gas left
		after the Blast Wave.
	RA&R	Model where the X-ray radiation processed
		by the torus and observed in the MIR is pro-
		portional to its covering factor (left half of Fig-
		ure 4.2).
Torus	Wada	Model based on a radiative fountain (right
		half of Figure 4.2, Eq. 4.10).
	Fiducial torus	Combination of RA&R and Wada torus mod-
		els.
	Fiducial + noBW	Combination of the fiducial torus model and
	(Fiducial torus + host,	the no BW host model.
	noBW)	
Host +	Fiducial + BW	Combination of the fiducial torus model and
torus	(Fiducial torus + host, BW)	the BW host model.

TABLE 4.1: Summary of the different models studied in the paper. They are separated by their area of appliance (host galaxy, torus or both) and by model (no-BW/BW, RA&R/Wada/Fiducial, or a combination).

the ones assumed in Wada. When using Eq 4.10, an increasing AGN power increases the angle $\theta_{\rm crit}$, reducing the chance of intersecting the torus. Note that it is assumed in this model that $r_0 > r_{\rm dust}$ which is always the case for $L_{\rm X} < 10^{47}$ erg s⁻² if one defines r_0 as

$$r_0 = \left(\frac{3L_{\rm X}}{4\pi\Lambda_{\rm cool}}\right)^{1/3},\tag{4.11}$$

where the radiative cooling with cooling rate $\Lambda_{\rm cool}$ is balanced by the X-ray heating rate $\rho_g^2 \Lambda_{\rm cool} = 3L_{\rm X}/(4\pi r_0^3)$, ρ_g being the average gas density in the gas sphere with $r=r_0$. Wada also assumes that $r_{\rm d}=1.3(L_{\rm X}/10^{46})^{1/2}$ pc [e.g., Lawrence, 1991] and $\Lambda_{\rm cool}=10^{-22}n_H^{-2}$ erg cm³ s⁻² ($n_{\rm H}=\rho_{\rm g}/m_{\rm p}$, where $m_{\rm p}$ is the proton mass).

A combination of the two models is also studied, and it is labelled in the following plots as the *fiducial* torus model. In this combined model, I first calculate the critical angle from the Wada model, and I distinguish CTN from CTK depending on the angle α with respect to $\theta_{\rm crit}$. More specifically, if $\alpha > 90 - \theta_{\rm crit}$, then the AGN will be CTN with $N_H < 10^{22}$ cm⁻², if $\alpha < 90 - \theta_{\rm crit}$, then three possibilities can arise following RA&R: 1) if $\alpha < 27$ deg then CTK, if $27 < \alpha < 52$ deg high CTN, $52 < \alpha < 70$ deg low CTN.

I include these dust obscured torus models in each galaxy in post-processing in the GAEA catalogues. A summary of all models can be found in Table 4.1.

4.3 Methodology of the Evolutionary models

Starting from the GAEA catalogues, I then assign a degree of obscuration to each AGN depending on whether I follow an Orientation and/or an Evolutionary approach, as follows. Under the Orientation model, as described in Section 4.2, I calculate the column density by defining the geometry of the gas component of the host galaxy using an exponential gas density profile, to which I will also add a torus-like component around the central SMBH. In the Evolutionary model², I instead assign a column density by randomly drawing a time within the LC (see Figure 4.3) of each AGN, having a different obscuration pre-peak, post-peak and at the peak. I then define models that combine elements from the Evolutionary framework and the Orientation scenario (described in Section 4.2), and I label these combinations as hybrid models. For all my Evolutionary models, I also study the effect of including a torus-like component. Finally, for completeness I also explore Evolutionary models in which the level of obscuration is not determined by the position of the AGN within the LC, but only dictated by the level of starburstness in the galaxy or by the strength (mass ratio) of the merger. A detailed description of all the models considered is provided in the next Sections, while a summary of the main features of each model can be found in Table 4.2.

4.3.1 Analytically integrated light curve

Each accretion event onto the SMBH in HQ11-GAEA realization is characterized by a $\Delta M_{\rm BH}$ which is gradually deposited onto the central SMBH following a predefined LC, which regulates the time evolution of the gas accretion rate over the lifetime of the AGN episode. The shape of the LC broadly follows expectations from numerical experiments and theoretical arguments [e.g., Springel et al., 2005, Hopkins et al., 2006a, Lapi et al., 2006, Shen, 2009, Shankar, 2010]. It is characterized by an exponential prepeak regime, followed by a post-peak power-law phase, to mimic the effects of a self-regulated growth of the SMBH, which initially grows exponentially at or above the Eddington limit, then switching to a less rapid accretion mode when the gas reservoir reduces [e.g., Granato et al., 2004, Monaco et al., 2007, Fontanot et al., 2020]. Both parts of the LC are going to be dependent on the same set of parameters, as described below.

²I stress that with the word "Evolution" in this thesis usually refers to the *short* evolution of the SMBH and galaxy within the timeframe of the AGN LC and not to the overall evolution of the system on longer cosmological timescales.

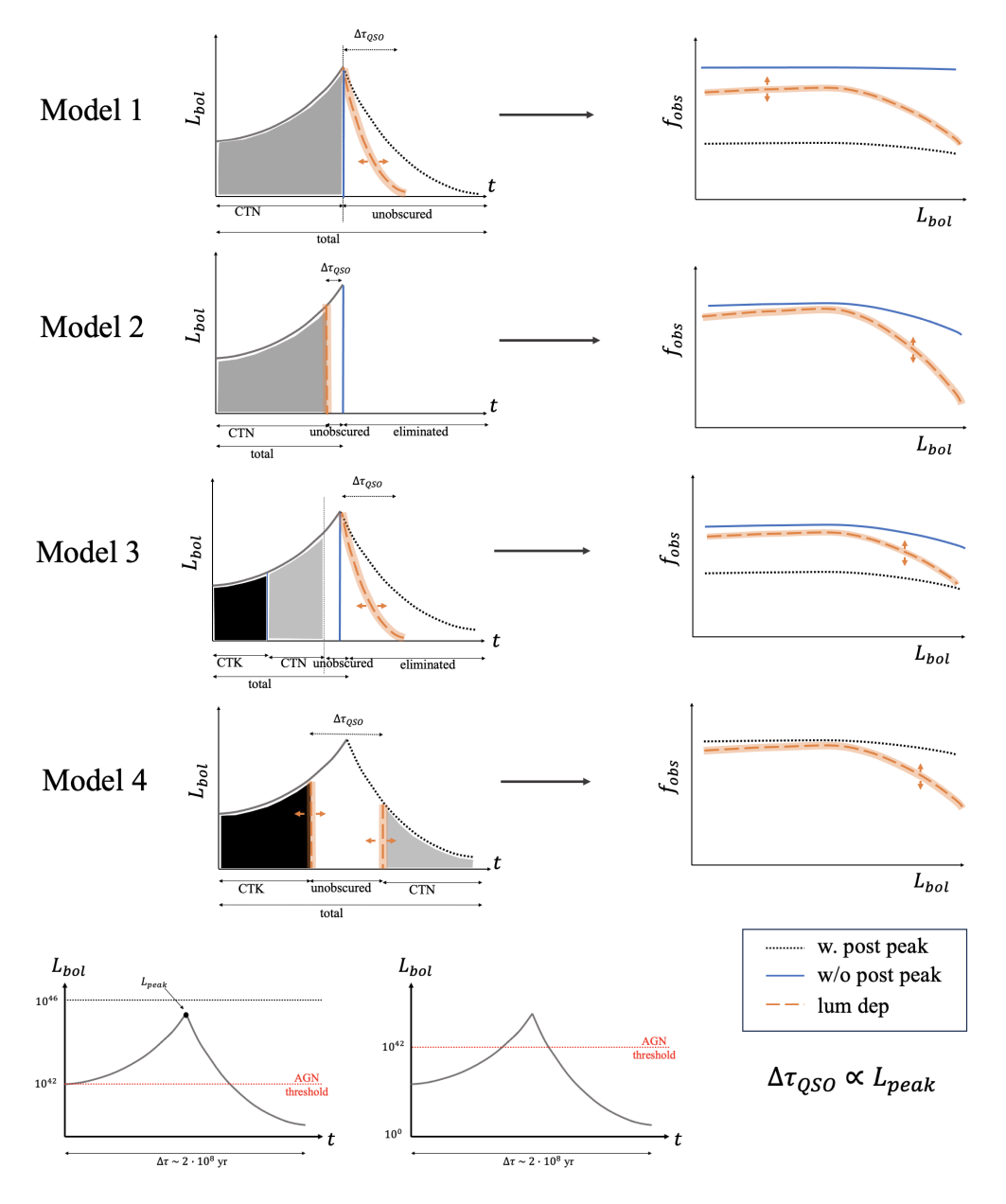


FIGURE 4.3: Diagrams of the Evolutionary models 1, 2, 3, and 4, and the work of the optically/UV visible window. Obscuration in Models 1 and 2 constitutes column densities between 10^{22} and 10^{24} cm $^{-2}$ (CTN), in Model 3 the pre-peak obscured phase is divided in two with column densities between 10^{22} and 10^{24} cm $^{-2}$ (CTN) and between 10^{24} and 10^{26} cm $^{-2}$ (CTK), and in Model 4 the pre-peak obscured phase has column densities between 10^{24} and 10^{26} cm $^{-2}$ (CTK) and the post-peak obscured phase has column densities between 10^{22} and 10^{24} cm $^{-2}$ (CTN). In all cases, dark shadow corresponds to CTK obscuration, light shadow represents the CTN obscured phase, and uncoloured area corresponds with the optically/UV visible phase. We include the effect of each model specification to the CTN obscured fractions.

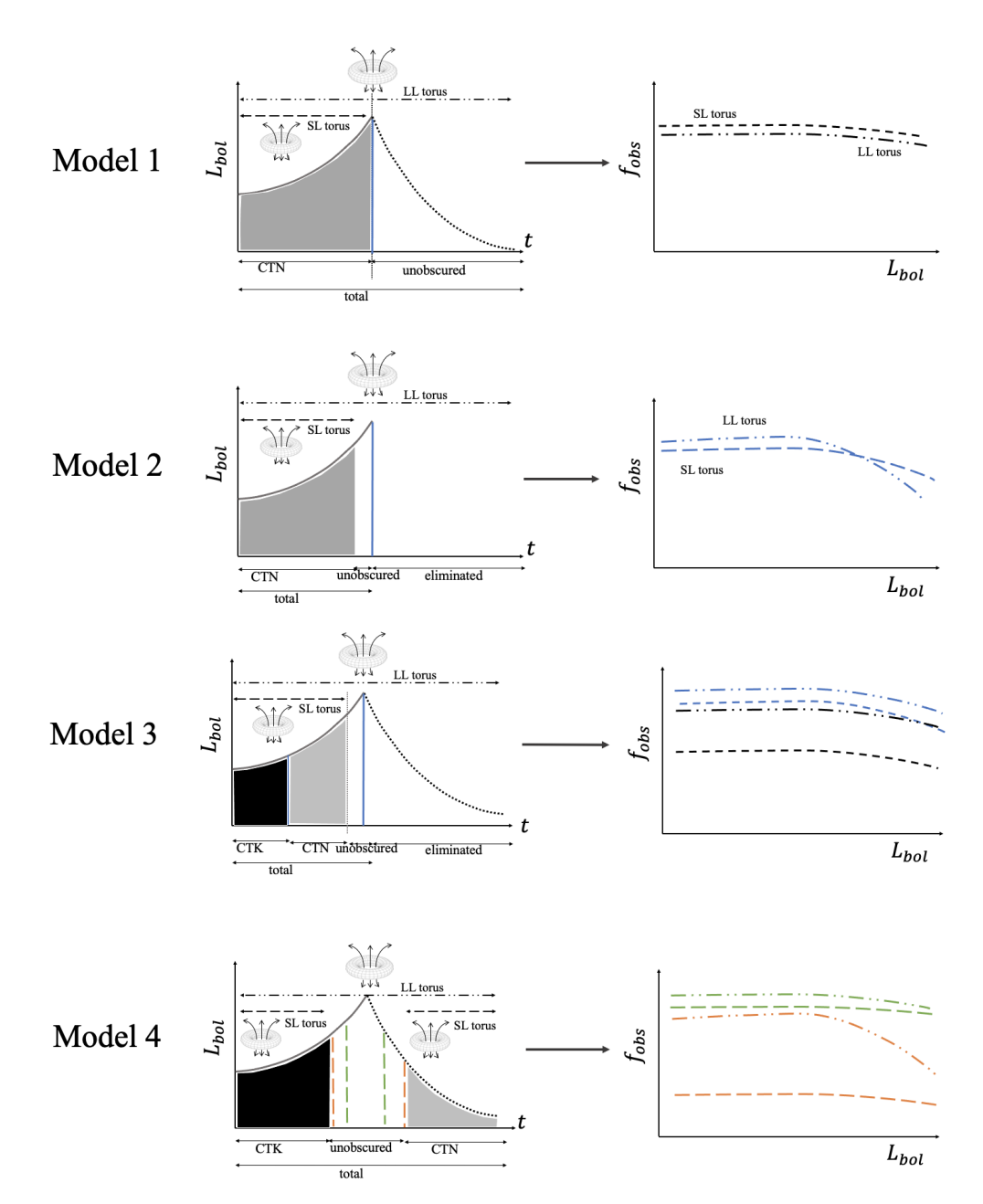


FIGURE 4.3: **(Cont.)** Diagrams of the Evolutionary models 1, 2, 3, and 4, and the work of the optically/UV visible window. Obscuration in Models 1 and 2 constitutes column densities between 10^{22} and 10^{24} cm $^{-2}$ (CTN), in Model 3 the pre-peak obscured phase is divided in two with column densities between 10^{22} and 10^{24} cm $^{-2}$ (CTN) and between 10^{24} and 10^{26} cm $^{-2}$ (CTK), and in Model 4 the pre-peak obscured phase has column densities between 10^{24} and 10^{26} cm $^{-2}$ (CTK) and the post-peak obscured phase has column densities between 10^{24} and 10^{24} cm $^{-2}$ (CTN). In all cases, dark shadow corresponds to CTK obscuration, light shadow represents the CTN obscured phase, and uncoloured area corresponds with the optically/UV visible phase. We include the effect of each model specification to the CTN obscured fractions.

TABLE 4.2: Summary of the different models studied in the paper. They are separated by their area of appliance (host galaxy, torus or both) and by model.

Part	Model	Summary	Figure	Comparison
	Model 1	CTN pre-peak, visible peak ($\Delta \tau_{\rm QSO} \sim 10^{7-8} { m yr}$) and post-	6.1	
Evolutionary		peak	0.1	w/ o tuiti dep
models	Model 2	CTN pre-peak, visible peak ($\Delta \tau_{\rm QSO} \sim (1-5) \cdot 10^7 { m yr}$), no		
		post-peak		
	Model 3 Model 4	CTK 1/3 pre-peak, CTN 2/3 pre-peak, visible peak CTK pre-peak, CTN post-peak, visible peak	6.3	w/o lum dep
E	Fiducial	Model from Chapter 5 with torus present during the whole	Chapter	These models are included in the
Iorus	(long-lived)	TC	5, Fig 5.6	host+torus comparison
	Short-lived	Model from Chapter 5 with torus only present during the obscured phase of the AGN	Chapter 5, Fig 5.4,5.5	,
Exzolution	Model 1	CTN pre-peak, visible peak ($\Delta \tau_{\rm QSO} \sim 10^{7-8} \ {\rm yr}$) and post-	6.4	Long vs short-lived torus
EVOIUUII		peak with a long/short-lived torus	Ħ.	
Tor118	Model 2	CTN pre-peak, visible peak ($\Delta \tau_{\rm QSO} \sim (1-5) \cdot 10^7 \; { m yr}$), no		
201		post-peak with a long/short-lived torus		
	Model 3	CTK 1/3 pre-peak, CTN 2/3 pre-peak, visible peak	7	Long vs short lived torus and LC
		$(\Delta au_{ m QSO} \sim 10^{7-8} { m \ yr})$, no post-peak with a long/short-lived	C.O	length
		torus		
	Model 4	CTK pre-peak, CTN post-peak, visible peak ($\Delta au_{QSO} \sim$		Long vs short lived torus and
		10^{7-8} yr) with a long/short-lived torus		visibility window
Hybrid	Model 3	CTK 1/3 pre-peak, CTN 2/3 pre-peak, visible peak, no	9.9	Host galaxy vs host+torus
model	,	post-peak, N_H comes from Chapter 5 and long-lived torus)	
	Model 4	CTK pre-peak, CTN post-peak, visible peak where the N _H		
			1	17. 67. 11. 74.
z-evolution	Model 3	Model 3 nne-tuning lum dep vs Model 3 nybrid	0./	Models from Figure 6.3 and 6.3
Starburst	$ m \mid SFR > 100~M_{\odot}/yr$	$N_{\rm H}$ from Chapter 5 + galaxies with SFR $> 100~{ m M}_{\odot}/{ m yr}$ are	6.9	Host from Chapter 5 vs host+SFR
		CIN		> 100 M☉/ yr vs nost+s5rK
	$SFR > (1,4)SFR_{MS}$	$N_{ m H}$ from Chapter 5 + galaxies with SFR $> (1,4) m SFR_{MS}$ are CTK		$> (1,4) \mathrm{SFR}_{\mathrm{MS}}$
Mergers	Merger rate >	$N_{ m H}$ from Chapter 5 + galaxies with merger rate > 0.33 are	6.10	Host from Chapter 5
	0.33	CTK (w/o fiducial torus)		vs host-mergers vs
				host+torus+mergers

The exponential regime is described as:

$$\dot{M}_{\rm BH}(t) = \dot{M}_{\rm BH}^{\rm peak} \exp\left(\frac{t_{\rm peak} - t}{t_{\rm Edd}}\right),\tag{4.12}$$

where $\dot{M}_{\rm BH}(t)$ is the accretion rate onto the central SMBH, $\dot{M}_{\rm BH}^{\rm peak}$ is the QSO-mode peak accretion rate, $t_{\rm peak}$ is the time corresponding to the peak accretion rate since the triggering episode (most of the time a merger), t is the time stamp within the LC, and $t_{\rm Edd}$ is the Eddington time corresponding to $4.5 \cdot 10^7$ years for the chosen value of the radiative efficiency ($\epsilon_{rad} = 0.15$, also used for luminosity calculation).

The second regime is defined as in Hopkins et al. [2006a],

$$\dot{M}_{\rm BH} = \frac{\dot{M}_{\rm BH}^{\rm peak}}{1 + \left| \frac{t - t_{\rm peak}}{t_{\rm Edd}} \right|^2}.$$
(4.13)

The LC put forward above is a flexible mathematical model that can be adapted to explore the impact of varying the relative time lengths of the pre- and post-peak phases in the predicted fractions of obscured AGN [see also Appendix B in Alonso-Tetilla et al., 2024]. In the original LC model presented by F20 (their, Eq. 13), the peak values were chosen by adopting a first regime where the BH accretes exponentially at $\dot{M}_{\rm edd}$, until it reaches a critical BH mass $M_{\rm BH}^{\rm crit}$ ($\dot{M}_{\rm BH}^{\rm crit} = \dot{M}_{\rm BH}^{\rm peak}$)

$$M_{\rm BH}^{\rm crit} = f_{\rm crit} 1.07 (M_{\rm BH}^{\rm in} + \Delta M_{\rm BH}),$$
 (4.14)

where $\Delta M_{\rm BH}$ represents the total mass accreted in the event, $M_{\rm BH}^{\rm in}$ is the initial mass of the SMBH, and I fix the scaling factor for 'critical mass' of BH as $f_{\rm crit}=0.4$ as in F20 which was originally fixed based on direct observations and numerical simulations by Somerville et al. [2008] [see also Marulli et al., 2008, Bonoli et al., 2010].

The original F20 LC, calibrated on the Hopkins et al. [2007] prescriptions built around the idea of a critical accretion rate $M_{\rm BH}^{\rm crit}$, tends to generate quite narrow LCs, sometimes close to delta functions, due to the fact that after triggering the accretion rate rapidly approaches the critical accretion rate thus generating a fast switch from Eddington-limited to power-law modes.

In this thesis instead, I bypass the critical accretion rate limitation. In the LC reference model, I keep unaltered the original F20 values of $\dot{M}_{\rm BH}^{\rm crit}$ and $t_{\rm peak}$, but allow for extended pre- and post-peak phases following Eqs. 4.12 and 4.13, without the constraints imposed by the critical accretion rate criteria and the moment of the accretion triggering and still matching the observed AGN LF. In addition, I will also explore more flexible models where both the $t_{\rm peak}$ and $\dot{M}_{\rm BH}^{\rm peak}$ parameters are also varied. I verified that my

predicted AGN LFs generated by the new LCs fall within the observational determinations by Shen et al. [2020] at $z \lesssim 3$, and also the implied SMBH mass functions are similar to those reported by F20.

It is important to note that my method may yield slightly higher BH mass estimates than initially prescribed. The prerequisite for each assumed individual input LC is to be consistent with the observed bolometric AGN LF at least at z < 3, which is the main focus of this thesis without modifying any of the GAEA free parameters. Indeed, I verified that all my model variants are within the observational limits of Shen et al. [2020] (see AGN LF in Chapter 6, Figure 6.11).

4.3.2 Pure evolutionary models

In my pure Evolution models, the level of obscuration in an AGN is solely controlled by the time at which the AGN is observed within the LC [e.g., Sanders et al., 1988]. In my Evolutionary models, each source is randomly sampled within the LC and assigned a luminosity and a certain degree of obscuration (a value of the line-of-sight $N_{\rm H}$ column density) based on its position in the LC. The early phases of the life of an AGN are considered the most obscured, as the AGN radiation is expected to clear out its environment at later times, making the source also optically and UV visible [e.g., Hopkins et al., 2006a, Gilli et al., 2007, Kocevski et al., 2015]. However, more recent works suggest a more complex evolution [e.g., Lapi et al., 2006, 2014, Aversa et al., 2015]. As visually represented in Figure 4.3, in this thesis I consider four physically motivated scenarios that account for host galaxy obscuration, representing the cold gas or dust contribution (but not a torus-like component):

- *Model* 1: this model follows the traditional view of evolutionary models in which AGN are obscured pre-peak, and become optically/UV visible post-peak. I assume obscuration can only reach Compton-thin levels in the pre-peak phase, with a random value within $22 < \log N_{\rm H}/{\rm cm}^{-2} < 24$. In Model 1 the optical/UV "visibility window" $\Delta \tau_{\rm QSO}$ is the whole extent of the LC after the time of peak luminosity.
- *Model* 2: this model is inspired by the seminal works by Granato et al. [2004] and Lapi et al. [2006]. In this scenario, the source starts CTN until the BH feedback and the strong early episodes of star formation efficiently eject and/or consume the gas reservoir in the host galaxy and around the SMBH, thus rapidly shutting off the accretion on the central object, and consequently the LC sharply decreases to zero after the peak. The AGN in this scenario becomes optically/UV visible for a relatively brief interval of time $\Delta \tau_{\rm OSO}$ around the peak.
- Model 3: is a variation of Model 2 in which I also include an initial Compton-thick (CTK) phase followed by a CTN phase. The peak and the post-peak phases are

unobscured (20 < log $N_{\rm H}/{\rm cm}^{-2}$ < 22). This model can adopt a flexible post-peak phase. If I make use of the total LC, I label it *with post-peak*. If, similarly to Model 2, the accretion turns off quickly after the peak, I label the model it *without post-peak*. In Model 3 the optical/UV visibility window $\Delta \tau_{\rm QSO}$ is the total extent of the LC after the CTN phase.

• *Model 4*: in this model the early phases of the AGN present CTK obscuration, followed by a period of $\Delta \tau_{\rm QSO}$ optical/UV visibility, hereafter labelled as *visibility window*. Later on, in this model I assume that ejected gas falls back into the galaxy causing CTN obscuration.

The first four rows of Figure 4.3 sketch the four models introduced above. In the left column we report the idealised LC characterizing each model, and in the right column the corresponding foreseen effects on the obscured fractions of AGN as a function of luminosity $f_{obs}(L)$, which will be discussed in detail in Chapter 6. It can be seen from Figure 4.3 that the removal of a prolonged post-peak phase (blue lines) is expected to significantly increase the fractions $f_{obs}(L)$ at all luminosities as the visibility window $\Delta \tau_{\rm OSO}$ shrinks while the obscured pre-peak phases remain unaltered. It is important to stress at this point that the overall extent of the AGN LC is fixed in my models to $\sim 2 \cdot 10^8$ years as in F20 at z=2.4, although it could be shorter than this in models without a post-peak phase, as, for example, in Model 2. I note that the exact value for the full temporal length of the LC has a relatively minor impact to both the predicted bolometric LF and the obscured fractions of AGN. What is more relevant is the choice of the relative lengths of the pre- and post-peak phases, which correspond to different levels of obscuration in my Evolutionary models. In addition, I also verified that most of my sources are already shining above the limiting luminosity of the observational surveys, $L_{\rm bol} \gtrsim 10^{42}$, and thus prolonging the LCs would mostly add luminosities below the detection limit of the data, without any impact on the predicted $f_{\rm obs}(L)$ above $L_{\rm bol} \gtrsim 10^{42}\,{\rm erg s^{-1}}$. This is graphically visualized in the bottom panels of Figure 4.3 which depicts two limiting cases of an AGN with a LC with luminosities for most of the time above the minimum luminosity of the surveys $L_{\rm bol} \gtrsim 10^{42}\,{\rm erg s^{-1}}$ (left column), and one with a LC in which only luminosities around the peak are above $L_{\rm bol} \gtrsim 10^{42}\,{\rm erg s^{-1}}$ (right column). Most of the sources in our models broadly fall within these two limiting cases, with a larger proportion of AGN with fainter luminosities, as relatively fewer AGN reach very bright luminosities around their peaks.

Once an LC is chosen, I assign to each active galaxy a Hydrogen column density $N_{\rm H}$ and bolometric luminosity by randomly extracting the time of observation from the LC. If I observe the galaxy in a phase of CTN obscuration, I assign $N_{\rm H}$ at random in the range $22 < \log(N_{\rm H}/{\rm cm}^{-2}) < 24$. The optically/UV visible phase is characterized by $20 < \log(N_{\rm H}/{\rm cm}^{-2}) < 22$, while the CTK column densities are uniformly extracted in the range $24 < \log(N_{\rm H}/{\rm cm}^{-2}) < 26$. In this approach, we bypass any information

on the amount and/or geometry of the cold gas within the host galaxy, with the aim to characterize the general conditions under which a pure Evolutionary sequence of obscured/unobscured phases can reproduce current data sets.

4.3.2.1 Fine-tuned luminosity models

In all the reference models I assume that the visibility window is constant for all galaxies. However, it may be expected that in more luminous AGN, with allegedly an increased ejective power, the UV/optically visible window $\Delta \tau_{\rm QSO}$ may be longer than for less luminous sources. This process would, in turn, generate shorter obscuration phases, and thus a reduced fraction of obscured sources at higher luminosities, as visually sketched in the first rows of Figure 4.3 with orange, dashed lines. In order to test this possibility, I assume $\Delta \tau_{\rm QSO}$ to slightly increase with peak luminosity in Model 1, following the empirical formula

$$\Delta \tau_{\text{QSO}} = \Delta t_{\text{post-peak}} \cdot \left[1 - \left(\frac{L_{\text{lim}}}{L_{\text{peak}}} \right)^{\alpha} \right] \cdot 10^{7} \,[\text{yr}], \qquad (4.15)$$

where $\alpha=0.1$, $L_{\rm lim}=10^{45}$ erg/s, and $\Delta t_{\rm post-peak}=f(t_{\rm peak})$ refers to the time of the post-peak phase which varies from source to source, but limited in the range 10^7 and $2\cdot 10^8$ years, the maximum extent of the LC at my redshift of reference z=2.4. I also impose that $\Delta \tau_{\rm QSO}$ never falls below 10^7 yr, i.e., the reference value for models with constant visibility window, as I noticed that this choice provides a better match to the fraction of obscured AGN at fainter luminosities. Similarly, Model 2 has a fine-tuned visibility window:

$$\Delta \tau_{\text{QSO}} = \Delta t_{\text{pre-peak}} \cdot \left[1 - \left(\frac{L_{\text{lim}}}{L_{\text{peak}}} \right)^{\alpha} \right] \cdot 10^{7} \,[\text{yr}] \,. \tag{4.16}$$

Note that in Model 1 I am fine-tuning the visibility window by decreasing the time of the post-peak phase (Eq. 4.15) and in Model 2 I use the pre-peak phase instead (Eq. 4.16). Therefore, in Model 1 I keep constant the CTN phase, while in Model 2 I decrease it as the visibility window increases. The form and choice of parameters for the luminosity-dependent expressions of $\Delta\tau_{\rm QSO}$ given above have been empirically calibrated via trial and error to produce an improved match to the fractions of obscured AGN measured by U14 and A19, which sharply drop with increasing AGN luminosity. Equations 4.15 and 4.16 ensure that the more luminous AGN will be characterized by longer visibility windows, more specifically AGN with peak luminosity $L_{\rm peak} \lesssim 10^{43}$ erg/s will have a $\Delta\tau_{\rm QSO} \sim 10^7$ yr, which steadily increases for more luminous sources approaching values of $\Delta\tau_{\rm QSO} \sim 5 \cdot 10^7$ yr for $L_{\rm peak} \lesssim 10^{45}$ erg/s and $\Delta\tau_{\rm QSO} \sim 8 \cdot 10^7$ yr for $L_{\rm peak} \sim 10^{46}$ erg/s.

4.3.2.2 Contribution from a torus-like component

Evolutionary models introduced so far do not include a possible contribution from a central torus-like structure. However, it is now clear from both direct and indirect (via, e.g., Spectral Energy Distribution (SED) fitting) observations [Combes et al., 2019, García-Burillo et al., 2019, 2021] that such element is an essential ingredient required to fully model the observational properties of AGN [see Netzer, 2015, Ramos Almeida and Ricci, 2017, Hickox and Alexander, 2018, for reviews], especially in sources with $\log_{10}(N_{\rm H}/{\rm cm}^{-2}) > 24$ [Risaliti et al., 1999, Marchesi et al., 2018]. As already mentioned in Section 4.2, the torus can be described as a compact reservoir of low angular momentum dusty gaseous material, and/or part of a windy outflowing structure connected to the accretion disc [Hönig, 2019, and references therein]. Irrespective of its underlying nature, a torus around a SMBH significantly contributes to absorb UV light from the accretion disc and reprocess it in IR bands. Despite GAEA includes the modelling of gas reservoirs around the central SMBH (and the subsequent accretion of this material), it does not explicitly treat the dynamical and geometrical properties of the accretion disc and the torus around the central SMBH. Therefore, I include a modelling of the torus following the prescriptions I developed in Section 4.2. I define as the fiducial torus model a combination of the models proposed by Wada [2015] and Ramos Almeida and Ricci [2017]. The former model analytically connects the dependence of the torus size and thickness on AGN luminosity/accretion rate and SMBH mass, and assumes that in an AGN there is always enough circumnuclear material to feed a torus. The latter more empirical model by Ramos Almeida and Ricci [2017] assumes that the column density increases for larger inclination angles, with maximum CTK column densities for lines of sight close the centre of the torus, without any explicit dependence on SMBH accretion rate or mass (see Chapter 4.2 for full details).

In what follows, we will explore variants of our Evolution models in which we add the torus component, as sketched in the bottom row of Figure 4.3. We label as *short-lived* those Evolution models where we assume the torus is only present during the obscured phases within the LC, while we label *long-lived* those Evolution models where we assume the torus survives the peak activity of the AGN and lasts for the whole duration of the LC. Including a torus will always boost the fraction of obscured AGN, especially in the CTK regime, and will also tend to produce obscured fractions that decrease with increasing luminosity as the thickness of the torus itself shrinks with with AGN luminosity [Wada, 2015]. Therefore, the torus model is expected to provide predictions that may be somewhat degenerate with those from a luminosity-dependent $\Delta \tau_{\rm OSO}$ (Section 4.3.2.2), and we will discuss some implications of this in Section 6.2.

4.3.3 Orientation and evolution hybrid model

Including a torus component in an Evolution model, as described in the previous Section, is a first step towards a more complete model for the obscuration of AGN. In addition, a more realistic modelling of AGN obscuration should take into account the overall distribution of cold gas in the host galaxy during the LC, e.g., during the growth episode of the central SMBH. In the real Universe, we would thus expect that a combination of Orientation and Evolution effects could simultaneously contribute to the line-of-sight $N_{\rm H}$ column density of an AGN [e.g., Hickox and Alexander, 2018, Zhou et al., 2018, Gilli et al., 2022, Pouliasis et al., 2024].

To this purpose, in this thesis I also put forward comprehensive models in which the $N_{\rm H}$ column densities originate from the gas distribution in the host galaxy using the geometry and the exponential density profile described in Section 4.2. I then assign a bolometric AGN luminosity to the SMBH based on the retrieved value of $N_{\rm H}$ and the type of LC assumed in the model, following the different LC models described in Section 2.5.2. For example, using Model 1, a density profile-based column density of $\log_{10}(N_{\rm H}/{\rm cm}^{-2}) < 22$ would have a bolometric luminosity chosen at random within the visible post-peak phase of the LC, whilst column densities $\log_{10}(N_{\rm H}/{\rm cm}^{-2}) > 22$ would have assigned a random bolometric luminosity within the obscured pre-peak phase of the LC. Taking into account that column density and luminosity, we analyse the new obscured fractions. For Models 3 and 4 I take into account the three portions of the LC, including the CTK one.

As already mentioned, the column density $N_{\rm H}$ associated to each galaxy is computed following the modelling of Section 4.2. In brief, this model strictly assumes an exponential profile for the gas component, with a scale radius of $R_{\rm d,gas}=0.3 \cdot R_{\rm d,\star}$ which aligns with present ALMA observations of high-z galaxies [see, e.g. Puglisi et al., 2019]. I will discuss below the implications of relaxing these assumptions for both the scale radius and also gas profile in the context of the present modelling. This model is called the *hybrid* model since it includes key variables from both Orientation (density profile gas distributions) and Evolutionary models (light curves), as well as explores other aspects from the models (e.g., a torus component from the Orientation model).

4.3.4 High star-forming galaxies and major mergers as CTK sources

As anticipated in Section 2.5.4, in the context of Evolutionary models [e.g., Granato et al., 2004, Alexander et al., 2005, Granato et al., 2006, Hopkins et al., 2010], it is expected that newly formed, dust-enshrouded galaxies, often characterized by intense starburst episodes possibly triggered by major mergers, and usually associated with high gas column densities [Mihos and Hernquist, 1996, Di Matteo et al., 2008, Zhou et al., 2018, Renaud et al., 2022], are the obvious sites of obscured CTK AGN, especially

at z > 1. It is thus a natural question to ask whether there are sufficient starbursts or major mergers to explain the significant fractions of CTK AGN observed at different redshifts, a question that I will address in Section 6.5.

Here I explore the role of dusty starburst in creating CTK obscuration in AGN. I first assume that all obscured sources are derived from the host of the galaxies, and the CTK sources are simply defined to be the ones characterized by a star formation rate (SFR) above some ad-hoc threshold above the Main Sequence (MS). In other words, in this alternative approach I am not assuming any underlying geometry for the cold gas but simply relying on the level of SFR to label an AGN as CTK or not, while the CTN AGN continue to be simply defined by the intrinsic gas content and geometry of the host galaxy. The main limitation of this approach is to use a suitable definition for starburst galaxies. In the following, I take advantage of the GAEA model and label as CTK sources those that are selected above a threshold at their SFR peak. Alternatively, I also adopt a different definition of starburst galaxies as those objects lying four times above the MS, which is a common definition of starburst often adopted in observational studies [e.g., Carraro et al., 2020].

Similarly, I can assume that CTK AGN are mainly connected with merger events [e.g., Lanzuisi et al., 2015, Bickley et al., 2024]. GAEA allows to track the events responsible for triggering AGN activity (either disc instabilities or mergers). At the redshift of interest, z=2.4, the large majority of simulated AGN (>99%) are a result of mergers (either minor or major). I then explore a variant of the model in which CTK sources are those galaxies that have undergone a recent merger above a chosen mass ratio.

4.4 Obscuration in Eddington ratio distributions of semi-analytic galaxies

In this thesis, I also investigate the statistical distributions in Eddington ratio of obscured and unobscured AGN using the GAEA semi-analytic model [F20]. My methodology builds upon the work in Section 4.2 and 4.3, which provide a comprehensive framework for understanding AGN obscuration through models of orientation and evolutionary processes. This Section outlines the key steps and calculations used to explore the relationship between column density, Eddington ratio, and AGN obscuration.

4.4.1 Column density calculation

The column density ($N_{\rm H}$) of the host galaxy plays a crucial role in determining whether an AGN is obscured or unobscured. For this analysis, I adopt the column density values provided by the different models detailed in Section 4.2 (Orientation models) and

Section 4.3 (Evolutionary models) based on a combination of galactic properties, including gas mass and scale length, which are consistent with observational data.

In a pure orientation model, each GAEA host galaxy is characterised by a scale length and a cold gas mass that in turn implies a specific column density when assuming an exponential density profile and a disc morphology. Following the calculation described in Section 4.2, I find that the host galaxy produces very little number of obscured galaxies with column densities above $\log_{10}(N_{\rm H}/{\rm cm}^{-2}) > 24$ (Compton-thick obscuration, CTK), most of them being optically/UV visible (20 $< \log_{10}(N_{\rm H}/{\rm cm}^{-2}) < 22$) or Compton-thin obscured (CTN, 22 $< \log_{10}(N_{\rm H}/{\rm cm}^{-2}) < 24$) thus suggesting the contribution of other sources of obscuration, like a central torus (Section 4.2.2). In the case of Evolutionary models, the column density is assigned depending on the selected time within the LC of the galaxy, whether pre- or post-peak (see Section 4.3).

Evolutionary models mentioned so far exclude the potential influence of a central torus-like structure. However, both direct and indirect observations [via, e.g., SED fitting Combes et al., 2019, García-Burillo et al., 2019, 2021] have shown that such a structure is crucial for accurately modelling AGN properties, especially in sources with $\log_{10}(N_{\rm H}/{\rm cm^{-2}}) > 24$. The torus, described as a compact, dusty gas reservoir with low angular momentum or part of a windy outflow linked to the accretion disc, plays a key role in absorbing UV light from the accretion disc and re-emitting it in the IR bands. Although GAEA models gas reservoirs and subsequent accretion onto the SMBH, it does not explicitly address the dynamics and geometry of the torus and accretion disc. Therefore, I incorporate torus modelling using the approach described in Section 4.2, also used in Section 4.3. The *fiducial* torus model combines elements from Wada [2015] and Ramos Almeida and Ricci [2017]. The former relates torus size and thickness to AGN luminosity/accretion rate and SMBH mass, assuming adequate circumnuclear material for torus formation, while the latter suggests that column density increases with inclination angle, peaking at the torus centre, without explicit dependence on SMBH properties.

4.4.2 Eddington ratio calculation

The Eddington ratio ($\lambda_{\rm Edd}$) is a key parameter in understanding AGN activity, representing the ratio of the AGN bolometric luminosity ($L_{\rm bol}$) to the Eddington luminosity ($L_{\rm Edd}$). The bolometric luminosity is estimated from the AGN accretion rate, which is itself derived from the black hole growth rate within the GAEA model (see Section 4.2.1). For my analysis, I calculate the Eddington ratio for each galaxy in the GAEA catalogue using the bolometric luminosities provided by the models described in Sections 4.2 and 4.3, which discuss alternative approaches for calculating $L_{\rm bol}$ based on different assumptions on the evolution and orientation of the galaxy.

As mentioned in previous sections, the GAEA bolometric luminosity is calculated as $L_{\rm bol} = L_{\rm bol}^{QSO} + L_{\rm bol}^{Radio}$, where $L_{\rm bol}^{QSO}$ is the luminosity of the QSO-mode and $L_{\rm bol}^{Radio}$ the luminosity of the radio-mode of each galaxy. The bolometric luminosity is of special interest for SAM at local redshifts, since the accretion of hot gas (radio-mode) has a higher impact in low redshifts than high redshifts, where the accretion of cold gas (QSO-mode) has a more impactful effect, to the point of being able to reproduce higher luminosity functions with galaxies with only QSO-mode accretion. The QSO-mode from GAEA is described and studied in detail in F20, however I study the effect of a different LC in Chapter 6 (see also Chapter 5), where I explore the impact of different LC characteristics in the AGN obscuration, using the $L_{\rm bol}^{QSO}$ from GAEA as consistent LC peak.

Once L_{bol} is determined, I calculate L_{Edd} using the formula

$$L_{\rm Edd} = 1.26 \times 10^{38} \left(\frac{M_{\rm BH}}{M_{\odot}}\right) \, {\rm erg \, s^{-1}},$$
 (4.17)

where $M_{\rm BH}$ is the mass of the central black hole. GAEA provides SMBH accretion rates for the QSO and radio-mode [for more information, see F20], as well as the SMBH mass at each accreted moment. For Orientation models, I will use the peak luminosity of each galaxy and its corresponding BH mass, while for Evolutionary models I will use the accretion selected depending on the obscuration of the galaxy at a specific LC phase. The Eddington ratio is then obtained as $\lambda_{\rm Edd} = \frac{L_{\rm bol}}{L_{\rm Edd}}$ (see Eq. 2.4). Note that many observations [e.g., Aird et al., 2018, Georgakakis et al., 2017a, Laloux et al., 2024] use an alternative calculation:

$$\lambda_{\text{Edd}} = \frac{L_{\text{bol}}}{L_{\text{Edd}}} \simeq \lambda = \frac{25 \cdot L_X (2 - 10 \text{keV})}{1.26 \cdot 10^{38} \cdot 0.002 M_{\star}},$$
(4.18)

with M_{\star} in solar mass units and X-ray luminosity in ergs⁻¹, which is a simplistic scaling relation to make the accretion rate L_X/M_{\star} resemble the Eddington ratio. For this relation, I will be using the normalized function, which follows:

$$\int P(\lambda, N_{\rm H}, z, M_{\star}) d\log \lambda = 1. \tag{4.19}$$

For the purpose of this **thesis**, I assume that scaling relation is equivalent, although in my data there is a minor difference in the relation when using BH mass or stellar mass.

4.5 Clustering analysis with semi-analytic galaxies

The spatial distribution of galaxies encodes critical information about the underlying matter distribution and the processes that govern structure formation in the universe. The two-point correlation function (2pcf) $\omega_p(r_p)$, quantifies the excess probability of finding a pair of galaxies separated by a distance r_p compared to a random distribution.

The two-point correlation function, $\omega_p(r_p)$, is generally defined as:

$$\omega_p(r_p) = \frac{\langle n(r_1)n(r_2)\rangle}{\langle n\rangle^2} - 1, \tag{4.20}$$

where $n(r_1)$ and $n(r_2)$ represent the number densities of objects at positions r_1 and r_2 , $\langle n \rangle$ is the mean number density, and $\langle \cdot \rangle$ denotes an ensemble average over all pairs separated by distance $r_p = |r_2 - r_1|$. This function quantifies deviations from a random distribution, where $\omega_p(r_p) = 0$ corresponds to no clustering.

In the following, I will show predictions on the projected 2-point correlation function (2pcf) $\omega_p(r_p)$ calculated using the Python *Corrfunc* package [Sinha and Garrison, 2020]. This function computes the projected correlation function in a periodic cosmological box, which counts the position pairs that are separated by less than the r_p bins in the X-Y plane, and less than $\pi_{\rm max}$ in the Z-dimension. From many estimators that could be used to define Eq. 4.20, in this thesis and in the Python *Corrfunc* package I use the Landy-Szalay estimator to compute $\omega_p(r_p)$, which defines Eq. 4.20 as:

$$\omega_p(r_p) = \frac{DD(r_p) - 2DR(r_p) + RR(r_p)}{RR(r_p)}.$$
(4.21)

To compute $\omega_p(r_p)$, pair counts are performed for the observed dataset and a random catalogue. The data-data pairs $(DD(r_p))$ are the number of pairs of galaxies in the observed dataset separated by distance r_p . The random-random pairs $(RR(r_p))$ are the number of pairs in a randomly distributed catalogue of the same spatial and selection properties as the observed dataset. And the data-random pairs $(DR(r_p))$ are the number of cross-pairs between the observed and random datasets.

Distances are binned into intervals to improve statistical robustness. Random catalogues are generated to mimic the survey geometry and selection effects, ensuring an unbiased estimate of $\omega_p(r_p)$. Depending on the value of the correlation, the particles distance can show if the result indicates clustering or not and at what level of separation, showing homogeneity or heterogeneity. $\omega_p(r_p)$ at small scales $(r_p < 1 \text{ Mpc})$ reflects non-linear clustering due to local gravitational interactions, intermediate scales $(1 \lesssim r_p \lesssim 50 \text{ Mpc})$ captures the large-scale structure, including filamentary and void structures, and large scales (r > 100 Mpc) shows homogeneity, consistent with the cosmological principle.

Chapter 5

Probing the roles of the orientation, and multi-scale gas distributions in shaping the obscuration of Active Galactic Nuclei through cosmic time

In this Chapter I present the results of the Orientation model applied to the GAEA AGN catalogue, where I assume that the column density is calculated from an Exponential density profile and the AGN peak luminosity, as detailed in Section 5.1, including a study of the dependence on gas disc scale thickness in Section 5.2. I also include a torus-like component that creates the CTK obscuration and some CTN obscuration in Section 5.3. I evaluate the effect of changing some of the variables, like the light curve in Section 5.4 or the gas fractions in Section 5.5. I finish the Chapter discussing the limitations of the Orientation model in Section 5.6.

This chapter has been published as part of Alonso-Tetilla et al. [2024].

5.1 The role of galaxy size and AGN feedback in shaping the obscured AGN fraction with L_X

In what follows, when discussing the dependence of AGN obscured fractions on X-ray luminosity, I focus on the mean redshift of z = 2.4, around the peak of AGN emissivity with available observational constraints. I will then show the fiducial model against data in other bins of redshift. In the left panel of Figure 5.1, I provide a comparison of the predicted mean column densities from the models as a function of X-ray luminosity

compared with the mean empirical column densities extracted from the average

$$\langle \log N_{\rm H} \rangle = \int f(\log N_{\rm H} | L_{\rm X}) \cdot \log N_{\rm H} \cdot d \log N_{\rm H},$$
 (5.1)

where $f(\log N_{\rm H}|L_{\rm X})$ is the conditional column density distribution derived by U14 and A19. The results clearly highlight the importance of the correct recovery of the gas scale radii as a function of galaxy stellar mass, as seen from the significant difference between the AGN obscured fractions using GAEA disc radii and van der Wel et al. [2014] relation for the effective radius:

$$R_{\rm eff}(m_{\star})/\rm kpc = A \cdot m_{\star}^{\alpha} \tag{5.2}$$

where $m_\star \equiv M_\star/7 \cdot 10^{10} M_\odot$ and the parameters A and lpha values are described in Table 1 of van der Wel et al. [2014], depending on redshift. In my reference model I assume gas disc thickness as $h = R_d/8$ following Nath Patra [2020]. I will show the effect on the prediction of a different assumption for h in the Section 5.2. As robust and extensive measurements of the gas sizes are only available for sporadic samples [see Nelson et al., 2016, Puglisi et al., 2019, for comparison between ionised gas or cold gas and stellar disc radii in a statistical sample of $z\sim 1.5$ galaxies], in what follows I assume the $R_{\rm d,gas} = N \cdot R_{\rm d,\star}$, with $R_{\rm d,\star} = 1.68 R_{\rm eff}$, and N = 0.3, inspired by the recent ALMA/submillimetre observations by Puglisi et al. [2019] suggesting that on average the gas disc radius is about 1/3 of the stellar component, which is at variance with previous works that assumed $R_{\rm d,\star}=R_{\rm d,gas}$ [e.g., Tamburro et al., 2008, Leroy et al., 2008, Swinbank et al., 2017, Gilli et al., 2022, Liao et al., 2023]. I note that assuming large gas scale lengths comparable to the stellar disc ones would induce too low CTN fractions, as shown in Figure 5.2, when adopting exponential profiles. I first use the gas disc sizes directly predicted by the GAEA model, and I obtain a weak positive dependence of N_H versus AGN luminosity, which is at odds with observational constraints. Puglisi et al. [2019] results are complete on the main sequence only above $10^{11} M_{\odot}$, but there are no results for lower masses. In order to explore the effect of the dependence of disc sizes on stellar mass, I also use the fitting formulae from van der Wel et al. [2014]. Using this empirical model, the situation clearly improves and the observed dependence of N_H with X-ray luminosity is recovered, although its slope is still shallower than in the observed data. It is important to keep in mind that van der Wel et al. [2014] measure half-light radii of the stellar component. It is also worth noticing that the GAEA model predicts a disc size versus stellar mass relation which is consistent with van der Wel et al. [2014] data [Zoldan et al., 2019], but with a slightly shallower slope. I study the GAEA gas fractions and its comparison with observed data in Section 5.5 [see also Hirschmann et al., 2016], where I find that using different gas fractions produce the same results. The results thus highlight the need for a relatively steep disc size vs stellar mass relation in order to recover the trend of obscuration with bolometric luminosity. I explore the impact of varying the ratio $N = R_{\rm d,gas}/R_{\rm d,\star}$ within reasonable values in Figure 5.2, which shows

that only models with $N \lesssim 0.3$ can generate a fraction of CTN AGN broadly consistent with current data (solid, blue and dotted, green lines). The effect of varying the gas disc thickness instead is marginal and definitely negligible with respect to the impact of the BW and/or the choice of gas disc sizes, as discussed in Section 5.2.

The middle panel of Figure 5.1 compares the predicted fraction of obscured CTN AGN, with the data by U14, B15, and both of the A19 models, as labelled. The *fiducial* model (without BW, assuming the stellar mass dependence of the $R_{\rm d,\star}$ from van der Wel et al. [2014], and $R_{\rm d,gas}=0.3R_{\rm d,\star}$) presents a decreasing trend in the obscured fraction with increasing X-ray luminosity, which is also present when including the BW model. This decreasing trend, which is aligned with observations [e.g., Gilli et al., 2007, Hasinger, 2008, Ueda et al., 2014, Buchner et al., 2015, Ananna et al., 2019], is mainly induced by the lower luminosity AGN, which tend to have a relatively higher fraction of high column densities being generally hosted in lower mass and more compact galaxies. As seen in Eq. (4.4), in fact, at fixed line-of-sight angle, a smaller $R_{\rm d,gas}$ would increase the upper end of the integral and thus the corresponding $N_{\rm H}$.

When including the BW in Figure 5.1, the predicted fractions drop by \sim 30% at low luminosities and \sim 15% at higher luminosities. Although the impact of the BW is somewhat degenerate with the exact choices of gas fractions and/or shape of the still poorly constrained $R_{\rm d,gas}-M_{\star}$ relation, it is still relevant to highlight two effects of the BW model. First, with all other parameters kept fixed, the BW model makes it usually harder for galaxy scale obscuration to make a significant contribution to the fraction of obscured AGN, due to some gas being removed from the galaxy when the BW is bigger than the extension of the gas disc. Second, at least within the remit of the Menci et al. [2019] model, the BW is not the cause behind the drop in the fraction of obscured AGN with luminosity, a trend which in the model is instead mostly driven by the (positive) correlation between $R_{\rm d,gas}$ and M_{\star} .

The right panel of Figure 5.1 shows that the galaxy-scale obscuration, irrespective of the specific parameters adopted in input, falls drastically short in producing any CTK AGN at any X-ray luminosity, at least in the case of an exponential gas density profile, suggesting that something in the current model is still missing.

To further clarify the importance of the dependence between gas disc sizes and galaxy stellar mass, in Figure 5.2 I plot the predicted fraction of CTN obscuration for four different values of the variable N of the $R_{\rm d,gas}=N\cdot R_{\rm d,star}$ relation, where the fiducial model (solid blue line) is N=0.3 as previously defined, and the other three lines are for different choices of N, as labelled. I also include a model with the original GAEA $R_{\rm d}$ for comparison (cyan long dot-dashed line). The smaller the N value, the larger the overall implied mean column densities. The value N=0.3 has been chosen following the results of Puglisi et al. [2019], which is the average ratio between the stellar and sub-mm radius in sub-mm compact galaxies. Lower N generates more compact

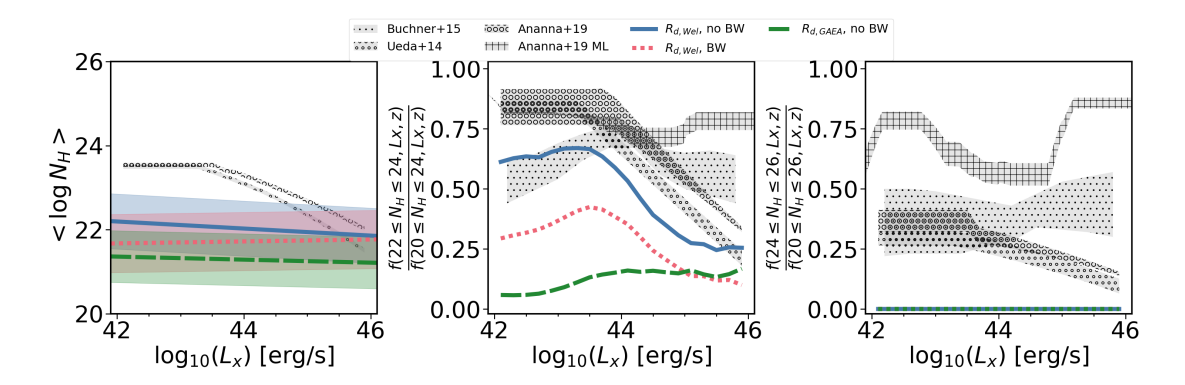


FIGURE 5.1: Mean column density distribution and obscured fractions at z=2.4 depending on the X-ray luminosity. Green dashed lines correspond to the model using the (gas) scale length from GAEA and without BW. Blue solid and red dotted lines are calculated with the scale length fit from van der Wel et al. [2014] no-BW and BW models respectively. All three lines assume $R_{\rm d,gas}=0.3\cdot R_{\rm d,\star}$. Left panel: Column density distributions predicted by each model, as labelled. Lines correspond to the mean values of the column density at fixed AGN X-ray luminosity, and the coloured areas mark the predicted σ region around the mean. Middle panel: CTN obscured fractions. Grey areas correspond to the observations by U14, B15, and A19 as labelled. Right panel: CTK obscured fractions. Observations with the same format as in the middle panel.

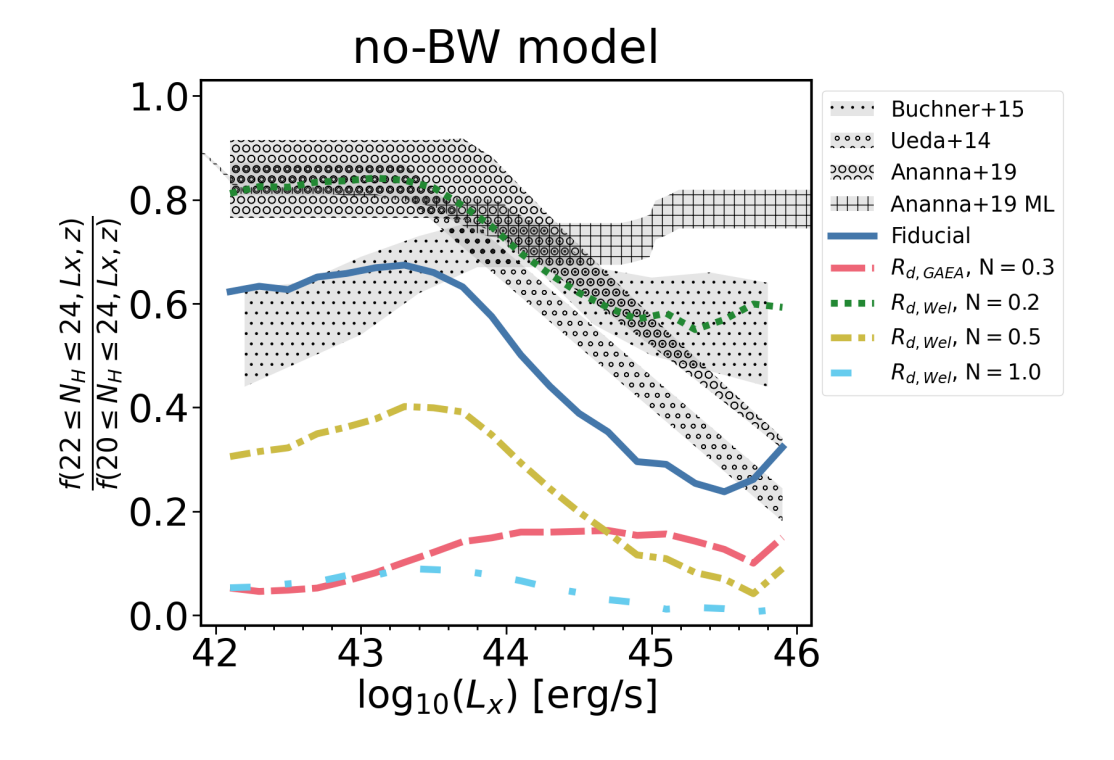


FIGURE 5.2: Predicted fraction of CTN obscuration as a function of X-ray luminosity and without a BW for different values of the relation between gas disc radius $R_{\rm d,gas}$ and stellar disc radius $R_{\rm d,\star}$, $R_{\rm d,gas}=N\cdot R_{\rm d,\star}$, as labelled, with a fixed thickness of $h=R_{\rm d}/8$ at redshift z=2.4. I explore N=0.2, N=0.3, N=0.5, and N=1.0. Fiducial model refers to the model using van der Wel et al. [2014] fit and N=0.3 (see text). The observational data is shown as in Figure 5.1.

and obscured galaxies, to the point where I can reproduce the full fraction of CTN as measured by U14 (see N=0.2, dotted green line for U14, A19 at lower luminosities and B15, A19, -updated Ueda version- at higher luminosities). This trend indicates that, with sufficiently compact galaxies, I can reproduce the CTN obscured fractions without the need for any other obscuration component. However, due to the lack of extensive measurements of the molecular gas disc size in statistical samples of main-sequence galaxies, I cannot confirm (nor reject) that all galaxies at high redshift present gas scale lengths below 0.7 kpc, which are the values obtained when assuming N=0.2. In this Chapter I choose a value of N=0.3 in order to be conservative, and in line with some of the latest observations [Puglisi et al. 2019, see also Elbaz et al., 2018, Franco et al., 2020, Puglisi et al., 2021, Gómez-Guijarro et al., 2022]. Meanwhile, I have confirmed that any combination of input parameters explored in this Chapter can hardly generate any significant number of CTK AGN, although a few more could be formed when switching to a Sérsic gas density profile, as further discussed below.

The analysis of Figures 5.1 and 5.2 has been carried out under two major assumptions: 1) the gas fractions do not evolve significantly during the life span of the AGN, and 2) the X-ray luminosity associated to $N_{\rm H}$ for each source is the peak luminosity within the AGN LC. The former assumption might be extreme as gas fractions decay in time due to gas consumption via star formation and, as predicted by many galaxy evolution models, via AGN feedback which can both heat and expel gas [e.g., Granato et al., 2004, Hopkins et al., 2006a, Croton et al., 2006]. The second assumption is a somewhat natural choice in GAEA as AGN light curves tend to be quite narrow due to an emission bulk highly concentrated in time, a combination of large initial SMBH masses (most of the AGN in GAEA at z < 3.3 are re-activations), and a rapid fading phase for less luminous objects (the large majority of events). In addition, following F20, the peak of the LC is shorter because the bolometric luminosities significantly drop when they enter the radiatively inefficient mode, below 10% Eddington luminosity. In order to check the robustness of my conclusions against the above assumptions, I develop several additional models where either a) I associate an X-ray luminosity randomly chosen within the AGN LC to the column density, b) I deploy a column density which decreases exponentially over time, or c) I assume a more extended input AGN LC. I report the results of the new additional models in Section 5.4, where I show that, in all cases, the main results are similar to the ones obtained in the fiducial model.

As a final check, I compare the fiducial host model against U14 and A19 for the obscured fraction distributions in the column density plane in Figure 5.3. I note that the column density distributions as a function of X-ray luminosity from A19 were recently confirmed in the mid-infrared (MIR) at $z \le 0.8$ by Carroll et al. [2023]. I immediately note that, as expected from my previous findings, the reference models fall severely short in matching the fraction of CTK AGN when only the obscuration from the host galaxy is included. In addition, Figure 5.3 also reveals that, although the fiducial model

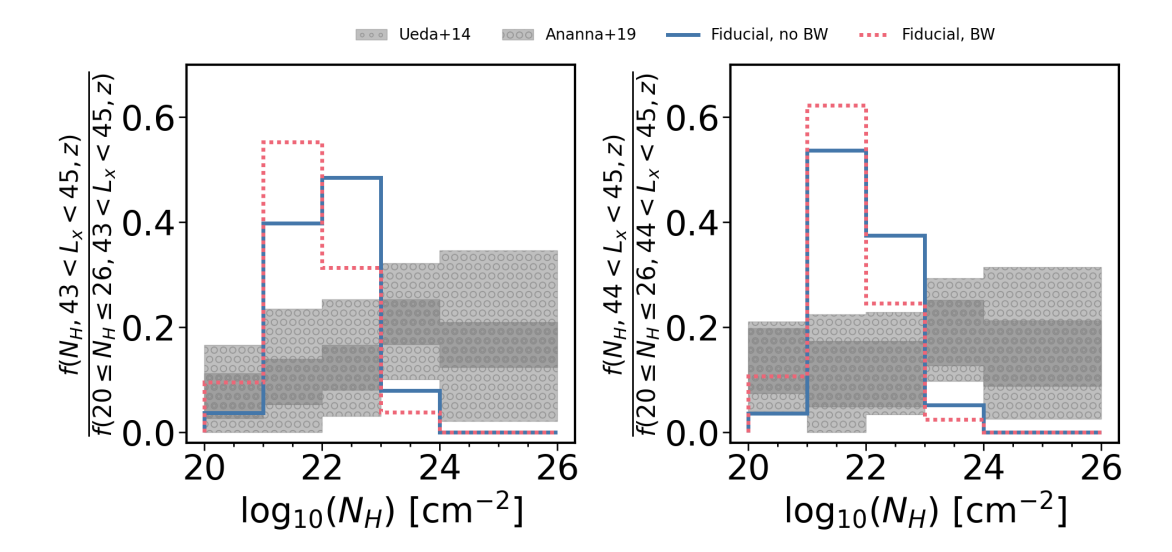


FIGURE 5.3: Obscured fractions of galaxies between $L_X = 10^{43}$ erg/s and $L_X = 10^{45}$ erg/s (left panel) and between $L_X = 10^{44}$ erg/s and $L_X = 10^{45}$ erg/s (right panel) as a function of the column density for the fiducial host model with (dotted red line) and without (blue solid line) BW at redshift z = 2.4. Observational data correspond to U14 and A19, as labelled.

(without a torus) can predict an overall inverse dependence of obscured fraction with increasing X-ray luminosity similarly to what observed in the data (Figure 5.2), it still struggles in fully reproducing the breakdown of CTN AGN at fixed X-ray luminosity. The fiducial model generates similar fractions of $N_{\rm H} \sim 10^{22}-10^{23}~{\rm cm}^{-2}$ as in the data, but less AGN with $N_{\rm H} \sim 10^{20}~{\rm cm}^{-2}$ and significantly more AGN with $N_{\rm H} \sim 10^{21}~{\rm cm}^{-2}$. I will see below that including a torus in the fiducial model provides an improved match to the data on the $N_{\rm H}$ distribution at fixed X-ray luminosity.

5.2 Dependence on gas disc scale thickness

In this thesis I have assumed that a reasonable definition for the disc thickness is $h=R_{\rm d}/8$, as suggested by, e.g., Nath Patra [2020]. Here I explore the impact on the results when adopting a different definition. The one by Ojha [2001], who proposes $h=R_{\rm d}/15$, leads to thinner discs for all galaxies. Other works also use $h=0.15\cdot R_{\rm eff}\sim R_{\rm eff}/6$ as fixed value [e.g., see Gilli et al., 2022, , where they use $R_{\rm eff}=1.678R_{\rm d}$, and references therein], which leads to thicker discs. I assume constant disc thickness throughout the redshifts studied, as observed by Hamilton-Campos et al. [2023] in galaxies z>1.

In Figure 5.4 I show the CTN obscured fractions without BW and for the three different disc thickness definitions. The exact value of disc thickness h, when chosen within the observational range, does not significantly alter the overall shape of the predicted CTN fractions, except for a luminosity-dependent increase of around 10 - 20% at all

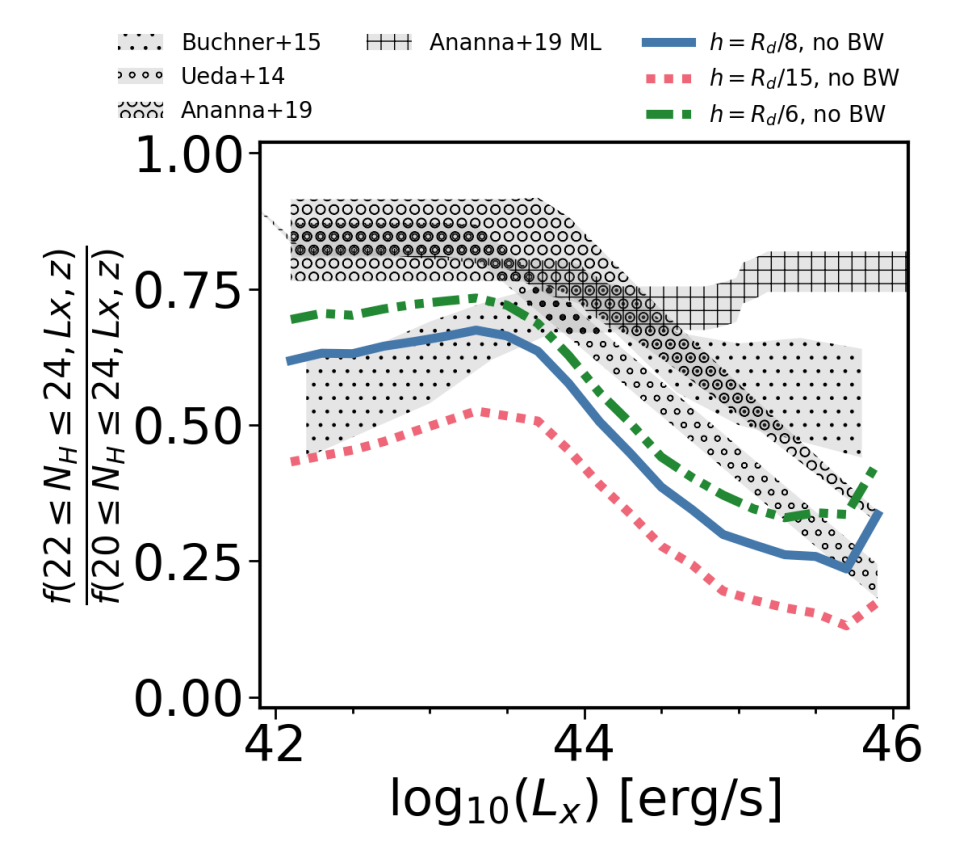


FIGURE 5.4: Host galaxy CTN obscured sources for the fiducial host galaxy model without BW modifying the prescription of the scale height at redshift z=2.4. I compare the disc heights $h=R_{\rm d}/6$, $h=R_{\rm d}/8$ and $h=R_{\rm d}/15$. Observations as in Figure 5.1.

X-ray luminosities. The disc thickness can therefore be safely considered as a second-order parameter in the column density calculation compared to other more impactful assumptions in the model. See for example the fiducial no-BW model (solid blue line) using $h = R_{\rm d}/8$, compared with $h = R_{\rm d}/15$ (dotted red line). Therefore, the effect of the BW, as seen in Figure 5.1, is larger than the effect of changing disc thickness.

5.3 The contribution of the torus to the AGN obscured fraction

So far, I have been considering only the contribution to the $N_{\rm H}$ column density of the large-scale distribution of gas in the host galaxies. I now proceed with the inclusion of the torus as an independent source of AGN obscuration. Figure 5.5 shows the three models described in Section 4.2: Wada, RA&R and the *fiducial* torus model, a combination of the other two with no contribution to the obscuration from the host galaxy.

The implementation of the Wada torus model (red, dotted lines of Figure 5.5) in the mock galaxy catalogue produces, using their suggested parameters, a significant fraction of CTK AGN of \sim 85% at low luminosity, with a steep decrease to \sim 25% at brighter

luminosities (right panel of Figure 5.5). This trend is mostly a consequence of the dependencies of the torus radius (the radius within which the X-ray heating is effective) and $\theta_{\rm crit}$ on luminosity, with the former increasing and the latter decreasing with increasing luminosity (see Section 4.2.2). Both variables are contributing by lowering the probability for the central SMBH to be obscured along any random line-of-sight, especially in the more luminous AGN. The torus also significantly contributes to the obscuration of AGN in the CTN regime (middle panel). The average value of 50% of CTN obscuration across all luminosities (middle panel of Figure 5.5) naturally arises from my adopted assumption (see Section 4.2.2) of assigning a column density to all non-CTK obscuration uniformly distributed between $20 < \log(N_H/cm^{-2}) < 24$.

Figure 5.5 also includes the RA&R model (long-dashed, green lines), which relies on constant limit values for the α angle depending on the column density and the line-of-sight, creating constant fractions of obscured AGN for both CTN and CTK. In the case of the CTN, the model presents a mean value around 67%, while the CTK predicted fraction is \sim 30%, with negligible dependence on AGN luminosity, as expected. The predicted fractions of CTN and CTK AGN from this torus model alone are already significant enough to be comparable to the observations of B15 for both CTN and CTK.

The *fiducial* torus model (solid, blue lines in Figure 5.5) includes the luminosity dependent features of the Wada torus model, as well as the angle dependency of the $N_{\rm H}$ distribution from RA&R. This fiducial model, in line with the RA&R model, naturally predicts a $\sim\!30\%$ fraction of CTK at low luminosities (right panel), reflecting the assumed value from RA&R model that sources below 27 deg are CTK, but gradually decreasing to a few percent at bright luminosities due the (negative) luminosity dependence of the opening angle. A similar trend is observed in CTN (middle panel), showing a value at faint luminosities close to the one predicted by the RA&R model, and then gradually decreasing at higher luminosities.

In Figure 5.6, I sum the predicted large-scale obscuration from the host galaxy gas with the small-scale obscuration from the torus for different redshifts. The fiducial torus and host model, which is the combination of my preferred models from Figure 5.1 and Figure 5.5, is reported here, with and without the inclusion of the BW (red, dotted and blue, solid lines, respectively). The reference model provides a good match to the U14 data at least at z>2. Overall, the fraction of CTK is roughly constant across cosmic times, and slightly decreasing at lower redshifts and at luminosities below $L_{\rm x}\sim 10^{44}$ erg/s. The fraction of CTN AGN is also roughly constant at $z\gtrsim 2$, but then steadily decreasing in normalization with cosmic time especially at lower luminosities. The progressively increasing drop in the fractions of low luminosity obscured AGN at z<1 is mostly driven by the increasing number of radio-mode sources in the model. In Figure 5.6, the yellow dot-dashed line shows a realization where I compute the bolometric luminosity using QSO-mode accretion only: this implies that I remove from the estimate all sources powered by radio-mode accretion, that are not obscured by the host

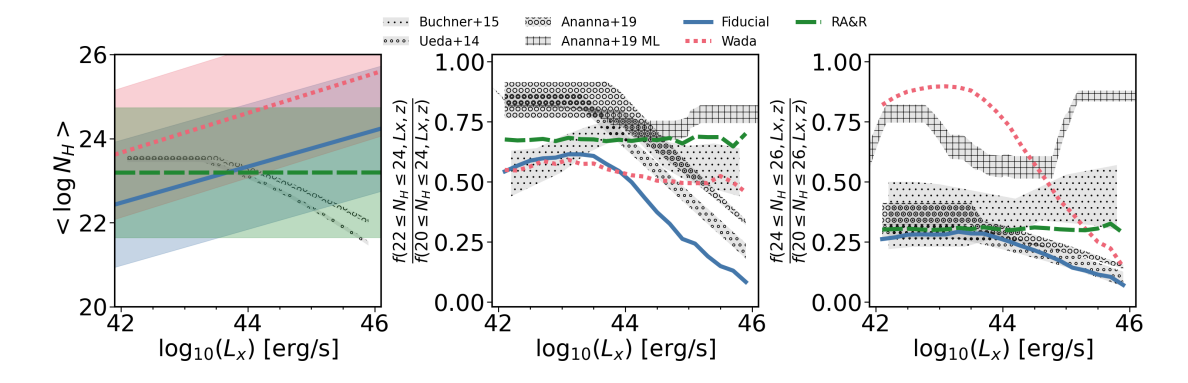


FIGURE 5.5: Column density distribution and obscured fractions depending on the X-ray luminosity for different types of torus models at redshift z=2.4. Fiducial model (blue solid line) refers to a combination of Wada and RA&R torus models (see text), red dotted line shows the Wada torus model, and green dashed line is the RA&R model. Observations shown as in Figure 5.1. **Left panel:** Mean column density distribution along with its σ (coloured area). **Middle panel:** CTN obscured fractions. **Right panel:** CTK obscured fractions.

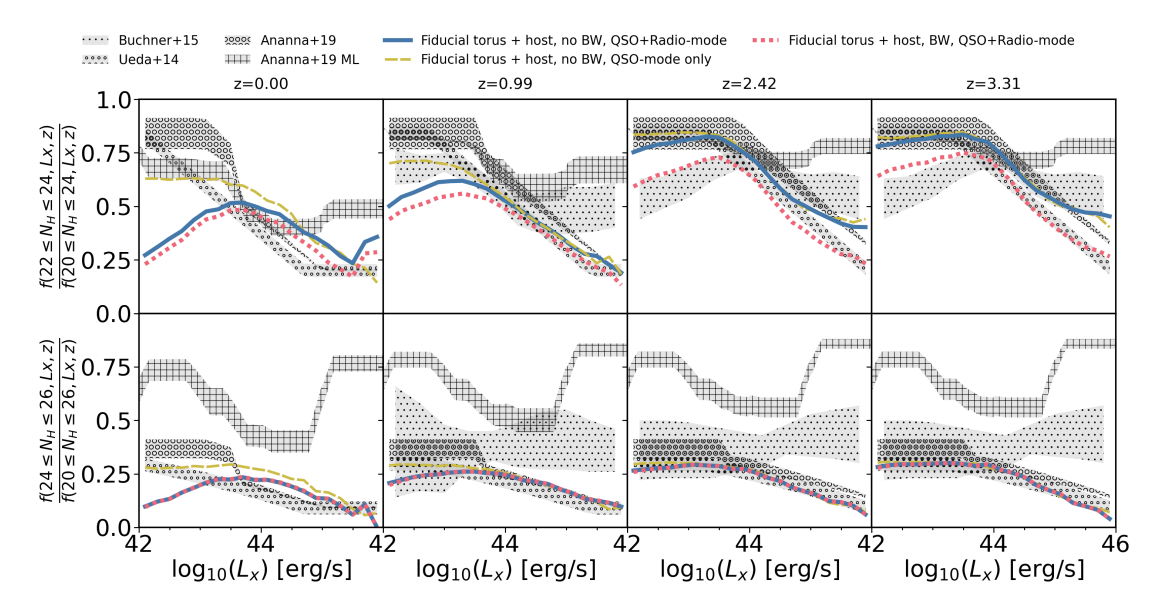


FIGURE 5.6: Compton-thin and thick obscured AGN fractions depending on the X-ray luminosity for galaxies including BW (dashed red) or without the BW (solid blue line) and the fiducial torus model. Each panel corresponds with a different redshift as labelled. Observations shown as in Figure 5.1.

by construction (since their gas content is almost zero), which results in an increase of the obscured fractions. Radio-mode has a marked effect only in the $z\sim 0$ panel, due to the overall decline of the AGN space density and the increase of massive and gas-poor galaxies which are not largely represented in the sample of obscured X-ray AGN. In this redshift range, neglecting the radio-mode accretion in the luminosity calculation increases the CTN and CTK AGN obscured fractions at low luminosity, bringing them in better agreement with the available constraints. This is mainly due to the fact that by removing radio-mode dominated sources I am preferentially removing model galaxies that are expected to be unobscured in my modelling. Indeed, radio-mode dominated

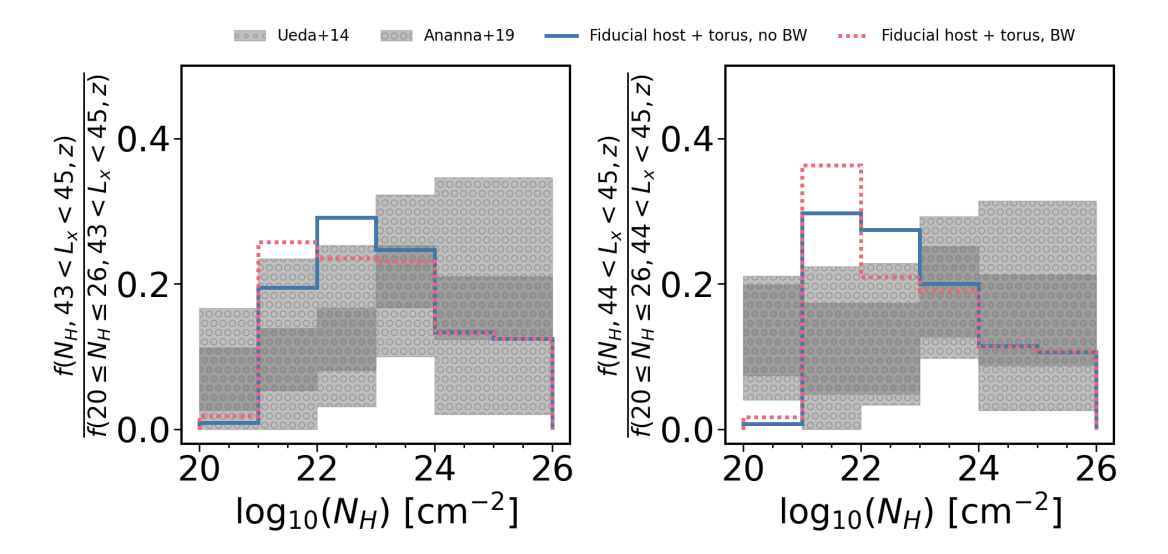


FIGURE 5.7: Obscured fractions of galaxies between $L_{\rm X}=10^{43}$ erg/s and $L_{\rm X}=10^{45}$ erg/s (left panel) and between $L_{\rm X}=10^{44}$ er/s and $L_{\rm X}=10^{45}$ erg/s (right panel) as function of the column density for the fiducial galaxy model (host and torus) with (dotted red line) and without (blue solid line) BW at redshift z=2.4. Observational data correspond with U14 and A19, as labelled.

sources are mostly massive galaxies, that, by construction, have a negligible gas content and low bolometric luminosities. As expected, the impact of removing the radio-mode channel on the predictions strongly decreases at increasing redshift and is completely marginal at the redshift of interest for this Chapter.

For completeness, I compare the fiducial model against U14 and A19 for the obscured fraction distributions in the column density plane in Figure 5.7. I note that the inclusion of the fiducial torus component improves the match to observations compared to a model inclusive of only the obscuration from the host galaxy (Figure 5.3). In the left panel I show the fractions of all galaxies within X-ray luminosities between $10^{43} - 10^{45}$ erg/s. For column densities between $N_{\rm H} \sim 10^{20} - 10^{21}$ cm⁻², I still predict a relative deficit of obscured sources. However, the model tends to better align with the data at larger $N_{\rm H}$ column densities, although the uncertainties in the current available data are still significant. The full model host galaxy+torus tends to smooth out the sharp peak observed before in Figure 5.3, in better, albeit not perfect, agreement with the data. I note that the fraction of CTK AGN I predict from the reference model is never too large, roughly consistent with the one inferred by U14 and A19 from fits to the X-ray background, but never beyond the ~ 10 -15% limit. The inclusion of the AGN BW has a minimal impact on the predicted $N_{\rm H}$ distributions.

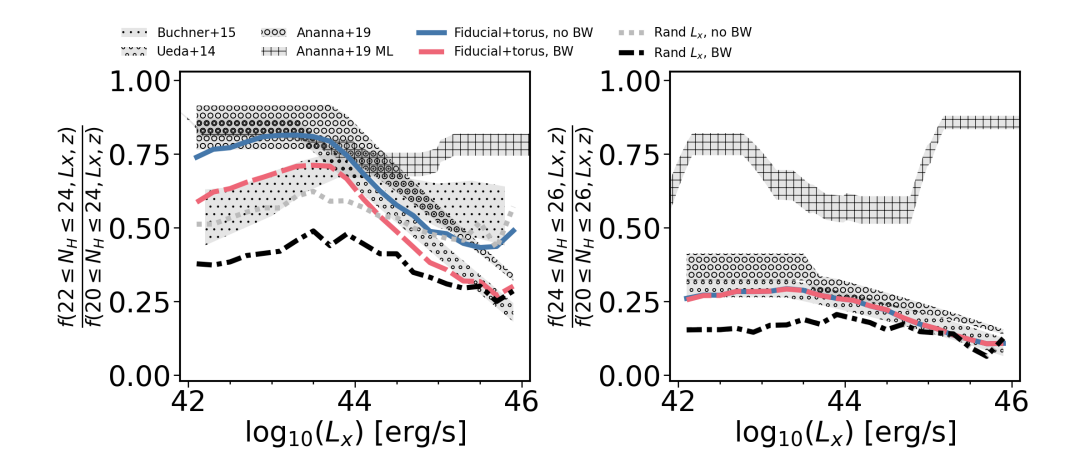


FIGURE 5.8: CTN (left panel) and CTK (right panel) obscured fractions for the fiducial model without BW (solid blue line), fiducial model with the BW (dashed red line), no BW model but using the randomly picked X-ray luminosity (dotted black line), and the BW model using the randomly picked X-ray luminosity (dash-dotted grey line).

Observations as in Figure 5.1.

5.4 Dependence on light curve

To determine the dependence of AGN obscured fractions on luminosity, it is necessary in the first place to calculate and modify the AGN luminosity of all sources in the mock catalogue. As mentioned before, I compute the bolometric luminosity from the QSO and radio accretion rates from GAEA following F20, and then I use Duras et al. [2020] to determine the X-ray luminosity. But throughout this Chapter, I have been using the peak accretion rate (and therefore the peak bolometric luminosity and peak X-ray luminosity) as the value assigned to each column density. Using another luminosity within the LC could lead to different results.

The results of this test are shown in Figure 5.8. In the left panel, CTN fractions decrease when using a random value within the original GAEA LC, except at higher luminosities. When using the GAEA LC, we use the peak luminosity of the LC. Choosing random X-ray luminosities within the GAEA predicted AGN evolution tends to pick more frequently luminosities lower than the peak, and during the post-peak, more extended phase, therefore always selecting lower luminosities than those produced by the GAEA LC, and effectively both shifting the AGN obscured fractions to the left and evenly distribute the obscuration among the different possible luminosities from 10^{42} erg/s to the AGN peak luminosity. This effect is causing many AGN to be selected at luminosities below the 10^{42} erg/s limit, thus decreasing the fractions at faint, but not necessarily at high luminosities.

The HQ11-GAEA assumes the Hopkins et al. [2006a] LC. To test the effect of the shape of the LC on my results, I deploy a slightly different alternative modelling: the light curve model (LC) described in Section 4.3.

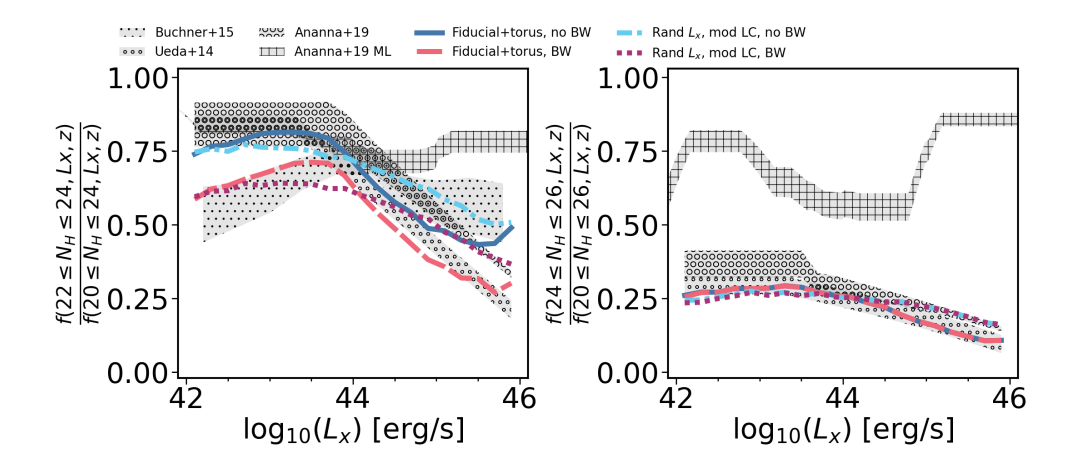


FIGURE 5.9: AGN obscured fractions depending on the X-ray luminosity randomly selected within the LC assuming the model from Section 4.3, for both with and without the BW at redshift z=2.4. Observations as in Figure 5.1. **Left panel:** CTN obscured fractions. **Right panel:** CTK obscured fractions.

The above model, although still very similar to the original in GAEA, tends to produce more extended curves rather than sharp peaks, with more long-lasting pre- and post-peak phases. I will deeply explore the effects of changing the LC in the next Chapter, but here I present the results using both the GAEA original and new LC models in Figure 5.9, for models with and without BW. X-ray luminosities are assigned at random within the LC. The overall shapes and normalizations of the predicted CTN fractions are very similar to the GAEA ones, with only a slight decrease of the fractions of obscured AGN in both the CTN and CTK regimes at lower luminosities and an increase at higher luminosities, flattening the fractions and slope. Choosing random X-ray luminosities within the extended AGN curves tends to pick more frequently luminosities lower than the peak, especially during the (longer) post-peak phase. This selection again causes many AGN to fall below the 10^{42} erg/s cut, thus decreasing the fraction of faint AGN.

5.4.1 Dependence on time-varying HI column density

In this Section I test the impact on the AGN obscured fraction of allowing the gas mass, and thus the $N_{\rm H}$, to vary within the relatively short timescale of the AGN LC. In other words, I here test a variant of the reference model in which I include an efficient AGN feedback and/or star-formation rate consumption that can significantly and rapidly decrease the initial gas mass. To this purpose, I follow Granato et al. [2004] who suggest that the gas mass can in some instances decrease exponentially due to AGN feedback, and assume that the $N_{\rm H}$ column density evolves with time as

$$N_{\rm H} = N_{\rm H, peak} \cdot \exp\left(-\frac{t - t_0}{\tau}\right),\tag{5.3}$$

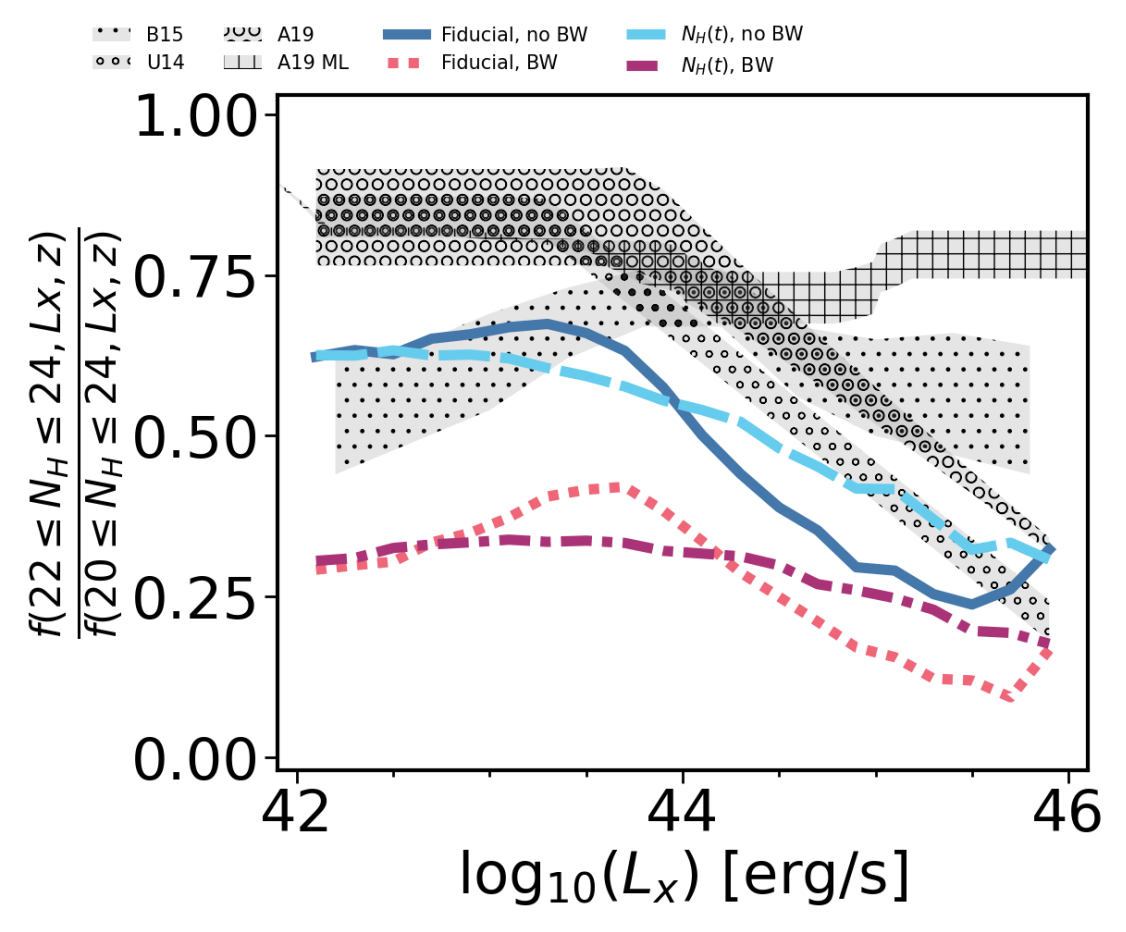


FIGURE 5.10: Host galaxy CTN obscured fractions for the fiducial model without BW (solid blue line), fiducial model with the BW (dotted red line), no BW model but using the randomly picked X-ray luminosity with a time dependent column density (dashed cyan line), and the BW model by using the randomly picked X-ray luminosity with a time dependent column density (dash-dotted pink line) at redshift z=2.4. Observations as in Figure 5.1.

where $N_{\rm H,peak}$ is the column density at the peak luminosity calculated from Equation 4.4 or 4.5, t_0 is the start of the LC, and $\tau = 2$ Gyr to roughly mimic the time behaviour predicted by Granato et al. [2004]. The time t in Eq 5.3 is the time, within the light curve, corresponding to the $L_{\rm X}$ selected at random for each source as discussed previously.

I show the results in Figure 5.10 for the fiducial host model. When comparing with the outputs in Figure 5.1, it is clear that the predicted fractions with a strongly decreasing gas mass are close to the ones with constant $N_{\rm H}$, as expected given the relatively short AGN lifetimes. Therefore, for simplicity I continue assuming a constant $N_{\rm H}$ throughout the lifetime of the AGN as this time-dependent evolution of the column density is not going to heavily impact the results.

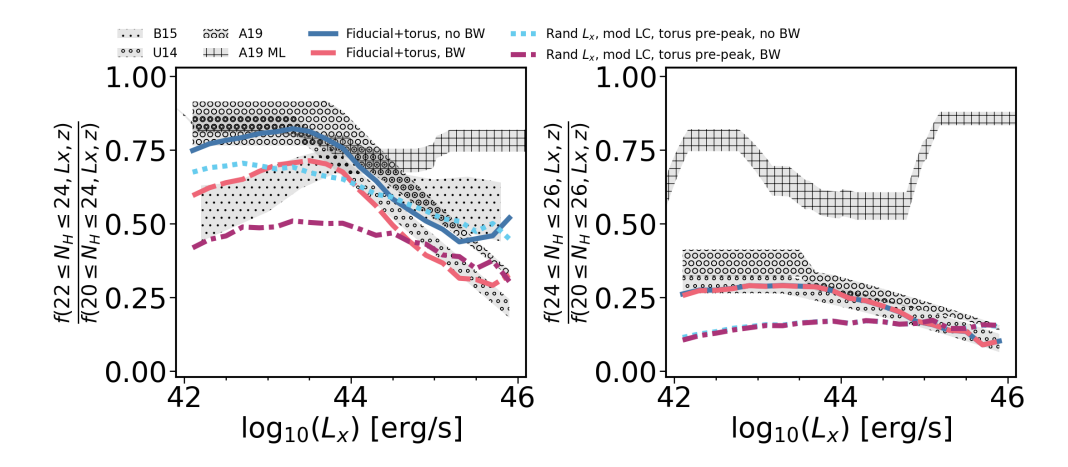


FIGURE 5.11: AGN obscured fractions depending on the X-ray luminosity of the fiducial galaxy model compared against the random X-ray luminosity within the *modified* light curve, for both BW and no-BW, assuming that the fiducial torus model only appears in the pre-peak phase at redshift z=2.4. Observations as in Figure 5.1. **Left panel:** CTN obscured fractions. **Right panel:** CTK obscured fractions.

5.4.2 Effect of the short-lived torus

Once I have a working model with random X-ray luminosity in the LC model, I can test other physically motivated prescriptions for AGN obscuration. As an example, I can test the impact on my results of a potentially short-lived torus component, appearing only during a specific portion of the AGN lifetime. In order to test this idea, I build a toy model where the torus is only present during the pre-peak phase, but rapidly disappears, due to, e.g., AGN feedback and/or gas consumption, during the post-peak phase. In this scenario, if the source is selected in the case of pre-peak, I include the column density coming from the fiducial torus model. On the contrary, if the source is in the post-peak phase, I do not include the torus. I develop further this scenario within the Evolutionary model framework in Chapter 6. I compare the predictions of this toy model against the fiducial model from Figure 5.6 in Figure 5.11. It is interesting to see that with this new prescription for a shorter appearance of the torus (dot-dashed, purple and blue, dotted lines in Figure 5.11), the fraction of obscured AGN decreases, in particular the CTK AGN now reduce to \sim 13%, which is noticeably below any of my comparison data sets. This suppression is also evident in CTN obscuration, where it becomes even more marked when including the BW.

I find that if I go back to a standard Wada torus model (Figure 5.12), which was predicting a larger fraction of CTK sources than the reference model (Figure 5.1), I can recover a sufficiently high fraction of CTK comparable to the number observed (dot-dashed, purple and blue, dotted lines). I conclude that the features of the specific torus model adopted are degenerate with the lifetime of the torus. Thus, I explore this degeneracy in Chapter 6.

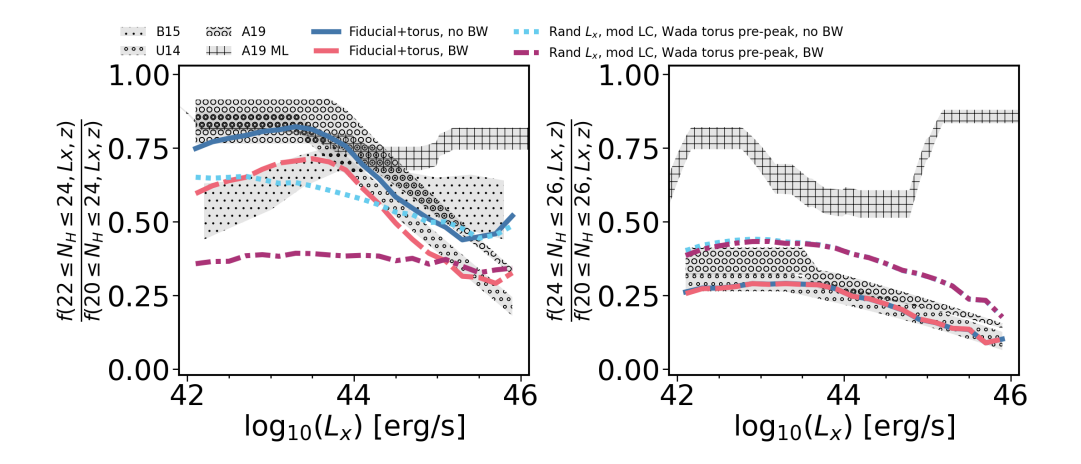


FIGURE 5.12: AGN obscured fractions depending on the X-ray luminosity of the fiducial galaxy model compared against the random X-ray luminosity within the *modified* light curve, for both BW and no-BW model, assuming that the Wada torus model only appears in the pre-peak phase at redshift z=2.4. Observations as in Figure 5.1. **Left panel:** CTN obscured fractions. **Right panel:** CTK obscured fractions.

5.5 Dependence of the AGN obscured fractions on the gas fractions in the host galaxies

The column densities are directly proportional to the amount of cold gas mass $M_{\rm cold}$ in the host galaxy, I expect a variation of $M_{\rm cold}$ to have an impact on the implied fractions of obscured AGN. In this Section, I replace the gas fraction predicted by GAEA (and self-consistently computed in the model as a balance between cooling, star formation and AGN feedback), with the empirical relations derived from the GOODS-S, GOODS-N and the COSMOS fields sample [Santini et al., 2014]. This choice allows me to check the impact on the predicted $N_{\rm H}$ distributions when varying the underlying gas fraction in the model. The analytic fit by Santini et al. [2014] suggests an SFR-dependent total gas mass of the form

$$M_{\rm gas} = \frac{f_{\rm gas}}{1 - f_{\rm gas}} M_{\star},\tag{5.4}$$

with gas fractions calculated as

$$\log f_{\rm gas} = \alpha + \beta * (\log M_{\star} - 11), \tag{5.5}$$

with M_{\star} in units of M_{\odot} .

The variables α and β depend on the SFR of the galaxy and can be found in Table 1 of Santini et al. [2014].

Figure 5.13 compares the reference model with cold gas masses from GAEA with the ones using Santini et al. [2014]. The GAEA models with and without BW (solid blue and red dot-dashed lines, respectively) have broadly similar predictions for the fractions of

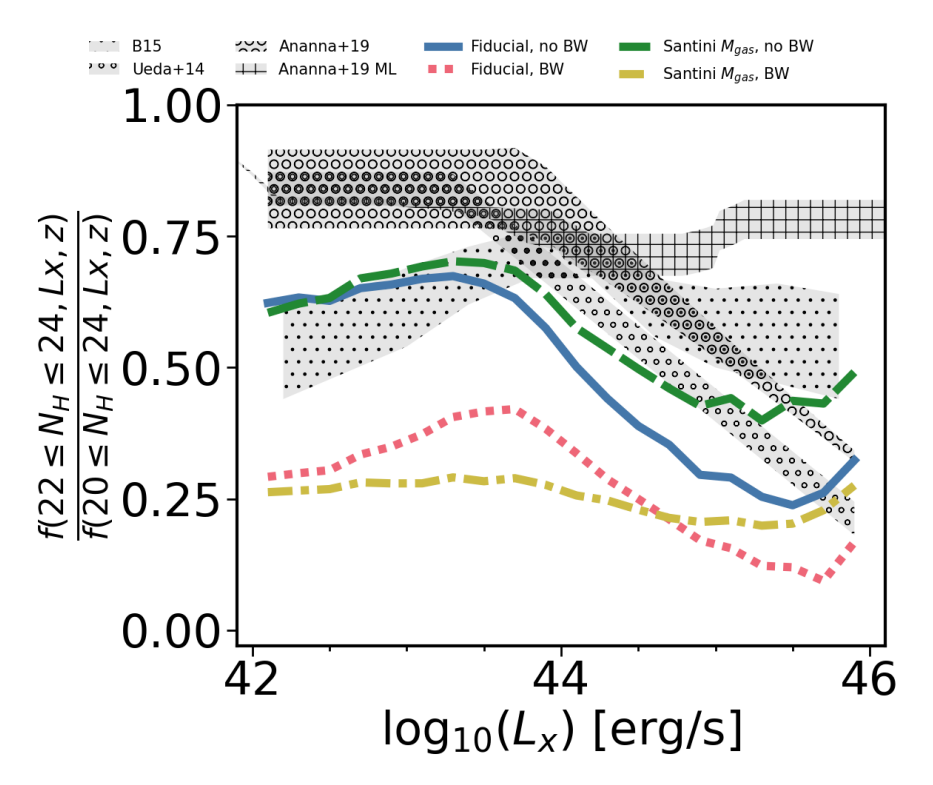


FIGURE 5.13: CTN obscured fractions of the host galaxy using the empirical relation from Santini et al. [2014] to estimate cold gas fractions at redshift z=2.4. I compare with the original GAEA cold gas fractions as in the fiducial host model. Observations as in Figure 5.1.

CTN AGN to the models assuming the cold gas masses from Santini et al. [2014] with and without BW (dashed green and dash-dotted yellow lines, respectively). The gas mass calculation in Santini et al. [2014] is dependent on the stellar mass and two parameters, α and β , which scale with the SFR. Consequently, galaxies with higher SFRs and greater stellar masses are predicted to have larger gas masses. This implies that more luminous galaxies are likely to show higher levels of obscuration, leading to an increase in the obscured fraction at higher luminosities compared to the gas fractions predicted by the GAEA model. Although Santini et al. [2014] does not explicitly incorporate a direct relationship between gas mass and redshift, the model does establish a connection between gas mass and stellar mass, which is intrinsically linked to the redshift evolution of galaxies. Despite relatively minor differences, the mean CTN fractions are similar, proving that the gas fractions from GAEA are sufficiently reliable and not biasing the core results.

5.6 Discussion on the limitations of an orientation model and the inclusion of a torus model

By modelling the small- and large-scale obscuration of AGN on a galaxy-by-galaxy basis, I have been able to pin down, in the context of an Orientation model, the main parameters driving AGN obscuration (namely galaxy structure and the torus component). Here I discuss the robustness of these results starting from the assumptions, compare with other related works in the literature, and connect with Evolutionary models.

The reference model for this study is the state-of-the-art semi-analytic model GAEA, which provides a self-consistent baseline population of galaxies, with their central SMBHs and accretion rate distributions consistent with the total AGN luminosity function [see F20]. The aim of this Section is to probe the impact of the results on some underlying assumptions and also input parameters. In an empirical/data-driven fashion, I thus change in turn some of these main input parameters. I have already seen that although GAEA correctly predicts the increase of the mean galaxy size with increasing galaxy stellar mass, only when assuming the steeper empirical relation from van der Wel et al. [2014] I obtain the right trend of $N_{\rm H}$ with $L_{\rm X}$. However, an $R_{\rm d,\star}=R_{\rm d,gas}$ relation is insufficient to reproduce the necessary CTN sources to reproduce observations (Figure 5.2). I thus need a more compact gas component, as suggested by recent results from ALMA by Puglisi et al. [2019, 2021]. Further observational constraints in the cold gas mass disc radii are needed in order to test the results, such as measurements of molecular gas disc sizes, and/or larger galaxy samples with AGN detections. I also study the effect of varying, within observational constraints, the gas disc scale height h (see Section 5.2). I find that the gas scale height h plays a minor role in the overall results when compared to other variables like the BW.

Additionally, the modelling of an AGN-driven BW feedback capable of removing significant portions of the cold gas mass from the inner regions, affects somewhat the normalization of the fraction of obscured AGN, but not its luminosity dependence. The only dependence of the BW with the luminosity comes from the opening angle calculation, which will produce all possible angle values between $\log_{10} L_X = 40 - 44$ [erg/s] to then exponentially saturate at 90 degrees between $\log_{10} L_X = 44 - 46$ [erg/s]. Therefore, a luminosity dependence of the BW will only slightly affect higher luminosities, as seen in Figure 5.6. The two variables of gas disc sizes and the impact of a BW appear therefore somewhat degenerate, as increasing the latter requires steepening the former. More robust constraints on the $R_{\rm d,gas}-M_{\star}$ and/or the presence of BWs in AGN will help in further guiding the models.

Other assumptions seem to play a minor role in setting the obscuration levels in AGN. For example, I checked the effect of adopting the empirical gas fractions as function of

stellar mass and SFR by Santini et al. [2014], which yields similar results to the reference model based on the GAEA gas fractions (see Section 5.5).

By applying the *fiducial torus* model to my galaxies, I am including a luminosity dependency on the obscured fractions, as seen by U14 and A19, which ultimately originates from the radiative fountain of Wada (Figure 4.2). However, the results obtained by B15 or A19 ML suggest a less dependent obscured fraction with luminosity, more in line with RA&R model, which alone falls short in reproducing the observations despite the increase in the covering factor following new results [e.g., Tanimoto et al., 2019, 2020, 2022, Ogawa et al., 2021, Yamada et al., 2021, 2023]. Including a luminosity dependence in this model could be achieved by including a dependency on the Eddington rate instead of a constant value of the torus critical angle for all galaxies [Ricci et al., 2017c, Yamada et al., 2021, Ogawa et al., 2021].

My results, strictly based on exponential gas disc profiles, suggests that, at least at $z \lesssim 3$, galaxy-scale obscuration may not be sufficient to account for the significant fraction of CTK AGN, and may even fall short in reproducing all CTN AGN. Nevertheless, some care is needed in extrapolating this conclusion at higher z. In fact, in many high-z star-forming galaxies (harbouring a growing central BH), most of the host galaxy obscuration is not associated to an extended gaseous HI disk, but rather to a roughly spherical and compact (about 1 kpc) central region, rich in molecular gas and dust, where most of the star-formation is taking place [e.g., Knapen et al., 2006, Chen et al., 2016, Molina et al., 2023]. There, the equivalent gas column densities may be extremely high, to provide an obscuration comparable, or even heavier than from the nuclear torus [cf. Gilli et al., 2022]. The best model is in agreement with the recent predictions by Gilli et al. [2022] who propose that the total covering factor from the interstellar medium within galaxies is not sufficient to produce CTK obscuration at $z \lesssim 3$. However, its contribution to obscuration can drastically increase at higher redshifts due to an overall strong increase in the gas cloud surface density in the host galaxies.

Chapter 6

Probing the roles of evolution in shaping the obscuration of Active Galactic Nuclei through cosmic time

In the previous Chapter, I have analysed GAEA AGN catalogue under the Orientation model, where I assumed that the column density is calculated from an Exponential density profile and the AGN peak luminosity. I also included a torus-like component that creates the CTK obscuration and some of the CTN obscuration of the galaxy. I evaluated the effect of changing some of the initial variables and find that, irrespective of the luminosity used within the GAEA light curve (LC) -the accretion rate or AGN luminosity dependency with time-, the column density distribution did not substantially vary when I assumed a time-varying HI column density (see Section 5.4.1). In this Chapter, I bypass completely any notion I have of the AGN accretion and simply assume that there is sufficient gas and/or dust in the galaxy to obscure the AGN in some specific periods within the lifetime of the AGN, as in pure Evolutionary models. This means that the column density will evolve within the LC. I assume 4 types of Evolutionary models depending on where the obscuration phase is: Model 1 assumes CTN obscuration pre-peak luminosity and unobscuration (or optically/UV visibility) at the peak and post-peak [e.g., Granato et al., 2006, Hopkins et al., 2008]; Model 2 presents CTN obscuration pre-peak, optically/UV visibility at the peak, and a sharp decline of accretion after the peak [e.g., Lapi et al., 2006]; Model 3 has a CTK obscured phase during some part of the pre-peak, followed by a phase of CTN obscuration, to have optically/UV visibility around the peak and post-peak, including or not a sharp accretion decline [e.g., Lapi et al., 2014]; finally, Model 4 assumes an initial CTK obscured phase, followed by the unobscured peak and a CTN obscured post-peak phase.

In this Chapter I present the main results of assuming different LCs as inputs in the GAEA model, as detailed in Section 4.3. I will start showing the predictions from Models 1 and 2, and then move to those from Models 3 and 4, in Section 6.1. The effect of including a torus model is shown in Section 6.2, whilst the outputs of the Orientation and Evolution mixed model are given in Section 6.3, and the predictions of the reference models at different redshifts in Section 6.4. Finally, the results from alternative models based on SFR and merger thresholds are presented in Sections 6.5 and 6.6 respectively.

6.1 The role of evolution in shaping the obscured AGN fraction with L_X

I show the CTN fractions depending on the X-ray luminosity of the first two Evolutionary models in Figure 6.1. In Model 1 (left panel), the obscuration is present in the pre-peak luminosity phase followed by an optically/UV visible post-peak phase. In Model 2 (right panel) I assume that the LC goes rapidly to zero right after the peak. The AGN becomes, therefore, optically/UV visible only at the peak luminosity, being CTN until then. In this case, I find a higher fraction of CTN galaxies compared to Model 1, as expected since I am decreasing the probability of a galaxy to be optically/UV visible with respect to Model 1 which has an extended post-peak phase. These models by design do not produce any CTK obscuration.

In Figure 6.2 I show the $\Delta \tau_{OSO}$ (Equations 4.15 and 4.16 as described in Section 4.3) probability density. A constant visibility window $\Delta \tau_{QSO}$ tends to produce a rather flat fraction of CTN AGN as a function of luminosity in both Models 1 and 2, which would be broadly in line with what derived from A19-ML, but not with other data sets. In Model 1, the $\Delta \tau_{OSO}$ encompasses nearly the entire post-peak LC, such that $\Delta \tau_{OSO} =$ $t_{\rm end~of~LC} - t_{\rm peak}$. For approximately 50% of the galaxies, this results in $\Delta \tau_{\rm QSO} \sim 2 \times 10^8$ yr (meaning that the peak happens at the beginning of the LC), distributed at all L_X , with the remainder of the galaxies uniformly distributed in the range between $\Delta \tau_{\rm OSO} \sim$ $10^7 - 10^8$ yr. Conversely, Model 2 is by design characterized by a constant visibility window $\Delta \tau_{\rm OSO} \sim 10^7$ yr for all galaxies. To align the model predictions to the U14, A19 data instead, and generate the same steep drop in their observed CTN AGN fractions, I need to accordingly modulate the optically visible window, by gradually increasing $\Delta \tau_{OSO}$ with AGN luminosity, thus reducing the probability for AGN to be CTN at high luminosities. In physical terms, this would imply that the more luminous AGN should be able to more rapidly clear the surroundings, as expected in some AGN feedback models [e.g., Menci et al., 2019].

I show in Figure 6.1 the effects of assuming such a luminosity dependence in $\Delta \tau_{\rm QSO}$, following the empirical expressions given in Eqs. 4.15 and 4.16. Both Models 1 and 2 can produce a good match to the U14, A19 data, but with different visible timescales.

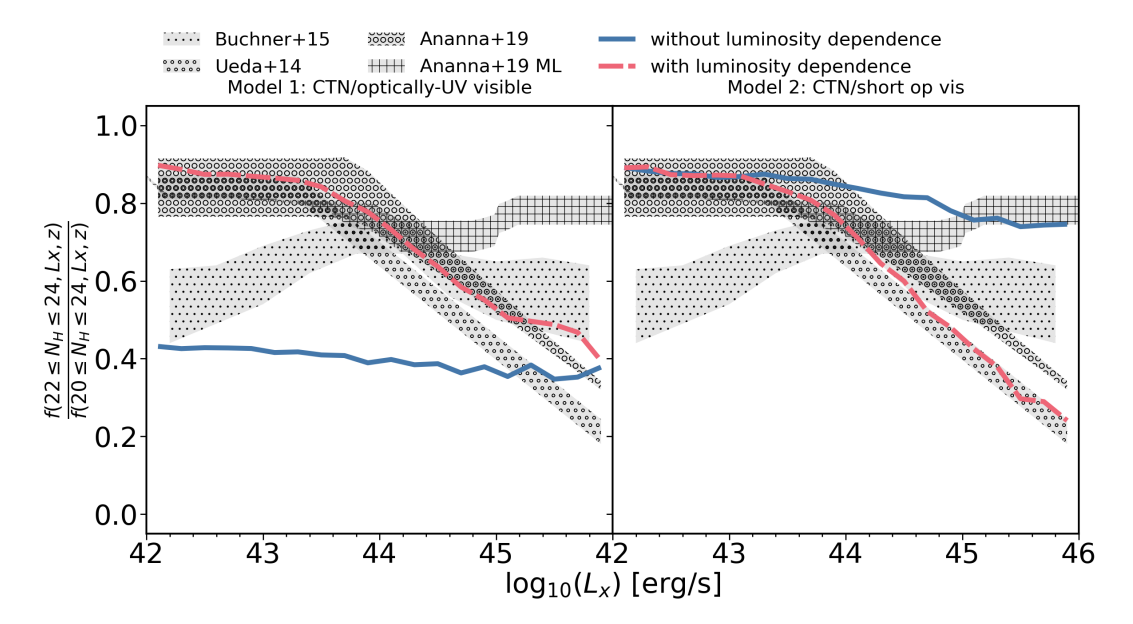


FIGURE 6.1: CTN obscured fractions depending on the X-ray luminosity and assuming Model 1 and 2 LCs. The column density of the host galaxy is assigned depending on the LC without a fine-tuned luminosity dependency (solid line) or with a fine-tuned luminosity dependency (dashed line, read text for more information). The observations correspond with U14, A19 and B15. A luminosity dependent visibility window model with a post-peak LC phase that decreases with luminosity reproduces better the U14, A19 CTN fractions than models without a luminosity dependency.

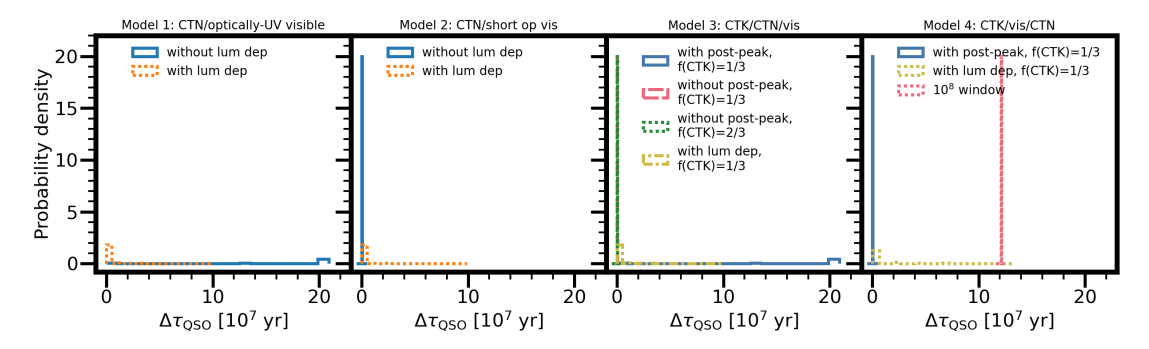


FIGURE 6.2: Visibility window time distributions for Models 1-4 with and without luminosity dependency, as labelled. For Model 3 I also include the model without a post-peak and bigger fraction of the pre-peak as CTK phase (2/3 instead of 1/3, yellow dash-dotted line). In Model 4 I also include the effect of making a bigger constant window in 10^8 yr.

In Model 1 (Eq 4.15), a luminosity dependence implies the post-peak to increase with luminosity, where the majority of galaxies have $\Delta \tau_{\rm QSO} \sim 10^7$ yr at $\log L_{\rm X} \sim 43$ [erg/s] (see Figure 6.2), with some galaxies reaching values up to $\Delta \tau_{\rm QSO} \sim 8 \cdot 10^7$ yr at $\log L_{\rm X} \sim 46$ [erg/s]. Similarly, for Model 2 (Eq 4.16), a luminosity dependence implies the pre-peak division between CTN and optically/UV visible to change, proportionally decreasing the time the LC is considered CTN, starting with $\Delta \tau_{\rm QSO} \sim 10^7$ yr at $\log L_{\rm X} \sim 43$ [erg/s], values extend up to $\Delta \tau_{\rm QSO} \sim 10^8$ yr $\log L_{\rm X} \sim 46$ [erg/s].

In Figure 6.3 I show the predictions for Models 3 and 4 (left and right panels, respectively) for both CTN and CTK AGN fractions (top and bottom panels, respectively),

since Models 3 and 4 produce sources with CTK obscuration. Model 3 has two variants, one without post-peak phase [inspired by the results of, e.g., Lapi et al., 2006, 2014] and one with a total post-peak phase [e.g., Aversa et al., 2015, Shen et al., 2020]. In the former, I assume the AGN in the initial 1/3 of the LC to be in a CTK phase, followed by a longer CTN phase (\sim 2/3 of the LC) and a constantly short visible window of $\Delta \tau_{\rm OSO} = 10^7$ yr as seen in Figure 6.2. This rendition of the model, with no post-peak phase (red dashed line), predicts sensible fractions of CTK AGN of \sim 25%, and \sim 85% of CTN AGN, with weak evolution with AGN luminosity. By increasing the CTK phase by up to 2/3 of the pre-peak phase LC, clearly proportionally increases the CTK fraction and only slightly decreases the CTN one (dotted green lines). When including the post-peak phase in Model 3 (solid, blue lines) it boosts the optical/UV phase by largely decreasing the predicted fractions of CTN and CTK AGN. In this model, where the window has different extensions of the post-peak phase for each individual AGN, $\sim 50\%$ of the AGN present $\Delta \tau_{\rm OSO} \sim 10^8$ yr (see Figure 6.2), but I find shorter windows for the rest of the galaxies, similarly to Model 1. In models with extended post-peak LCs it is thus challenging to reproduce simultaneously the large fractions of CTN and CTK sources in pure evolutionary models, unless I either allow for some portions of the LC to be obscured even within the post-peak phase and/or assume some luminosity dependence in the visibility window, as I showed in Figure 4.3. I discuss both alternative options in what follows.

Model 4, reported in the right panel of Figure 6.3, is characterized by a long post-peak phase and an optically/UV visible window at the peak of the LC of $\Delta \tau_{\rm QSO} \sim 10^7$ yr, preceded/followed by a CTK/CTN phase. Model 4 tends to naturally produce a fraction of obscured AGN close to half of CTK sources and a similar fraction of CTN sources to Model 3 without a post-peak phase.

Both Models 3 and 4, irrespective of the exact length of the LC, tend to predict flat fractions of obscured AGN with X-ray luminosity. To induce a luminosity dependence stronger than the one included by the models in the predicted AGN fractions, I adopt the luminosity dependent $\Delta\tau_{\rm QSO}$ given in Eqs. 4.15 and 4.16, respectively (see Figure 6.2. The latter generate a strong luminosity dependence especially in the CTN AGN fractions, as in Figure 6.1. The effect is very similar to Models 1 and 2. For Model 3, $\Delta\tau_{\rm QSO}$ is 10^7 yr for most galaxies, having some galaxies with windows up to $8 \cdot 10^7$ yr for higher luminosities. In Model 4, a similar situation is in effect, with windows going up to $\sim 1.1 \cdot 10^8$ yr.

All in all, I conclude that reproducing the observed high fractions of CTN/CTK AGN in pure Evolutionary models only, like the ones explored here, requires either LCs without a post-peak phase or LCs with a substantial portion of the post-peak phase turned back to a CTN/CTK regime, a condition that should be tested against detailed AGN feedback models and observations. For example, in Menci et al. [2019], outflows can reach distances of 20 kpc in about 10⁷ yr perpendicular to the disk, but take around

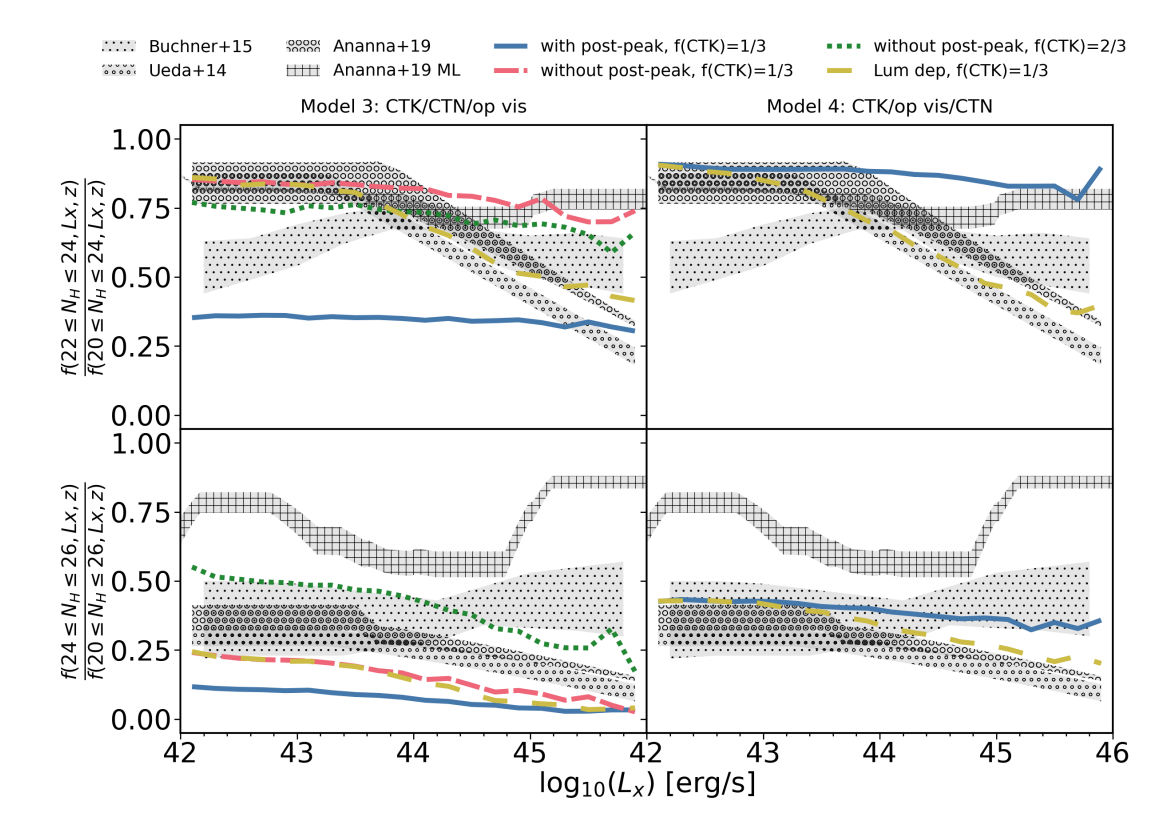


FIGURE 6.3: CTN and CTK obscured fractions depending on the X-ray luminosity and assuming Model 3 and 4 LCs. The optically/UV visibility window of Model 3 corresponds with the complete post-peak phase of the LC for the 'with post-peak' solid line, and just the peak luminosity of the LC for the 'without post-peak' dashed and dotted lines. The fraction of the LC assigned to the obscured phase is the first 1/3 for the dashed line and 2/3 for the dotted line. The observations are the same as in Figure 6.1. A luminosity dependent visibility window model with a post-peak LC phase that decreases with luminosity improves Models 3 and 4 when compared to U14, A19 CTN fractions than models without a luminosity dependency.

10⁸ yr to reach the same distance within the plane of the disk, implying that gas expulsion along the plane of the disk may be less efficient within a single AGN lifetime. This could contribute to the post-peak phase, where AGN reverse back to a CTN/CTK regime due to less efficient clearing of gas along the plane of the disc.

6.2 The impact of a torus component within an Evolutionary model

Many groups have found clear evidence of the presence of a torus at the centre of local AGN observed with sufficient sensitivity [see García-Burillo et al., 2016, 2019, 2021, Combes et al., 2019, Gámez Rosas et al., 2022, Isbell et al., 2022, 2023, for molecular and dusty tori with ALMA, and infrared observations]. In this Section I explore the impact of including a torus component within the Evolutionary models. I can assume that the

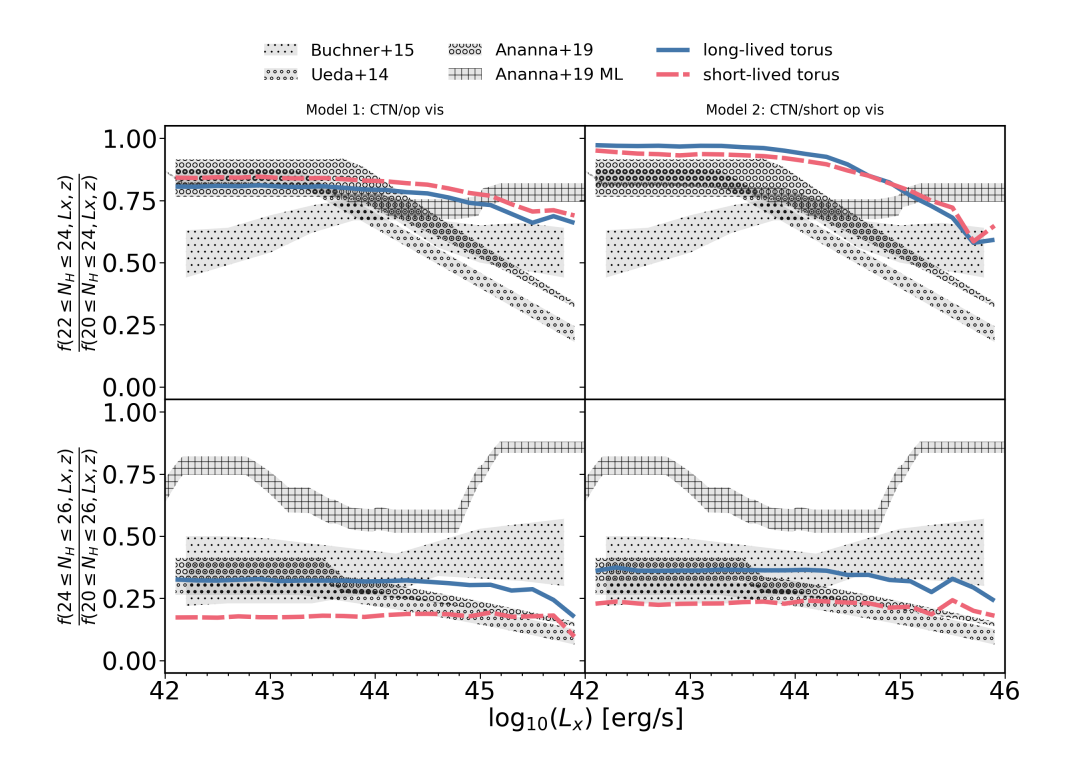


FIGURE 6.4: CTN and CTK obscured fractions depending on the X-ray luminosity including the fiducial torus within Evolutionary Models 1 and 2. The torus can be long-lived (alive during the whole LC) or short-lived (alive during the obscured phases of the LC. The observations are the same as in Figure 6.1. A torus component can help to reproduce the CTK AGN obscured fractions under Models 1 and 2.

torus is a short-lived structure, only contributing to the obscuration along the line of sight during the CTK/CTN phases of the AGN, or I can also assume that the torus is a long-lived structure that survives the AGN feedback blowout during the optically visible part of the LC.

In Figure 6.4, I show that in Evolutionary Models 1 and 2 (without the fine-tuned luminosity dependency) including the reference torus model from Section 4.2, calibrated on the most recent observations in the local Universe, the fractions of obscured CTK sources are boosted (bottom panels), along with the CTN ones (top panels), in better agreement with the data. Choosing for the torus to be present only during the CTN/CTK phase (short-lived, long-dashed red lines) or during the whole AGN LC (long-lived, solid blue lines), has a relatively modest effect in these models, only increasing the CTK fractions by a \sim 20%. The predicted obscured AGN fractions now also tend to show more pronounced dependence on AGN luminosity due to the inclusion of the torus and its opening angle, while the visibility window $\Delta \tau_{\rm QSO}$ is not affected by the torus. As discussed in Chapter 5, the torus tends to produce fewer obscured sources at high luminosities. This is because, in the Wada model, the torus opening angle increases with AGN luminosity, thereby reducing the obscuring solid angle, in a fashion that resembles the luminosity fine-tuning.

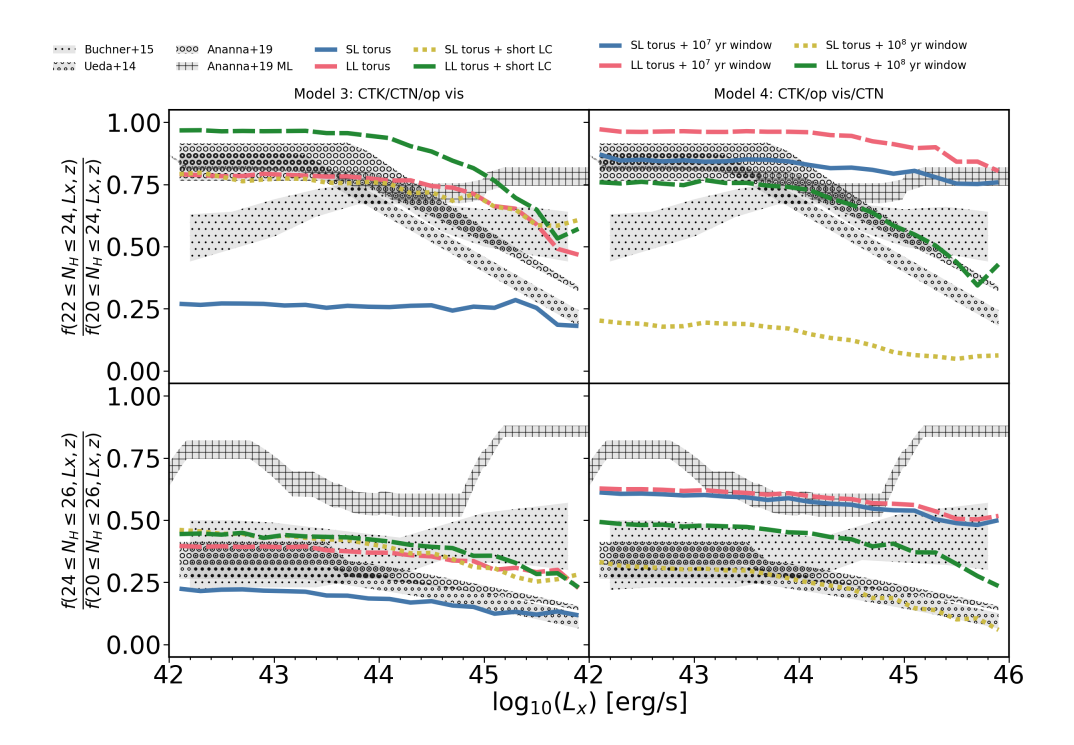


FIGURE 6.5: CTN and CTK obscured fractions depending on the X-ray luminosity including the fiducial torus within Evolutionary Models 3 and 4. The torus can be long-lived or short-lived. In Model 3, the LC can have a long post-peak (solid blue and dashed red lines) or short post-peak (dotted yellow and dashed green lines). In Model 4, the LC can have a short optically/UV visibility window ($\Delta \tau_{\rm QSO} \sim 10^7$ yr, solid blue and dashed red lines) or a long one ($\Delta \tau_{\rm QSO} \sim 10^8$ yr, dotted yellow and dashed green lines). The observations are the same as in Figure 6.1. The relation between the torus model and the visibility window is degenerate.

In Figure 6.5 I show the predictions of Models 3 and 4 with the addition of a long-and short-lived torus. In the left panel of Figure 6.5 I report the predicted fractions of CTN/CTK AGN for Model 3 with a post-peak phase and with a long- and short-lived torus component (solid blue and dashed red lines, respectively). It is clear that in models with a post-peak phase LC, the inclusion of a torus only has a significant impact in boosting the CTN/CTK AGN fractions when it is long-lived, as expected given the relatively short CTK phases. Alternatively, when eliminating the post-peak phase in the LC in Model 3, both the short- and long-lived torus models (dashed green and dotted yellow lines, respectively) tend to boost the CTN/CTK fractions. Since the torus obscures originally optically/UV visible AGN, the obscured fractions increase for both torus models. Therefore, I need to explore how increasing or decreasing $\Delta \tau_{\rm QSO}$ affect the results when a torus model is included. Interestingly, the inclusion of a torus generates a pronounced luminosity dependence in CTN/CTK AGN fractions, especially if long-lived, in line with the U14, A19 data, as in Figure 6.4.

The right panel of Figure 6.5 shows the predictions of Model 4 with the inclusion of a long- and short-lived torus component and a short UV/optical visibility window of $\Delta \tau_{\rm OSO} \sim 10^7$ yr (solid blue and dashed red lines, respectively) and a longer $\Delta \tau_{\rm OSO} \sim 10^8$

yr (dotted yellow and dashed green lines, respectively). I also show the case of a longer $\Delta \tau_{\rm QSO}$ in Figure 6.2, right panel. In the former case, with a short visibility window, the predicted obscured AGN fractions are similar for both short- and long-lived tori models, as expected given that the difference in the torus lifetime is only 10^7 yr, in this case. However, when the optical/UV visibility window is increased to $\Delta \tau_{\rm QSO} \sim 10^8$ yr, then the difference in the predicted fractions becomes more noticeable (dotted yellow and dashed green lines). In addition, only one variant of Model 4 presents significant luminosity dependence in line with the U14, A19 data, namely the long-lived torus with $\Delta \tau_{\rm QSO} \sim 10^8$ yr (dotted yellow lines). This result arises because, with a long visibility window, most of the obscuration is due to the persistent torus, which lives throughout the entire LC. Since the torus is the primary source of obscuration, the luminosity dependency observed in the fiducial model of Chapter 5 emerges over the relatively constant shape produced by the LC alone.

All in all, I conclude that the addition of a torus can have profound implications on the predicted CTN/CTK LCs in Evolutionary models but under the specific condition that it must be a long-lived structure around the central SMBH throughout the LC.

6.3 Hybrid model

So far, I have built AGN obscuration by first randomly assigning a luminosity from the LC to any given AGN and then, based on their position within the LC, allocate a column density N_H according to the models presented in Figure 4.3. I now explore a variant to this Evolutionary model in which I first compute the N_H column density associated to each source and then assign a bolometric luminosity based on their level of obscuration and the specific LC model considered. For example, in Model 3, which is initially CTK, then CTN and optically visible, a galaxy with column density $\log N_{\rm H}/{\rm cm}^{-2} < 22$ would be assigned a bolometric luminosity at random within the optically/UV visible portion of the LC, while a source with $\log N_{\rm H}/{\rm cm}^{-2} > 24$ would have a luminosity selected from the initial CTK phase of the LC. Line of sight $N_{\rm H}$ column densities are calculated from the cold gas mass characterizing each galaxy in GAEA, assuming an exponential geometry with disc geometry, as detailed in Section 4.2. I discuss below (Section 6.11) the impact of switching to a Sérsic geometry for the gas component, which would affect the Orientation model and subsequently also the analysis of the hybrid model and the study of starburst and mergers, since they also use the column density calculated from the disc geometry. I call these model variants "hybrid" models because the N_H is calculated from a geometrical, orientation baseline, but then it is preferentially picked in specific phases of the LC.

In Figure 6.6, I show the mixed model when applied to Evolutionary Models 3 and 4. I compare the fractions with column densities coming from the host galaxy alone

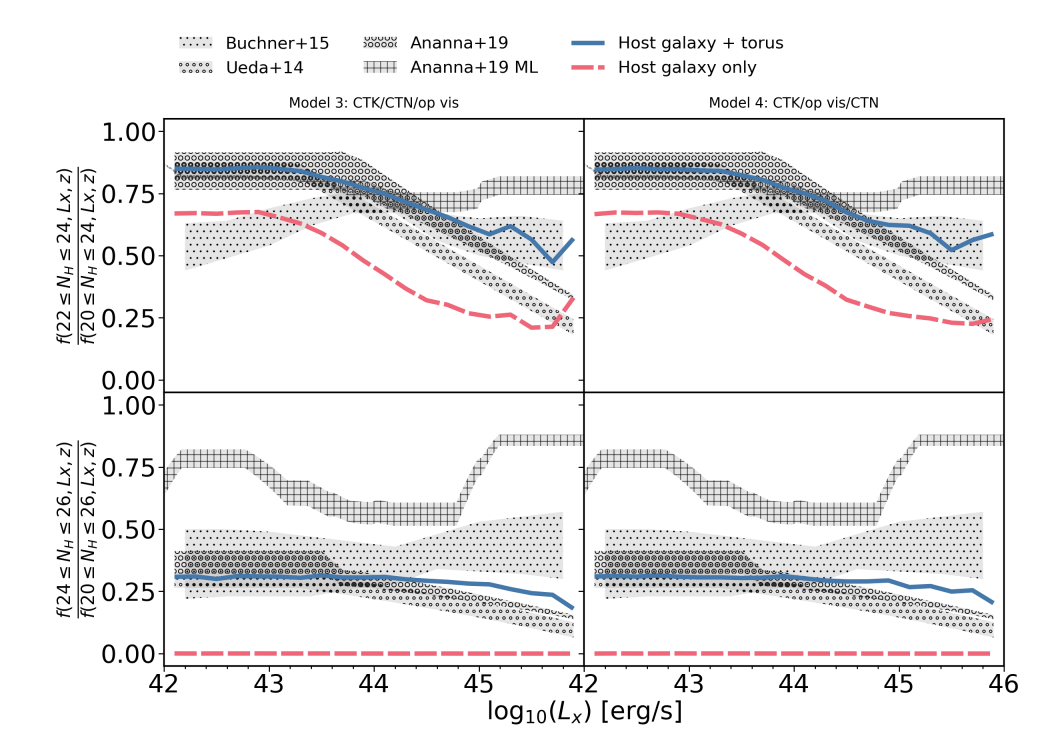


FIGURE 6.6: CTN and CTK obscured fractions depending on the X-ray luminosity assuming the mixed model (using Evolutionary Models 3 and 4 together with the Orientation model from Section 4.2). Here, the torus model is always long-lived. The optically/UV visible window of Model 4 is $\Delta \tau_{\rm QSO} \sim 10^7$ yr, while Model 3 uses all the post-peak phase as window. The observations are the same as in Figure 6.1. Under a model that includes both Orientation and Evolutionary models, orientation dominates over the evolution at redshift z=2.4.

(dashed red lines), and when I include also the fiducial torus model (solid blue lines). I find that the predicted fractions of CTK/CTN AGN are very similar in both models. I also note that the inclusion of a torus boosts, as expected, the AGN fractions in particular for CTK sources, which are otherwise difficult to generate in large quantities relying solely on the cold gas masses present in the host galaxies (see host galaxy only in the bottom panels, I further discuss this point in the following Sections). All in all, the results in Figure 6.6 align with the conclusions from Chapter 5: the details of the shape of the LC or the exact luminosity assigned to an AGN within the LC, play a minor role in modulating the distributions of obscured AGN when N_H is calculated from a geometrical/orientation perspective as I already hinted in Chapter 5. In Chapter 5, in fact, I found that the degree of compactness and, to a lesser extent, the amount of cold gas in the host galaxy, are the main drivers in shaping the AGN fractions with luminosity for redshift z>1. Nevertheless, given the poor knowledge of gas fractions and geometry in high-redshift galaxies, it is still relevant to explore pure Evolutionary models in which I bypass the direct $N_{\rm H}$ calculation and only rely on knowledge of the LC, as performed in the previous Sections.

6.4 Redshift evolution

In all the comparisons so far between model predictions and data I focused on a reference redshift of z = 2.4, which is an epoch dominated by strong AGN and host galaxy star formation activity, and during which I would expect AGN moving from a more obscured phase to a more transparent one [e.g., Granato et al., 2004, Alexander et al., 2005]. Here I aim to explore the predictions of the reference evolutionary models at other epochs, namely z = 1, and 3.3. I focus only on Model 3, noticing that similar results are found for the other models, not changing my conclusions. This model has been selected over the others since it presents the best match with U14, A19, the targeted observations. Figure 6.7 reports the predictions of Model 3 without post-peak and without a torus but with a luminosity-dependent $\Delta \tau_{\rm OSO}$ (Eq. 4.16, solid blue lines), and the reference Model 3 with a long-lived torus (dotted red lines). I find that similar fractions of CTN/CTK AGN are found at all redshifts explored here, in line with the data, with possibly a small decrease towards z = 1 in the CTN fractions. The inclusion of the post-peak phase in Model 3, long-lived torus model, enhances the effect of the evolutionary obscuration over the torus, hiding the luminosity dependency of the torus. Evolutionary models would thus point to similar physical processes shaping obscured AGN fractions at different epoch, as was also proposed by other theoretical approaches [e.g., Lapi et al., 2006], despite the different conditions in the host galaxies and AGN triggering mechanisms (disk instabilities tend to become more significant in GAEA at lower redshifts). I note that, as I move to lower redshift, the galaxies experience longer post-peak phases and less accretion events, enhancing the probability of observing fewer galaxies in the pre-peak phase at late times, and thus a possible reduction in the fraction of obscured AGN, especially in the CTN regime. The observed reduction in luminosity dependence at lower redshifts, attributed to the influence of the torus, is not present in the Orientation model (Chapter 5) due to the increase of obscuration from the Evolutionary model, which counterbalance the one from the torus.

In summary, the results of the different luminosity-dependent LC models are consistent across redshifts $z \sim 1-3$, as e.g. shown in the Model 3. However, the long-lived torus scenario, as discussed in Chapter 5, overproduces the CTN and CTK fractions at lower redshifts. While my conclusions at redshift z=2.4 are robust within the studied redshift range, they would require further investigation and validation at lower redshifts. At these lower redshifts, the torus may have a more pronounced impact due to variations in galactic geometry or extended LCs timescales, which could influence the observed obscuration fractions.

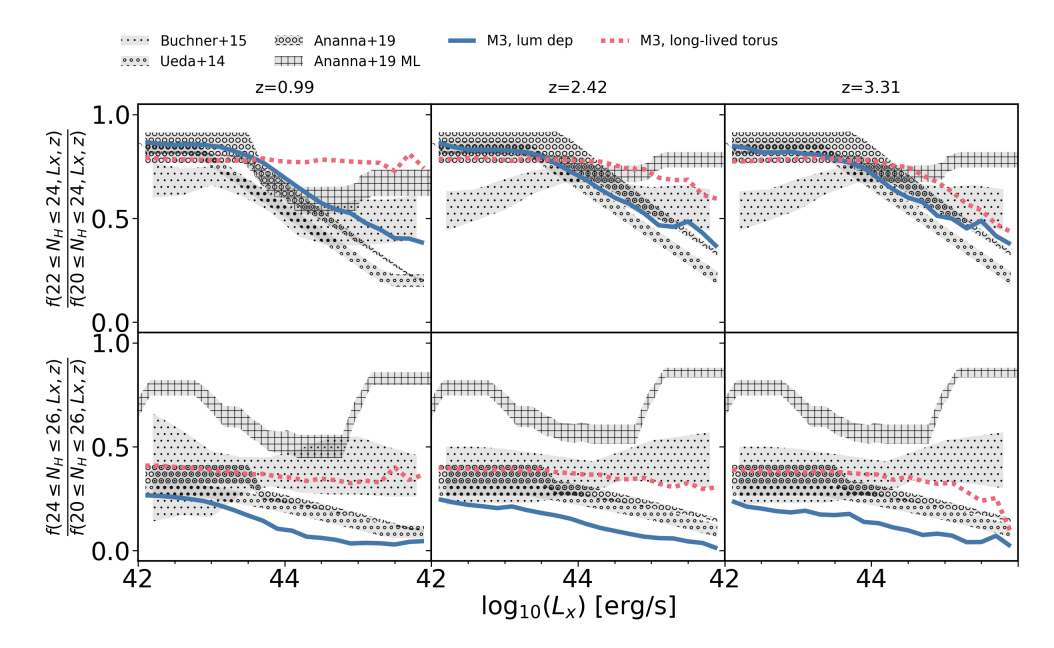


FIGURE 6.7: Redshift evolution of Model 3 fine-tuned (solid line) and Model 3 with the long-lived torus (dotted line) for redshifts z=0.99,2.42, and 3.31. The observations are the same as in Figure 6.1. The luminosity dependency and the torus model are affected by a z-dependency, especially at lower redshifts.

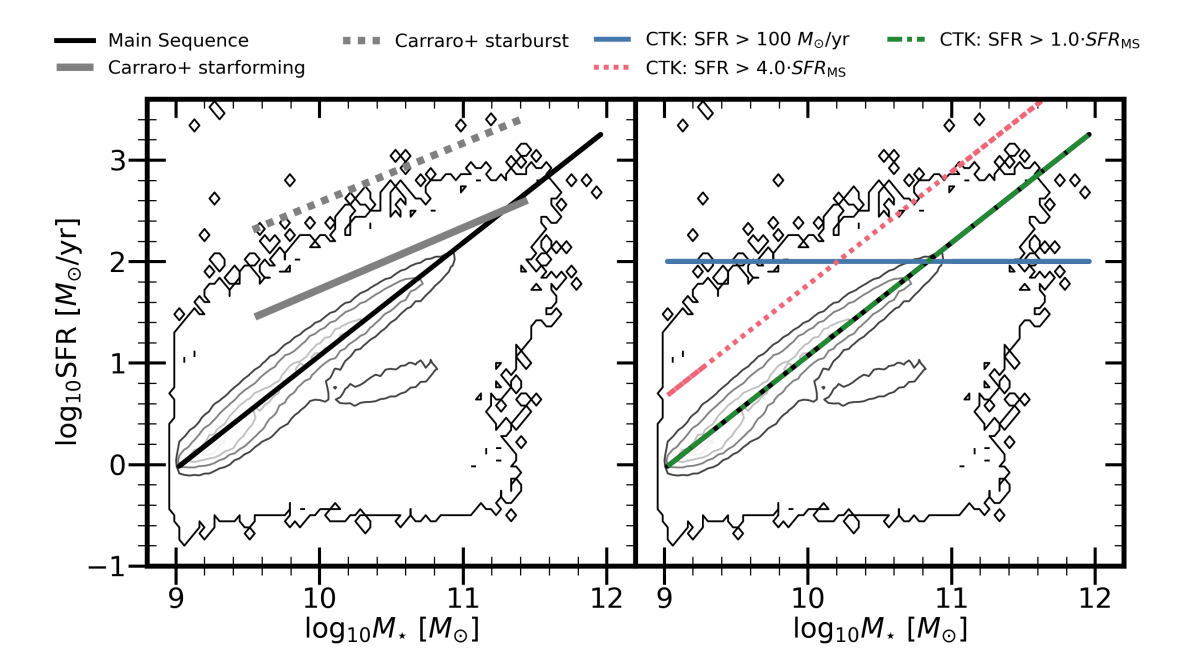


FIGURE 6.8: AGN distribution at redshift z=2.4 with contours at 100%, 95%, 75%, 50%, and 25% with the MS (black line). **Left panel:** empirical MS for the total population and for the starburst from Carraro et al. [2020]. **Right panel:** CTK obscuration limit on the assumptions that these sources are residing in host galaxies with SFRs above 100 M_{\odot}/yr (solid, blue lines), and 4 times the GAEA predicted MS (dotted red line), at the MS (dot-dashed green line).

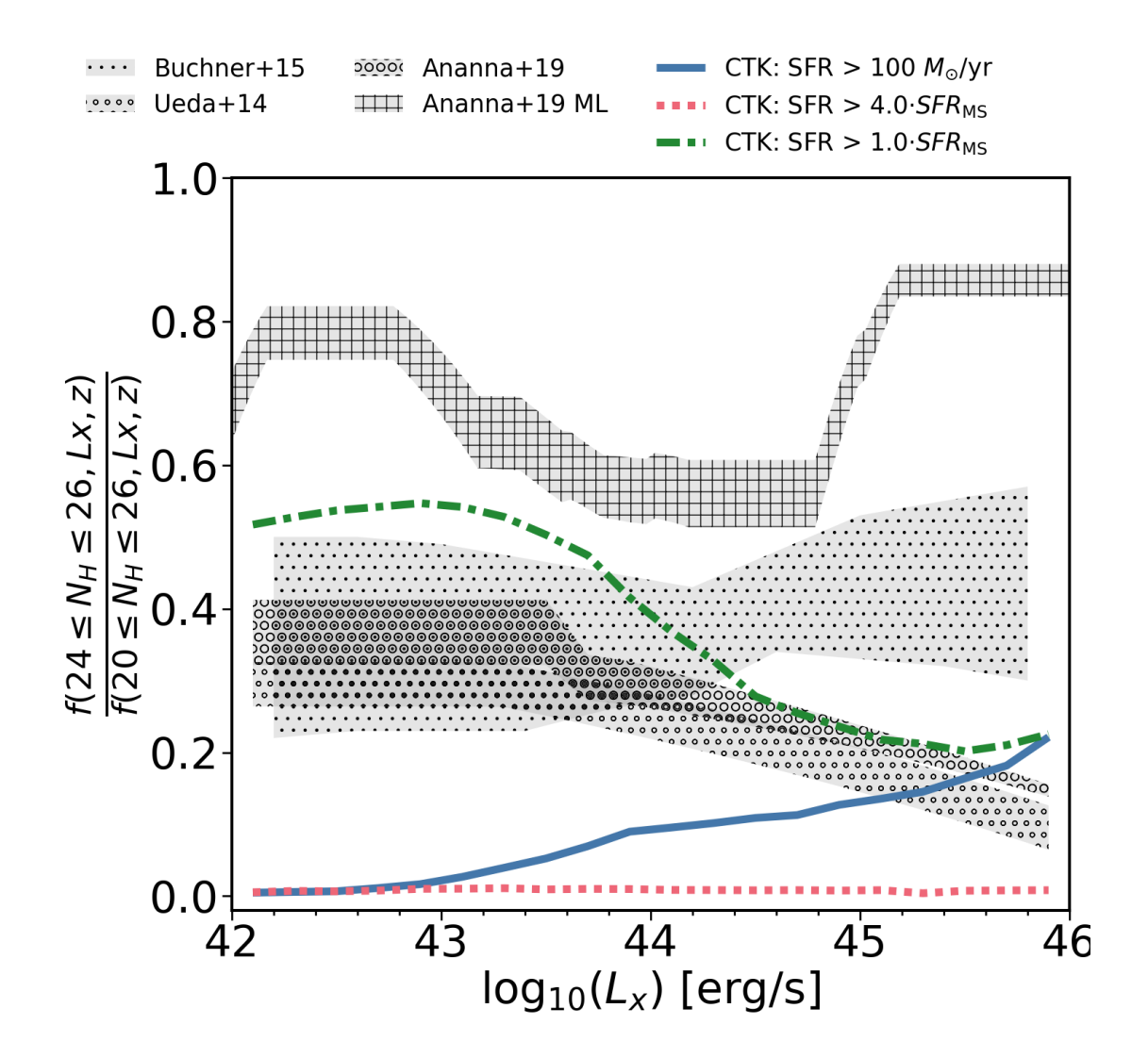


FIGURE 6.9: CTK obscured fractions depending on the X-ray luminosity of the starburst obscuration models. In each model, I assume as CTK obscured galaxies those above the limit indicated either in SFR, or MS (Main Sequence). The observations are the same as in Figure 6.1. The SFR limit of best model to reproduce the CTK obscured fractions is related to the Main Sequence.

6.5 Can starburst alone explain the fraction of obscured AGN at z>1?

In the previous Sections I adopted Evolutionary models built around the basic assumption that within the early growth of the central SMBH, the AGN/galaxy undergoes a CTN/CTK obscured phase. During the early phases of galaxy growth, especially for moderate/massive galaxies at z>1, the ones of interest to this thesis, one expects large gas reservoirs, along with intense star formation episodes coupled to proficient dust formation [e.g, Granato et al., 2015, Bate, 2022]. Therefore, many early starbursts could be associated to obscured AGN and indeed, observations tend to suggest a link

between X-ray activity at $z\sim 1-3$ and, for example, submillimetre/Herschel galaxies [e.g., Alexander et al., 2005, Banerji et al., 2015, Lim et al., 2020]. X-ray luminosity shows a correlation with SFR, at least on average, across all types of host galaxies and over a large redshift range [e.g., Ranalli et al., 2003, Persic and Rephaeli, 2007, Mineo et al., 2012, Carraro et al., 2020, Bayliss et al., 2020, Mountrichas and Shankar, 2023, Riccio et al., 2023], with starbursts usually hosting the brightest AGN. If starforming/starburst galaxies are located in the pre-peak phase of AGN activity [e.g., Figure 7 in Mountrichas and Shankar, 2023], I would expect that, irrespective of the details of the underlying AGN LC, all galaxies above a certain threshold of (specific) star formation should be obscured and eventually CTK. Indeed, as mentioned earlier, Andonie et al. [2024] recently found clear evidence for some highly starforming galaxies to be CTK AGN. Here I test whether GAEA galaxies characterized by a sufficiently large SFR could account for all CTK AGN at z>2, as expected in pure Evolutionary models [e.g., Sanders et al., 1989, Hopkins et al., 2008], without any reference to the underlying LC or gas fractions in the host.

Figure 6.8 presents the distribution of 100%, 95%, 75%, 50%, and 25% of the total AGN population, represented as contours, with GAEA's MS depicted as a black line in both panels. The left panel also includes the empirical MS from Carraro et al. [2020] (solid grey line) and the primary distribution of starburst galaxies (dotted grey lines). It is important to note that the distribution shown corresponds to the AGN population, rather than the total galactic population, and thus the AGN MS is expected to lie above the overall galactic distribution [Mountrichas et al., 2024]. However, the GAEA AGN distribution appears lower than the MS reported by Carraro et al. [2020] and Popesso et al. [2023] at similar redshifts, and is similar to Santini et al. [2017], and does not exhibit a significant concentration of sources near the starburst empirical model. The right panel illustrates the three different CTK selection criteria: SFRs above $100 \, \mathrm{M}_{\odot}/\mathrm{yr}$ (solid blue lines), four times the GAEA-predicted MS (dotted red line), and at the MS (dot-dashed green line).

Note that my targeted observations [U14, A19] do not include any mention to starburst or high SFR galaxies and their relation to obscuration. In Figure 6.9 I show the predicted fractions of CTK AGN on the assumptions that these sources are residing in host galaxies with SFRs above $100 \, \mathrm{M}_{\odot}/\mathrm{yr}$ (solid, blue lines), and 4 times the GAEA predicted MS (dotted red line), at the MS (dot-dashed green line), as usually assumed in observations [e.g., Carraro et al., 2020]. Therefore, I am no longer doing a similar galaxy and AGN selection to U14, A19, but instead exploring what results I find if I include an SFR selection instead of a $N_{\rm H}$ selection, and if this selection can significantly affect previous results and conclusions. An SFR cut of 200-300 $\,\mathrm{M}_{\odot}/\mathrm{yr}$ has been historically used when analysing observational data and starbursts [e.g., Gilli et al., 2014, Perrotta et al., 2023, Andonie et al., 2024, Cenci et al., 2024]. However, I use a cut of $100 \, \mathrm{M}_{\odot}/\mathrm{yr}$ to avoid underproducing the number of starburst galaxies relative to the total galaxy

population as GAEA is known for generating a lower MS (Hirschmann et al. [2016], also see Carraro et al. [2020] as an example of observed MS that is slightly higher than GAEA). Here X-ray luminosities are taken to be the peak luminosities in the LCs, for simplicity, but assigning any other X-ray luminosity at random within the LC would yield very similar results, as discussed in Chapter 5.

In Figure 6.9, the fraction of CTK AGN exhibits a complex behaviour, showing distinct trends based on the different SFR and MS criteria. The constant SFR criterion (solid blue line) displays a relatively flat, increasing trend across the luminosity range, suggesting that extremely high SFRs appear only in very luminous galaxies, as expected. In contrast, the 4 times over the MS criteria (red dotted line) exhibit an almost flat and close to zero CTK fractions, since the very few galaxies over the limit are distributed along all X-ray luminosities, producing zero fractions. Very high SFR galaxies can still be CTK [Andonie et al., 2024], but in the model those do not represent the bulk of the population. More relevantly, I note that my selection of sources only just above the MS produces a fraction of CTK AGN that aligns with the A19-ML data at all luminosities, at least at z > 2, overproducing U14, A19 at all luminosities and B15 at faint and medium luminosities. However, this model incorporates too many MS galaxies, which are usually not selected as starburst in observations, and may not possess the right amount of compactness and cold gas required to reach a CTK level of $N_{\rm H}$.

6.6 The contribution of mergers to the fraction of obscured AGN

As anticipated above, several models suggest that starbursts may be triggered by major mergers [e.g., Mihos and Hernquist, 1996, Di Matteo et al., 2008, Zhou et al., 2018, Renaud et al., 2022], and thus ultimately major mergers could be associated to obscured AGN [e.g., Polletta et al., 2008, Riechers et al., 2013, Gilli et al., 2014, Ishibashi and Fabian, 2016]. Indeed, in GAEA mergers trigger both accretion onto the central SMBH and an increase in the SFR. However, galaxies that experienced recent merger events do not necessarily position themselves above the MS [e.g., Wang et al., 2019, Bluck et al., 2023, Blánquez-Sesé et al., 2023], although they could still be rich in gas and with an active central SMBH. Therefore, it could be argued that a major merger event, more than just a cut in SFR/sSFR, may be a more stringent tracer of a CTK AGN. In this Section I explore this possibility by selecting all galaxies in GAEA that had a recent major merger in the redshift of interest. More specifically, I select all AGN galaxies that have been triggered within 0.5 Gyr of the epoch of observation by a major merger with a progenitor mass ratio above 1/3 [e.g., Stewart et al., 2009, Conselice et al., 2022].

In Figure 6.10, I show the results for three scenarios. The first scenario assumes the host column density from the Orientation model for minor and non-mergers, and $N_{\rm H} > 10^{24} {\rm cm}^{-2}$ for major mergers (dashed red line). The second scenario also assumes the

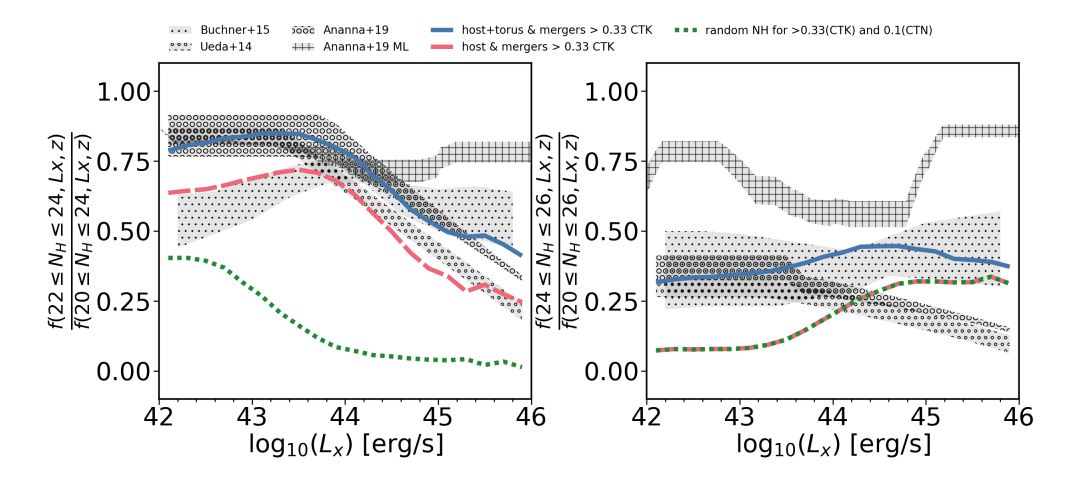


FIGURE 6.10: CTN and CTK obscured fractions depending on the X-ray luminosity of the merger obscuration model. If the galaxy underwent a major merger (merger ratio > 0.33), the $N_{\rm H}$ is increased to be CTK by construction. Solid blue and dashed red lines correspond to models where the galaxies with merger ratio < 0.33 have a column density calculated as in Section 4.2 (host or host+torus respectively), while dotted green assumes random column density. The observations are the same as in Figure 6.1. The merger ratio of the best model to reproduce the CTK obscured fractions is constant and the model must include a torus-like component that produces CTK obscuration.

host column density from the Orientation model but adding the torus component (solid blue line). The third scenario assumes that disc instabilities and those with a merger ratio below 1/10 have $N_{\rm H} \sim 10^{20}-10^{22} {\rm cm}^{-2}$, those with a ratio between 0.1 and 1/3 are CTN, and those with a ratio above 1/3 are CTK. Merger fraction value do not present an AGN luminosity dependency [Hewlett et al., 2017, Villforth, 2023, Sharma et al., 2024], and thus I assume a constant merger ratio limit of 1/3 for all AGN. The model that utilizes the N_H values from the Orientation model for galaxies without a major merger yields a fraction similar to that described in Section 4.2. This model (dashed red line) shows a luminosity dependence akin to observational data but slightly underestimates the CTN fractions, particularly at lower luminosities. When the fiducial torus model is incorporated, the fractions increase as anticipated, due to the inclusion of a torus component with CTN obscuration. However, the model that randomly assigns column densities (dotted green line) exhibits a less steep decline with luminosity, aligning with U14, A19 findings at lower luminosities and B15 at higher luminosities. For the CTK fractions, the dashed red and dotted green lines represent essentially the same model since both define CTK in the same manner, whereas the torus model increases the fractions as expected. Nonetheless, the luminosity dependence of this model diverges from observations, as it shows an increase with luminosity, contrary to empirical data. The best merger model takes into account the Orientation model column density calculation with the torus model. All in all, a major merger model seems to fall short in reproducing the fractions of CTK AGN at lower luminosities, although major mergers alone may be sufficient to explain the large fractions at high luminosities, in line with some direct

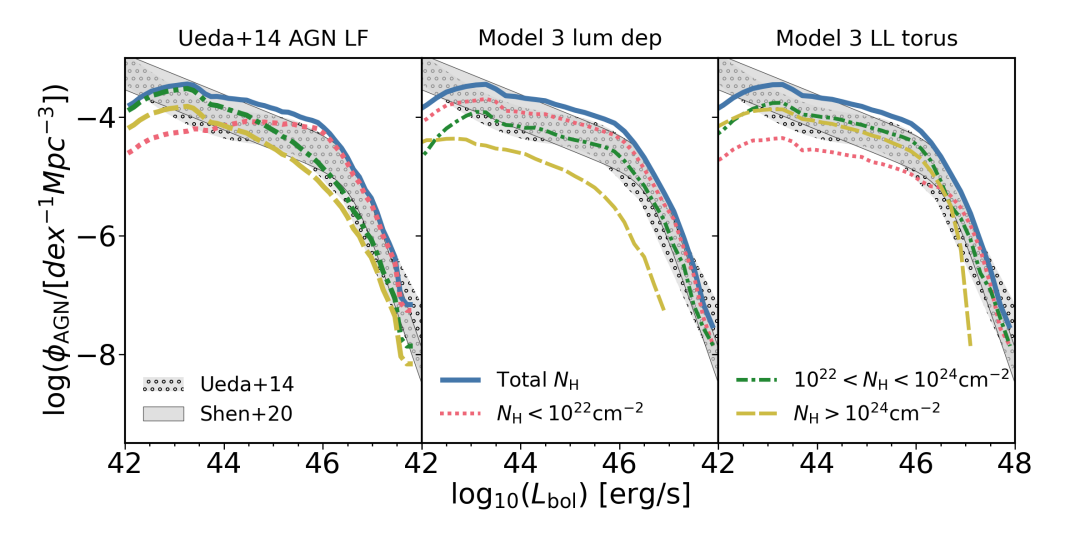


FIGURE 6.11: **Left panel:** AGN LF using U14 model as prediction of the total AGN LF for then to apply the column density and obscure fractions proportions as per U14. **Middle panel:** Model 3 with the luminosity dependenc. **Right panel:** Model 3 with the long-lived torus. The lines refer to redshift z=2.42 for all the galaxies (solid blue line), CTN (green dash-dotted line), CTK (yellow dashed line) and optically/UV visible sources (red dotted line). The observations corresponds to U14 (dotted area) and Shen et al. [2020] (shaded area) AGN LF respectively. The total LC produces an AGN LF that matches with observations, while different $N_{\rm H}$ cuts provide different results depending on the Evolutionary model used.

observations [Treister et al., 2010, 2014, Gao et al., 2020, Tan et al., 2024].

6.7 Dependence of the predicted AGN number densities on the input parameters/assumptions

I begin with predictions from the state-of-the-art semi-analytic model GAEA, which offers a self-consistent population of galaxies and their central SMBHs. This model includes accretion rate distributions that accurately reproduce the observed bolometric AGN LF [see F20, and Figure 6.11]. In a data-driven and empirical manner, I then sequentially alter some key underlying assumptions, but ensuring in each case that the model predictions are consistent with AGN number counts at z < 3. In this section I discuss the dependence of the AGN LF with respect the studied model assumptions and compare to the observations as another sanity check.

In Figure 6.11 I show the AGN LF I find with my LC (Eqs. 4.12 & 4.13), and the AGN LF, in turn, of the optically/UV visible, CTN and CTK sources for Models 3 with a luminosity dependency and Model 3 with a long-lived torus. I also compare my results with the AGN LF predictions for each $N_{\rm H}$ cuts from U14 obscuration model applied to my galaxies. For this, I have retrieved the AGN LF needed in order to find the AGN fractions for each separate $N_{\rm H}$ cut. As mentioned before, my LCs broadly reproduce the observed AGN LF from Ueda et al. [2014], Shen et al. [2020]. However, the distinct

contributions from CTN and CTK sources to the total AGN LF vary noticeably when including a torus component in the model as already seen in Figure 6.7. In particular, the torus produces a boost in the fraction of CTK sources at all luminosities (right panel), whilst reducing the number of unobscured AGN ($N_{\rm H} < 10^{22}~{\rm cm}^{-2}$) and having a mild impact on the faction of CTN AGN. A torus component would thus tend to induce a predominance of CTN/CTK AGN below the knee of the AGN LF (dashed and dot-dashed lines in the right panel), a trend that can be directly tested in deep X-ray surveys. Therefore, although the two models may be roughly degenerate in the predicted CTN fractions, their absolute numbers of CTK AGN number densities could be very different.

The peak luminosity value ($L_{\rm peak}$) and its temporal position within the LC ($t_{\rm peak}$) play crucial roles in determining the obscuration number densities within the AGN LF. In the LC, the position of $t_{\rm peak}$ is driven by the moment the accretion rate reaches its maximum value (Eq. 4.14). Notably, randomly shifting $t_{\rm peak}$ does not affect the relative fractions of obscured AGN because $t_{\rm peak}$ is already uniformly distributed across all possible values within the corresponding redshift. Altering $L_{\rm peak}$ instead moves proportionally the AGN LF towards brighter or fainter luminosities, without significantly impacting its shape nor the implied AGN obscured fractions.

6.8 Assessing the definition of starburst in relation to the Main Sequence and SFR

The definition of *starburst* is intrinsically linked to the MS of star formation. The classification of galaxies as a starburst in fact often depends on its position relative to the MS: if the MS is set too high or too low, it directly influences the identification and prevalence of starburst galaxies. Currently, GAEA intrinsic MS is lower than new observational studies [Carraro et al., 2020, Popesso et al., 2023], consistent with discussions in Hirschmann et al. [2016]. However, recent works [Fu et al., 2024] have advocated for a lower MS, with findings from Leja et al. [2022] and Koprowski et al. [2024] aligning more closely with my results. Despite these variations in the MS, the precise positioning of the MS does not fundamentally alter my definition of starburst.

I started by adopting the observational definition of starbursts being those galaxies placed 4 times above the MS, which I label as CTK, irrespective of their gas fractions, geometry or underlying AGN LC. This choice may be subject to uncertainties. For example, Sargent et al. [2014] emphasize the variability in SFR and their implications for defining starburst conditions, which highlights the difficulty of defining starburst from purely SFR conditions. Nevertheless, the results on the lack of CTK AGN at faint luminosities are robust against the exact choice of starburst definition.

6.9 Breaking degeneracies via AGN clustering

I found that to reproduce the data on obscured AGN with a strong luminosity dependence, it is necessary to either introduce a luminosity dependence in the UV/optical visibility window, increasing for the luminous sources, or to invoke a long-living torus component, the thickness of which decreases with AGN power. This long-living torus does not rule out the possibility of a torus life cycle where it gets destroyed and re-forms during several AGN periods as suggested by, e.g., García-Burillo et al. [2019]. All the variants of Model 3 predict somewhat lower visibility windows with $\Delta \tau_{\rm QSO} \sim 10^7-10^8$ yr, while I require $\Delta \tau_{\rm QSO} = 10^8$ yr for Model 4 to reproduce observations. AGN clustering could help to break these model degeneracies, for example, with a quasar clustering by measuring correlation length of quasars when comparing the two-point cross-correlation function of quasars and their surrounding galaxies, as well as the galaxy auto-correlation function. Here I only discuss comparison with literature results, leaving a more focused study on clustering for future work.

My models forecast a visibility window in the range of $\Delta \tau_{\rm QSO} \sim 10^7-10^8$ yr, either constant for all galaxies or depending on the post-peak phase, also depending on the effect of the luminosity dependency and the torus model used. This is consistent with the quasar clustering analysis from Eilers et al. [2024], that point to short QSO visibility windows in the range 10^5-10^7 yr. Building on the observational results from Eilers et al. [2024], Pizzati et al. [2024] build a semi-empirical model of QSOs supporting a strong evolution of the duty cycle approaching 10^8 yr at $z\sim 2-3$. This value would be consistent with the luminosity-dependent model, or with a torus model with an underlying prolonged LC. These results match with Richstone et al. [1998], who suggested a visibility window of about 10^6-10^8 yr at $z\sim 3$ based on QSO space density [see also the discussion in Martini, 2004].

6.10 Orientation vs Evolutionary models

The *mixed* model incorporating the torus successfully reproduces the obscured fractions shown in Chapter 5. I know that some CTK obscuration must partially originate from a torus-like component, as evidenced in observations [e.g., García-Burillo et al., 2019, 2021, Sengupta et al., 2023, Pouliasis et al., 2024] and theoretical models [e.g., Bannikova et al., 2012, Tanimoto et al., 2020, Alonso-Tetilla et al., 2024]. When comparing the Orientation and Evolutionary models, the evolution of the host galaxy appears to have a secondary effect (see Figure 6.3). More specifically, including a torus implies introducing in the model a strong orientation component that tends to dominate the obscured fractions and this holds true irrespective of the type and extent of the LCs or the amount of gas mass in the host, as long as the torus is present for a large portion of

the AGN lifetime. As discussed in the next Section, allowing for a more compact structure for the gas component can significantly increase the fractions of CTN and partially CTK AGN, so such configurations could reduce the role of the torus in shaping the number of obscured AGN, especially in the CTN regime.

6.11 The effect of alternative density profiles and their relation with gas compactness

In Section 4.2, I introduced the compactness parameter N as the ratio between the gas scale length and the stellar scale length, $R_{\rm d,gas} = N \cdot R_{\rm d,\star}$, following the relationship established in Section 4.2 following the results by Puglisi et al. [2019] [see also Puglisi et al., 2021, Liu et al., 2024]. I found that a minimum compactness N=0.3 is necessary for galaxies with an exponential density profile to achieve sufficient CTN obscuration comparable to observational data (see Chapter 5). This finding indicated that ISM obscuration alone is insufficient to account for the complete obscured fractions observed, needing an additional component, such as a torus, to produce the bulk of the CTK obscuration in galaxies.

As discussed in Chapter 5, this conclusion was based on the strict assumption of forcing an exponential profile to the gas component all host galaxies. However, there is evidence for more compact/complex morphologies defining starforming and dust-enshrouded galaxies at higher redshifts [Tan et al., 2024, Hodge et al., 2024]. To this purpose, I have explored the implications of switching to a Sérsic gas density profile for the galaxies under the Orientation model which I discuss here.

I find that when implementing a Sérsic profile whilst maintaining a compactness ratio $N=R_{\rm d,gas}/R_{\rm d,\star}\sim 0.3$, similar to what suggested in observations [Puglisi et al., 2019, 2021], there is a tendency for the models to generate very large, saturated fractions of CTN AGN close to unity, irrespective of the Sérsic index chosen. A Sérsic profile also tends to generate a larger fraction of CTK sources, as discussed above, introducing a potential degeneracy between the torus and the geometry of the galaxy, complicating the distinction between torus-driven and host galaxy-driven obscuration. Recent observations by the JWST are crucial in disentangling this degeneracy. Studies by Silverman et al. [2023] and Petter et al. [2023] provide insights into the distinction between torus and host galaxy obscuration, and orientation and evolution, from an observational perspective.

To re-establish a good alignment with the observed CTN fractions, especially in terms of the U14, I would require the compactness ratio to decrease to value $N \sim 0.01-0.1$, which are much lower values than what estimated by hydrodynamic simulations and dedicated observations [Puglisi et al., 2019, 2021]. I thus retain the exponential

profile for the gas component in the AGN hosts at z < 3. Indeed, Lyu et al. [2024] find that starforming galaxies at z < 2.5, well characterized by an exponential profile for the stellar component, also have a more compact starforming disc close to exponential [Magnelli et al., 2023, Shen et al., 2023] consistent with what expected from the wet compaction scenario [Tacchella et al., 2015, Barro et al., 2017, Lapiner et al., 2023]. In Lyu et al. [2024], they also find that a high percentage of massive galaxies ($\sim 30\%$ of $M_{\star} > 10^{10.5} M_{\odot}$) have compact star-forming cores, while Puglisi et al. [2021] report even a higher percentage ($\sim 50\%$ of $M_{\star} > 10^{11} M_{\odot}$) [see also Magnelli et al., 2023, Pozzi et al., 2024].

6.12 The implications of Little Red Dots and other AGN populations

Recent studies of Little Red Dots (LRDs), facilitated by JWST observations [e.g., Akins et al., 2023, 2024, Matthee et al., 2024, Pérez-González et al., 2024, Polletta et al., 2024, Durodola et al., 2024] have been identified with extremely compact and highly obscured galaxies but invisible in X-ray wavelengths, and therefore not in the X-ray catalogues. LRDs could potentially provide an additional source of CTK AGN, although it is not clear if these sources are intrinsically X-ray weak [e.g., Maiolino et al., 2024], or even fully-fledged obscured AGN [e.g., Baggen et al., 2024]. They are mostly located at z > 4 according to current observations [e.g., Akins et al., 2023, Iani et al., 2024, Kokorev et al., 2024], and would not be recorded in the AGN LFs or obscured fractions based on the X-ray data that I am using as a reference to calibrate the models in this thesis. I will thus not consider them explicitly in this thesis. I note, however, that even allowing for a significantly larger fraction of CTK AGN in the reference data, also hinted by the A19-ML results, would just strengthen my conclusions on the need for a longlived torus-like component, or in pure Evolutionary models, by a more extended CTK phase, generated by either a brief post-peak phase, as in Model 3, or a more extended CTK post-peak phase, as in Model 4. Indeed, Maiolino et al. [2024] discussed the concrete possibility for many high-z LRDs to be CTK sources with obscuration arising from central dust-free CTK clouds.

Besides LRDs, there are other population of sources like changing-look AGN [e.g., Ricci and Trakhtenbrot, 2023] or galaxies with clumpiness in their gas disc or the torus [e.g., Gilli et al., 2022] that could be missed in the obscured fractions of the models. However, works like Greenwell et al. [2024, and references therein] show that those sources might produce only a small fraction of the obscuration unless systematically missed in observational samples.

6.13 Comparison with previous works

My Evolutionary models bear similarities to those by Di Matteo et al. [2005], which predict a specific duration for the luminous episode of a self-regulated BH. It typically lasts until the feedback energy expels enough gas to significantly reduce the accretion rate, effectively ending the quasar phase, producing a very short or negligible postpeak phase, similar to Model 3. While the exact duration can vary depending on the specific conditions of each galaxy merger, the simulations provide a framework to predict that this luminous episode is relatively short and self-limiting due to the feedback processes. Despite my LC featuring a longer pre-peak evolution and a more rapid post-peak decline than their model, I find similar LC results. Additionally, Georgantopoulos et al. [2023] suggest that unobscured AGN tend to reside in younger galaxies, whereas obscured AGN are found in galaxies between the young and old population stages. These interesting results would challenge both traditional Orientation and Evolutionary models, but would possibly be more aligned with Model 4, where obscuration could still occur even during later phases of the AGN activity. On the other hand, Parlanti et al. [2023] used JWST images to demonstrate that dust-obscured galaxies represent an evolutionary stage preceding the unobscured quasar phase. This finding aligns well with the traditional Evolutionary model, but could still be accommodated within Model 4 which allows for both a brief visible QSO phase and then a more obscured one at a larger stage. Lapi et al. [2014] proposed an Evolutionary model where galaxies have an early phase with high SFR, obscured AGN, and rising luminosity, followed by a transition phase when the gas reservoir is formed, the AGN feedback starts, the AGN luminosity increases, but there is a decrease of obscuration. Similarly to all the models, at the peak luminosity I am assuming that the AGN is a bright quasar with optical/UV visibility, with a rapid SFR decline and low ($N_{\rm H} < 10^{22} {\rm cm}^{-2}$) obscuration. However, the suggested late phase with declining AGN luminosity and residual star formation would present minimal obscuration, in line with Models 1, 2 and 3. They also find that the length of the LC and the CTK phase depend on stellar mass, shortening the post-peak phase as in my models, in broad agreement with my models with a luminosity-dependent visibility window.

Chapter 7

Complementary model predictions: Eddington ratio distributions and spatial distribution

In previous Chapters I discussed 1) the physical properties of galaxies within Orientation models and 2) the general shape of the AGN light curves within the context of the most popular Evolutionary model, that can generate sufficient CTN and CTK AGN as observed in deep X-ray surveys. In this Chapter I move a step forward and analyse the prediction of the reference Orientation and Evolutionary models on two other fundamental aspects of AGN taxonomy: Eddington ratio distributions and spatial distributions (clustering). This Chapter's aims are:

- to test if and when the chosen light curves and obscuration models are able to generate distributions of Eddington ratios aligned with current data;
- to determine whether reference models can predict AGN clustering patterns that could vary with the level of obscuration in the host galaxies.

In this Chapter I will make use of the reference models from Chapters 5 and 6. From the Evolutionary model, I will consider Models 3 and 4 with and without a luminosity dependence and with and without a long-lived torus. I will then adopt two versions of the reference Orientation model, one with obscuration arising only from the host galaxy, and one inclusive also of the central torus.

7.1 Eddington ratio distributions

I start in Figure 7.1 by comparing the predictions from the reference Evolutionary models at redshift z = 2.4 characterised by a LC with exponential increase and a power-law

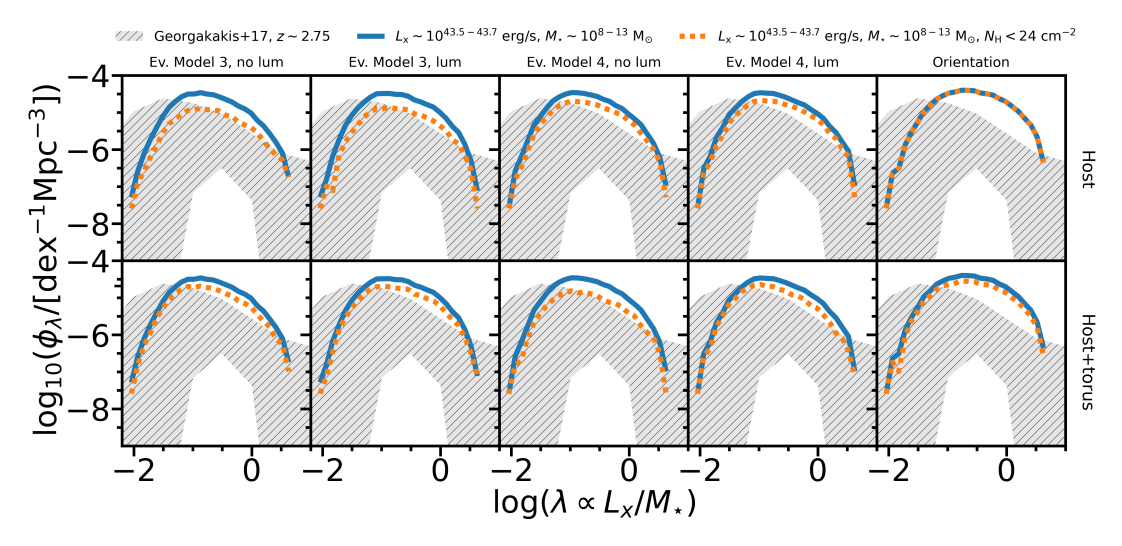


FIGURE 7.1: Accretion-rate function using Orientation and Evolutionary models as labelled for the total column density distribution (solid line), and AGN with $N_{\rm H} < 10^{24}~{\rm cm}^{-2}$ (dotted line). The observational data are from Georgakakis et al. [2017a] at redshift $z \sim 2.75$.

decline, as shown in Figure 4.3 and discussed in Section 4.3. I compare the predictions with the observational findings by Georgakakis et al. [2017a] at redshift $z \sim 2.75$, which have been introduced in Section 2.6.3. The Figure includes AGN with a luminosity $L_{\rm X} > 10^{43.5-43.7}$ erg/s and stellar mass $M_{\star} > 10^{8-13}$ M_{\odot}. Note that I label the specific accretion rate as $\lambda \propto L_{\rm X}/M_{\star}$, while the Eddington rate as $\lambda_{\rm Edd} = L_{\rm bol}/L_{\rm Edd}$, as described in Section 4.4. In this Chapter I will continue using Duras et al. [2020] as conversion between L_{bol} and L_X . Figure 7.1 shows that all models tend to generate Eddington ratio distributions for moderately luminous AGN in broad agreement with Georgakakis et al. [2017a] roughly consistent with the upper envelope of the data once the AGN with $N_{\rm H} > 24~{\rm cm}^{-2}$ are removed from the number counts. The range of Xray sources is very narrow to reproduce the observational results, since increasing the range increases the accretion-rate function. It is interesting to note that the predicted Eddington ratio distributions have a modest dependence on the underlying assumptions on, e.g., the shape of the LC or even if the N_H is assigned in terms of a LC or a torus. This behaviour can be, at least in part, traced back to the fact that the $N_{\rm H}$ distributions have weak dependence on the X-ray luminosity in either model, as discussed in the previous Chapters. Assigning a N_H at random within the LC, or at the peak luminosity, for example, does not impact the fractions of obscured AGN. The exact gas fractions in the galaxies also have little impact on the overall fractions of obscured AGN.

Figure 7.2 presents the specific accretion rate (SAR) of unobscured ($N_{\rm H} \sim 10^{20-22} {\rm cm}^{-2}$) and CTN obscured ($N_{\rm H} \sim 10^{22-24} {\rm cm}^{-2}$) AGN, compare with the data from Laloux et al. [2024]. Laloux et al. [2024] found evidence for more obscured sources having, on average, lower SARs than unobscured sources. In the Laloux et al. [2024] data there is a slight tendency for unobscured sources to have larger λ , which at face value would

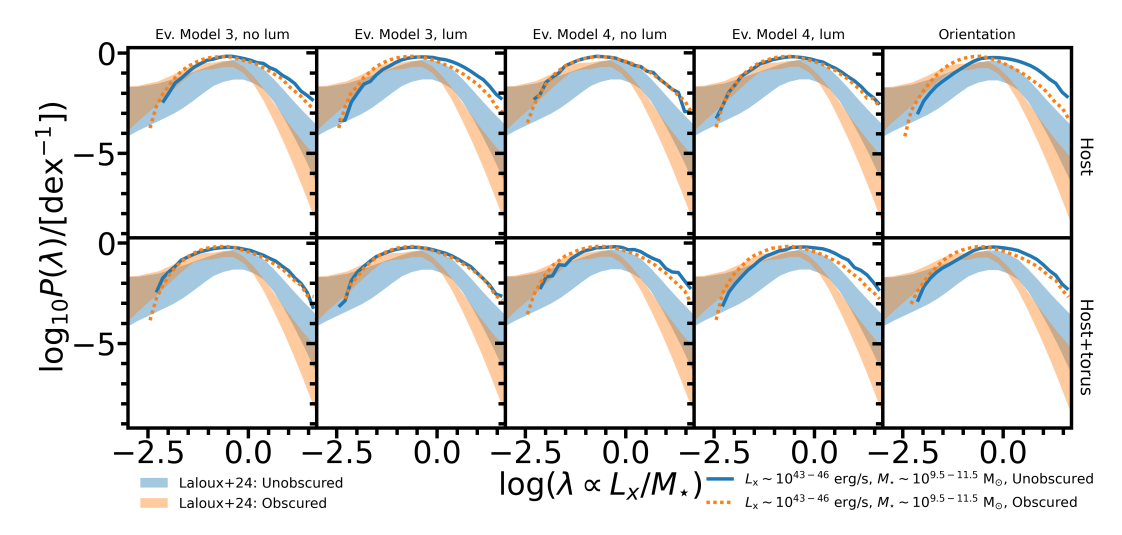


FIGURE 7.2: Normalized specific accretion-rate function using Orientation and Evolutionary models as labelled for unobscured column density distribution ($N_{\rm H} < 10^{22}$ cm⁻², solid line), and CTN obscured with $10^{22} < N_{\rm H} < 10^{24}$ cm⁻² (dotted line). The plotted SARDs are normalized to unity for each obscuration bin following Equation 4.19. The observational data are from Laloux et al. [2024] from redshift bin $z \sim 2-2.5$.

be at variance with basic expectations from traditional Evolutionary models, which place the more obscured sources during the early stages of galaxy evolution (AGN with higher Eddington ratios). However, this trend is quite mild and the two distributions are nearly consistent within the errors. Indeed, interestingly all our reference models reported in Figure 7.2 show very similar predictions between them and with the observational data, with the obscured and unobscured AGN sharing very similar distributions in λ , with a slight tendency for obscured AGN to have lower Eddington ratios, mirroring what seen in the data. From Figure 7.2, it is evident that only the Orientation model, and to a lesser extent the inclusion of a torus, generates a noticeable difference in the obscured/unobscured SARs. This distinction arises because the orientation model is the only one incapable of producing CTK fractions without relying on the presence of a torus. The models also align in capturing the right shape of the $P(\lambda)$, locating around the same peak, with only a slight overabundance at large SARs.

In Figure 7.3 I compare the obscured CTN fractions with data from Laloux et al. [2024]. Note that there are many other works that study the effects of the obscuration in Eddigton ratio distributions or SARDs [Ricci et al., 2017b, 2022a, Georgakakis et al., 2020, Ananna et al., 2022b], however Laloux et al. [2024] is the only one that also includes galaxies at the redshifts of interest here. Most curves are highly irregular, despite including the same AGN selection criteria as Laloux et al. [2024] (i.e., $\log L_X = 42 - 46$ [erg/s] and $M_{\star} = 9.5 - 11.5$ [M_{\odot}]). These irregularities could be an effect of the assumption of a constant M_{\star} throughout the LC. The random selection of luminosities in the Evolutionary models appears to have a minimal role in the shape of the curves, as the curves remain broadly consistent across different iterations. I find Model 3 with a torus to align with the increase of SAR in Laloux et al. [2024] at medium λ , and the

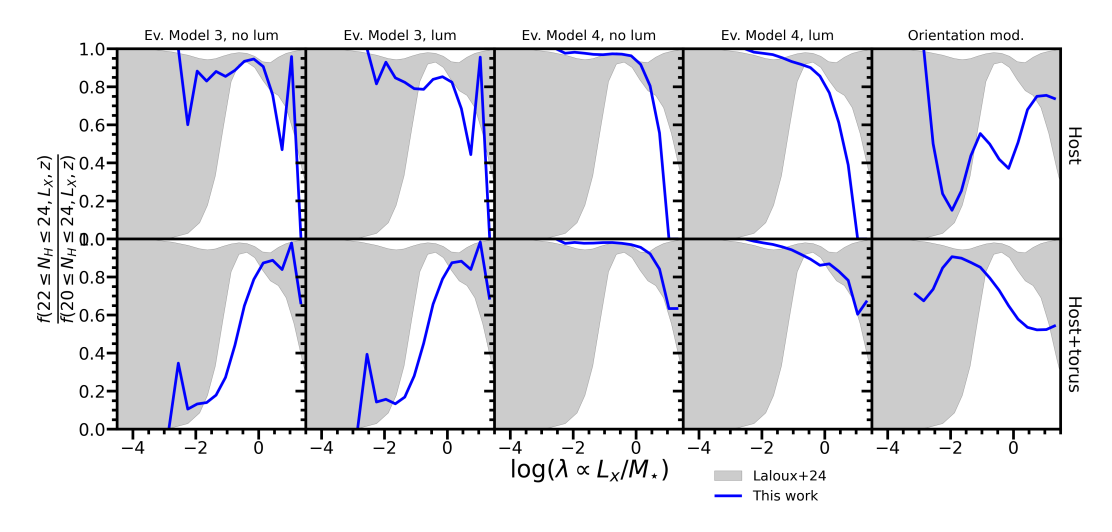


FIGURE 7.3: CTN obscured fractions using Evolutionary models from Chapter 6 and the Orientation models from Chapter 5 at redshift z=2.42. The grey areas correspond with the observational data to Laloux et al. [2024] at z=2-2.5.

Orientation model of host and torus to align with the decrease of SAR at high λ values, while the other models tend to overproduces the number of CTN sources at intermediate and high SAR. It is interesting to note from Figure 7.3 that, despite all models tending to be degenerate in the overall distribution of SARs (Figure 7.2), the relative fractions of CTN AGN differ for different models, thus providing a further clue on the origin of obscuration in AGN when comparing with data. In particular, I find that Model 3, with a short post-peak phase, tends to perform better than others providing a distribution as a function of λ in line with data. This success is ultimately due to the fact that the fraction of unobscured AGN at larger luminosities in Model 3 is relatively less than in other model realizations, thus boosting the fraction of CTN AGN as a function of λ . On the contrary, Orientation models, with or without a torus, still generate too many unobscured AGN in particular at high luminosities, the fractions of CTN AGN as a function of luminosity tend in fact to drop steadily (see, e.g., Figure 5.4), which in turn is mirrored in Figure 7.3. At fixed stellar mass, the more luminous sources, and thus, the sources with higher λ , tend to have less CTN AGN in Orientation models than in Model 3, thus explaining the behaviors seen in Figure 7.3. At some level, a strong drop in the fractions of CTN AGN with X-ray luminosity, as observed in U14, A19, may not be in full agreement with a significant fraction of CTN at large λ as observed by Laloux et al. [2024], who in fact find that there is a higher probability to find obscured AGN at larger luminosities (c.f. their Figure B1).

7.1.1 The *forbidden* region

According to Fabian et al. [2008, 2009], as the Eddington ratio increases, the AGN enters a *forbidden* region in the $N_{\rm H}-\lambda$ plane where the radiation pressure acting on dust grains becomes significant enough to destabilize the system. This instability triggers

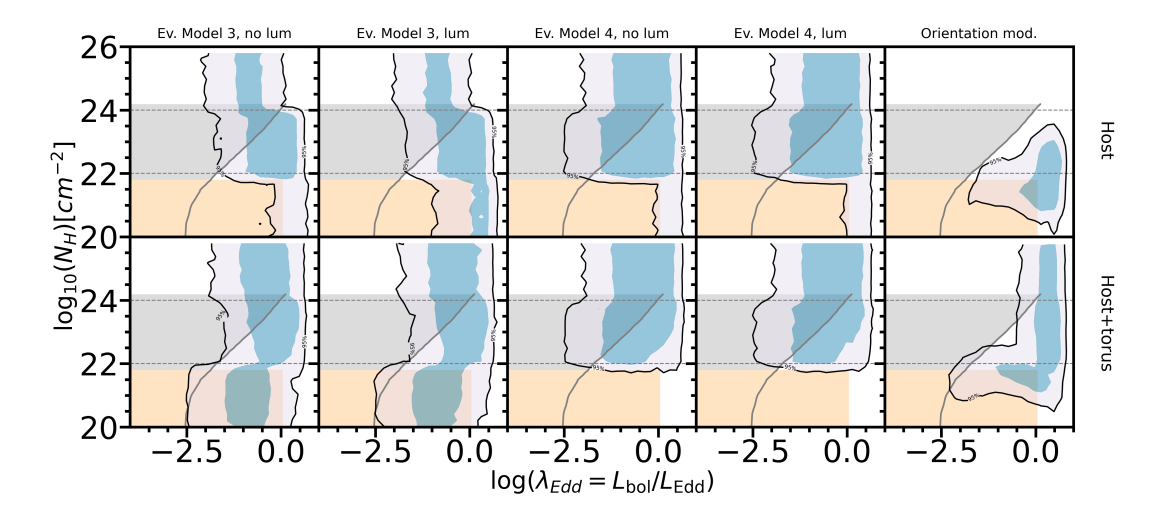


FIGURE 7.4: Column density using Evolutionary Models 3 and 4 from Chapter 6 and the Orientation model from Chapter 5. The lines correspond to 2σ and the coloured areas to $1-2\sigma$ at redshift z=2.4. Grey (long-lived absorption from clouds near the centre of the galaxy, upper left region) and yellow (outer dust lanes that can obscure over much of the plane at low column densities) areas and the black limit (effective Eddington limit with a standard ISM grain abundance) come from Fabian et al. [2008, 2009] at redshift z=0. The upper right region is called "the forbidden region" (here in white) as the Fabian et al. [2008] sample avoided that region.

outflows that can gradually expel the CTN obscuring material, leading to a decrease in the covering factor of the obscurer. In the final stage of black hole growth, the AGN transitions into a phase characterized by rapid accretion with minimal obscuration, represented by a low covering factor in the bottom right corner of the Eddington ratio-obscuration diagram (Figure 7.4). As the AGN continues to accrete material, the gas and dust are either consumed by the black hole or expelled by radiation-driven winds, leading to a gradual decrease in the accretion rate. Eventually, the system reverts to a quiescent state, completing a cycle of AGN activity. This explanation of the Fabian et al. [2008] model was first discussed by Ricci et al. [2022a].

Figure 7.4 compares observational data with the preferred Evolutionary and Orientation models, making use of the Eddington rate $\lambda_{\rm Edd}$. The top panels of Figure 7.4 show the model predictions for the $N_{\rm H}$ distributions in the $N_{\rm H}-\lambda$ plane for obscuration arising only from the gas in the galaxy. For completeness, the bottom panels also report the model predictions when including the central torus component. It is evident that the latter has a minor impact on the $N_{\rm H}-\lambda$ AGN distributions of the Evolutionary models, which already contained non-negligible fractions of CTN and CTK AGN, but a more marked one for Orientation models. The Fabian et al. [2008] model mostly focuses on large-scale outflows, not necessarily on the small scales of the torus, nevertheless I still include these predictions as well and discuss their implications below. The AGN sample (z=2.4) was selected to match the criteria used by Laloux et al. [2024, redshift $z\sim 2-2.5$]. The area surrounded by a black line corresponds to the region of the space parameter containing 95% of the entire AGN population, while the blue

inner area corresponds to the area containing 68% of the AGN population. The column density distribution of the selected sources is compared with Fabian et al. [2008, 2009]. All the models populate the *forbidden* / outflow region, except for the host galaxy in the Orientation model, and the torus model heavily affect the column density distribution and the relation of CTN/unobscured sources. Also, all the models produce significant numbers of CTN and CTK sources, especially at higher Eddington ratios, although the CTN and unobscured sources distribution vary a lot depending on the source of obscuration. Notably, the luminosity dependence produces very little effect in Model 3 and none in Model 4, ultimately completely hidden by the torus model. Note that the model data corresponds with redshift z = 2.4, while the region limits from Fabian et al. [2008, 2009] at redshift z = 0. Nevertheless, the forbidden region is expected to be pushed to even larger $N_{\rm H}$ and λ , overall further shrinking the region of parameters of this region in the $N_{\rm H}-\lambda$ plane. According to the predictions and data by Laloux et al. [2024], the forbidden region should in fact be restrained to $\log N_{\rm H} > 23$ and $\log \lambda > -1$ at z = 2.5. Vijarnwannaluk et al. [2024] also find (Type 2) AGN galaxies in the forbidden zone, suggesting that these AGN are either actively producing dusty outflows or that the X-ray emission is affected by heavy ISM absorption [Ishibashi and Fabian, 2015] associated with large scales (kpc-scale gas). Their results are consistent with a radiation-pressure regulated torus [Ananna et al., 2022a, Ricci et al., 2022a], and an Evolutionary models with the host galaxy ISM contributing to the obscured fraction.

All the reference Evolutionary models considered in this thesis are weakly sensitive to the details of the light curve, predicting a similar pattern in the $N_{\rm H}-\lambda$ plane, with vertical distributions of $N_{\rm H}$ peaked around values of $\lambda \sim 0.1-1$. This behavior is expected because most of the obscured AGN in the Evolutionary models, which are preferentially located before the peak and are thus accreting around the Eddington limit, have CTN/CTK column densities assigned at random, and thus the distributions appear as vertical stripes in the $N_{\rm H}-\lambda$ plane. In other words, the Evolutionary models discussed so far do not explicitly couple the time evolution in $N_{\rm H}(t)$ to AGN feedback within the LC. On a similar note, the Orientation model also predicts the core of the AGN population to be located at or around the Eddington limit and with vertical distributions of $N_{\rm H}$ which span up to 10^{22} if only the galactic component is considered, or up to 10^{26} if the torus is also folded in, as discussed in, e.g., Chapter 5.

In Figure 7.5, I show the impact of the forbidden region on the obscured fractions of galaxies, under the assumption that galaxies within this region rapidly transition to unobscured column densities. The forbidden region is defined as the area identified by Laloux et al. [2024] for galaxies at redshift z=2.5 (see their Figure 13). As a result of this transition, the CTN obscured fractions decrease compared to the predictions of our models presented in Chapters 5 and 6. This reduction is attributed to the increased number of unobscured sources originating from the forbidden region. Since the clearance of HI gas associated with this transition affects only the host galaxy and does not

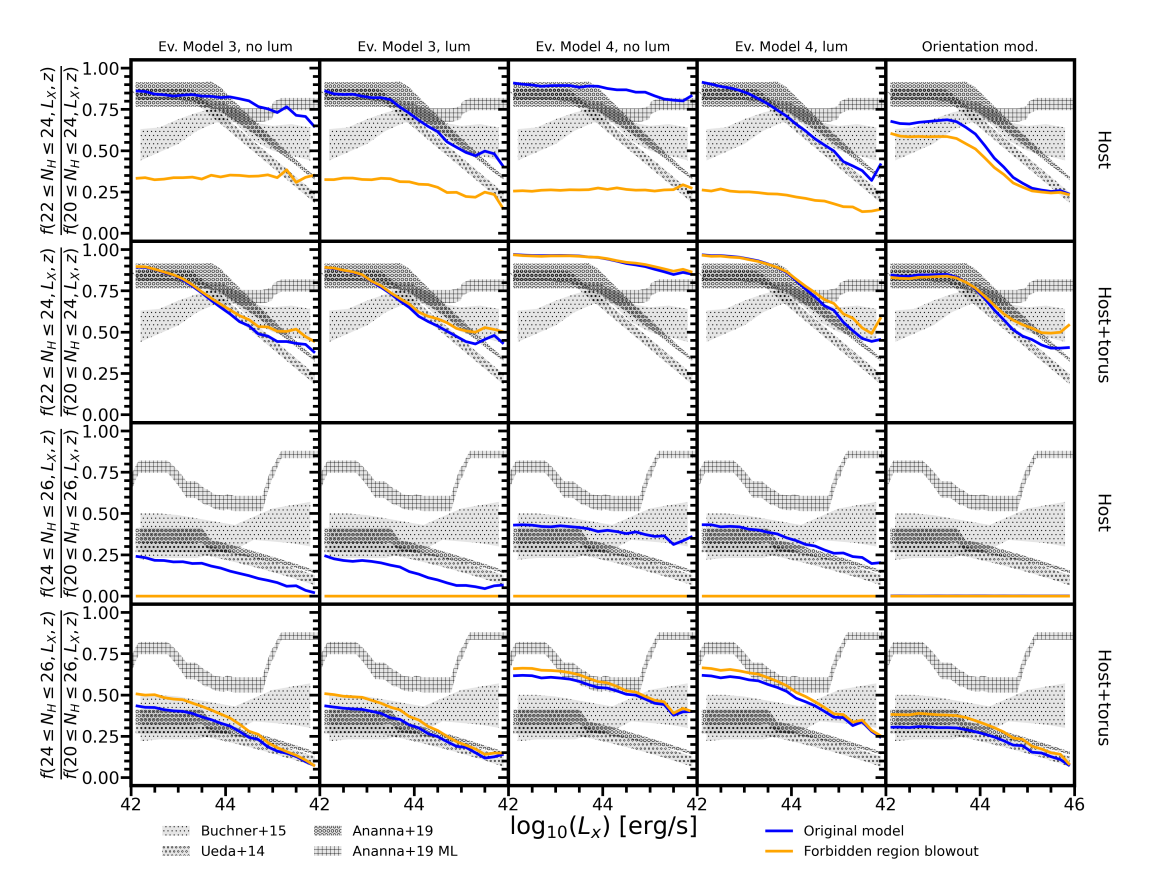


FIGURE 7.5: CTN and CTK obscured fractions for the studied models assuming that galaxies with a host column density above $\log N_{\rm H} = 23~{\rm cm}^{-2}$ and below the limit defined by Laloux et al. [2024] at redshift z=2.5 quickly move to a value below $\log N_{\rm H} = 22~{\rm cm}^{-2}$. Thus, the torus is the solely creator of CTK column density. The blue lines correspond with the original models described in previous Chapters, while the orange lines refer to the models including Laloux et al. [2024] limit.

extend to the torus, when the torus is included in the model I successfully reproduce the CTN and CTK obscured fractions, consistent with the predictions of the model explored in Chapter 5. Therefore, I find that models cannot simultaneously account for the obscured fractions observed in both the Fabian et al. [2008, 2009] and Ueda et al. [2014], Ananna et al. [2019] datasets.

It is interesting to note that the forbidden region may not be such a hard physical limit after all, as several groups have now found increasing evidence for AGN populating that region, at different redshifts and luminosities. Yamada et al. [2021], Toba et al. [2022], Musiimenta et al. [2023] are broad studies that find galaxies that populate the forbidden region, which expect to find more examples with a more extended study. Those studies therefore expect to find more AGN populating the forbidden region, in agreement with the obscured fractions found by Laloux et al. [2024]. It has also been recently proposed that at least type 2 AGN in the forbidden region may be either caught at the time of the outflow or may be affected by heavy ISM absorption associated with

large scales, and thus with "boosted" spurious $N_{\rm H}$ column densities. The data are nevertheless, still sparse to draw any firm conclusions on the existence or not of a forbidden region.

7.1.2 Eddington ratio distributions in Orientation and Evolutionary models

The Orientation model states that the differences between obscured and unobscured AGN are primarily due to their orientation relative to the observer. According to this model, the obscurer, typically identified as a torus-like component, obstructs the line of sight in obscured AGN but is absent or non-obstructive in unobscured AGN. Since the intrinsic properties of the central engine, such as the accretion rate, should be independent of orientation, I would expect the Eddington ratio distributions of obscured and unobscured AGN to exhibit similar shapes.

My findings support this expectation. Specifically, the results demonstrate that the Eddington ratio distributions and specific accretion rates for both obscured and unobscured AGN indeed share similar characteristics, affirming that Orientation and Evolutionary models predict similar behaviours. Therefore, using only Eddington ratios or specific accretion rates may not be the best way to distinguish among models. However, further study needs to be implemented in order to confirm these results, specially when increasing the AGN selection range, and the inclusion of a stellar mass and black hole mass evolution.

7.1.3 The role of Orientation and the torus and its connection with Evolutionary models

Orientation models offer a complementary perspective by focusing on the angle at which the AGN is observed relative to its obscuring structure, typically modelled as a dusty torus. The unification model [Antonucci, 1993, Urry and Padovani, 1995], predicts that the differences between Type 1 (unobscured) and Type 2 (obscured) AGN can be attributed primarily to the orientation of the torus with respect to the line of sight. This study extends this orientation-based approach by integrating it with Evolutionary models, demonstrating that the inclusion of a torus component significantly improves the fit to observed data. This finding is consistent with the results of studies like those by Elitzur [2007], Elitzur and Ho [2009], which emphasized the role of the torus in shaping the observed properties of AGN, especially in the CTK regime. They argued that the torus is a dynamic structure, potentially linked to the broader AGN fuelling processes, and its geometry and composition can vary over time, further complicating the relationship between obscuration and Eddington ratio. This supports the idea that higher accretion rates are associated with more significant obscuration, contrary to the

findings of Ricci et al. [2017b], possibly due to the increased inflow of material that feeds both the SMBH and the surrounding torus, which I find in my results.

While Evolutionary and Orientation models each offer valuable insights, the results suggest that a hybrid approach is necessary to fully capture the complexity of AGN behaviour. Hickox and Alexander [2018] argue that while the traditional Orientation/Unification model explains some AGN properties, it fails to account for variability driven by accretion rates and feedback mechanisms. They propose that combining orientationbased models with evolutionary considerations offers a more comprehensive understanding of AGN diversity. In a similar way, Hopkins et al. [2006b] highlight the role of host galaxy evolution, particularly during mergers, in shaping AGN obscuration. They argue that obscuration is not merely a matter of orientation but is closely tied to the galaxy evolutionary state, needing a model that integrates these dynamics. Ishibashi et al. [2018] explore how radiation pressure and feedback mechanisms influence AGN obscuration, suggesting that these interactions must be considered alongside orientation effects to fully understand AGN behavior. In my case, I find that an Evolutionary model might reproduce CTN obscuration better at low λ and the Orientation model at high λ . All in all, these studies support a model that integrates both orientation and evolution to describe AGN obscuration. Their findings suggest that the evolutionary stage of the AGN and its host galaxy determines the availability of material for the torus, which in turn influences the observed obscuration.

7.2 Studying the obscuration using Clustering

As explained in Section 2.7, the two-point correlation function (2pCF) is a key tool for studying the large-scale structure of the Universe, galaxy evolution, and the connection between galaxies and dark matter halos. For AGN, it helps explore clustering patterns based on black hole mass, Eddington ratio, and obscuration levels, distinguishing between Orientation and Evolutionary models of AGN behaviour.

Observations show that obscured AGN often cluster more strongly than unobscured ones, particularly at intermediate redshifts, suggesting they inhabit denser environments or massive halos. The 1-halo term reflects small-scale interactions, while the 2-halo term indicates large-scale environmental effects. Studies using models like GAEA aim to test AGN evolution theories and the role of obscuration, with 2pCF providing critical insights into AGN clustering and environmental influences.

In this Section I study the effect of obscuration in clustering analysis as described in Section 4.5. I will start showing the predictions from the Orientation model using only the host galaxy column density calculation and the model that also includes the fiducial torus model in Section 7.2.1. Finally, the results from Evolutionary Models 3 with a luminosity dependence and with a long-lived torus are presented in Section 7.2.2.

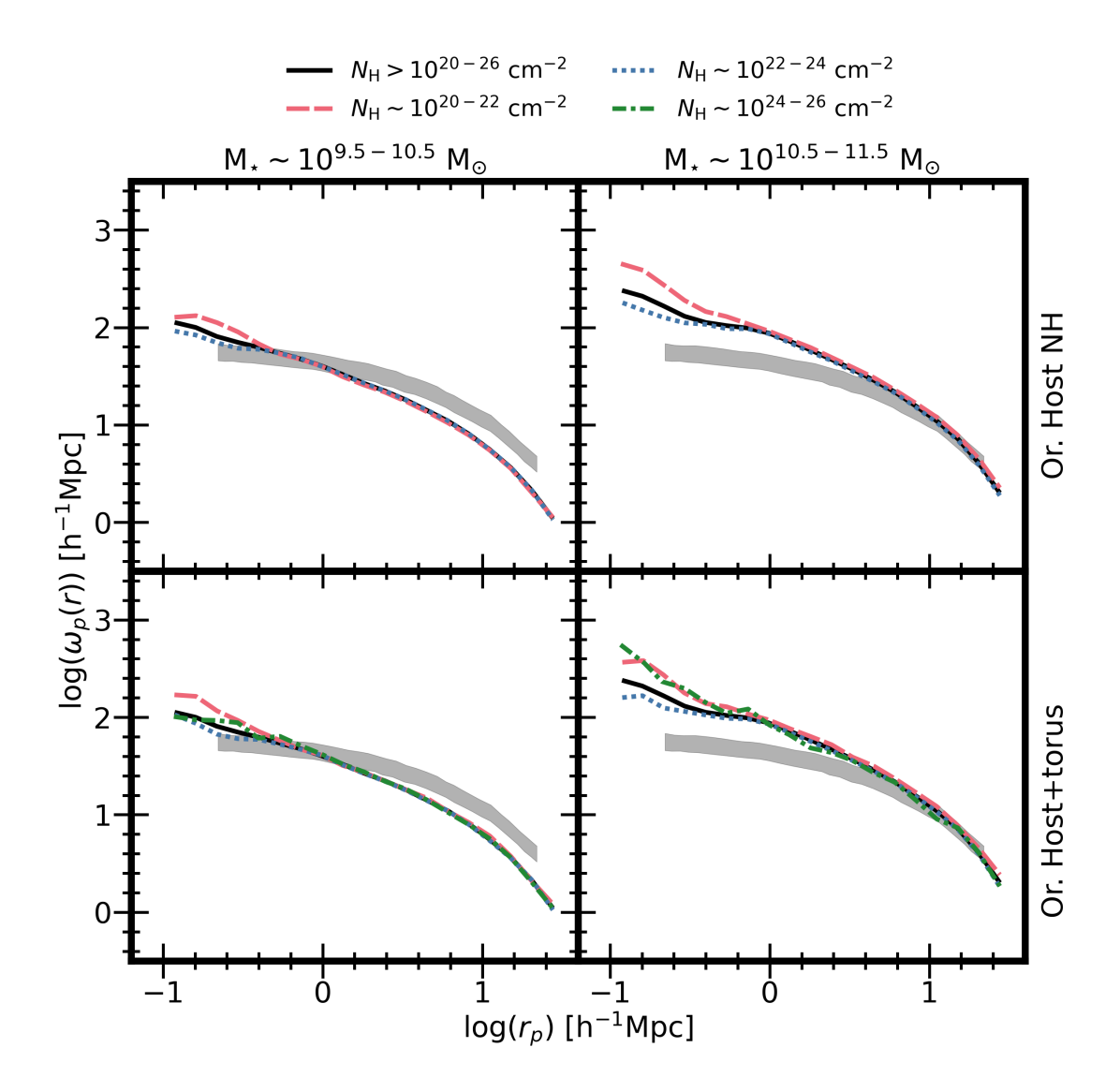


FIGURE 7.6: Projected 2-point correlation function at different bins of stellar mass and column density (as labelled). Grey area corresponds to the total column density bin of redshift 1.1 < z < 3 from Viitanen et al. [2023]. **Upper panels:** column density calculated using the Orientation model for the host galaxy. **Bottom panels:** column density calculated using the Orientation model for the host galaxy and fiducial torus model.

7.2.1 Clustering in the Orientation model

In Figure 7.6, I present the projected two-point correlation function (2pCF) for different stellar mass and column density bins, using the Orientation model. I compare the results with the X-ray selected data from Viitanen et al. [2023] for redshift 1.1 < z < 3. The 2pCF exhibits a clear trend of increasing clustering strength with stellar mass at fixed redshift (z = 2.4), consistent with expectations, as more massive galaxies are known to be more strongly clustered [Coil, 2013, Cochrane et al., 2018]. This enhanced clustering is reflected in the correlation length, which increases with stellar mass due to

the tendency of these galaxies to reside in denser, more clustered, more massive dark matter halos.

The CTK column density bin is not included in the host model because there are insufficient galaxies with CTK obscuration, as discussed in previous Chapters. Notably, the column density selection does not significantly influence the 2pCF at $r_p > 1$ Mpc/h across models, except for the host+torus model, where some degree of divergence is observed in the CTK bin. This variation arises from the inclusion of the torus model, which generates CTK sources, unlike the host galaxy model. However, the instability in the correlation at $r_p \sim 0$ is primarily attributed to the small number of galaxies available for analysis in this specific stellar mass and column density bin, a factor that fluctuates across different renditions of the Figure, and it is exacerbated when decreasing the stellar mass bin.

At scales below $\sim 1 \text{Mpc/h}$, within the 1-halo term, the column density cuts exhibit slight variations, particularly in the higher stellar mass bins and when incorporating the torus model. Differences in column density could indicate variations in local environments, as denser regions may exhibit stronger galaxy clustering, especially in intermediate stellar mass bins. However, since this effect is not consistently observed across all models, I can rule out this as the primary cause. In regions of high column density, interactions involving cold gas may influence the clustering signal, resulting in observed differences across column density bins, particularly when column density is computed based on cold gas mass. The results exhibit minor variations in each iteration of the figure, suggesting that the observed discrepancies on small scales are influenced by the inherent randomness in the calculations, which is an unavoidable aspect of this model. Additionally, these discrepancies may arise from the limited number of galaxy pairs at small separations. However, when selecting a smaller subsample of galaxies, the discrepancies either persist or the number of galaxies within the bin becomes insufficient for robust analysis. While increasing the bin size reduces the variance between iterations, the discrepancies do not fully disappear. Consequently, the observed variations are likely attributable to one or more of the following factors: the randomization inherent in certain aspects of the column density calculation, intrinsic properties of the AGN and their host galaxies, or the environmental conditions surrounding the AGN. To further investigate these possibilities, the Evolutionary model, which excludes cold gas mass in its column density calculation, can be used to confirm whether these differences are indeed linked to gas interactions.

I checked that the results do not vary when smaller stellar mass bins ($\Delta M_{\star} = 0.5 \, \mathrm{M}_{\odot}$) are used. I also confirm that the clustering increases with redshift as consequence of the evolution of the stellar mass, as expected [Allevato et al., 2011, Viitanen et al., 2023].

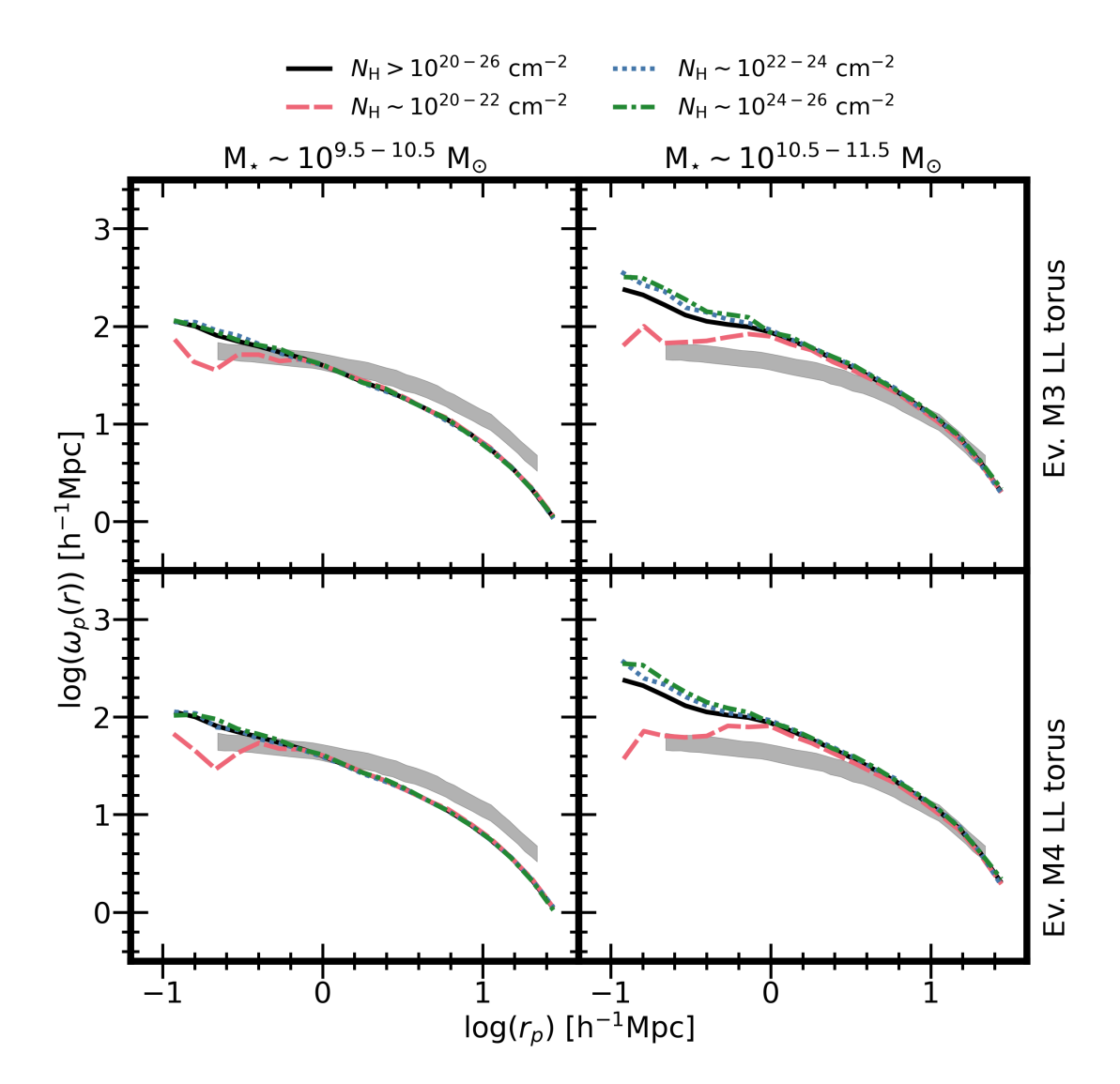


FIGURE 7.7: Projected 2-point correlation function at different bins of stellar mass (as labelled). Each line corresponds to a different column density bin. Grey area corresponds to the total column density bin of redshift 1.1 < z < 3 from Viitanen et al. [2023]. **Upper panels:** column density calculated using the Evolutionary Model 3 including the long-lived fiducial torus model. **Bottom panels:** column density calculated using the Evolutionary Model 4 including the long-lived fiducial torus model.

7.2.2 Clustering in the Evolutionary model

In Figure 7.7, I present the projected 2pCF for different stellar mass and column density bins using the Evolutionary model. I compare the results with the data from Viitanen et al. [2023] for redshift 1.1 < z < 3. Consistently with previous findings, the selection of column density does not significantly impact the 2pCF at >1 Mpc/h across the models. The correlation instability observed in the host and torus models (Figure 7.6) appears as well in the lowest and highest stellar mass bins of both Models 3 and 4 with a long-lived torus. Again, this instability is primarily attributed to the limited number of galaxies available, confirmed by selecting smaller galaxy samples and enlarging the

bin, for analysis in these specific stellar mass and column density bins, a factor that varies across different iterations of the Figure. The highly obscured AGN bin is the most sensitive to the exact choice of the limits in redshift, stellar mass and obscuration [Viitanen et al., 2023].

At <1 Mpc/h, slight variations in the column density cuts are observed at both lower and higher stellar mass bins. The instability in the correlation is again largely driven by the small sample size in these bins, especially for galaxies in the unobscured column density cut at lower stellar mass (dashed red line) and the CTK-obscured cut at higher stellar mass (green dash-dotted line). As tested, this effect is mitigated when the long-lived torus model is included, which is the result shown in this figure, as it facilitates a more even distribution of column density across all stellar mass bins.

In all models and stellar mass bins, variations in the column density cuts are more pronounced at <1 Mpc/h, particularly in the higher stellar mass bins and when the torus model is incorporated. While the variations in local environments, as discussed in Section 7.2.1, may still influence the results, especially in the intermediate stellar mass bins, the differences in column density cuts are not associated with the cold gas mass of the galaxies. This is because the obscuration is linked to the luminosity within the light curve, rather than to cold gas mass which is assumed to remain rather similar within the initial time of the LC. Since I have tested that the discrepancy does not come from low number of pairs nor the bin, and they appear both when using cold gas mass and the LC, the observed differences in the 2pCF are attributed to either environmental effects, like AGN located in dense cluster environments may experience interactions that strip HI gas, or intrinsic properties. However, further study on the reasons behind the discrepancy between clustering at different column density bins and the clustering difference between our two models fall outside the scope of this analysis. I specifically note that visible sources present lower clustering in these models than in Orientation models. Therefore, the differences in them models at <1 Mpc/h might be the door to decide on a preferred model. Further observational clustering studies focused on low scales and column density are needed to explore this possibility.

I conclude that, as found by Allevato et al. [2011], Viitanen et al. [2023], the clustering at medium and longer scales does not change when different cuts of column density are used, at fixed stellar mass and redshift. This result is consistent using different obscuration models. Further study is needed to explore the clustering differences at smaller scales. There are other studies such as Hickox et al. [2011], DiPompeo et al. [2014, 2016, 2017], Jiang et al. [2016], Koutoulidis et al. [2018], Powell et al. [2018], Petter et al. [2023], Rosado et al. [2024] that find different clustering strengths at different column densities, although I note that they also consider different cuts of stellar mass, since they find that unobscured AGN are more massive than obscured AGN. Therefore, those differences may be explained by the different stellar mass cut, not by intrinsic differences between AGN obscuration, as recently highlighted by Córdova Rosado et al. [2024].

Chapter 8

Conclusions

In this thesis, I have explored a range of mechanisms and models that contribute to my understanding of AGN obscuration and evolution, using mostly (but not uniquely) comprehensive semi-analytic and semi-empirical models. By examining key aspects such as Orientation effects, the role of the torus, and Evolutionary models, I have provided insights into how AGN are shaped by their environments and internal processes. The analysis of this thesis has also incorporated the influence of light curves, gas fractions, starburst events, and mergers, as well as more complex models that combine orientation and evolutionary scenarios. I also provide predictions for the AGN clustering properties and Eddington ratio distributions for my favoured models, which I use as complementary tools to explore the viability of Orientation and Evolutionary models against current data sets.

8.1 The role of the Orientation model

The source of obscuration in AGN is still highly uncertain, as it can arise from the large-scale obscuration of the galaxy, and/or from an inner dusty torus component around the central SMBH. In this thesis, I have modelled from first principles, in the framework of a comprehensive semi-analytic model, the origin of obscuration in AGN in the context of pure orientation models with a first incursion into some evolutionary components that might play a key role in the obscuration definition. The main results on this part of the thesis can be summarized as follows:

On the strict assumption of an exponential cold gas density profile, I find that
the fraction of CTN obscuration contributed by only the large-scale galaxy obscuration is not enough to reproduce the current observational constraints, like
the obscured fraction dependency with luminosity at all redshifts and the level of

- obscuration required at redshift z = 2.4, unless I assume very compact galaxies (Figures 5.1, and 5.2).
- The inclusion of a physically-motivated, AGN-driven shock BW shuffle around the gas creating a hole and shifting gas outside, and thus modifying the overall $N_{\rm H}$ column densities. However, the BW is not the main driver behind the drop of the obscured CTN fractions with X-ray luminosity, which is mostly driven by the gas disc sizes increasing with stellar mass (Figure 5.2). The results point to the morphology of the cold gas component as the main driver shaping the properties of the obscuration of AGN, at least in CTN sources.
- Irrespective of the exact parameters and model assumptions, the large-scale gas distributions fall short in reproducing any significant fraction of CTK obscuration (Figures 5.1 and 5.3), at least at $z \le 3.3$, and when adopting a strictly exponential profile for the cold gas component.
- The inclusion of a dusty torus with opening angle depending on both AGN luminosity and BH mass as in Wada [2015] with the $N_{\rm H}$ limits discussed by Ramos Almeida and Ricci [2017] (adopted as a fiducial torus model in this thesis), nicely matches the full distribution of CTK obscuration as a function of X-ray luminosity, and also contributes to the fraction of CTN AGN. The full fiducial model also broadly, albeit not perfectly, aligns with the AGN $N_{\rm H}$ distributions at fixed X-ray luminosity.
- Within the remit of the model explored here, the presence of an inner torus appears to be an essential and ubiquitous contributor to AGN obscuration, especially for the more luminous CTN and most of the CTK sources.
- A time-dependent torus model disappearing in the post-peak phase might be able to reproduce the CTN and CTK obscuration, but it heavily depends on how the torus and the AGN light curve are modelled (see Section 5.4).

8.2 The role of the Evolutionary model

Complementary to Orientation models, in this thesis I have also modelled the obscuration in AGN using a comprehensive semi-analytic framework that incorporates various Evolutionary models, a torus model, and a mixed model combining evolution and orientation effects. Additionally, I have investigated the impact of starburst activity and mergers on obscuration. My main results regarding Evolutionary models can be summarized as follows:

 Traditional Evolutionary models characterized by light curves (LCs) with a long post-peak phase and CTN/CTK obscuration only pre-peak, tend to struggle in reproducing the observed large fractions of CTN/CTK X-ray AGN at 1 < z < 3 (see Figure 6.7). This aligns with feedback models suggesting that outflows may not be as efficient removing the gas around the centre in galaxies [Menci et al., 2019] (see Figure 6.1).

- Evolutionary models characterized by LCs with a sharp drop after the peak (Models 2 and 3), or with a CTN phase reappearing after the peak (Model 4), are favoured in reproducing the high fractions of CTN/CTK AGN (see Figures 6.1 and 6.3).
- A steep drop in the obscured fractions of AGN as observed in some data sets can be reproduced in the pure Evolutionary models only by including a luminosity dependence in the UV/optical visibility window, increasing from $\Delta \tau_{\rm QSO} = 10^7 \ \rm yr$ to $\Delta \tau_{\rm QSO} = 8 \cdot 10^7 \ \rm yr$ for the more luminous sources (see Figure 6.3).
- All the models tend to align with the fractions of obscured X-ray AGN when the visibility window is of the order of $\Delta \tau_{\rm QSO} \sim 10^7 10^8$ yr (see Figure 6.3).
- Including a torus component in Evolutionary models, which lives throughout the AGN lifetime even beyond the peak, and with a thickness decreasing with increasing AGN power, can increase the CTN and CTK AGN whilst also inducing a significant luminosity dependence in line with some of the data, in particular U14. An inner geometrical component like a torus would imply that orientation effects tend to constitute a key source of obscuration even in Evolutionary models (see Figure 6.4 and 6.5).
- I find that the fraction of sources in the model observationally defined as starbursts lying 4 times above the MS, falls short in reproducing the CTK fractions (see Figure 6.9). Similarly, also the major mergers with ratio > 1/3 tend to be too few, except possibly for the most luminous AGN (see Figure 6.10).

The current results support an LC model with a luminosity dependent post-peak phase, a pre-peak with CTK and then CTN obscuration, and an optically/UV visible peak with a long-lived torus model. Although it may represent a challenge in my framework to reproduce current data with traditional Evolutionary models, a torus-like component may play a pivotal role in shaping obscuration in AGN. This thesis' predictions can be tested with current and new facilities such as JWST, ALMA or Athena.

8.3 The Eddington ratio distribution effect

In addition to the AGN obscuration study on X-ray, in this thesis I have also included the analysis of AGN obscuration depending on the specific accretion rate and the Eddington ratio. The specific accretion rates distribution (SARD) predicted by the models aligns with the observational data from Georgakakis et al. [2017a] and Laloux et al. [2024] at redshift z=2.4. Both Evolutionary and Orientation models reproduce the overall shape of the SARD with slight differences in the predictions of obscured and unobscured AGN, as found by Laloux et al. [2024]. The comparison of the SARD for obscured and unobscured AGN also supports the notion that obscured sources generally exhibit lower SARD values, mirroring observations from Laloux et al. [2024]. However, the models show that the difference between these populations is minimal, either with Orientation or Evolutionary models, which suggests that despite of the slight effect of obscuration at the overall accretion rates, this method does not help to disentangle which model, if Orientation or Evolution, is preferred.

The analysis of the "forbidden" region, where AGN outflows occur due to increased radiation pressure, suggests that this region is not as sparsely populated as previously thought. This finding is at odds with data from Fabian et al. [2008], but consistent with Laloux et al. [2024] an references therein, that observe a significant number of AGN in these outflow phases, especially at higher redshifts. However, these results require further analysis and compatibility with other datasets [Ueda et al., 2014, Ananna et al., 2019, e.g.,], which is outside of the scope of this thesis.

The study demonstrates both Evolutionary and Orientation models capture the presence of CTK sources, especially at high Eddington ratios, though there is some variability in the fraction of obscured AGN predicted by each model. This discrepancy points to the need for a hybrid approach to fully understand the interplay between accretion rates and obscuration. This hybrid model approach aligns with other studies, such as Hopkins et al. [2006a], Hickox and Alexander [2018], which emphasize that AGN obscuration is not merely a matter of just Orientation but is also influenced by the galaxy evolutionary stage, mergers, and feedback processes.

8.4 The role of clustering

As an additional study, in this thesis I have also analysed the clustering of AGN using different stellar mass and column density bins, to compare the 2-point correlation function (2pCF) and see if the column density affects the AGN clustering. I have also checked different Orientation and Evolutionary models, to confirm that the clustering results are invariant to the model used.

The results show a clear trend of stronger clustering (larger 2pCF) with increasing stellar mass at a fixed redshift, consistent with previous studies that link higher stellar mass galaxies with denser, more massive dark matter halos. Incorporating a torus model in the Orientation model introduces variations in the clustering, especially for CTK sources, due to the lack of CTK sources in the Orientation model without a torus. However, the overall influence of column density on the 2pCF remains low. At smaller

8.5. Future work 119

scales (below 1 Mpc/h), minor variations in clustering strength are observed, particularly in higher stellar mass bins and with the torus model, which are largely driven by the randomization of some parts of our column density calculations, but could also indicate local environmental effects, such as interactions involving cold gas. However, this hypothesis is not confirmed in this model, nor with the current data. Similarly, Evolutionary models show that column density selection does not significantly impact clustering on large scales, also finding the same differences at smaller scales than in the Orientation model, confirming the model used does not have a large impact in the results. However, the minor differences at small scales, with more targeted observations, could be the door for future clustering studies.

Finally, the results presented here provide a solid foundation for future work. The study of AGN clustering will benefit greatly from ongoing and upcoming large-scale surveys, such as eROSITA and the forthcoming Athena mission, which will provide much larger and more diverse samples of AGNs across a wide redshift range. These surveys will offer the opportunity to refine our understanding of how obscuration, AGN activity, and galaxy environment evolve together, particularly for heavily obscured AGNs like CTK sources, where current sample sizes remain limited.

8.5 Future work

Based on the results presented in this thesis, I can explore different ways for future research to advance our understanding of AGN obscuration and its relationship with host galaxy properties, environmental factors, and redshift evolution.

- Exploring Different Gas Density Profiles and N values: In this thesis, I primarily used an exponential gas density profile for modeling the column densities in AGN obscuration and adopt N=0.3 as the relation between gas and stellar radii. However, a deeper modelying of the structure of the gas in galaxies can be carried out, changing the profile and gas-stellar radii relation, which requires more observational results to anchor the models.
- Refining Torus Models: One of the key results in this thesis highlights the necessity of a torus component with luminosity-dependent thickness to explain obscured AGN, particularly Compton-thick (CTK) sources. Future work could explore more sophisticated torus models, including hydrodynamical simulations that account for clumpy or non-uniform tori. Observational efforts using high-resolution infrared or submillimeter imaging (e.g., ALMA) could further constrain the physical structure and evolution of the torus in AGN of varying luminosities.

- Exploring Multi-phase Obscuration: The analysis of this thesis has shown that galaxy-scale gas distributions and torus-linked obscuration are both necessary to explain the full range of observed column densities. Future studies could examine multi-phase gas obscuration models that incorporate both cold, dense molecular gas and warm, ionized components. This could offer new insights into the transitional phases between galaxy-scale obscuration and torus-driven effects, and how they evolve across different AGN stages.
- Light Curves and AGN Lifecycles: This study has demonstrated the influence
 of different AGN LCs on the observed obscuration patterns. Future work could
 include exploring variability on shorter timescales, with LCs with less sparse triggerings and accretion events, which could directly impact the time-dependent obscuration and visibility of AGN. This will help refine models that combine AGN
 lifecycles with obscuration mechanisms, providing a more complete picture of
 AGN evolution and feedback.
- Incorporating Time-dependent Feedback Mechanisms: While AGN feedback is known to influence the obscuration through clearing gas and shaping the environment, a more detailed, time-dependent treatment of feedback would be valuable for both simulations and observational researchers. Investigating how AGN-driven winds and outflows interact with obscuring material over time, possibly using hydrodynamical simulations coupled with feedback prescriptions, could refine our understanding of the feedback-obscuration relationship.
- Expanding Redshift Coverage: The results presented focus primarily on obscuration patterns up to $z\lesssim 3$. Extending the analysis to higher redshifts would provide insights into the earliest stages of galaxy and AGN co-evolution, especially before the peak of cosmic star formation and black hole growth at $z\sim 4-6$, which could also impact the SMBH seeds. Deep X-ray and infrared surveys targeting this epoch could reveal whether the need for a torus persists and how galaxy-scale gas contributes to obscuration at earlier times, especially with the new studies focusing on Little Red Dots (LRDs) and new JWST data.
- Eddington Ratio and Obscuration: Another aspect worth exploring in more detail is the relationship between Eddington ratio distributions and obscuration. I touched upon this in my analysis, but future work could model how AGN at different accretion rates might interact with their surrounding gas differently, influencing both feedback and obscuration patterns. This could improve our understanding of how black hole growth is regulated across different stages of AGN evolution.
- AGN Clustering and Environment: This thesis has touched on the clustering differences between obscured and unobscured AGN, but future work could focus on improving the comparison of AGN clustering measurements at various

redshifts and luminosities with observational data. By leveraging large surveys such as eROSITA or Euclid, I can assess how the environments of AGN, particularly those with heavy obscuration, evolve over cosmic time. Combining these observational data with theoretical models of AGN-host co-evolution will help disentangle the influence of large-scale structure and mergers on AGN activity.

• Other Simulations with Observational Comparisons: Finally, extending the use of different semi-analytic, semi-empirical and hydrodynamic simulations that incorporate realistic feedback, galaxy evolution, and AGN LC models would provide more precise predictions about obscuration patterns. It is also important to include some types of galaxies that have been recently discovered or recently found to impact some aspects of the obscuration, such as LRDs or changing-look AGN. These objects, although only providing a small contribution to obscuration, would be interesting to explore in theoretical models to predict what is the actual extent of their effect. Comparing these simulations directly with new observational data, particularly from next-generation telescopes like the JWST and the Square Kilometer Array (SKA), will help validate or refine current models of AGN obscuration.

8.6 Take-home messages

What is the effect of the host galaxy in shaping the AGN obscuration? The host galaxy plays a significant role in AGN obscuration, particularly through galaxy-scale gas distributions. Galaxy-scale obscuration, driven by cold gas in the supermassive black hole, can contribute to the overall column density of AGN. However, this alone cannot reproduce the high fraction of CTK AGN. For intermediate levels of obscuration, such as CTN AGN, the host galaxy gas obscuration may suffice, especially if the gas reservoirs are compact and dense. Thus, while the host galaxy shapes obscuration, it is often insufficient without additional nuclear components like the torus, unless changing the density profile to a model that produces much more obscuration, like a Sérsic profile. However, a Sérsic profile would require a very small radii for the gas and dust, smaller than the assumption of this thesis, which is not in line with recent ALMA findings.

What is the effect of the torus in shaping the AGN obscuration under an Orientation model and Evolutionary models? In the Orientation model, the torus is essential in shaping AGN obscuration, as the line-of-sight determines whether the central region is visible or obscured. A thick enough torus can hide the AGN from certain viewing angles, causing the observed obscuration to vary primarily due to orientation effects. In Evolutionary models, the torus also plays a critical role but can be viewed as part of

the AGN intrinsic evolution. A torus with thickness that decreases as AGN luminosity increases is necessary to align model predictions with those deep X-ray data that suggest a sharp decrease of the obscured fractions at high luminosities [e.g, Ueda et al., 2014, Merloni et al., 2014].

What is the effect of the gas fractions in shaping the AGN obscuration? Gas fractions, particularly in the host galaxy, significantly impact AGN obscuration by contributing to the overall column density along the line of sight. Higher gas fractions in galaxies tend to increase the obscuration level. In particular, dense gas can enshroud the AGN during certain evolutionary phases, especially in starburst or post-merger scenarios. However, while higher gas fractions may contribute to obscuration in the CTN regime, they are not sufficient to explain the number of CTK AGN, which still requires the presence of a torus or other dense nuclear obscurers, when accounting for both analytically calculated or empirically implemented gas fractions.

What is the effect of the light curve in shaping the AGN obscuration under Orientation and Evolutionary models? The AGN LC, which reflects the accretion rate over time, affects how long the AGN remains obscured in both Orientation and Evolutionary models. In Orientation models, the LC determines the AGN intrinsic brightness but does not directly affect obscuration, which is driven by the torus and the line of sight, since the column density is assumed constant throughout the AGN evolution in this scenario. In Evolutionary models, the AGN is more likely to be obscured during periods of high accretion, particularly in the early stages of its evolution, with luminosity gradually diminishing as the gas is consumed or expelled by feedback. In this thesis I favour a model that includes an initial CTK phase followed by a CTN phase that gets cleared out when the AGN reaches its maximum luminosity, or a model that comprises a CTK phase pre-peak and a CTN phase post-peak. Nevertheless, even in these models a long-lived torus component can help in better matching the significant fractions of CTK AGN.

Is there any other variable that could affect AGN obscuration? Several other factors can influence AGN obscuration:

- **AGN Feedback:** AGN feedback, which includes both radiative and kinetic modes, can clear out gas from the nuclear region, reducing obscuration over time. This is especially relevant in Evolutionary models. However, I showed that an AGN feedback-induced blast wave, although capable of clearing the inner regions of the galaxy, does not significantly decrease the *N*_H associated to any given galaxy, and it is not responsible for the luminosity dependence of the obscured fractions.
- Mergers and Starbursts: Galaxy interactions, particularly mergers, can funnel
 gas toward the galactic center, enhancing obscuration temporarily during AGN
 activity peaks. Nevertheless, my models suggest that mergers and starbursts, if

anything, can mostly contribute to the most luminous CTN AGN, falling short in reproducing the moderate to faint CTK AGN.

Do I find differences in the clustering of AGN with different obscuration? The obscuration itself, at least at the level implemented in my models, does not strongly impact clustering across different models, except for CTK AGN, which can exhibit stronger clustering in some models, but only at small scales, below 1 Mpc/h. I thus conclude that, at least based on the level of modelling performed in this thesis, differences in the clustering measurements in observed sources could be at least in part explained to selection effects, either different stellar mass and/or redshift cuts.

What is the predicted redshift evolution of AGN obscuration? At higher redshifts, galaxies tend to reside in denser environments and are more gas-rich, leading to higher levels of obscuration, particularly in the early phases of AGN activity. Nevertheless, the relative fractions of CTN and CTK sources, I found, are relatively stable with cosmic time at higher redshifts, in line with what suggested by current observational data. Further analysis needs to be done at lower redshifts to reach a conclusion.

In conclusion, this thesis has explored the complex interplay between host galaxy properties, torus components, AGN feedback, and evolutionary processes in shaping AGN obscuration. By leveraging a combination of cosmological models, I have provided new insights into how different mechanisms contribute to the column densities observed in obscured AGN, particularly in the Compton-thick regime. While the host galaxy gas distribution and light curve plays a significant role, my findings also favour the presence of a nuclear torus to explain the high obscuration levels seen across various redshifts and luminosities, whilst providing a framework for describing the relative, but more modest, contributions of gas fractions, AGN feedback, and starbursts in modulating obscuration in AGN.

Appendix A

Study of molecular gas in a semi-analytical context

A.1 Updated gas model implementation in GAEA SAM model

GAEA SAM model is in constant development to implement the new studies. Despite F20 being the preferred version of the model in this thesis, there is an on-going project to fully merge that version with the implementations described in Xie et al. [2017]. As mentioned before, F20 version already implements Xie et al. [2017] improved modelling of disc sizes, tracing the evolution of angular momentum by following the mass and energy exchanges among different galaxy components. However, in Xie et al. [2017] they propose a new methodology to incorporate a distinction in the molecular and atomic gas, allowing further analysis on the molecular gas fraction, the depletion time, or the total gas fraction evolution on redshift. The new run of the GAEA code including Xie et al. [2017] implementations will be referred as *GAEA-merged* [corrected and final version published in De Lucia et al., 2024], while F20 version of the code will be called *GAEA*.

The latest update of the GAEA-merged semi-analytic model introduces several improvements and new implementations to enhance galaxy evolution predictions. Key updates include:

- Incorporation of a non-instantaneous model of chemical enrichment that accounts for the mass-dependent lifetimes of stars, refining gas, metals, and energy ejection [De Lucia et al., 2014].
- Enhanced treatment of stellar feedback based on high-resolution hydrodynamical simulations [Hirschmann et al., 2016].
- Detailed tracking of angular momentum [Xie et al., 2017].

- Explicit division of cold gas into atomic and molecular components [Xie et al., 2017].
- Non-instantaneous modeling of cold and hot gas stripping in satellite galaxies [Xie et al., 2020].
- New model to account for cold gas accretion onto SMBHs and the onset of AGN-driven outflows [Fontanot et al., 2020].

The model published has been calibrated against several key observational constraints, such as the galaxy stellar mass function at z < 3, AGN LF at z < 4, and the local HI and H_2 mass function. It also successfully reproduces the evolution of quenched galaxies up to $z \sim 4$ and predicts the emergence of the first massive quenched galaxies at $z \sim 6-7$. Additionally, future work will focus on the properties of high-redshift galaxies as observed by JWST. The model continues to align with other recent observational constraints, such as the evolution of mass-metallicity relations and the cosmic star formation rate density at high redshifts.

In some initial developments of the new GAEA-merged code, a basic test on the basic performance of the code was necessary. I found that the merged code, under the same initial parameters, was calibrated to perfectly reproduce GAEA. The code worked similarly under different initial parameters (e.g., SFR efficiency, AGN efficiency, BH growth rate). Note that the code used here is not the one published in De Lucia et al. [2024], but an earlier version of the code. This project was used to improve and update the code, helping to develop the code to its current level.

A.2 Molecular gas fraction, total gas fraction, and depletion time

A fundamental study that can be done with this new model is to examine AGN and no-AGN galaxies to check if each group follows a specific pattern, different than the other. I found that, in terms of stellar mass, SFR or molecular mass, galaxies with AGN do not show any particularity, besides the AGN appearing more distributed to higher molecular gas masses and SFR across all stellar masses [Mountrichas et al., 2022].

Due to the limitations of the model, reliable results cannot be obtained for galaxies with stellar masses below $10^9\,M_\odot$. Although the GAEA-merged model can achieve a resolution down to $10^8\,M_\odot$ thanks to the P-Millennium Simulation merger trees [Fontanot et al., 2024], my analysis is constrained to higher mass galaxies. Additionally, the state of the implementation used requires a thorough revision of each code volume, and certain cosmological simulation boxes were unavailable. As a result, this study focuses

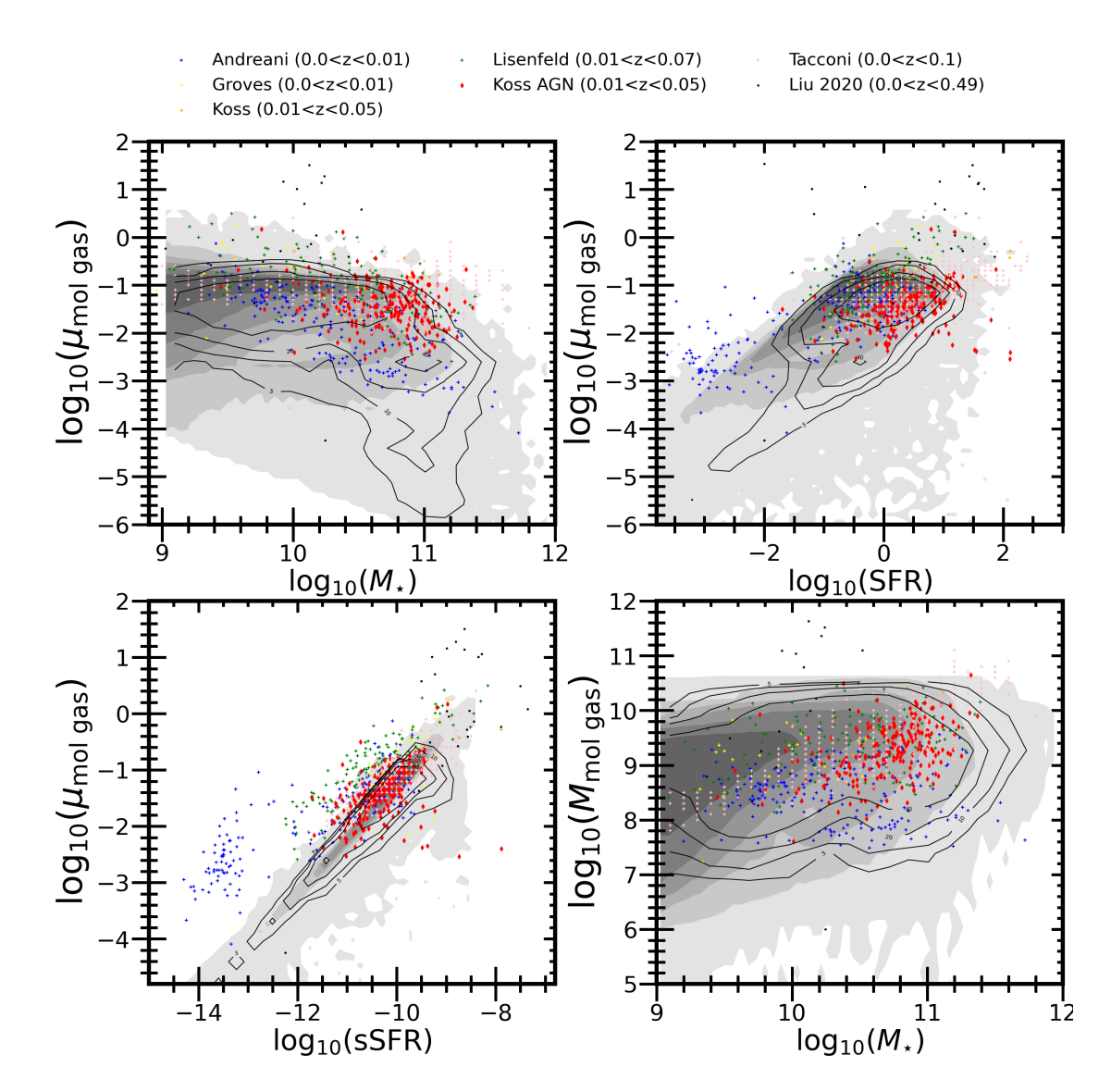


Figure A.1: Molecular gas fraction of galaxies (grey area) with a stellar mass above $10^9~{\rm M}_{\odot}$ and AGN (contours) with luminosities above $L_{\rm bol} \sim 10^{42}~{\rm erg/s}$ at redshift z=0. Points correspond to Andreani et al. [2018], Groves et al. [2015], Lisenfeld et al. [2017], Koss et al. [2021] (AGN samples), Tacconi et al. [2018] and Liu et al. [2021]. Contours define the 5%, 10%, 20% and 40% of the total AGN distribution.

on only \sim 6.4% of the total simulation volume, corresponding to \sim 33.8 Mpc³. However, the largest halo at each redshift is contained within the selected cosmological box, making this \sim 6.4% sufficient to capture general trends, fractions, and galaxy behavior, despite the statistical limitations. These limitations are expected to have a more pronounced impact on the results at higher redshifts, although strong conclusions can still be reached.

Figure A.1 presents an analysis of molecular gas properties at redshift z=0. I calculate the molecular gas fraction as $\mu=M_{H_2}/M_{\star}$, being M_{H_2} the molecular gas and M_{\star} the stellar mass. The grey-shaded region represents the galaxy density, while the black contours correspond to galaxies hosting an AGN, defined as those with $\log(L_{\rm bol}/{\rm erg/s}) >$

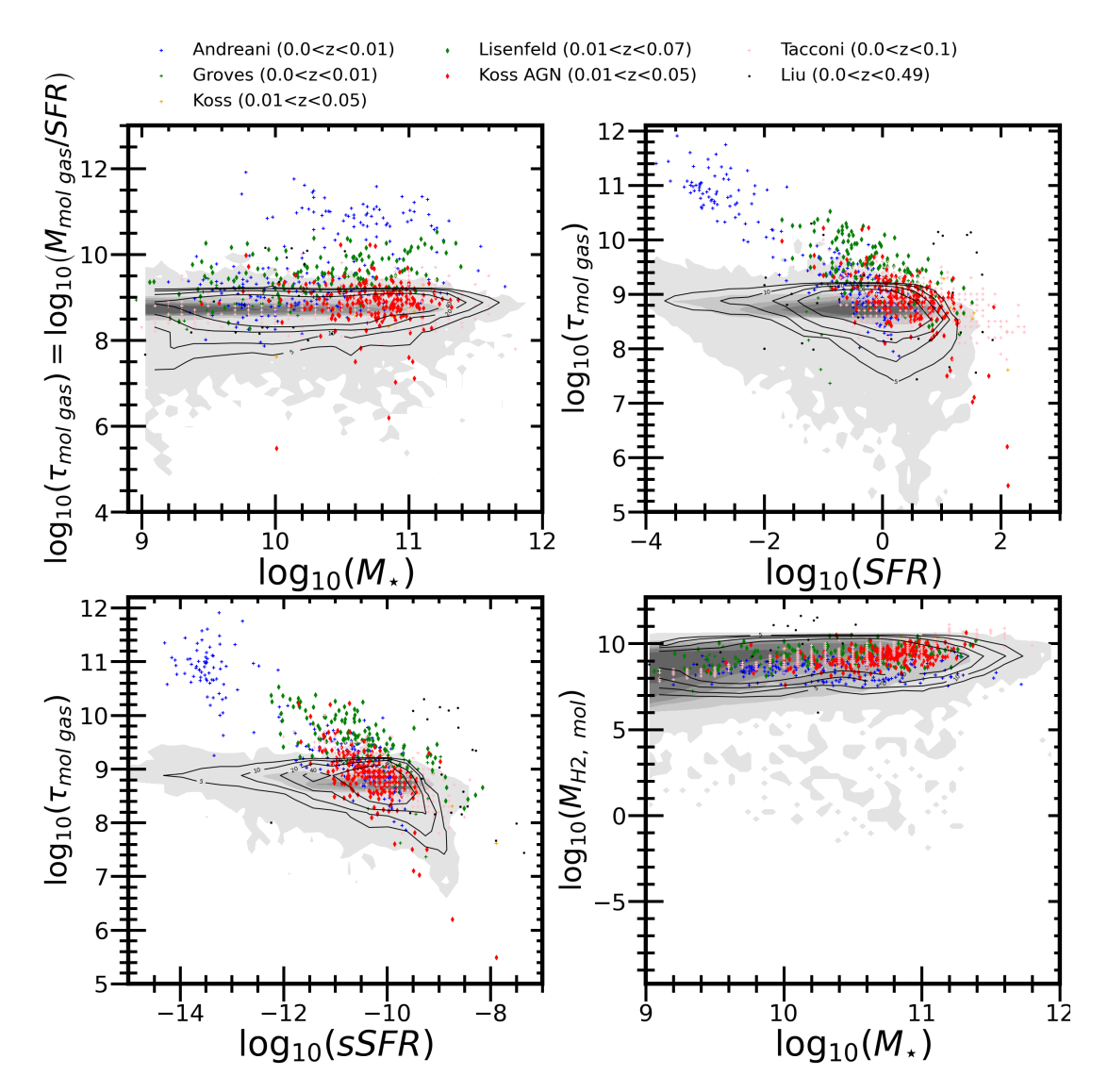


Figure A.2: Depletion time of galaxies (grey area) with a stellar mass above $10^9~{\rm M}_{\odot}$ and AGN (contours) with luminosities above $L_{\rm bol} \sim 10^{42}~{\rm erg/s}$ at redshift z=0. Points correspond to Andreani et al. [2018], Groves et al. [2015], Koss et al. [2021], Lisenfeld et al. [2017], Koss et al. [2021], Tacconi et al. [2018] and Liu et al. [2021]. Contours define the 5%, 10%, 20% and 40% of the total AGN distribution.

42. The colored and differently styled points indicate various AGN observations as labeled, covering redshifts in the range 0.0 < z < 0.49, from Andreani et al. [2018], Groves et al. [2015], Koss et al. [2021], Lisenfeld et al. [2017], Koss et al. [2021], Tacconi et al. [2018] and Liu et al. [2021]. Observed AGN-hosting galaxies fall within the high-density regions of the simulation AGN contours, showing a strong correlation between simulation and observations across multiple panels: molecular gas fraction versus stellar mass, SFR, and specific SFR, as well as the dependence of molecular gas on stellar mass. Observations from Liu et al. [2021] consistently lie on the upper bounds of these relations, likely reflecting redshift evolution since these galaxies are at the higher end of the redshift range. Conversely, the data from Andreani et al. [2018] tend to fall outside the relations probably because the galaxies targeted in their observations have larger

gas mass than the limits of the GAEA catalogue. Overall, most observed galaxies exhibit a pattern consistent with the simulation.

The observational data used comprises a selection of no-AGN galaxies and AGN galaxies, corresponding to the grey areas and the black lines of the figures. The selection of this data has been done to include a wide range of values of key variables (molecular gas mass, stellar mass, SFR, etc) to challenge the limits of the GAEA galaxies. As observed in Figure A.1, GAEA galaxies present a very sharp cut in depletion time (due to the molecular gas limit) and stellar mass, which affects to the comparison with more extreme data such as Andreani et al. [2018], Koss et al. [2021]. Therefore, the comparison with the observational data is mere orientation to show the limitations of the catalogue for future reference, indicating that the simulation used calculates the bulk of the population, even if missing extreme cases.

Similarly, Figure A.2 explores the molecular gas depletion time ($\tau_{\text{mol/gas}}$) and the dependence of molecular hydrogen (H_2) on stellar mass. I calculate the depletion time as $\tau = M_{H_2}/SFR$, being M_{H_2} the molecular gas and SFR the starformation rate. Once again, the observed AGN-hosting galaxies align well with the high-density regions of the simulation's AGN contours, showing strong correlation between the simulation and observations across multiple panels: depletion time versus stellar mass, SFR, and sSFR, as well as the dependence on stellar mass. As with the molecular gas properties, Liu et al. [2021] observations consistently occupy the upper bounds of these relations, reflecting their higher redshift galaxies, while the data from Andreani et al. [2018] tend to be outside of the galaxy distribution. Overall, the majority of observed galaxies exhibit behaviour consistent with the simulation.

Figure A.3 illustrates the distribution of stellar mass and SFR relative to the fraction of atomic and molecular gas. The comparison between AGN and non-AGN galaxies reveals that AGN galaxies (in contours) tend to have a higher stellar mass compared to their non-AGN counterparts (grey area). Additionally, AGN galaxies exhibit a higher fraction of atomic and molecular gas at lower SFR values. This suggests that AGN galaxies not only have more substantial stellar masses but also retain a greater proportion of their gas content even when their SFRs are lower. Similarly to the previous figures, the observational data is shown as a reference of the bulk of the population and the grey area nor the lines have been selected to match the selection of the observational data.

To fully confirm the results, it would be necessary to analyse the entire volume of the cosmological simulation box. Note that the galaxies present in the Andreani et al. [2018] sample do not follow the simulated galaxies distribution, but this is not related to missing volume. Further exploration of the simulation and the observations is needed to

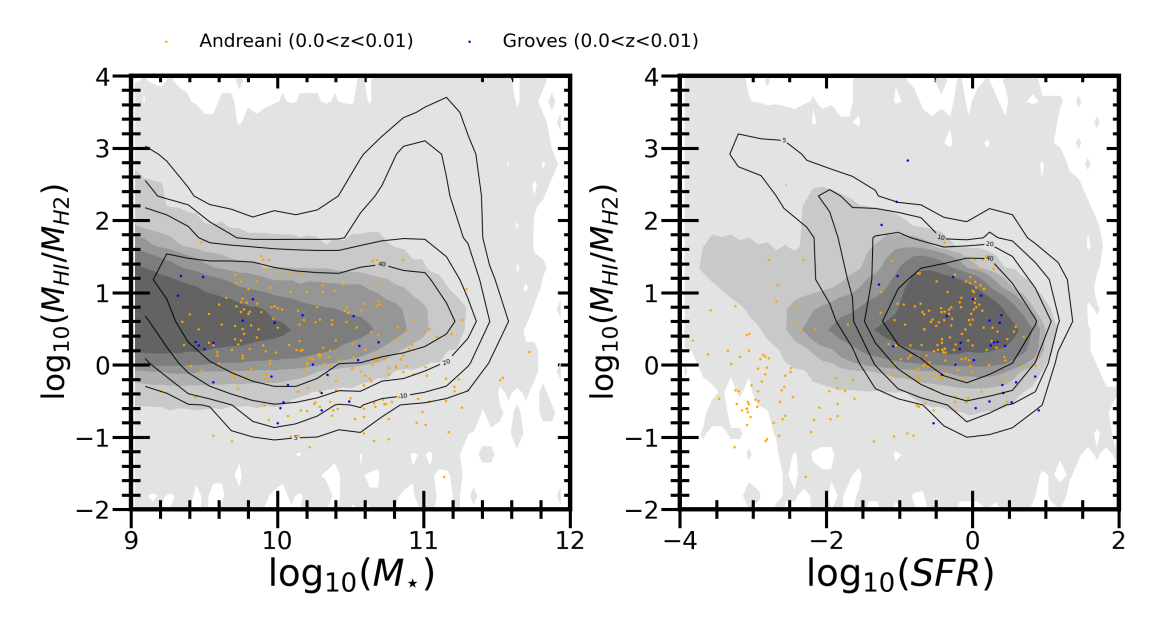


FIGURE A.3: Molecular and atomic gas fraction of galaxies (grey area) with a stellar mass above $10^9~{\rm M}_{\odot}$ and AGN (contours) with luminosities above $L_{\rm bol} \sim 10^{42}~{\rm erg/s}$ at redshift z=0. Points correspond to Andreani et al. [2018], Groves et al. [2015]. Contours define the 5%, 10%, 20% and 40% of the total AGN distribution.

understand the difference of behaviour, but this is a project out of the scope of this thesis, since the aim of this Appendix is simply to demonstrate that the simulation generally works and that follows general trends. Examining the complete sample could also reveal new characteristics of the galaxy population and additional differences between the general galaxy population and the AGN-hosting subsample. This investigation will be addressed in future work.

A similar study can be done at all available redshifts of the simulation. In Figure A.4 I show the molecular gas properties at redshift z=2.42, with galaxies in a grey, shaded region and AGN in black contours. The simulated galaxies present lower stellar masses and lower SFR with respect of the data of Tacconi et al. [2018], Kaasinen et al. [2019], Liu et al. [2021] than at redshift z=0.0, although the sSFR is consistent with observations. They also present lower molecular gas mass, but the molecular gas fraction is of the same order. AGN galaxies present a similar distribution than the total galaxy distribution, since the black lines (AGN galaxies) roughly follow the same pattern as the grey area (no-AGN galaxies).

In Figure A.5 I also find the depletion time to be of the same order of magnitude of the observations, both in stellar mass and SFR. However, the H_2 gas is lower than the data for both all galaxies and AGN galaxies.

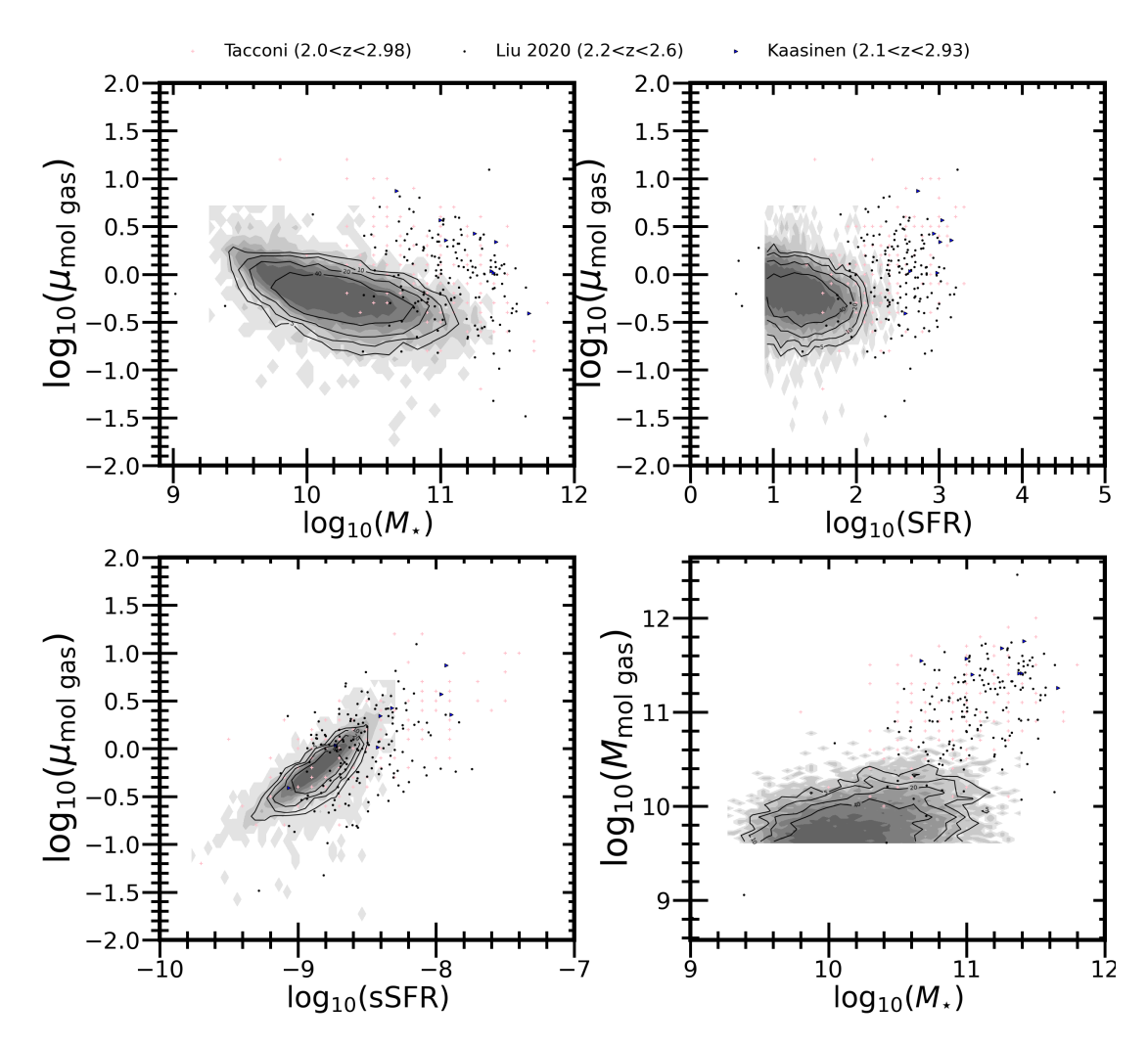


FIGURE A.4: Molecular gas fraction of galaxies (grey area) with a stellar mass above $10^9~{\rm M}_{\odot}$ and AGN (contours) with luminosities above $L_{\rm bol} \sim 10^{42}~{\rm erg/s}$ at redshift z=2.42. Points correspond to Tacconi et al. [2018], Kaasinen et al. [2019] and Liu et al. [2021]. Contours define the 5%, 10%, 20% and 40% of the total AGN distribution.

A.3 Redshift evolution of the molecular gas fraction and depletion time

Figure A.6 illustrates the distributions of molecular gas fraction $(M_{cold}/(M_{cold}+M_{\star}))$, SFR, and stellar mass for AGN and non-AGN galaxies with $M_{\star} \sim 10^{10-11}~\rm M_{\odot}$ as a function of redshift. Observational data from Groves et al. [2015], Kakkad et al. [2017], Andreani et al. [2018], Tacconi et al. [2018], Kaasinen et al. [2019], Koss et al. [2021], Suzuki et al. [2021], Liu et al. [2021] are represented by red, green, orange, and black dots, while data from the GAEA-merged simulation are shown in blue. The blue dots appear stacked due to their selection from a specific redshift bin. The blue and yellow lines denote selection limits: the blue line corresponds to $\log M_{\rm mol} = 10 + \log z$, and the yellow line to $\log M_{\rm mol} = 9.4 + 2\log z$ in the left panel. In the middle panel, the blue

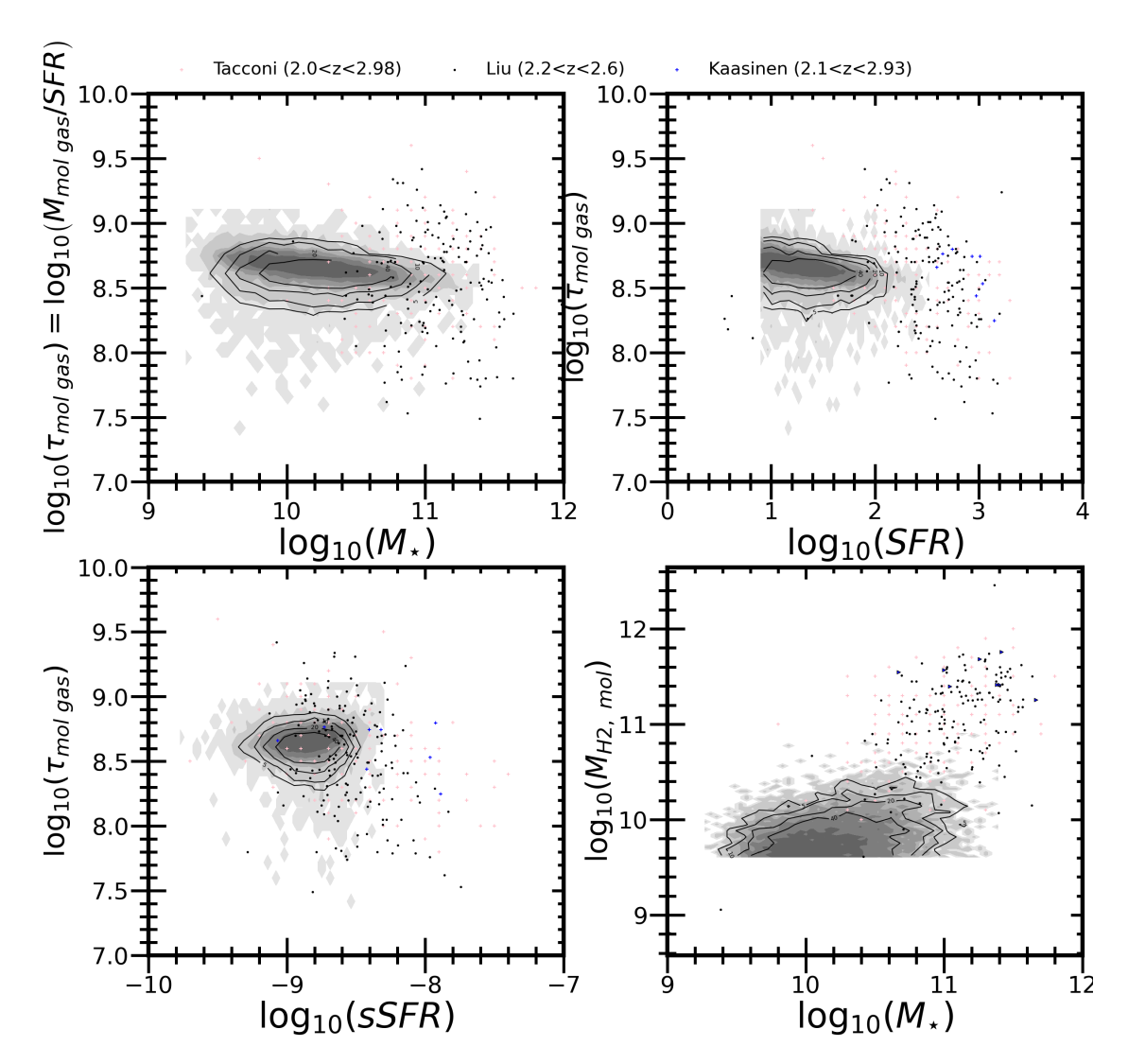


Figure A.5: Depletion time of galaxies (grey area) with a stellar mass above $10^9~M_{\odot}$ and AGN (contours) with luminosities above $L_{bol} \sim 10^{42}~erg/s$ at redshift z=2.42. Points correspond to Tacconi et al. [2018], Kaasinen et al. [2019] and Liu et al. [2021]. Contours define the 5%, 10%, 20% and 40% of the total AGN distribution.

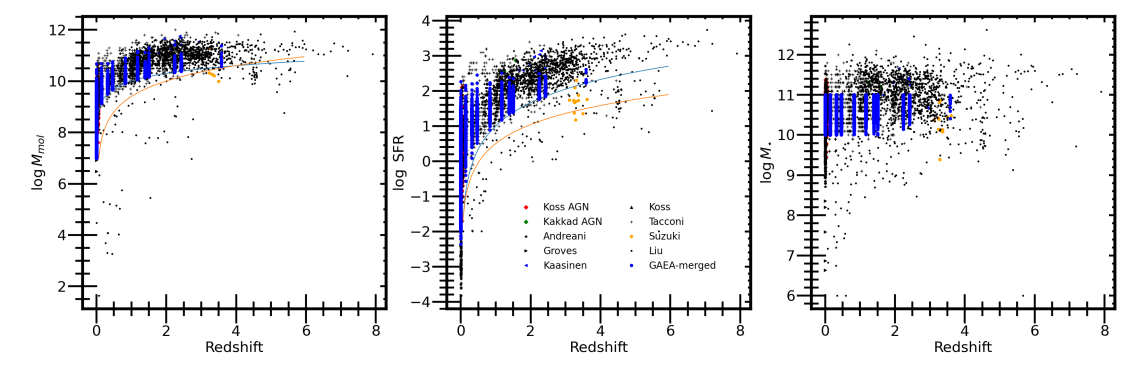


FIGURE A.6: Molecular gas, SFR and stellar mass distributions of GAEA-merged galaxies over redshift for a stellar mass selection of $M_{\star} \sim 10^{10-11}~\rm M_{\odot}$. Observational points correspond to Groves et al. [2015], Kakkad et al. [2017], Andreani et al. [2018], Tacconi et al. [2018], Kaasinen et al. [2019], Koss et al. [2021], Suzuki et al. [2021], Liu et al. [2021].

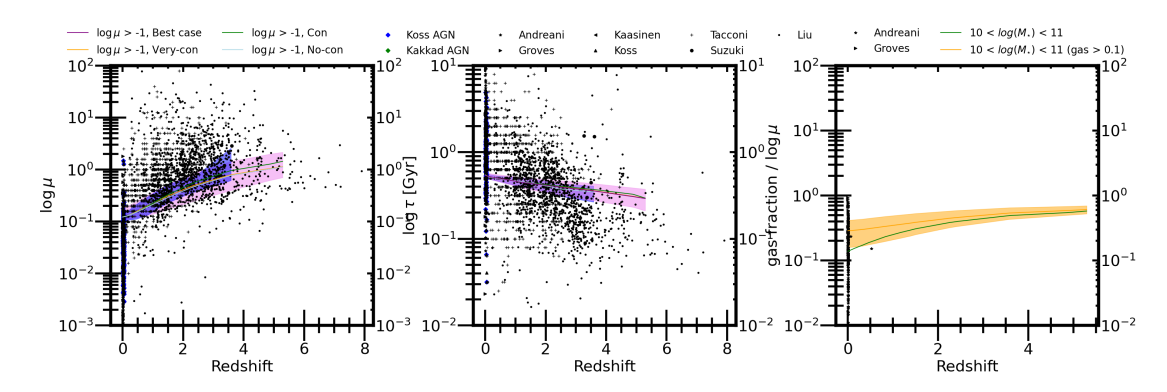


FIGURE A.7: Molecular gas fraction, depletion time and gas fraction evolution on redshift of GAEA-merged galaxies for a stellar mass selection of $M_{\star} \sim 10^{10-11} \ \mathrm{M}_{\odot}$. Observational points correspond to Groves et al. [2015], Kakkad et al. [2017], Andreani et al. [2018], Tacconi et al. [2018], Kaasinen et al. [2019], Koss et al. [2021], Suzuki et al. [2021], Liu et al. [2021].

line follows $\log SFR = 1 + 2.2 \log z$, and the yellow line $\log SFR = 0.5 + 1.8 \log z$. These lines serve as visual aids. The distributions of molecular gas, SFR, and stellar mass for the galaxies align with observational trends.

Figure A.7 presents the molecular fraction, depletion time, and gas fraction as a function of redshift. Observational data from Groves et al. [2015], Kakkad et al. [2017], Andreani et al. [2018], Tacconi et al. [2018], Kaasinen et al. [2019], Koss et al. [2021], Suzuki et al. [2021], Liu et al. [2021] are included. In the left and middle panels, galaxies from the GAEA-merged simulation with $M_{\star} \sim 10^{10-11}\,\mathrm{M}_{\odot}$ are plotted with various filters: best case, conservative cut, very conservative cut, and no-conservative cut. The no-conservative cut includes galaxies above $\log M_{\rm mol} = 10 + \log z$ and $\log SFR =$ $1 + 2.2 \log z$, similar to the blue line in Figure A.6. The conservative cut includes galaxies above $\log M_{\rm mol} = 9.4 + 2 \log z$ and $\log SFR = 0.5 + 1.8 \log z$, similar to the yellow line in Figure A.6. The very conservative cut includes galaxies with $\log SFR > -4$ and $\log M_{\rm mol} > 7$, while the best case considers only the stellar mass selection. In the left panel, the conservative cut provides the best match to the observed distribution, indicated by the purple area. Similar results are found in the middle panel for depletion time, with no clear preferred cut. The right panel shows gas fraction trends, with limited data available above $z \sim 0$. The difference between the green and yellow lines reflects the selection of galaxies with positive gas mass, as labelled. Note that the observational data just show the trends of the general overall galaxy population and we are not making, in general, a selection in the GAEA galaxy catalogue to match the observational data. Therefore, the comparison is only meaningful in terms of general distribution and to confirm if the simulation is producing galaxies within the observational limits and to show what are the limits of the simulation.

A.4 Discussion and conclusions

These preliminary tests of the updated GAEA-merger code provide valuable insights into the implementation of the new gas prescription. While the results generally align with observations from the local universe, there remain areas for improvement. For instance, certain galaxies observed in the real universe [e.g., Andreani et al., 2018], such as highly star-forming galaxies or those with exceptionally high gas masses, are not reproduced in the simulation. Additionally, the simulated galaxy distribution underestimates the observed distribution at higher redshifts.

Despite these limitations, the relative distribution of galaxies and AGN-host galaxies at redshift z=0 remains consistent with observational data, although the simulation does not produce extreme galaxies (e.g., high molecular gas mass). Given that the AGN modelling has not been altered from the previous version of the code, similar results are expected for AGN-related properties.

In future work, this simulation will help to separate the effects of molecular and cold gas mass, which were previously studied together in GAEA due to limitations in distinguishing between them.

Appendix B

Studying the roles of density profiles and gas distribution in shaping the obscuration of hydrosimulated Active Galactic Nuclei though cosmic time

For completeness, in this thesis I also provide an in-depth study of some high-resolution hydrodynamical simulations of zoom-in disc galaxies comprising AGN feedback. My goal is to study the type and amount of $N_{\rm H}$ column densities generated by a selfconsistent numerical models in a realistic cosmological context to compare with the analytic Orientation and Evolutionary models discussed previously. For this work, I choose to focus on the simulations developed by Valentini et al. [2020]. By comparing the density profile derived from high-resolution hydrodynamical simulations with those inferred from SAMs, I want to test the reliability of using simplified density profiles in broader cosmological studies. My findings will contribute to the understanding of whether an uniform approach to modelling gas density in galaxies can be adopted, or if a more detailed, simulation-specific information is necessary to accurately represent the gas distribution and its observational consequences. This paper investigates the role of AGN feedback in the formation and evolution of galaxies, particularly latetype galaxies. AGN activity is crucial for regulating star formation and gas cooling processes in galaxies. More specially, Valentini et al. [2020] in their simulations aim to address the following still open questions:

 How do accreting black holes transfer feedback energy to the surrounding multiphase ISM?

- How does AGN feedback influence the properties of the host galaxy?
- How do different models and regimes of gas accretion affect the coevolution of black holes and their host galaxies?
- Does AGN feedback significantly impact the circulation of heavy elements within the galaxy?

To explore these questions, Valentini et al. [2020] employ the MUPPI [MUlti Phase Particle Integrator Valentini et al., 2017] sub-resolution model in their cosmological simulations. MUPPI describes a multiphase ISM and solves equations for mass and energy flows within different phases during the simulation time-step, enabling a detailed modeling of AGN feedback effects.

In general, they find that all simulated galaxies have dominant, extended discs with a limited bulge component, however the gaseous discs are generally more extended than the stellar ones. Most galaxies exhibit a well-defined spiral pattern in their discs, and galaxies simulated with AGN feedback show more extended stellar and gaseous discs compared to those without AGN feedback. However, their morphologies are generally more disturbed, especially in the outer regions. The properties and evolution of the central black holes significantly influence the host galaxy evolution, with AGN feedback playing a critical role in shaping the observed features of the galaxies. Overall, their results indicate that AGN feedback has a significant impact on the structure and morphology of galaxies, driving both the expansion of discs and the disturbance of outer regions, while also regulating gas accretion and outflows.

B.1 Fiducial galaxy

Particularly, at z=0, our fiducial galaxy presents less extended stellar and gas discs than the simulated galaxy with no AGN feedback, indicating that the AGN feedback contributes to the expansion of these components. They define the galactic radius as $R_{\rm gal}=0.1R_{\rm vi}$, chosen to select the region of the computational domain where the central galaxy resides. This radius is used for both gas and stellar particles, and for the fiducial galaxy the galactic radius is $R_{\rm gal}=24.15$ kpc.

Also, this galaxy shows a more disturbed morphology, particularly in the outer regions, attributed to the highly dynamic environment and ongoing AGN feedback. It also presents gas above and around the galactic plane, suggesting ongoing gas accretion. Finally, the mean values for the coupling factors for the hot and cold phases (C_h and C_c) indicate a balanced distribution of AGN feedback energy between the hot and cold gas phases [Valentini et al., 2020].

B.2 HI column density in hydrodynamic simulated galaxies

I want to study the obscuration of this galaxy making use of the cold gas particles of the galaxy. For this reason, the best way to study the obscuration is to calculate the HI column density along different lines-of-sight. To do so in a simulated galaxy, I can employ two complementary approaches that use the positional and mass data of individual HI gas particles: the particle number density method and the bin density method.

In the particle number density method, I start by preparing the input data, which includes the positions (x_i, y_i, z_i) and masses m_i of the gas particles, as well as the particle mass resolution m_p . I am interested in the most extreme lines-of-sight, such as the z-axis, the plane perpendicular to the disc, or the xy-plane, the plane parallel to the disc. Assuming the line-of-sight is along the z-axis, I project the positions of the gas particles onto the xy-plane, resulting in projected coordinates (x_i, y_i) .

Next, I bin the particles within each grid cell based on their projected x and y coordinates, identifying all particles that lie within each cell. For each bin, I calculate the number density n_i of each particle using the formula:

$$n_i = f_H \frac{m_i}{m_p \cdot V_p} \tag{B.1}$$

where m_i is the mass of the gas particle, m_p is the mass of a single hydrogen atom $(m_p = 1.67 \times 10^{-24} \, \mathrm{g})$, and V_p is the volume occupied by the particle. I also need to take into account the relation between cold gas and HI particles, which usually would be $f_H = 0.76$ [e.g., Popping et al., 2014]. But to properly compare with previous chapters, where I assume that the $M_{\rm gas}$ consists of 100% hydrogen (see Section 4.2), I use $f_H = 1$. The contributions from all particles within each column (bin) are summed to determine the HI column density $N_{\rm H}$ for that bin. The column density for a cell centered at (x,y) is given by:

$$N_{\rm H}(x,y) = \sum_{i \in \rm bin} n_i \cdot dz \tag{B.2}$$

where dz is the thickness of the slice along the z-axis that each particle represents. I am going to use this method for my results since I already have all the information regarding the particle mass. A similar approach is followed if instead of the z-axis, I assign another line-of-sight. The variable dz will be then dependant of the angle with the axis perpendicular to the galactic disc and x and y coordinates.

In the bin density method, the same input data is used. I define a grid over the region of interest and project the positions of the HI particles onto the *xy*-plane. For each grid

cell, I identify all particles within the column along the *z*-axis. Instead of calculating the number density directly, I sum the contributions of particle masses within each cell. The HI column density $N_{\rm H}$ in a cell centered at (x,y) is given by:

$$N_{\rm H}(x,y) = \sum_{i} \frac{m_i}{m_p \cdot A_{\rm cell}}$$
 (B.3)

where the summation is over all particles within the column through the grid cell, and A_{cell} is the area of the grid cell.

Both methods aim to provide an accurate calculation of the HI column density, but they emphasize different aspects of the particle distribution. The particle number density method explicitly accounts for the volume each particle occupies, providing a detailed representation of the local density variations within each bin. The bin density method, on the other hand, focuses on the total mass of HI particles within each grid cell, summing these contributions to obtain the column density.

The particle number density method is particularly useful when the spatial distribution and local density variations are critical, as it uses the number density and particle volume directly in the calculation. This is the reason why I chose this approach for my results, since the density variations are of special interest for these galaxies in the study of AGN feedback. The bin density method is more straightforward in scenarios where the total mass of particles within a column is of primary interest.

These methodologies align with established techniques and provide a robust framework for studying simulated galaxy data, as demonstrated by Monaghan [1992], Navarro et al. [1996], Springel [2005], and provide a comprehensive and precise approach to calculating the HI column density from a simulated galaxy, facilitating detailed analysis of the HI distribution and its implications for galaxy structure and evolution.

B.2.1 HI column density calculation

Figure B.1 illustrates the spatial distribution of cold gas particles in the galaxy at redshift z=0.0. The left panel presents the projection in the xy plane, while the right panel showcases the distribution in the xz plane. Overlaid in a contrasting color are the particles selected from a cylindrical region with a radius of 0.002 Mpc and a height of 0.2 Mpc for the calculation of the HI column density at the disc plane. This specific cylinder height was chosen to ensure the inclusion of all relevant particles within the observational volume. The column density of the cylinder corresponds with the column density of the plane of the disc, or $\alpha=90^\circ$ if α is the angle against the vertical axis z (line-of-sight), and it has a value of $N_{\rm H}=1.14\cdot 10^{22}$ cm⁻². However, if I calculate the cylinder in the vertical axis z, the equivalent of a $\alpha=0^\circ$, I have $N_{\rm H}=4.50\cdot 10^{22}$

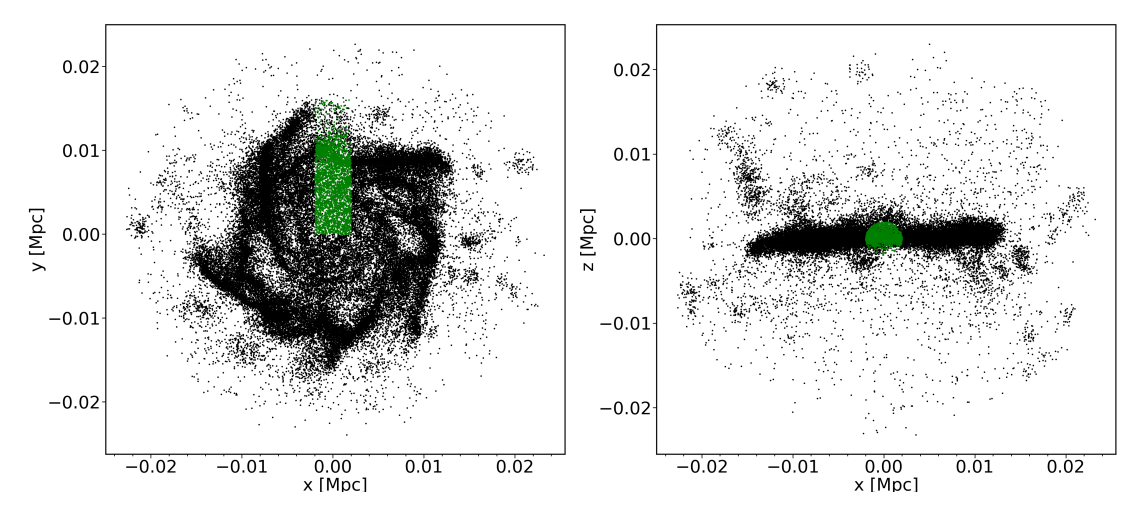


FIGURE B.1: Spatial distribution of cold gas particles (black) in the galaxy at redshift z=0.0. The left panel displays the projection in the xy plane, while the right panel shows the xz plane. In green are the particles selected from a cylindrical region defined by a radius of 0.002 Mpc and a height of 0.2 Mpc.

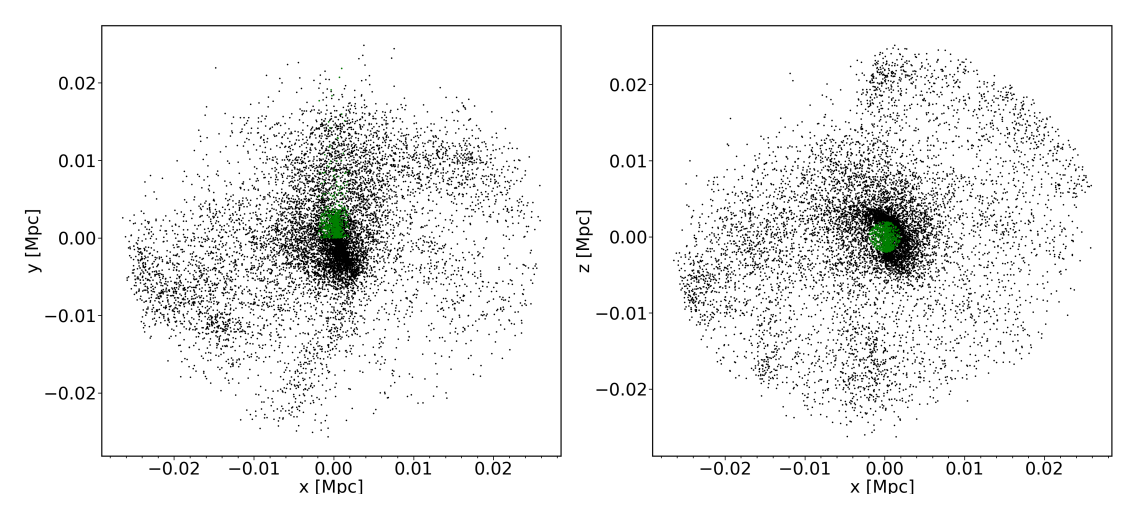


FIGURE B.2: Spatial distribution of cold gas particles (black) in the galaxy at redshift z=2.39. The left panel displays the projection in the xy plane, while the right panel shows the xz plane. In green are the particles selected from a cylindrical region defined by a radius of 0.002 Mpc and a height of 0.2 Mpc.

cm⁻². According to the obscuration definition used in this thesis, the fiducial galaxy is a Compton-thin (CTN) galaxy ($10^{22} < N_{\rm H}/{\rm cm}^{-2} < 10^{24}$).

In a similar fashion, I can study the column density of the galaxy at a higher redshift. Figure B.2 illustrates the spatial distribution of cold gas particles in the galaxy at redshift z=2.39. The left panel presents the projection in the xy plane, while the right panel showcases the distribution in the xz plane. Again, a contrasting colour mark the selected particles from a cylindrical region with a radius of 0.002 Mpc and a height of 0.2 Mpc. The column density of the cylinder corresponds with the column density of the plane of the disc, or $\alpha=90^\circ$ if α is the angle against the vertical axis z, and it has a value of $N_{\rm H}=8.49\cdot 10^{18}$ cm⁻². However, if I calculate the cylinder in the vertical axis z,

TABLE B.1: Basic variables of the Fiducial galaxy from Valentini et al. [2020] calculated in this Appendix. The differences between the paper and this Table come from the definition of the constant $h_{100}=0.73$, which has been selected to follow Fontanot et al. [2020] and I decide to keep it consistent within the thesis.

Redshift	z=0	z = 2.39	Method
R _{gas}	24.15 kpc	26.82 kpc	Furthest particle
R_{\star}	17.63 kpc	19.58 kpc	Furthest particle
$\log_{10} M_{\star}$	$11.45~\mathrm{M}_\odot$	$10.87~\mathrm{M}_\odot$	Sum of particles within the box
$\log_{10} M_{\rm gas}$	$10.14~{ m M}_{\odot}$	$9.57~\mathrm{M}_\odot$	Sum of particles within the box
$N_{\rm H}^{\rm sim}(\alpha=90^\circ)$	$1.14 \cdot 10^{22} \text{ cm}^{-2}$	$8.49 \cdot 10^{18} \text{ cm}^{-2}$	Number density
$N_{\rm H}^{\rm sim}(\alpha=0^{\circ})$	$4.50 \cdot 10^{22} \text{ cm}^{-2}$	$1.40 \cdot 10^{21} \text{ cm}^{-2}$	Number density

the equivalent of a $\alpha=0^\circ$, I have $N_{\rm H}=1.40\cdot 10^{21}~{\rm cm}^{-2}$. According to the obscuration definition used in this thesis, the fiducial galaxy is optically/UV visible. These results, as well as the particle distribution, point out that the galaxy, ending as a spiral galaxy at z=0, presents irregular characteristics at $z\sim 2.4$, with a notably low ISM column density.

The results about the fiducial galaxy have been summarised in Table B.1¹. It is interesting to notice that when using the number density, I find a decrease of obscuration with redshift, mostly due to the clearly less number of gas particles within any line of sight due to the irregular nature of the galaxy structure.

According to the literature [e.g., D'Amato et al., 2020], the ISM column density of high redshift galaxies can substantially contribute to the obscuration to the point of reaching CTK obscuration, or at least CTN levels [see also Gilli et al., 2022]. Therefore, such a low column density, as we find in the fiducial galaxy at z = 2.39, is remarkable. Since the stellar mass, the cold gas mass and the exponential density profile methodology have been proven to follow observations and produce high column densities, the discrepancy from the literature seems to come from the scale length and the definition of the radius. The radius of the fiducial galaxy, calculated by measuring the distance between the furthest particle and the centre of the galaxy, is large, even larger than the value at z = 0. However, as previously observed [e.g., van der Wel et al., 2014, Puglisi et al., 2019, 2021], particularly the gas radius of a galaxy decreases with increasing redshift. The stellar scale length for this galaxy at redshift z=0 is $R_{\rm d}\sim 6.4$ kpc, which corresponds with the predicted $R_{\rm d}\sim 6.3$ kpc if using van der Wel et al. [2014]. But at redshift z=2.39, I find $R_{\rm d}\sim4.2$ kpc using the furthest particle, and $R_{\rm d}\sim2.1$ kpc using van der Wel et al. [2014]. The difference in the results at high redshift indicates that the value of the furthest particle might be overestimated, and the discussion develops to what constitutes the border of a galaxy. A quick look to Figure B.2 confirms the lack of a defined structure, making the irregularity of the galaxy a problem for the actual

¹Despite certain data from the Table being available in Valentini et al. [2020], I decided to recalculate some of them to be consistent within the Chapter. This is possible thanks to the availability of the galaxy box supplied by Milena Valentini.

definition of its radius. Therefore, the next step of this analysis should follow the study of the superficial density profile and the use of an improved definition of the galaxy radius, which is out of the scope of this thesis. The analysis would also benefit from using other galaxies, for example the rest of the galaxies from Valentini et al. [2020].

Appendix C

Industrial secondment in OLT

As part of the Marie Curie Innovative Training Network (ITN) program, I completed an industrial secondment at the company OmegaLambdaTec (OLT) GmbH (Garching, Bayern, Germany) as a Data Scientist. They aim to create pioneering smart data solutions for the key challenges of the energy transition by using Smart Data, Physical Analytics and AI solutions in the areas of data-driven forecasting, anomaly detection, simulation-based optimisation and digital twin simulations¹.

During this secondment, the objective of my work was to study the trajectory, total travelled time, and time spent on ports of commercial ships to find common trajectories and best-case scenarios to predict possible delays and trajectory forecast. All ships have a transceiver on bord for automatic tracking of the position and characteristics of the ship called AIS or automatic identification system. This tracking system is used by vessel traffic services (VTS), which, together with marine radar, helps tracking direction, origin, destination, position and other basic variables, as well as useful for collision avoidance. With this information I can study basic water transport routs and port behaviour, allowing me to later predict best trajectories and estimate time of arrival (ETA) for cargo ships transporting goods from Asia to European ports.

My main responsibilities during this secondment were:

- · Becoming familiar with the AIS dataset;
- Performing data cleaning and developing a structured database;
- Identifying ships that followed specific itineraries of interest;
- Analyzing ship trajectories, including ports of loading, intermediate stops, departure and arrival times;

- Predicting best trajectories and ETA;
- Extracting useful insights from the data to support accurate ETA predictions.

References

- J. Afonso, A. Hopkins, B. Mobasher, and C. Almeida. Dependence of Dust Obscuration on Star Formation Rates in Galaxies. , 597(1):269–273, November 2003. .
- J. Aird, A. L. Coil, A. Georgakakis, K. Nandra, G. Barro, and P. G. Pérez-González. The evolution of the X-ray luminosity functions of unabsorbed and absorbed AGNs out to $z\sim5$., 451(2):1892-1927, August 2015.
- J. Aird, A. L. Coil, and A. Georgakakis. X-rays across the galaxy population II. The distribution of AGN accretion rates as a function of stellar mass and redshift. , 474: 1225–1249, January 2018. .
- Hollis B. Akins, Caitlin M. Casey, Natalie Allen, Micaela B. Bagley, Mark Dickinson, Steven L. Finkelstein, Maximilien Franco, Santosh Harish, Pablo Arrabal Haro, Olivier Ilbert, Jeyhan S. Kartaltepe, Anton M. Koekemoer, Daizhong Liu, Arianna S. Long, Henry Joy McCracken, Louise Paquereau, Casey Papovich, Nor Pirzkal, Jason Rhodes, Brant E. Robertson, Marko Shuntov, Sune Toft, Guang Yang, Guillermo Barro, Laura Bisigello, Véronique Buat, Jaclyn B. Champagne, Olivia Cooper, Luca Costantin, Alexander de La Vega, Nicole E. Drakos, Andreas Faisst, Adriano Fontana, Seiji Fujimoto, Steven Gillman, Carlos Gómez-Guijarro, Ghassem Gozaliasl, Nimish P. Hathi, Christopher C. Hayward, Michaela Hirschmann, Benne W. Holwerda, Shuowen Jin, Dale D. Kocevski, Vasily Kokorev, Erini Lambrides, Ray A. Lucas, Georgios E. Magdis, Benjamin Magnelli, Jed McKinney, Bahram Mobasher, Pablo G. Pérez-González, R. Michael Rich, Lise-Marie Seillé, Margherita Talia, C. Megan Urry, Francesco Valentino, Katherine E. Whitaker, L. Y. Aaron Yung, Jorge Zavala, Cosmos-Web Team, and Ceers Team. Two Massive, Compact, and Dust-obscured Candidate z 8 Galaxies Discovered by JWST., 956(1):61, October 2023.
- Hollis B. Akins, Caitlin M. Casey, Erini Lambrides, Natalie Allen, Irham T. Andika, Malte Brinch, Jaclyn B. Champagne, Olivia Cooper, Xuheng Ding, Nicole E. Drakos, Andreas Faisst, Steven L. Finkelstein, Maximilien Franco, Seiji Fujimoto, Fabrizio Gentile, Steven Gillman, Ghassem Gozaliasl, Santosh Harish, Christopher C. Hayward, Michaela Hirschmann, Olivier Ilbert, Jeyhan S. Kartaltepe, Dale D. Kocevski, Anton M. Koekemoer, Vasily Kokorev, Daizhong Liu, Arianna S. Long, Henry Joy McCracken, Jed McKinney, Masafusa Onoue, Louise Paquereau, Alvio

Renzini, Jason Rhodes, Brant E. Robertson, Marko Shuntov, John D. Silverman, Takumi S. Tanaka, Sune Toft, Benny Trakhtenbrot, Francesco Valentino, and Jorge Zavala. COSMOS-Web: The over-abundance and physical nature of "little red dots"–Implications for early galaxy and SMBH assembly. *arXiv e-prints*, art. arXiv:2406.10341, June 2024.

- Masayuki Akiyama, Kouji Ohta, Toru Yamada, Nobunari Kashikawa, Masafumi Yagi, Wataru Kawasaki, Masaaki Sakano, Takeshi Tsuru, Yoshihiro Ueda, Tadayuki Takahashi, Ingo Lehmann, Günther Hasinger, and Wolfgang Voges. Optical Identification of the ASCA Large Sky Survey. , 532(2):700–727, April 2000.
- Masayuki Akiyama, Yoshihiro Ueda, Kouji Ohta, Tadayuki Takahashi, and Toru Yamada. Optical Identification of the ASCA Medium Sensitivity Survey in the Northern Sky: Nature of Hard X-Ray-Selected Luminous Active Galactic Nuclei. , 148(2): 275–315, October 2003. .
- Masayuki Akiyama, Yoshihiro Ueda, Mike G. Watson, Hisanori Furusawa, Tadafumi Takata, Chris Simpson, Tomoki Morokuma, Toru Yamada, Kouji Ohta, Fumihide Iwamuro, Kiyoto Yabe, Naoyuki Tamura, Yuuki Moritani, Naruhisa Takato, Masahiko Kimura, Toshinori Maihara, Gavin Dalton, Ian Lewis, Hanshin Lee, Emma Curtis-Lake, Edward Macaulay, Frazer Clarke, John D. Silverman, Scott Croom, Masami Ouchi, Hitoshi Hanami, Jorge Díaz Tello, Tomohiro Yoshikawa, Naofumi Fujishiro, and Kazuhiro Sekiguchi. The Subaru-XMM-Newton Deep Survey (SXDS). VIII. Multi-wavelength identification, optical/NIR spectroscopic properties, and photometric redshifts of X-ray sources. , 67(5):82, October 2015.
- A. Akylas, A. Georgakakis, I. Georgantopoulos, M. Brightman, and K. Nandra. Constraining the fraction of Compton-thick AGN in the Universe by modelling the diffuse X-ray background spectrum. , 546:A98, October 2012. .
- D. M. Alexander and R. C. Hickox. What drives the growth of black holes? , 56(4): 93–121, June 2012. .
- D. M. Alexander, F. E. Bauer, S. C. Chapman, I. Smail, A. W. Blain, W. N. Brandt, and R. J. Ivison. The X-Ray Spectral Properties of SCUBA Galaxies. , 632(2):736–750, October 2005. .
- D. M. Alexander, J. M. Simpson, C. M. Harrison, J. R. Mullaney, I. Smail, J. E. Geach, R. C. Hickox, N. K. Hine, A. Karim, M. Kubo, B. D. Lehmer, Y. Matsuda, D. J. Rosario, F. Stanley, A. M. Swinbank, H. Umehata, and T. Yamada. ALMA observations of a z ≈ 3.1 protocluster: star formation from active galactic nuclei and Lyman-alpha blobs in an overdense environment. , 461(3):2944–2952, September 2016. .
- V. Allevato, A. Finoguenov, N. Cappelluti, T. Miyaji, G. Hasinger, M. Salvato, M. Brusa, R. Gilli, G. Zamorani, F. Shankar, J. B. James, H. J. McCracken, A. Bongiorno, A. Merloni, J. A. Peacock, J. Silverman, and A. Comastri. The XMM-Newton Wide Field

Survey in the COSMOS Field: Redshift Evolution of AGN Bias and Subdominant Role of Mergers in Triggering Moderate-luminosity AGNs at Redshifts up to 2.2., 736(2):99, August 2011.

- V. Allevato, F. Shankar, C. Marsden, U. Rasulov, A. Viitanen, A. Georgakakis, A. Ferrara, and A. Finoguenov. Building Robust Active Galactic Nuclei Mock Catalogs to Unveil Black Hole Evolution and for Survey Planning., 916(1):34, July 2021.
- Alba V. Alonso-Tetilla, Francesco Shankar, Fabio Fontanot, Nicola Menci, Milena Valentini, Johannes Buchner, Brivael Laloux, Andrea Lapi, Annagrazia Puglisi, David M. Alexander, Viola Allevato, Carolina Andonie, Silvia Bonoli, Michaela Hirschmann, Iván E. López, Sandra I. Raimundo, and Cristina Ramos Almeida. Probing the roles of orientation and multiscale gas distributions in shaping the obscuration of active galactic nuclei through cosmic time. , 527(4):10878–10896, February 2024.
- Tonima Tasnim Ananna, Ezequiel Treister, C. Megan Urry, C. Ricci, Allison Kirkpatrick, Stephanie LaMassa, Johannes Buchner, Francesca Civano, Michael Tremmel, and Stefano Marchesi. The Accretion History of AGNs. I. Supermassive Black Hole Population Synthesis Model., 871(2):240, February 2019.
- Tonima Tasnim Ananna, C. Megan Urry, Claudio Ricci, Priyamvada Natarajan, Ryan C. Hickox, Benny Trakhtenbrot, Ezequiel Treister, Anna K. Weigel, Yoshihiro Ueda, Michael J. Koss, F. E. Bauer, Matthew J. Temple, Mislav Baloković, Richard Mushotzky, Connor Auge, David B. Sanders, Darshan Kakkad, Lia F. Sartori, Stefano Marchesi, Fiona Harrison, Daniel Stern, Kyuseok Oh, Turgay Caglar, Meredith C. Powell, Stephanie A. Podjed, and Julian E. Mejía-Restrepo. Probing the Structure and Evolution of BASS Active Galactic Nuclei through Eddington Ratios. , 939(1): L13, November 2022a. .
- Tonima Tasnim Ananna, Anna K. Weigel, Benny Trakhtenbrot, Michael J. Koss, C. Megan Urry, Claudio Ricci, Ryan C. Hickox, Ezequiel Treister, Franz E. Bauer, Yoshihiro Ueda, Richard Mushotzky, Federica Ricci, Kyuseok Oh, Julian E. Mejía-Restrepo, Jakob Den Brok, Daniel Stern, Meredith C. Powell, Turgay Caglar, Kohei Ichikawa, O. Ivy Wong, Fiona A. Harrison, and Kevin Schawinski. BASS. XXX. Distribution Functions of DR2 Eddington Ratios, Black Hole Masses, and X-Ray Luminosities. , 261(1):9, July 2022b.
- Carolina Andonie, David M. Alexander, Claire Greenwell, Annagrazia Puglisi, Brivael Laloux, Alba V. Alonso-Tetilla, Gabriela Calistro Rivera, Chris Harrison, Ryan C. Hickox, Melanie Kaasinen, Andrea Lapi, Iván E. López, Grayson Petter, Cristina Ramos Almeida, David J. Rosario, Francesco Shankar, and Carolin Villforth. Obscuration beyond the nucleus: infrared quasars can be buried in extreme compact starbursts., 527(1):L144–L150, January 2024.

P. Andreani, A. Boselli, L. Ciesla, R. Vio, L. Cortese, V. Buat, and Y. Miyamoto. The bivariate luminosity and mass functions of the local HRS galaxy sample. The stellar, dust, and gas mass functions. , 617:A33, September 2018. .

- Robert Antonucci. Unified models for active galactic nuclei and quasars. , 31:473–521, January 1993. .
- Manuel Aravena, Leindert Boogaard, Jorge Gónzalez-López, Roberto Decarli, Fabian Walter, Chris L. Carilli, Ian Smail, Axel Weiss, Roberto J. Assef, Franz Erik Bauer, Rychard J. Bouwens, Paulo C. Cortes, Pierre Cox, Elisabete da Cunha, Emanuele Daddi, Tanio Díaz-Santos, Hanae Inami, Rob Ivison, Mladen Novak, Gergö Popping, Dominik Riechers, Paul van der Werf, and Jeff Wagg. The ALMA Spectroscopic Survey in the Hubble Ultra Deep Field: The Nature of the Faintest Dusty Star-forming Galaxies. , 901(1):79, September 2020. .
- Lee Armus, Timothy Heckman, and George Miley. Multicolor Optical Imaging of Powerful Far-Infrared Galaxies: More Evidence for a Link Between Galaxy Mergers and Far-Infrared Emission., 94:831, October 1987.
- Michael Aumer, Simon D. M. White, Thorsten Naab, and Cecilia Scannapieco. Towards a more realistic population of bright spiral galaxies in cosmological simulations. , 434 (4):3142–3164, October 2013. .
- R. Aversa, A. Lapi, G. de Zotti, F. Shankar, and L. Danese. Black Hole and Galaxy Coevolution from Continuity Equation and Abundance Matching. , 810(1):74, September 2015. .
- Josephine F. W. Baggen, Pieter van Dokkum, Gabriel Brammer, Anna de Graaff, Marijn Franx, Jenny Greene, Ivo Labbé, Joel Leja, Michael V. Maseda, Erica J. Nelson, Hans-Walter Rix, Bingjie Wang, and Andrea Weibel. The Small Sizes and High Implied Densities of 'Little Red Dots' with Balmer Breaks Could Explain Their Broad Emission Lines Without an AGN. *arXiv e-prints*, art. arXiv:2408.07745, August 2024.
- J. A. Baldwin, M. M. Phillips, and R. Terlevich. Classification parameters for the emission-line spectra of extragalactic objects. , 93:5–19, February 1981. .
- Manda Banerji, R. G. McMahon, C. J. Willott, J. E. Geach, C. M. Harrison, S. Alaghband-Zadeh, D. M. Alexander, N. Bourne, K. E. K. Coppin, J. S. Dunlop, D. Farrah, M. Jarvis, M. J. Michałowski, M. Page, D. J. B. Smith, A. M. Swinbank, M. Symeonidis, and P. P. van der Werf. Cold dust emission from X-ray AGN in the SCUBA-2 Cosmology Legacy Survey: dependence on luminosity, obscuration and AGN activity. , 454(1):419–438, November 2015. .
- E. Yu. Bannikova, V. G. Vakulik, and A. V. Sergeev. N-body simulation of a clumpy torus: application to active galactic nuclei. , 424(2):820–829, August 2012. .

Joshua E. Barnes and Lars E. Hernquist. Fueling Starburst Galaxies with Gas-rich Mergers. , 370:L65, April 1991. .

- Guillermo Barro, S. M. Faber, David C. Koo, Avishai Dekel, Jerome J. Fang, Jonathan R. Trump, Pablo G. Pérez-González, Camilla Pacifici, Joel R. Primack, Rachel S. Somerville, Haojing Yan, Yicheng Guo, Fengshan Liu, Daniel Ceverino, Dale D. Kocevski, and Elizabeth McGrath. Structural and Star-forming Relations since $z\sim3$: Connecting Compact Star-forming and Quiescent Galaxies. , 840(1):47, May 2017. .
- Matthew R. Bate. Dust coagulation during the early stages of star formation: molecular cloud collapse and first hydrostatic core evolution. , 514(2):2145–2161, August 2022.
- M. B. Bayliss, M. McDonald, K. Sharon, M. D. Gladders, M. Florian, J. Chisholm, H. Dahle, G. Mahler, R. Paterno-Mahler, J. R. Rigby, E. Rivera-Thorsen, K. E. Whitaker, S. Allen, B. A. Benson, L. E. Bleem, M. Brodwin, R. E. A. Canning, I. Chiu, J. Hlavacek-Larrondo, G. Khullar, C. Reichardt, and J. D. Vieira. An X-ray detection of star formation in a highly magnified giant arc. *Nature Astronomy*, 4:159–166, February 2020.
- Max Beard. *Investigating the variability of low-mass active galactic nuclei in the X-ray, UV, and optical regimes*. PhD thesis, University of Southampton, United Kingdom, October 2023. URL https://eprints.soton.ac.uk/477714/.
- V. Beckmann and C. Shrader. The AGN phenomenon: open issues. In *Proceedings of "An INTEGRAL view of the high-energy sky (the first 10 years)" 9th INTEGRAL Workshop and celebration of the 10th anniversary of the launch (INTEGRAL 2012). 15-19 October 2012. Bibliotheque Nationale de France,* page 69, January 2012.
- Peter Behroozi, Risa H. Wechsler, Andrew P. Hearin, and Charlie Conroy. UNI-VERSEMACHINE: The correlation between galaxy growth and dark matter halo assembly from z=0-10. , 488(3):3143-3194, September 2019. .
- Stefano Bianchi, Vincenzo Mainieri, and Paolo Padovani. Active Galactic Nuclei and Their Demography Through Cosmic Time. In *Handbook of X-ray and Gamma-ray Astrophysics*, page 4. 2022. .
- Robert W. Bickley, Sara L. Ellison, Mara Salvato, Samir Salim, David R. Patton, Andrea Merloni, Shoshannah Byrne-Mamahit, Leonardo Ferreira, and Scott Wilkinson. X-ray AGNs with SRG/eROSITA: Multi-wavelength observations reveal merger triggering and post-coalescence circumnuclear blowout. *arXiv e-prints*, art. arXiv:2401.17277, January 2024.
- F. Bigiel and L. Blitz. A Universal Neutral Gas Profile for nearby Disk Galaxies. , 756 (2):183, September 2012. .

R. D. Blandford and M. J. Rees. Extended and compact extragalactic radio sources: interpretation and theory. , 17:265–274, March 1978. .

- D. Blánquez-Sesé, C. Gómez-Guijarro, G. E. Magdis, B. Magnelli, R. Gobat, E. Daddi, M. Franco, K. Whitaker, F. Valentino, S. Adscheid, E. Schinnerer, A. Zanella, M. Xiao, T. Wang, D. Liu, V. Kokorev, and D. Elbaz. The gas mass reservoir of quiescent galaxies at cosmic noon. , 674:A166, June 2023.
- Asa F. L. Bluck, Joanna M. Piotrowska, and Roberto Maiolino. The Fundamental Signature of Star Formation Quenching from AGN Feedback: A Critical Dependence of Quiescence on Supermassive Black Hole Mass, Not Accretion Rate., 944(1):108, February 2023.
- L. Boco, A. Lapi, F. Shankar, H. Fu, F. Gabrielli, and A. Sicilia. TwO Parameters Semi Empirical Model (TOPSEM): Galaxy Evolution and Bulge/Disk Dicothomy from Two-stage Halo Accretion. , 954(1):97, September 2023. .
- C. T. Bolton. Identification of Cygnus X-1 with HDE 226868. , 235(5336):271–273, February 1972. .
- H. Bondi. On spherically symmetrical accretion. , 112:195, January 1952. .
- Silvia Bonoli, Francesco Shankar, Simon D. M. White, Volker Springel, and J. Stuart B. Wyithe. On merger bias and the clustering of quasars. , 404(1):399–408, May 2010.
- Michael Boylan-Kolchin, Volker Springel, Simon D. M. White, Adrian Jenkins, and Gerard Lemson. Resolving cosmic structure formation with the Millennium-II Simulation., 398(3):1150–1164, September 2009.
- Johannes Buchner and Franz E. Bauer. Galaxy gas as obscurer II. Separating the galaxy-scale and nuclear obscurers of active galactic nuclei. , 465(4):4348–4362, March 2017. .
- Johannes Buchner, Antonis Georgakakis, Kirpal Nandra, Murray Brightman, Marie-Luise Menzel, Zhu Liu, Li-Ting Hsu, Mara Salvato, Cyprian Rangel, James Aird, Andrea Merloni, and Nicholas Ross. Obscuration-dependent Evolution of Active Galactic Nuclei., 802(2):89, April 2015.
- Johannes Buchner, Steve Schulze, and Franz E. Bauer. Galaxy gas as obscurer I. GRBs x-ray galaxies and find an N_H $^3 \propto M_- \{star\}$ relation. , 464(4):4545–4566, February 2017. .
- G. R. Burbidge, E. M. Burbidge, and A. R. Sandage. Evidence for the Occurrence of Violent Events in the Nuclei of Galaxies. *Reviews of Modern Physics*, 35(4):947–972, January 1963.

L. Burtscher, K. Meisenheimer, K. R. W. Tristram, W. Jaffe, S. F. Hönig, R. I. Davies, M. Kishimoto, J. U. Pott, H. Röttgering, M. Schartmann, G. Weigelt, and S. Wolf. A diversity of dusty AGN tori. Data release for the VLTI/MIDI AGN Large Program and first results for 23 galaxies. , 558:A149, October 2013. .

- R. Carraro, G. Rodighiero, P. Cassata, M. Brusa, F. Shankar, I. Baronchelli, E. Daddi, I. Delvecchio, A. Franceschini, R. Griffiths, C. Gruppioni, E. López-Navas, C. Mancini, S. Marchesi, M. Negrello, A. Puglisi, E. Sani, and H. Suh. Coevolution of black hole accretion and star formation in galaxies up to z = 3.5., 642:A65, October 2020.
- Rosamaria Carraro, Francesco Shankar, Viola Allevato, Giulia Rodighiero, Christopher Marsden, Patricia Arévalo, Ivan Delvecchio, and Andrea Lapi. An Eddington ratio-driven origin for the L_X M_* relation in quiescent and star-forming active galaxies. , 512(1):1185–1195, May 2022. .
- Christopher M. Carroll, Tonima T. Ananna, Ryan C. Hickox, Alberto Masini, Roberto J. Assef, Daniel Stern, Chien-Ting J. Chen, and Lauranne Lanz. A High Fraction of Heavily X-ray Obscured Active Galactic Nuclei. *arXiv e-prints*, art. arXiv:2303.08813, March 2023.
- A. Cattaneo, S. M. Faber, J. Binney, A. Dekel, J. Kormendy, R. Mushotzky, A. Babul, P. N. Best, M. Brüggen, A. C. Fabian, C. S. Frenk, A. Khalatyan, H. Netzer, A. Mahdavi, J. Silk, M. Steinmetz, and L. Wisotzki. The role of black holes in galaxy formation and evolution. , 460(7252):213–219, July 2009.
- A. Cavaliere, A. Lapi, and N. Menci. Quasar Feedback on the Intracluster Medium. , 581(1):L1–L4, December 2002. .
- Elia Cenci, Robert Feldmann, Jindra Gensior, James S. Bullock, Jorge Moreno, Luigi Bassini, and Mauro Bernardini. Starburst-induced Gas–Star Kinematic Misalignment., 961(2):L40, February 2024.
- Chien-Ting J. Chen, Ryan C. Hickox, Stacey Alberts, Chris M. Harrison, David M. Alexander, Roberto Assef, Mark Brodwin, Michael J. I. Brown, Agnese Del Moro, William R. Forman, Varoujan Gorjian, Andrew D. Goulding, Kevin N. Hainline, Christine Jones, Christopher S. Kochanek, Stephen S. Murray, Alexandra Pope, Emmanouel Rovilos, and Daniel Stern. A Connection between Obscuration and Star Formation in Luminous Quasars., 802(1):50, March 2015.
- Yan-Mei Chen, Yong Shi, Christy A. Tremonti, Matt Bershady, Michael Merrifield, Eric Emsellem, Yi-Fei Jin, Song Huang, Hai Fu, David A. Wake, Kevin Bundy, David Stark, Lihwai Lin, Maria Argudo-Fernandez, Thaisa Storchi Bergmann, Dmitry Bizyaev, Joel Brownstein, Martin Bureau, John Chisholm, Niv Drory, Qi Guo, Lei Hao, Jian Hu, Cheng Li, Ran Li, Alexandre Roman Lopes, Kai-Ke Pan, Rogemar A.

Riffel, Daniel Thomas, Lan Wang, Kyle Westfall, and Ren-Bin Yan. The growth of the central region by acquisition of counterrotating gas in star-forming galaxies. *Nature Communications*, 7:13269, October 2016.

- R. K. Cochrane, P. N. Best, D. Sobral, I. Smail, J. E. Geach, J. P. Stott, and D. A. Wake. The dependence of galaxy clustering on stellar mass, star-formation rate and redshift at z = 0.8-2.2, with HiZELS. , 475(3):3730-3745, April 2018. .
- Alison L. Coil. The Large-Scale Structure of the Universe. In Terry D. Oswalt and William C. Keel, editors, *Planets, Stars and Stellar Systems. Volume 6: Extragalactic Astronomy and Cosmology*, volume 6, page 387. 2013.
- Alison L. Coil, Antonis Georgakakis, Jeffrey A. Newman, Michael C. Cooper, Darren Croton, Marc Davis, David C. Koo, Elise S. Laird, Kirpal Nandra, Benjamin J. Weiner, Christopher N. A. Willmer, and Renbin Yan. AEGIS: The Clustering of X-Ray Active Galactic Nucleus Relative to Galaxies at z ~1., 701(2):1484–1499, August 2009.
- Shaun Cole and Nick Kaiser. Biased clustering in the cold dark matter cosmogony. , 237:1127–1146, April 1989. .
- Shaun Cole, Cedric G. Lacey, Carlton M. Baugh, and Carlos S. Frenk. Hierarchical galaxy formation. , 319(1):168–204, November 2000. .
- F. Combes, S. García-Burillo, A. Audibert, L. Hunt, A. Eckart, S. Aalto, V. Casasola, F. Boone, M. Krips, S. Viti, K. Sakamoto, S. Muller, K. Dasyra, P. van der Werf, and S. Martin. ALMA observations of molecular tori around massive black holes. , 623: A79, March 2019. .
- Christopher J. Conselice, Carl J. Mundy, Leonardo Ferreira, and Kenneth Duncan. A Direct Measurement of Galaxy Major and Minor Merger Rates and Stellar Mass Accretion Histories at Z; 3 Using Galaxy Pairs in the REFINE Survey. , 940(2):168, December 2022. .
- Asantha Cooray and Ravi Sheth. Halo models of large scale structure. , 372(1):1–129, December 2002. .
- Rodrigo Córdova Rosado, Andy D. Goulding, Jenny E. Greene, Grayson C. Petter, Ryan C. Hickox, Nickolas Kokron, Michael A. Strauss, Jahmour J. Givans, Yoshiki Toba, and Cassandra Starr Henderson. Cross-correlation of Luminous Red Galaxies with ML-selected AGN in HSC-SSP: Unobscured AGN residing in more massive halos. *arXiv e-prints*, art. arXiv:2409.08314, September 2024.
- Darren J. Croton, Volker Springel, Simon D. M. White, G. De Lucia, C. S. Frenk, L. Gao, A. Jenkins, G. Kauffmann, J. F. Navarro, and N. Yoshida. The many lives of active galactic nuclei: cooling flows, black holes and the luminosities and colours of galaxies. , 365(1):11–28, January 2006.

Q. D'Amato, R. Gilli, C. Vignali, M. Massardi, F. Pozzi, G. Zamorani, C. Circosta, F. Vito, J. Fritz, G. Cresci, V. Casasola, F. Calura, A. Feltre, V. Manieri, D. Rigopoulou, P. Tozzi, and C. Norman. Dust and gas content of high-redshift galaxies hosting obscured AGN in the Chandra Deep Field-South., 636:A37, April 2020.

- D. W. Darg, S. Kaviraj, C. J. Lintott, K. Schawinski, M. Sarzi, S. Bamford, J. Silk, D. Andreescu, P. Murray, R. C. Nichol, M. J. Raddick, A. Slosar, A. S. Szalay, D. Thomas, and J. Vandenberg. Galaxy Zoo: the properties of merging galaxies in the nearby Universe local environments, colours, masses, star formation rates and AGN activity., 401(3):1552–1563, January 2010.
- M. Davis, P. Guhathakurta, N. P. Konidaris, J. A. Newman, M. L. N. Ashby, A. D. Biggs, P. Barmby, K. Bundy, S. C. Chapman, A. L. Coil, C. J. Conselice, M. C. Cooper, D. J. Croton, P. R. M. Eisenhardt, R. S. Ellis, S. M. Faber, T. Fang, G. G. Fazio, A. Georgakakis, B. F. Gerke, W. M. Goss, S. Gwyn, J. Harker, A. M. Hopkins, J. S. Huang, R. J. Ivison, S. A. Kassin, E. N. Kirby, A. M. Koekemoer, D. C. Koo, E. S. Laird, E. Le Floc'h, L. Lin, J. M. Lotz, P. J. Marshall, D. C. Martin, A. J. Metevier, L. A. Moustakas, K. Nandra, K. G. Noeske, C. Papovich, A. C. Phillips, R. M. Rich, G. H. Rieke, D. Rigopoulou, S. Salim, D. Schiminovich, L. Simard, I. Smail, T. A. Small, B. J. Weiner, C. N. A. Willmer, S. P. Willner, G. Wilson, E. L. Wright, and R. Yan. The All-Wavelength Extended Groth Strip International Survey (AEGIS) Data Sets., 660 (1):L1–L6, May 2007.
- Gabriella De Lucia and Jérémy Blaizot. The hierarchical formation of the brightest cluster galaxies. , 375(1):2–14, February 2007. .
- Gabriella De Lucia, Luca Tornatore, Carlos S. Frenk, Amina Helmi, Julio F. Navarro, and Simon D. M. White. Elemental abundances in Milky Way-like galaxies from a hierarchical galaxy formation model. , 445(1):970–987, November 2014. .
- Gabriella De Lucia, Michaela Hirschmann, and Fabio Fontanot. Nature versus nurture: what regulates star formation in satellite galaxies?, 482(4):5041–5051, February 2019.
- Gabriella De Lucia, Fabio Fontanot, Lizhi Xie, and Michaela Hirschmann. Tracing the quenching journey across cosmic time., 687:A68, July 2024.
- P. Di Matteo, F. Bournaud, M. Martig, F. Combes, A. L. Melchior, and B. Semelin. On the frequency, intensity, and duration of starburst episodes triggered by galaxy interactions and mergers. , 492(1):31–49, December 2008.
- Tiziana Di Matteo, Volker Springel, and Lars Hernquist. Energy input from quasars regulates the growth and activity of black holes and their host galaxies. , 433(7026): 604–607, February 2005. .

M. A. DiPompeo, A. D. Myers, R. C. Hickox, J. E. Geach, and K. N. Hainline. The angular clustering of infrared-selected obscured and unobscured quasars. , 442(4): 3443–3453, August 2014. .

- M. A. DiPompeo, A. D. Myers, R. C. Hickox, J. E. Geach, G. Holder, K. N. Hainline, and S. W. Hall. Weighing obscured and unobscured quasar hosts with the cosmic microwave background. , 446(4):3492–3501, February 2015. .
- M. A. DiPompeo, R. C. Hickox, and A. D. Myers. Updated measurements of the dark matter halo masses of obscured quasars with improved WISE and Planck data. , 456 (1):924–942, February 2016. .
- M. A. DiPompeo, R. C. Hickox, S. Eftekharzadeh, and A. D. Myers. The characteristic halo masses of half-a-million WISE-selected quasars. , 469(4):4630–4643, August 2017. .
- Chris Done, S. W. Davis, C. Jin, O. Blaes, and M. Ward. Intrinsic disc emission and the soft x-ray excess in active galactic nuclei. *Monthly Notices of the Royal Astronomical Society*, 420(3):1848–1860, 02 2012. ISSN 0035-8711. URL https://doi.org/10.1111/j.1365-2966.2011.19779.x.
- Mauro D'Onofrio, Paola Marziani, and Cesare Chiosi. Past, Present and Future of the Scaling Relations of Galaxies and Active Galactic Nuclei. *Frontiers in Astronomy and Space Sciences*, 8:157, November 2021.
- E. Donoso, Lin Yan, D. Stern, and R. J. Assef. The Angular Clustering of WISE-selected Active Galactic Nuclei: Different Halos for Obscured and Unobscured Active Galactic Nuclei. , 789(1):44, July 2014.
- F. Duras, A. Bongiorno, F. Ricci, E. Piconcelli, F. Shankar, E. Lusso, S. Bianchi, F. Fiore, R. Maiolino, A. Marconi, F. Onori, E. Sani, R. Schneider, C. Vignali, and F. La Franca. Universal bolometric corrections for active galactic nuclei over seven luminosity decades. , 636:A73, April 2020.
- Emmanuel Durodola, Fabio Pacucci, and Ryan C. Hickox. Exploring the AGN Fraction of a Sample of JWST's Little Red Dots at 5 < z < 8: Overmassive Black Holes Are Strongly Favored. *arXiv e-prints*, art. arXiv:2406.10329, June 2024. .
- J. Ebrero, S. Mateos, G. C. Stewart, F. J. Carrera, and M. G. Watson. High-precision multi-band measurements of the angular clustering of X-ray sources. , 500(2):749–762, June 2009. .
- D. O. Edge, J. R. Shakeshaft, W. B. McAdam, J. E. Baldwin, and S. Archer. A survey of radio sources at a frequency of 159 Mc/s., 68:37–60, January 1959.
- J. R. Ehman, R. S. Dixon, and J. D. Kraus. The Ohio survey between declinations of 0 and 36 south. , 75:351–506, May 1970. .

Anna-Christina Eilers, Ruari Mackenzie, Elia Pizzati, Jorryt Matthee, Joseph F. Hennawi, Haowen Zhang, Rongmon Bordoloi, Daichi Kashino, Simon J. Lilly, Rohan P. Naidu, Robert A. Simcoe, Minghao Yue, Carlos S. Frenk, John C. Helly, Matthieu Schaller, and Joop Schaye. EIGER VI. The Correlation Function, Host Halo Mass and Duty Cycle of Luminous Quasars at *zrsim6*. *arXiv e-prints*, art. arXiv:2403.07986, March 2024.

- A. Einstein. Die Grundlage der allgemeinen Relativitätstheorie. *Annalen der Physik*, 354 (7):769–822, January 1916. .
- J. A. Ekers. The Parkes catalogue of radio sources, declination zone +20 to -90 . *Australian Journal of Physics Astrophysical Supplement*, 7:3–75, January 1969.
- D. Elbaz, R. Leiton, N. Nagar, K. Okumura, M. Franco, C. Schreiber, M. Pannella, T. Wang, M. Dickinson, T. Díaz-Santos, L. Ciesla, E. Daddi, F. Bournaud, G. Magdis, L. Zhou, and W. Rujopakarn. Starbursts in and out of the star-formation main sequence., 616:A110, August 2018.
- M. Elitzur. Unification Issues and the AGN Torus. In L. C. Ho and J. W. Wang, editors, *The Central Engine of Active Galactic Nuclei*, volume 373 of *Astronomical Society of the Pacific Conference Series*, page 415, October 2007. .
- Moshe Elitzur and Luis C. Ho. On the Disappearance of the Broad-Line Region in Low-Luminosity Active Galactic Nuclei. , 701(2):L91–L94, August 2009.
- Sara L. Ellison, David R. Patton, Luc Simard, and Alan W. McConnachie. Galaxy Pairs in the Sloan Digital Sky Survey. I. Star Formation, Active Galactic Nucleus Fraction, and the Mass-Metallicity Relation. , 135(5):1877–1899, May 2008. .
- Sara L. Ellison, J. Trevor Mendel, David R. Patton, and Jillian M. Scudder. Galaxy pairs in the Sloan Digital Sky Survey VIII. The observational properties of post-merger galaxies. , 435(4):3627–3638, November 2013. .
- M. Elvis, T. Maccacaro, A. S. Wilson, M. J. Ward, M. V. Penston, R. A. E. Fosbury, and G. C. Perola. Seyfert galaxies as X-ray sources. , 183:129–157, April 1978. .
- A. Elyiv, N. Clerc, M. Plionis, J. Surdej, M. Pierre, S. Basilakos, L. Chiappetti, P. Gandhi, E. Gosset, O. Melnyk, and F. Pacaud. Angular correlation functions of X-ray point-like sources in the full exposure XMM-LSS field., 537:A131, January 2012.
- D. Esparza-Arredondo, O. Gonzalez-Martín, D. Dultzin, J. Masegosa, C. Ramos-Almeida, I. García-Bernete, J. Fritz, and N. Osorio-Clavijo. The dust-gas AGN torus as constrained from X-ray and mid-infrared observations. , 651:A91, July 2021. .
- Event Horizon Telescope Collaboration, Kazunori Akiyama, Antxon Alberdi, Walter Alef, Keiichi Asada, Rebecca Azulay, Anne-Kathrin Baczko, David Ball, Mislav Baloković, John Barrett, Dan Bintley, Lindy Blackburn, Wilfred Boland, Katherine L.

Bouman, Geoffrey C. Bower, Michael Bremer, Christiaan D. Brinkerink, Roger Brissenden, Silke Britzen, Avery E. Broderick, Dominique Broguiere, Thomas Bronzwaer, Do-Young Byun, John E. Carlstrom, Andrew Chael, Chi-kwan Chan, Shami Chatterjee, Koushik Chatterjee, Ming-Tang Chen, Yongjun Chen, Ilje Cho, Pierre Christian, John E. Conway, James M. Cordes, Geoffrey B. Crew, Yuzhu Cui, Jordy Davelaar, Mariafelicia De Laurentis, Roger Deane, Jessica Dempsey, Gregory Desvignes, Jason Dexter, Sheperd S. Doeleman, Ralph P. Eatough, Heino Falcke, Vincent L. Fish, Ed Fomalont, Raquel Fraga-Encinas, William T. Freeman, Per Friberg, Christian M. Fromm, José L. Gómez, Peter Galison, Charles F. Gammie, Roberto García, Olivier Gentaz, Boris Georgiev, Ciriaco Goddi, Roman Gold, Minfeng Gu, Mark Gurwell, Kazuhiro Hada, Michael H. Hecht, Ronald Hesper, Luis C. Ho, Paul Ho, Mareki Honma, Chih-Wei L. Huang, Lei Huang, David H. Hughes, Shiro Ikeda, Makoto Inoue, Sara Issaoun, David J. James, Buell T. Jannuzi, Michael Janssen, Britton Jeter, Wu Jiang, Michael D. Johnson, Svetlana Jorstad, Taehyun Jung, Mansour Karami, Ramesh Karuppusamy, Tomohisa Kawashima, Garrett K. Keating, Mark Kettenis, Jae-Young Kim, Junhan Kim, Jongsoo Kim, Motoki Kino, Jun Yi Koay, Patrick M. Koch, Shoko Koyama, Michael Kramer, Carsten Kramer, Thomas P. Krichbaum, Cheng-Yu Kuo, Tod R. Lauer, Sang-Sung Lee, Yan-Rong Li, Zhiyuan Li, Michael Lindqvist, Kuo Liu, Elisabetta Liuzzo, Wen-Ping Lo, Andrei P. Lobanov, Laurent Loinard, Colin Lonsdale, Ru-Sen Lu, Nicholas R. MacDonald, Jirong Mao, Sera Markoff, Daniel P. Marrone, Alan P. Marscher, Iván Martí-Vidal, Satoki Matsushita, Lynn D. Matthews, Lia Medeiros, Karl M. Menten, Yosuke Mizuno, Izumi Mizuno, James M. Moran, Kotaro Moriyama, Monika Moscibrodzka, Cornelia Müller, Hiroshi Nagai, Neil M. Nagar, Masanori Nakamura, Ramesh Narayan, Gopal Narayanan, Iniyan Natarajan, Roberto Neri, Chunchong Ni, Aristeidis Noutsos, Hiroki Okino, Héctor Olivares, Gisela N. Ortiz-León, Tomoaki Oyama, Feryal Özel, Daniel C. M. Palumbo, Nimesh Patel, Ue-Li Pen, Dominic W. Pesce, Vincent Piétu, Richard Plambeck, Aleksandar PopStefanija, Oliver Porth, Ben Prather, Jorge A. Preciado-López, Dimitrios Psaltis, Hung-Yi Pu, Venkatessh Ramakrishnan, Ramprasad Rao, Mark G. Rawlings, Alexander W. Raymond, Luciano Rezzolla, Bart Ripperda, Freek Roelofs, Alan Rogers, Eduardo Ros, Mel Rose, Arash Roshanineshat, Helge Rottmann, Alan L. Roy, Chet Ruszczyk, Benjamin R. Ryan, Kazi L. J. Rygl, Salvador Sánchez, David Sánchez-Arguelles, Mahito Sasada, Tuomas Savolainen, F. Peter Schloerb, Karl-Friedrich Schuster, Lijing Shao, Zhiqiang Shen, Des Small, Bong Won Sohn, Jason SooHoo, Fumie Tazaki, Paul Tiede, Remo P. J. Tilanus, Michael Titus, Kenji Toma, Pablo Torne, Tyler Trent, Sascha Trippe, Shuichiro Tsuda, Ilse van Bemmel, Huib Jan van Langevelde, Daniel R. van Rossum, Jan Wagner, John Wardle, Jonathan Weintroub, Norbert Wex, Robert Wharton, Maciek Wielgus, George N. Wong, Qingwen Wu, Ken Young, André Young, Ziri Younsi, Feng Yuan, Ye-Fei Yuan, J. Anton Zensus, Guangyao Zhao, Shan-Shan Zhao, Ziyan Zhu, Juan-Carlos Algaba, Alexander Allardi, Rodrigo Amestica, Jadyn Anczarski, Uwe Bach,

Frederick K. Baganoff, Christopher Beaudoin, Bradford A. Benson, Ryan Berthold, Jay M. Blanchard, Ray Blundell, Sandra Bustamente, Roger Cappallo, Edgar Castillo-Domínguez, Chih-Cheng Chang, Shu-Hao Chang, Song-Chu Chang, Chung-Chen Chen, Ryan Chilson, Tim C. Chuter, Rodrigo Córdova Rosado, Iain M. Coulson, Thomas M. Crawford, Joseph Crowley, John David, Mark Derome, Matthew Dexter, Sven Dornbusch, Kevin A. Dudevoir, Sergio A. Dzib, Andreas Eckart, Chris Eckert, Neal R. Erickson, Wendeline B. Everett, Aaron Faber, Joseph R. Farah, Vernon Fath, Thomas W. Folkers, David C. Forbes, Robert Freund, Arturo I. Gómez-Ruiz, David M. Gale, Feng Gao, Gertie Geertsema, David A. Graham, Christopher H. Greer, Ronald Grosslein, Frédéric Gueth, Daryl Haggard, Nils W. Halverson, Chih-Chiang Han, Kuo-Chang Han, Jinchi Hao, Yutaka Hasegawa, Jason W. Henning, Antonio Hernández-Gómez, Rubén Herrero-Illana, Stefan Heyminck, Akihiko Hirota, James Hoge, Yau-De Huang, C. M. Violette Impellizzeri, Homin Jiang, Atish Kamble, Ryan Keisler, Kimihiro Kimura, Yusuke Kono, Derek Kubo, John Kuroda, Richard Lacasse, Robert A. Laing, Erik M. Leitch, Chao-Te Li, Lupin C. C. Lin, Ching-Tang Liu, Kuan-Yu Liu, Li-Ming Lu, Ralph G. Marson, Pierre L. Martin-Cocher, Kyle D. Massingill, Callie Matulonis, Martin P. McColl, Stephen R. McWhirter, Hugo Messias, Zheng Meyer-Zhao, Daniel Michalik, Alfredo Montaña, William Montgomerie, Matias Mora-Klein, Dirk Muders, Andrew Nadolski, Santiago Navarro, Joseph Neilsen, Chi H. Nguyen, Hiroaki Nishioka, Timothy Norton, Michael A. Nowak, George Nystrom, Hideo Ogawa, Peter Oshiro, Tomoaki Oyama, Harriet Parsons, Scott N. Paine, Juan Peñalver, Neil M. Phillips, Michael Poirier, Nicolas Pradel, Rurik A. Primiani, Philippe A. Raffin, Alexandra S. Rahlin, George Reiland, Christopher Risacher, Ignacio Ruiz, Alejandro F. Sáez-Madaín, Remi Sassella, Pim Schellart, Paul Shaw, Kevin M. Silva, Hotaka Shiokawa, David R. Smith, William Snow, Kamal Souccar, Don Sousa, T. K. Sridharan, Ranjani Srinivasan, William Stahm, Anthony A. Stark, Kyle Story, Sjoerd T. Timmer, Laura Vertatschitsch, Craig Walther, Ta-Shun Wei, Nathan Whitehorn, Alan R. Whitney, David P. Woody, Jan G. A. Wouterloot, Melvin Wright, Paul Yamaguchi, Chen-Yu Yu, Milagros Zeballos, Shuo Zhang, and Lucy Ziurys. First M87 Event Horizon Telescope Results. I. The Shadow of the Supermassive Black Hole., 875(1):L1, April 2019. .

- A. C. Fabian. Observational Evidence of Active Galactic Nuclei Feedback. , 50:455–489, September 2012. .
- A. C. Fabian and X. Barcons. The origin of the X-ray background. , 30:429–456, January 1992. .
- A. C. Fabian and K. Iwasawa. The mass density in black holes inferred from the X-ray background. , 303(2):L34–L36, February 1999. .
- A. C. Fabian, R. V. Vasudevan, and P. Gandhi. The effect of radiation pressure on dusty absorbing gas around active galactic nuclei. , 385(1):L43–L47, March 2008. .

A. C. Fabian, R. V. Vasudevan, R. F. Mushotzky, L. M. Winter, and C. S. Reynolds. Radiation pressure and absorption in AGN: results from a complete unbiased sample from Swift., 394(1):L89–L92, March 2009.

- Duncan Farrah, Sara Petty, Kevin S. Croker, Gregory Tarlé, Michael Zevin, Evanthia Hatziminaoglou, Francesco Shankar, Lingyu Wang, David L. Clements, Andreas Efstathiou, Mark Lacy, Kurtis A. Nishimura, Jose Afonso, Chris Pearson, and Lura K. Pitchford. A Preferential Growth Channel for Supermassive Black Holes in Elliptical Galaxies at $z\lesssim 2$. , 943(2):133, February 2023. .
- Edward Arthur Fath. The spectra of some spiral nebulae and globular star clusters. *Lick Observatory Bulletin*, 149:71–77, January 1909.
- Claude-André Faucher-Giguère and Eliot Quataert. The physics of galactic winds driven by active galactic nuclei. , 425(1):605–622, September 2012. .
- Leonardo Ferreira, Nathan Adams, Christopher J. Conselice, Elizaveta Sazonova, Duncan Austin, Joseph Caruana, Fabricio Ferrari, Aprajita Verma, James Trussler, Tom Broadhurst, Jose Diego, Brenda L. Frye, Massimo Pascale, Stephen M. Wilkins, Rogier A. Windhorst, and Adi Zitrin. Panic! at the Disks: First Rest-frame Optical Observations of Galaxy Structure at z ¿ 3 with JWST in the SMACS 0723 Field., 938 (1):L2, October 2022.
- Fabio Fontanot, Pierluigi Monaco, Stefano Cristiani, and Paolo Tozzi. The effect of stellar feedback and quasar winds on the active galactic nucleus population. , 373(3): 1173–1187, December 2006.
- Fabio Fontanot, Anna Pasquali, Gabriella De Lucia, Frank C. van den Bosch, Rachel S. Somerville, and Xi Kang. The dependence of AGN activity on stellar and halo mass in semi-analytic models. , 413(2):957–970, May 2011. .
- Fabio Fontanot, Michaela Hirschmann, and Gabriella De Lucia. Strong Stellar-Driven Outflows Shape The Evolution Of Galaxies At Cosmic Dawn. In *Galaxy Evolution Across Time*, page 77, June 2017.
- Fabio Fontanot, Gabriella De Lucia, Michaela Hirschmann, Lizhi Xie, Pierluigi Monaco, Nicola Menci, Fabrizio Fiore, Chiara Feruglio, Stefano Cristiani, and Francesco Shankar. The rise of active galactic nuclei in the galaxy evolution and assembly semi-analytic model. , 496(3):3943–3960, August 2020.
- Fabio Fontanot, Gabriella De Lucia, Lizhi Xie, Michaela Hirschmann, Carlton Baugh, and John C. Helly. Galaxy clustering in a new implementation of the GAEA semi-analytical galaxy formation model. *arXiv e-prints*, art. arXiv:2409.02194, September 2024. .

M. Franco, D. Elbaz, L. Zhou, B. Magnelli, C. Schreiber, L. Ciesla, M. Dickinson, N. Nagar, G. Magdis, D. M. Alexander, M. Béthermin, R. Demarco, E. Daddi, T. Wang, J. Mullaney, M. Sargent, H. Inami, X. Shu, F. Bournaud, R. Chary, R. T. Coogan, H. Ferguson, S. L. Finkelstein, M. Giavalisco, C. Gómez-Guijarro, D. Iono, S. Juneau, G. Lagache, L. Lin, K. Motohara, K. Okumura, M. Pannella, C. Papovich, A. Pope, W. Rujopakarn, J. Silverman, and M. Xiao. GOODS-ALMA: The slow downfall of star formation in z = 2-3 massive galaxies. , 643:A30, November 2020.

- K. C. Freeman. On the Disks of Spiral and S0 Galaxies., 160:811, June 1970. .
- Hao Fu, Francesco Shankar, Mohammadreza Ayromlou, Max Dickson, Ioanna Koutsouridou, Yetli Rosas-Guevara, Christopher Marsden, Kristina Brocklebank, Mariangela Bernardi, Nikolaos Shiamtanis, Joseph Williams, Lorenzo Zanisi, Viola Allevato, Lumen Boco, Silvia Bonoli, Andrea Cattaneo, Paola Dimauro, Fangzhou Jiang, Andrea Lapi, Nicola Menci, Stefani Petropoulou, and Carolin Villforth. Testing the key role of the stellar mass-halo mass relation in galaxy merger rates and morphologies via DECODE, a novel Discrete statistical sEmi-empiriCal mODEl. , 516(3):3206–3233, November 2022.
- Hao Fu, Francesco Shankar, Mohammadreza Ayromlou, Ioanna Koutsouridou, Andrea Cattaneo, Caroline Bertemes, Sabine Bellstedt, Ignacio Martín-Navarro, Joel Leja, Viola Allevato, Mariangela Bernardi, Lumen Boco, Paola Dimauro, Carlotta Gruppioni, Andrea Lapi, Nicola Menci, Iván Muñoz Rodríguez, Annagrazia Puglisi, and Alba V. Alonso-Tetilla. Unveiling the (in)consistencies among the galaxy stellar mass function, star formation histories, satellite abundances, and intracluster light from a semi-empirical perspective. , 532(1):177–197, July 2024.
- J. Fu, J. L. Hou, J. Yin, and R. X. Chang. Origin and Evolution of the Abundance Gradient Along the Milky Way Disk., 696(1):668–675, May 2009.
- Jian Fu, Qi Guo, Guinevere Kauffmann, and Mark R. Krumholz. The atomic-to-molecular transition and its relation to the scaling properties of galaxy discs in the local Universe. , 409(2):515–530, December 2010. .
- Jack F. Gallimore, Moshe Elitzur, Roberto Maiolino, Alessandro Marconi, Christopher P. O'Dea, Dieter Lutz, Stefi A. Baum, Robert Nikutta, C. M. V. Impellizzeri, Richard Davies, Amy E. Kimball, and Eleonora Sani. High-velocity Bipolar Molecular Emission from an AGN Torus., 829(1):L7, September 2016.
- Violeta Gámez Rosas, Jacob W. Isbell, Walter Jaffe, Romain G. Petrov, James H. Leftley, Karl-Heinz Hofmann, Florentin Millour, Leonard Burtscher, Klaus Meisenheimer, Anthony Meilland, Laurens B. F. M. Waters, Bruno Lopez, Stéphane Lagarde, Gerd Weigelt, Philippe Berio, Fatme Allouche, Sylvie Robbe-Dubois, Pierre Cruzalèbes, Felix Bettonvil, Thomas Henning, Jean-Charles Augereau, Pierre Antonelli, Udo Beckmann, Roy van Boekel, Philippe Bendjoya, William C. Danchi, Carsten Dominik,

Julien Drevon, Jack F. Gallimore, Uwe Graser, Matthias Heininger, Vincent Hocdé, Michiel Hogerheijde, Josef Hron, Caterina M. V. Impellizzeri, Lucia Klarmann, Elena Kokoulina, Lucas Labadie, Michael Lehmitz, Alexis Matter, Claudia Paladini, Eric Pantin, Jörg-Uwe Pott, Dieter Schertl, Anthony Soulain, Philippe Stee, Konrad Tristram, Jozsef Varga, Julien Woillez, Sebastian Wolf, Gideon Yoffe, and Gerard Zins. Thermal imaging of dust hiding the black hole in NGC 1068. , 602(7897):403–407, February 2022. .

- F. Gao, L. Wang, W. J. Pearson, Y. A. Gordon, B. W. Holwerda, A. M. Hopkins, M. J. I. Brown, J. Bland-Hawthorn, and M. S. Owers. Mergers trigger active galactic nuclei out to $z\sim0.6$., 637:A94, May 2020. .
- I. García-Bernete, A. Alonso-Herrero, D. Rigopoulou, M. Pereira-Santaella, T. Shimizu, R. Davies, F. R. Donnan, P. F. Roche, O. González-Martín, C. Ramos Almeida, E. Bellocchi, P. Boorman, F. Combes, A. Efstathiou, D. Esparza-Arredondo, S. García-Burillo, E. González-Alfonso, E. K. S. Hicks, S. Hönig, A. Labiano, N. A. Levenson, E. López-Rodríguez, C. Ricci, C. Packham, D. Rouan, M. Stalevski, and M. J. Ward. The Galaxy Activity, Torus, and Outflow Survey (GATOS). III. Revealing the inner icy structure in local active galactic nuclei. , 681:L7, January 2024.
- S. García-Burillo, F. Combes, C. Ramos Almeida, A. Usero, M. Krips, A. Alonso-Herrero, S. Aalto, V. Casasola, L. K. Hunt, S. Martín, S. Viti, L. Colina, F. Costagliola, A. Eckart, A. Fuente, C. Henkel, I. Márquez, R. Neri, E. Schinnerer, L. J. Tacconi, and P. P. van der Werf. ALMA Resolves the Torus of NGC 1068: Continuum and Molecular Line Emission. , 823(1):L12, May 2016.
- S. García-Burillo, F. Combes, C. Ramos Almeida, A. Usero, A. Alonso-Herrero, L. K. Hunt, D. Rouan, S. Aalto, M. Querejeta, S. Viti, P. P. van der Werf, H. Vives-Arias, A. Fuente, L. Colina, J. Martín-Pintado, C. Henkel, S. Martín, M. Krips, D. Gratadour, R. Neri, and L. J. Tacconi. ALMA images the many faces of the ¡ASTROBJ¿NGC 1068;/ASTROBJ; torus and its surroundings. , 632:A61, December 2019.
- S. García-Burillo, A. Alonso-Herrero, C. Ramos Almeida, O. González-Martín, F. Combes, A. Usero, S. Hönig, M. Querejeta, E. K. S. Hicks, L. K. Hunt, D. Rosario, R. Davies, P. G. Boorman, A. J. Bunker, L. Burtscher, L. Colina, T. Díaz-Santos, P. Gandhi, I. García-Bernete, B. García-Lorenzo, K. Ichikawa, M. Imanishi, T. Izumi, A. Labiano, N. A. Levenson, E. López-Rodríguez, C. Packham, M. Pereira-Santaella, C. Ricci, D. Rigopoulou, D. Rouan, T. Shimizu, M. Stalevski, K. Wada, and D. Williamson. The Galaxy Activity, Torus, and Outflow Survey (GATOS). I. ALMA images of dusty molecular tori in Seyfert galaxies. , 652:A98, August 2021.
- M. Gatti, F. Shankar, V. Bouillot, N. Menci, A. Lamastra, M. Hirschmann, and F. Fiore. Constraining AGN triggering mechanisms through the clustering analysis of active black holes. , 456(1):1073–1092, February 2016. .

J. E. Geach, R. C. Hickox, L. E. Bleem, M. Brodwin, G. P. Holder, K. A. Aird, B. A. Benson, S. Bhattacharya, J. E. Carlstrom, C. L. Chang, H. M. Cho, T. M. Crawford, A. T. Crites, T. de Haan, M. A. Dobbs, J. Dudley, E. M. George, K. N. Hainline, N. W. Halverson, W. L. Holzapfel, S. Hoover, Z. Hou, J. D. Hrubes, R. Keisler, L. Knox, A. T. Lee, E. M. Leitch, M. Lueker, D. Luong-Van, D. P. Marrone, J. J. McMahon, J. Mehl, S. S. Meyer, M. Millea, J. J. Mohr, T. E. Montroy, A. D. Myers, S. Padin, T. Plagge, C. Pryke, C. L. Reichardt, J. E. Ruhl, J. T. Sayre, K. K. Schaffer, L. Shaw, E. Shirokoff, H. G. Spieler, Z. Staniszewski, A. A. Stark, K. T. Story, A. van Engelen, K. Vanderlinde, J. D. Vieira, R. Williamson, and O. Zahn. A Direct Measurement of the Linear Bias of Mid-infrared-selected Quasars at z ≈ 1 Using Cosmic Microwave Background Lensing. , 776(2):L41, October 2013. .

- Karl Gebhardt, Ralf Bender, Gary Bower, Alan Dressler, S. M. Faber, Alexei V. Filippenko, Richard Green, Carl Grillmair, Luis C. Ho, John Kormendy, Tod R. Lauer, John Magorrian, Jason Pinkney, Douglas Richstone, and Scott Tremaine. A Relationship between Nuclear Black Hole Mass and Galaxy Velocity Dispersion. , 539(1): L13–L16, August 2000.
- A. Georgakakis, J. Aird, A. Schulze, T. Dwelly, M. Salvato, K. Nandra, A. Merloni, and D. P. Schneider. Observational constraints on the specific accretion-rate distribution of X-ray-selected AGNs., 471(2):1976–2001, October 2017a.
- A. Georgakakis, M. Salvato, Z. Liu, J. Buchner, W. N. Brandt, T. Tasnim Ananna, A. Schulze, Yue Shen, S. LaMassa, K. Nandra, A. Merloni, and I. D. McGreer. X-ray constraints on the fraction of obscured active galactic nuclei at high accretion luminosities. , 469(3):3232–3251, August 2017b. .
- Antonis Georgakakis, Angel Ruiz, and Stephanie M. LaMassa. Forward modelling the multiwavelength properties of active galactic nuclei: application to X-ray and WISE mid-infrared samples. , 499(1):710–729, November 2020. .
- I. Georgantopoulos, E. Pouliasis, G. Mountrichas, A. Van der Wel, S. Marchesi, and G. Lanzuisi. Comparing the host galaxy ages of X-ray selected AGN in COSMOS. Obscured AGN are associated with older galaxies. , 673:A67, May 2023. .
- I. M. George and A. C. Fabian. X-ray reflection from cold matter in Active Galactic Nuclei and X-ray binaries. , 249:352, March 1991. .
- G. Ghisellini. High energy emission from AGN. *Advances in Space Research*, 13(12): 587–596, December 1993.
- Riccardo Giacconi. History of X-ray telescopes and astronomy. *Experimental Astronomy*, 25(1-3):143–156, August 2009.
- R. Gilli, A. Comastri, and G. Hasinger. The synthesis of the cosmic X-ray background in the Chandra and XMM-Newton era. , 463(1):79–96, February 2007. .

R. Gilli, G. Zamorani, T. Miyaji, J. Silverman, M. Brusa, V. Mainieri, N. Cappelluti, E. Daddi, C. Porciani, L. Pozzetti, F. Civano, A. Comastri, A. Finoguenov, F. Fiore, M. Salvato, C. Vignali, G. Hasinger, S. Lilly, C. Impey, J. Trump, P. Capak, H. McCracken, N. Scoville, Y. Taniguchi, C. M. Carollo, T. Contini, J. P. Kneib, O. Le Fevre, A. Renzini, M. Scodeggio, S. Bardelli, M. Bolzonella, A. Bongiorno, K. Caputi, A. Cimatti, G. Coppa, O. Cucciati, S. de La Torre, L. de Ravel, P. Franzetti, B. Garilli, A. Iovino, P. Kampczyk, C. Knobel, K. Kovač, F. Lamareille, J. F. Le Borgne, V. Le Brun, C. Maier, M. Mignoli, R. Pellò, Y. Peng, E. Perez Montero, E. Ricciardelli, M. Tanaka, L. Tasca, L. Tresse, D. Vergani, E. Zucca, U. Abbas, D. Bottini, A. Cappi, P. Cassata, M. Fumana, L. Guzzo, A. Leauthaud, D. Maccagni, C. Marinoni, P. Memeo, B. Meneux, P. Oesch, R. Scaramella, and J. Walcher. The spatial clustering of X-ray selected AGN in the XMM-COSMOS field., 494(1):33–48, January 2009.

- R. Gilli, C. Vignali, M. Mignoli, K. Iwasawa, A. Comastri, and G. Zamorani. The X-ray to [Ne V]3426 flux ratio: discovering heavily obscured AGN in the distant Universe. , 519:A92, September 2010. .
- R. Gilli, J. Su, C. Norman, C. Vignali, A. Comastri, P. Tozzi, P. Rosati, M. Stiavelli, W. N. Brandt, Y. Q. Xue, B. Luo, M. Castellano, A. Fontana, F. Fiore, V. Mainieri, and A. Ptak. A Compton-thick Active Galactic Nucleus at z ~5 in the 4 Ms Chandra Deep Field South. , 730(2):L28, April 2011. .
- R. Gilli, C. Norman, C. Vignali, E. Vanzella, F. Calura, F. Pozzi, M. Massardi, A. Mignano, V. Casasola, E. Daddi, D. Elbaz, M. Dickinson, K. Iwasawa, R. Maiolino, M. Brusa, F. Vito, J. Fritz, A. Feltre, G. Cresci, M. Mignoli, A. Comastri, and G. Zamorani. ALMA reveals a warm and compact starburst around a heavily obscured supermassive black hole at z = 4.75., 562:A67, February 2014.
- R. Gilli, C. Norman, F. Calura, F. Vito, R. Decarli, S. Marchesi, K. Iwasawa, A. Comastri, G. Lanzuisi, F. Pozzi, C. Vignali, M. Brusa, M. Mignoli, and P. Cox. Supermassive Black Holes at High Redshift are Expected to be Obscured by their Massive Host Galaxies' Inter Stellar Medium. *arXiv e-prints*, art. arXiv:2206.03508, June 2022.
- C. Gómez-Guijarro, D. Elbaz, M. Xiao, M. Béthermin, M. Franco, B. Magnelli, E. Daddi, M. Dickinson, R. Demarco, H. Inami, W. Rujopakarn, G. E. Magdis, X. Shu, R. Chary, L. Zhou, D. M. Alexander, F. Bournaud, L. Ciesla, H. C. Ferguson, S. L. Finkelstein, M. Giavalisco, D. Iono, S. Juneau, J. S. Kartaltepe, G. Lagache, E. Le Floc'h, R. Leiton, L. Lin, K. Motohara, J. Mullaney, K. Okumura, M. Pannella, C. Papovich, A. Pope, M. T. Sargent, J. D. Silverman, E. Treister, and T. Wang. GOODS-ALMA 2.0: Source catalog, number counts, and prevailing compact sizes in 1.1 mm galaxies. , 658:A43, February 2022. .
- A. D. Goulding, D. M. Alexander, F. E. Bauer, W. R. Forman, R. C. Hickox, C. Jones, J. R. Mullaney, and M. Trichas. Deep Silicate Absorption Features in Compton-thick

Active Galactic Nuclei Predominantly Arise due to Dust in the Host Galaxy. , 755(1): 5, August 2012. .

- J. F. R. Gower, P. F. Scott, and D. Wills. A survey of radio sources in the declination ranges —07° to 20° and 40° to 80°., 71:49, January 1967.
- G. L. Granato, L. Silva, A. Lapi, F. Shankar, G. De Zotti, and L. Danese. The growth of the nuclear black holes in submillimetre galaxies. , 368(1):L72–L76, May 2006.
- Gian Luigi Granato, Gianfranco De Zotti, Laura Silva, Alessandro Bressan, and Luigi Danese. A Physical Model for the Coevolution of QSOs and Their Spheroidal Hosts. , 600(2):580–594, January 2004.
- Gian Luigi Granato, Cinthia Ragone-Figueroa, Rosa Domínguez-Tenreiro, Aura Obreja, Stefano Borgani, Gabriella De Lucia, and Giuseppe Murante. The early phases of galaxy clusters formation in IR: coupling hydrodynamical simulations with GRASIL-3D., 450(2):1320–1332, June 2015.
- Claire Greenwell, Poshak Gandhi, Daniel Stern, George Lansbury, Vincenzo Mainieri, Peter Boorman, and Yoshiki Toba. A population of Optically Quiescent Quasars from WISE and SDSS., 527(4):12065–12090, February 2024.
- Claire Louise Greenwell. *The selection, analysis and implications of rare AGN in large surveys.* PhD thesis, University of Southampton, United Kingdom, October 2023. URL https://eprints.soton.ac.uk/476205/.
- Norman A. Grogin, Dale D. Kocevski, S. M. Faber, Henry C. Ferguson, Anton M. Koekemoer, Adam G. Riess, Viviana Acquaviva, David M. Alexander, Omar Almaini, Matthew L. N. Ashby, Marco Barden, Eric F. Bell, Frédéric Bournaud, Thomas M. Brown, Karina I. Caputi, Stefano Casertano, Paolo Cassata, Marco Castellano, Peter Challis, Ranga-Ram Chary, Edmond Cheung, Michele Cirasuolo, Christopher J. Conselice, Asantha Roshan Cooray, Darren J. Croton, Emanuele Daddi, Tomas Dahlen, Romeel Davé, Duília F. de Mello, Avishai Dekel, Mark Dickinson, Timothy Dolch, Jennifer L. Donley, James S. Dunlop, Aaron A. Dutton, David Elbaz, Giovanni G. Fazio, Alexei V. Filippenko, Steven L. Finkelstein, Adriano Fontana, Jonathan P. Gardner, Peter M. Garnavich, Eric Gawiser, Mauro Giavalisco, Andrea Grazian, Yicheng Guo, Nimish P. Hathi, Boris Häussler, Philip F. Hopkins, Jia-Sheng Huang, Kuang-Han Huang, Saurabh W. Jha, Jeyhan S. Kartaltepe, Robert P. Kirshner, David C. Koo, Kamson Lai, Kyoung-Soo Lee, Weidong Li, Jennifer M. Lotz, Ray A. Lucas, Piero Madau, Patrick J. McCarthy, Elizabeth J. McGrath, Daniel H. McIntosh, Ross J. McLure, Bahram Mobasher, Leonidas A. Moustakas, Mark Mozena, Kirpal Nandra, Jeffrey A. Newman, Sami-Matias Niemi, Kai G. Noeske, Casey J. Papovich, Laura Pentericci, Alexandra Pope, Joel R. Primack, Abhijith Rajan, Swara Ravindranath, Naveen A. Reddy, Alvio Renzini, Hans-Walter Rix, Aday R. Robaina, Steven A. Rodney, David J. Rosario, Piero Rosati, Sara Salimbeni, Claudia Scarlata,

Brian Siana, Luc Simard, Joseph Smidt, Rachel S. Somerville, Hyron Spinrad, Amber N. Straughn, Louis-Gregory Strolger, Olivia Telford, Harry I. Teplitz, Jonathan R. Trump, Arjen van der Wel, Carolin Villforth, Risa H. Wechsler, Benjamin J. Weiner, Tommy Wiklind, Vivienne Wild, Grant Wilson, Stijn Wuyts, Hao-Jing Yan, and Min S. Yun. CANDELS: The Cosmic Assembly Near-infrared Deep Extragalactic Legacy Survey. , 197(2):35, December 2011. .

- Brent A. Groves, Eva Schinnerer, Adam Leroy, Maud Galametz, Fabian Walter, Alberto Bolatto, Leslie Hunt, Daniel Dale, Daniela Calzetti, Kevin Croxall, and Jr. Kennicutt, Robert. Dust Continuum Emission as a Tracer of Gas Mass in Galaxies. , 799(1):96, January 2015. .
- Philip J. Grylls, F. Shankar, J. Leja, N. Menci, B. Moster, P. Behroozi, and L. Zanisi. Predicting fully self-consistent satellite richness, galaxy growth, and star formation rates from the STatistical sEmi-Empirical modeL STEEL. , 491(1):634–654, January 2020. .
- Philip John Grylls. *Growing self consistent galaxies in empirically modelled environments using steel: the STatistical sEmi-Empirical modeL*. PhD thesis, University of Southampton, United Kingdom, June 2020. URL https://eprints.soton.ac.uk/447141/.
- Kathleen A. Hamilton-Campos, Raymond C. Simons, Molly S. Peeples, Gregory F. Snyder, and Timothy M. Heckman. The Physical Thickness of Stellar Disks to z ~2. *arXiv e-prints*, art. arXiv:2303.04171, March 2023.
- C. M. Harrison. Impact of supermassive black hole growth on star formation. *Nature Astronomy*, 1:0165, July 2017. .
- Christopher Mark Chris Harrison. *Observational constraints on the influence of active galactic nuclei on the evolution of galaxies*. PhD thesis, Durham University, UK, January 2014.
- Tilman Hartwig, Marta Volonteri, and Gohar Dashyan. Active galactic nucleus outflows in galaxy discs. , 476(2):2288–2307, May 2018. .
- G. Hasinger. Absorption properties and evolution of active galactic nuclei. , 490(3): 905–922, November 2008. .
- Steve Hatton, Julien E. G. Devriendt, Stéphane Ninin, François R. Bouchet, Bruno Guiderdoni, and Didier Vibert. GALICS- I. A hybrid N-body/semi-analytic model of hierarchical galaxy formation. , 343(1):75–106, July 2003. .
- T. M. Heckman. The broad line region in active nuclei and quasars Correlations with luminosity and radio emission. , 88(3):311–316, August 1980.
- Bruno M. B. Henriques, Simon D. M. White, Peter A. Thomas, Raul E. Angulo, Qi Guo, Gerard Lemson, and Volker Springel. Simulations of the galaxy population constrained by observations from z=3 to the present day: implications for galactic winds and the fate of their ejecta. , 431(4):3373-3395, June 2013. .

Bruno M. B. Henriques, Simon D. M. White, Peter A. Thomas, Raul Angulo, Qi Guo, Gerard Lemson, Volker Springel, and Roderik Overzier. Galaxy formation in the Planck cosmology - I. Matching the observed evolution of star formation rates, colours and stellar masses. , 451(3):2663–2680, August 2015.

- Bruno M. B. Henriques, Robert M. Yates, Jian Fu, Qi Guo, Guinevere Kauffmann, Chaichalit Srisawat, Peter A. Thomas, and Simon D. M. White. L-GALAXIES 2020: Spatially resolved cold gas phases, star formation, and chemical enrichment in galactic discs. , 491(4):5795–5814, February 2020. .
- Lars Hernquist and Neal Katz. TREESPH: A Unification of SPH with the Hierarchical Tree Method. , 70:419, June 1989. .
- A. Hewitt and G. Burbidge. A Revised and Updated Catalog of Quasi-stellar Objects. , 87:451, August 1993. .
- Timothy Hewlett, Carolin Villforth, Vivienne Wild, Jairo Mendez-Abreu, Milena Pawlik, and Kate Rowlands. The redshift evolution of major merger triggering of luminous AGNs: a slight enhancement at $z\sim2$., 470(1):755-770, September 2017.
- Ryan C. Hickox and David M. Alexander. Obscured Active Galactic Nuclei. , 56:625–671, September 2018. .
- Ryan C. Hickox, Adam D. Myers, Mark Brodwin, David M. Alexander, William R. Forman, Christine Jones, Stephen S. Murray, Michael J. I. Brown, Richard J. Cool, Christopher S. Kochanek, Arjun Dey, Buell T. Jannuzi, Daniel Eisenstein, Roberto J. Assef, Peter R. Eisenhardt, Varoujan Gorjian, Daniel Stern, Emeric Le Floc'h, Nelson Caldwell, Andrew D. Goulding, and James R. Mullaney. Clustering of Obscured and Unobscured Quasars in the Boötes Field: Placing Rapidly Growing Black Holes in the Cosmic Web., 731(2):117, April 2011.
- Kazuo Hiroi, Yoshihiro Ueda, Naoki Isobe, Masaaki Hayashida, Satoshi Eguchi, Mutsumi Sugizaki, Nobuyuki Kawai, Hiroshi Tsunemi, Masaru Matsuoka, Tatehiro Mihara, Kazutaka Yamaoka, Masaki Ishikawa, Masashi Kimura, Hiroki Kitayama, Mitsuhiro Kohama, Takanori Matsumura, Mikio Morii, Yujin E. Nakagawa, Satoshi Nakahira, Motoki Nakajima, Hitoshi Negoro, Motoko Serino, Megumi Shidatsu, Tetsuya Sootome, Kousuke Sugimori, Fumitoshi Suwa, Takahiro Toizumi, Hiroshi Tomida, Yohko Tsuboi, Shiro Ueno, Ryuichi Usui, Takayuki Yamamoto, Kyohei Yamazaki, and Atsumasa Yoshida. The First MAXI/GSC Catalog in the High Galactic-Latitude Sky., 63:S677–S689, November 2011.
- Michaela Hirschmann, Gabriella De Lucia, and Fabio Fontanot. Galaxy assembly, stellar feedback and metal enrichment: the view from the GAEA model. , 461(2):1760–1785, September 2016. .

JA Hodge, Ian Smail, F Walter, Elisabete da Cunha, AM Swinbank, M Rybak, B Venemans, WN Brandt, G Calistro Rivera, Scott C Chapman, et al. Alma reveals potential evidence for spiral arms, bars, and rings in high-redshift submillimeter galaxies. *The Astrophysical Journal*, 876(2):130, 2019.

- Jacqueline A. Hodge, Elisabete da Cunha, Sarah Kendrew, Juno Li, Ian Smail, Bethany A. Westoby, Omnarayani Nayak, Mark Swinbank, Chian-Chou Chen, Fabian Walter, Paul van der Werf, Misty Cracraft, Andrew Battisti, Willian N. Brandt, Gabriela Calistro Rivera, Scott C. Chapman, Pierre Cox, Helmut Dannerbauer, Roberto Decarli, Marta Frias Castillo, Thomas R. Greve, Kirsten K. Knudsen, Sarah Leslie, Karl M. Menten, Matus Rybak, Eva Schinnerer, Julie L. Wardlow, and Axel Weiss. ALESS-JWST: Joint (sub-)kiloparsec JWST and ALMA imaging of $z\sim 3$ submillimeter galaxies reveals heavily obscured bulge formation events. $arXiv\ e-prints$, art. arXiv:2407.15846, July 2024.
- Sebastian F. Hönig. Redefining the Torus: A Unifying View of AGNs in the Infrared and Submillimeter., 884(2):171, October 2019.
- Sebastian F. Hönig and Makoto Kishimoto. Dusty Winds in Active Galactic Nuclei: Reconciling Observations with Models. , 838(2):L20, April 2017. .
- Sebastian F. Hönig, Almudena Alonso Herrero, Poshak Gandhi, Makoto Kishimoto, Jörg-Uwe Pott, Cristina Ramos Almeida, Jean Surdej, and Konrad R. W. Tristram. New active galactic nuclei science cases with interferometry. An incomplete preview. *Experimental Astronomy*, 46(3):413–419, December 2018.
- Philip F. Hopkins. A New Public Release of the GIZMO Code. *arXiv e-prints*, art. arXiv:1712.01294, December 2017. .
- Philip F. Hopkins and Eliot Quataert. An analytic model of angular momentum transport by gravitational torques: from galaxies to massive black holes. , 415(2):1027–1050, August 2011. .
- Philip F. Hopkins, Lars Hernquist, Thomas J. Cox, Tiziana Di Matteo, Paul Martini, Brant Robertson, and Volker Springel. Black Holes in Galaxy Mergers: Evolution of Quasars., 630(2):705–715, September 2005.
- Philip F. Hopkins, Lars Hernquist, Thomas J. Cox, Tiziana Di Matteo, Brant Robertson, and Volker Springel. A Unified, Merger-driven Model of the Origin of Starbursts, Quasars, the Cosmic X-Ray Background, Supermassive Black Holes, and Galaxy Spheroids. , 163(1):1–49, March 2006a.
- Philip F. Hopkins, Rachel S. Somerville, Lars Hernquist, Thomas J. Cox, Brant Robertson, and Yuexing Li. The Relation between Quasar and Merging Galaxy Luminosity Functions and the Merger-driven Star Formation History of the Universe., 652(2): 864–888, December 2006b.

Philip F. Hopkins, Gordon T. Richards, and Lars Hernquist. An Observational Determination of the Bolometric Quasar Luminosity Function. , 654(2):731–753, January 2007. .

- Philip F. Hopkins, Lars Hernquist, Thomas J. Cox, and Dušan Kereš. A Cosmological Framework for the Co-Evolution of Quasars, Supermassive Black Holes, and Elliptical Galaxies. I. Galaxy Mergers and Quasar Activity. , 175(2):356–389, April 2008.
- Philip F. Hopkins, Joshua D. Younger, Christopher C. Hayward, Desika Narayanan, and Lars Hernquist. Mergers, active galactic nuclei and 'normal' galaxies: contributions to the distribution of star formation rates and infrared luminosity functions. , 402(3):1693–1713, March 2010. .
- Katelyn Horstman, Alice E. Shapley, Ryan L. Sanders, Bahram Mobasher, Naveen A. Reddy, Mariska Kriek, Alison L. Coil, Brian Siana, Irene Shivaei, William R. Freeman, Mojegan Azadi, Sedona H. Price, Gene C. K. Leung, Tara Fetherolf, Laura de Groot, Tom Zick, Francesca M. Fornasini, and Guillermo Barro. The MOSDEF survey: differences in SFR and metallicity for morphologically selected mergers at $z\sim2$. , 501 (1):137–145, February 2021. .
- Deidre A. Hunter, Bruce G. Elmegreen, Esther Goldberger, Hannah Taylor, Anton I. Ermakov, Kimberly A. Herrmann, Se-Heon Oh, Bradley Malko, Brian Barandi, and Ryan Jundt. Relationships between the Stellar, Gaseous, and Star Formation Disks in LITTLE THINGS Dwarf Irregular Galaxies: Indirect Evidence for Substantial Fractions of Dark Molecular Gas. , 161(2):71, February 2021.
- Edoardo Iani, Pierluigi Rinaldi, Karina I. Caputi, Marianna Annunziatella, Danial Langeroodi, Jens Melinder, Pablo G. Pérez-González, Javier Álvarez-Márquez, Leindert A. Boogaard, Sarah E. I. Bosman, Luca Costantin, Thibaud Moutard, Luis Colina, Göran Östlin, Thomas R. Greve, Gillian Wright, Almudena Alonso-Herrero, Arjan Bik, Steven Gillman, Alejandro Crespo Gómez, Jens Hjorth, Alvaro Labiano, John P. Pye, Tuomo V. Tikkanen, and Paul P. van der Werf. MIDIS: MIRI uncovers Virgil, an extended source at $z\simeq 6.6$ with the photometric properties of Little Red Dots. arXiv e-prints, art. arXiv:2406.18207, June 2024.
- Masatoshi Imanishi, Kouichiro Nakanishi, and Takuma Izumi. ALMA 0.1-0.2 arcsec Resolution Imaging of the NGC 1068 Nucleus: Compact Dense Molecular Gas Emission at the Putative AGN Location. , 822(1):L10, May 2016. .
- J. W. Isbell, K. Meisenheimer, J. U. Pott, M. Stalevski, K. R. W. Tristram, J. Sanchez-Bermudez, K. H. Hofmann, V. Gámez Rosas, W. Jaffe, L. Burtscher, J. Leftley, R. Petrov, B. Lopez, T. Henning, G. Weigelt, F. Allouche, P. Berio, F. Bettonvil, P. Cruzalebes, C. Dominik, M. Heininger, M. Hogerheijde, S. Lagarde, M. Lehmitz, A. Matter, A. Meilland, F. Millour, S. Robbe-Dubois, D. Schertl, R. van Boekel,

J. Varga, and J. Woillez. The dusty heart of Circinus. I. Imaging the circumnuclear dust in N-band., 663:A35, July 2022.

- J. W. Isbell, J. U. Pott, K. Meisenheimer, M. Stalevski, K. R. W. Tristram, J. Leftley, D. Asmus, G. Weigelt, V. Gámez Rosas, R. Petrov, W. Jaffe, K. H. Hofmann, T. Henning, and B. Lopez. The dusty heart of Circinus. II. Scrutinizing the LM-band dust morphology using MATISSE., 678:A136, October 2023.
- W. Ishibashi and A. C. Fabian. AGN feedback: galactic-scale outflows driven by radiation pressure on dust. , 451(1):93–102, July 2015. .
- W. Ishibashi and A. C. Fabian. AGN-starburst evolutionary connection: a physical interpretation based on radiative feedback. , 463(2):1291–1296, December 2016. .
- W. Ishibashi, A. C. Fabian, and R. Maiolino. The energetics of AGN radiation pressure-driven outflows. , 476(1):512–519, May 2018. .
- R. C. Jennison and M. K. Das Gupta. Fine Structure of the Extra-terrestrial Radio Source Cygnus I. , 172(4387):996–997, November 1953. .
- Fangzhou Jiang, Avishai Dekel, Jonathan Freundlich, Frank C. van den Bosch, Sheridan B. Green, Philip F. Hopkins, Andrew Benson, and Xiaolong Du. SatGen: a semi-analytical satellite galaxy generator I. The model and its application to Local-Group satellite statistics. , 502(1):621–641, March 2021.
- Ning Jiang, Huiyuan Wang, Houjun Mo, Xiao-Bo Dong, Tinggui Wang, and Hongyan Zhou. Differences in Halo-scale Environments between Type 1 and Type 2 AGNs at Low Redshift., 832(2):111, December 2016.
- Ignas Juodžbalis, Christopher J. Conselice, Maitrayee Singh, Nathan Adams, Katherine Ormerod, Thomas Harvey, Duncan Austin, Marta Volonteri, Seth H. Cohen, Rolf A. Jansen, Jake Summers, Rogier A. Windhorst, Jordan C. J. D'Silva, Anton M. Koekemoer, Dan Coe, Simon P. Driver, Brenda Frye, Norman A. Grogin, Madeline A. Marshall, Mario Nonino, Nor Pirzkal, Aaron Robotham, Russell E. Jr., Ryan, III Ortiz, Rafael, Scott Tompkins, Christopher N. A. Willmer, and Haojing Yan. EPOCHS VII: discovery of high-redshift (6.5 ; z ; 12) AGN candidates in JWST ERO and PEARLS data., 525(1):1353–1364, October 2023.
- M. Kaasinen, N. Scoville, F. Walter, E. Da Cunha, G. Popping, R. Pavesi, B. Darvish, C. M. Casey, D. A. Riechers, and S. Glover. The Molecular Gas Reservoirs of z \sim 2 Galaxies: A Comparison of CO(1-0) and Dust-based Molecular Gas Masses. , 880(1): 15, July 2019.
- D. Kakkad, V. Mainieri, M. Brusa, P. Padovani, S. Carniani, C. Feruglio, M. Sargent, B. Husemann, A. Bongiorno, M. Bonzini, E. Piconcelli, J. D. Silverman, and W. Rujopakarn. ALMA observations of cold molecular gas in AGN hosts at $z\sim1.5$ evidence of AGN feedback? , 468(4):4205–4215, July 2017. .

Simon J. Karl, Thorsten Naab, Peter H. Johansson, Hanna Kotarba, Christian M. Boily, Florent Renaud, and Christian Theis. One Moment in Time—Modeling Star Formation in the Antennae. , 715(2):L88–L93, June 2010.

- J. I. Katz. Nonrelativistic Compton scattering and models of quasars. , 206:910–916, June 1976. .
- J. A. Kegerreis, V. R. Eke, P. Gonnet, D. G. Korycansky, R. J. Massey, M. Schaller, and L. F. A. Teodoro. Planetary giant impacts: convergence of high-resolution simulations using efficient spherical initial conditions and SWIFT. , 487(4):5029–5040, August 2019. .
- K. I. Kellermann, R. Sramek, M. Schmidt, D. B. Shaffer, and R. Green. VLA Observations of Objects in the Palomar Bright Quasar Survey., 98:1195, October 1989.
- Jr. Kennicutt, Robert C., William C. Keel, J. M. van der Hulst, E. Hummel, and Kurt A. Roettiger. The Effects of Interactions on Spiral Galaxies. II. Disk Star Formation Rates., 93:1011, May 1987.
- E. Y. Khachikian and D. W. Weedman. An atlas of Seyfert galaxies. , 192:581–589, September 1974. .
- Meghana Killi, Darach Watson, Gabriel Brammer, Conor McPartland, Jacqueline Antwi-Danso, Rosa Newshore, Dan Coe, Natalie Allen, Johan P. U. Fynbo, Katriona Gould, Kasper E. Heintz, Vadim Rusakov, and Simone Vejlgaard. Deciphering the JWST spectrum of a 'little red dot' at $z\sim4.53$: An obscured AGN and its star-forming host. $arXiv\ e$ -prints, art. $arXiv\ 2312.03065$, December 2023.
- A. R. King, K. Zubovas, and C. Power. Large-scale outflows in galaxies. , 415(1):L6–L10, July 2011. .
- Andrew King. Black Holes, Galaxy Formation, and the M_{BH} - σ Relation. , 596(1):L27–L29, October 2003. .
- Andrew King and Ken Pounds. Powerful Outflows and Feedback from Active Galactic Nuclei. , 53:115–154, August 2015. .
- J. H. Knapen, E. L. Allard, L. M. Mazzuca, M. Sarzi, and R. F. Peletier. Star formation in the central regions of galaxies. *Astronomy and astrophysics*, 448(2), 2006. ISSN 1432-0746. Relation: http://www.rug.nl/date_submitted: 2006Rights: *University of Groningen*.
- Johan H. Knapen, Mauricio Cisternas, and Miguel Querejeta. Interacting galaxies in the nearby Universe: only moderate increase of star formation. , 454(2):1742–1750, December 2015. .

Dale D. Kocevski, Murray Brightman, Kirpal Nandra, Anton M. Koekemoer, Mara Salvato, James Aird, Eric F. Bell, Li-Ting Hsu, Jeyhan S. Kartaltepe, David C. Koo, Jennifer M. Lotz, Daniel H. McIntosh, Mark Mozena, David Rosario, and Jonathan R. Trump. Are Compton-thick AGNs the Missing Link between Mergers and Black Hole Growth? ,814(2):104, December 2015.

Anton M. Koekemoer, S. M. Faber, Henry C. Ferguson, Norman A. Grogin, Dale D. Kocevski, David C. Koo, Kamson Lai, Jennifer M. Lotz, Ray A. Lucas, Elizabeth J. Mc-Grath, Sara Ogaz, Abhijith Rajan, Adam G. Riess, Steve A. Rodney, Louis Strolger, Stefano Casertano, Marco Castellano, Tomas Dahlen, Mark Dickinson, Timothy Dolch, Adriano Fontana, Mauro Giavalisco, Andrea Grazian, Yicheng Guo, Nimish P. Hathi, Kuang-Han Huang, Arjen van der Wel, Hao-Jing Yan, Viviana Acquaviva, David M. Alexander, Omar Almaini, Matthew L. N. Ashby, Marco Barden, Eric F. Bell, Frédéric Bournaud, Thomas M. Brown, Karina I. Caputi, Paolo Cassata, Peter J. Challis, Ranga-Ram Chary, Edmond Cheung, Michele Cirasuolo, Christopher J. Conselice, Asantha Roshan Cooray, Darren J. Croton, Emanuele Daddi, Romeel Davé, Duilia F. de Mello, Loic de Ravel, Avishai Dekel, Jennifer L. Donley, James S. Dunlop, Aaron A. Dutton, David Elbaz, Giovanni G. Fazio, Alexei V. Filippenko, Steven L. Finkelstein, Chris Frazer, Jonathan P. Gardner, Peter M. Garnavich, Eric Gawiser, Ruth Gruetzbauch, Will G. Hartley, Boris Häussler, Jessica Herrington, Philip F. Hopkins, Jia-Sheng Huang, Saurabh W. Jha, Andrew Johnson, Jeyhan S. Kartaltepe, Ali A. Khostovan, Robert P. Kirshner, Caterina Lani, Kyoung-Soo Lee, Weidong Li, Piero Madau, Patrick J. McCarthy, Daniel H. McIntosh, Ross J. McLure, Conor McPartland, Bahram Mobasher, Heidi Moreira, Alice Mortlock, Leonidas A. Moustakas, Mark Mozena, Kirpal Nandra, Jeffrey A. Newman, Jennifer L. Nielsen, Sami Niemi, Kai G. Noeske, Casey J. Papovich, Laura Pentericci, Alexandra Pope, Joel R. Primack, Swara Ravindranath, Naveen A. Reddy, Alvio Renzini, Hans-Walter Rix, Aday R. Robaina, David J. Rosario, Piero Rosati, Sara Salimbeni, Claudia Scarlata, Brian Siana, Luc Simard, Joseph Smidt, Diana Snyder, Rachel S. Somerville, Hyron Spinrad, Amber N. Straughn, Olivia Telford, Harry I. Teplitz, Jonathan R. Trump, Carlos Vargas, Carolin Villforth, Cory R. Wagner, Pat Wandro, Risa H. Wechsler, Benjamin J. Weiner, Tommy Wiklind, Vivienne Wild, Grant Wilson, Stijn Wuyts, and Min S. Yun. CANDELS: The Cosmic Assembly Near-infrared Deep Extragalactic Legacy Survey—The Hubble Space Telescope Observations, Imaging Data Products, and Mosaics., 197(2):36, December 2011. .

Vasily Kokorev, Karina I. Caputi, Jenny E. Greene, Pratika Dayal, Maxime Trebitsch, Sam E. Cutler, Seiji Fujimoto, Ivo Labbé, Tim B. Miller, Edoardo Iani, Rafael Navarro-Carrera, and Pierluigi Rinaldi. A Census of Photometrically Selected Little Red Dots at 4 ; z ; 9 in JWST Blank Fields. , 968(1):38, June 2024.

M. P. Koprowski, J. V. Wijesekera, J. S. Dunlop, D. J. McLeod, M. J. Michałowski, K. Lisiecki, and R. J. McLure. Charting the main sequence of star-forming galaxies out to redshifts z-7. *arXiv e-prints*, art. arXiv:2403.06575, March 2024. .

John Kormendy and Luis C. Ho. Coevolution (Or Not) of Supermassive Black Holes and Host Galaxies. , 51(1):511–653, August 2013. .

- John Kormendy and Douglas Richstone. Inward Bound—The Search For Supermassive Black Holes In Galactic Nuclei. , 33:581, January 1995. .
- Michael J. Koss, Benjamin Strittmatter, Isabella Lamperti, Taro Shimizu, Benny Trakhtenbrot, Amelie Saintonge, Ezequiel Treister, Claudia Cicone, Richard Mushotzky, Kyuseok Oh, Claudio Ricci, Daniel Stern, Tonima Tasnim Ananna, Franz E. Bauer, George C. Privon, Rudolf E. Bär, Carlos De Breuck, Fiona Harrison, Kohei Ichikawa, Meredith C. Powell, David Rosario, David B. Sanders, Kevin Schawinski, Li Shao, C. Megan Urry, and Sylvain Veilleux. BAT AGN Spectroscopic Survey. XX. Molecular Gas in Nearby Hard-X-Ray-selected AGN Galaxies. , 252(2):29, February 2021.
- L. Koutoulidis, I. Georgantopoulos, G. Mountrichas, M. Plionis, A. Georgakakis, A. Akylas, and E. Rovilos. Dependence of clustering of X-ray AGN on obscuration. , 481(3): 3063–3069, December 2018. .
- A. V. Kravtsov, A. A. Vikhlinin, and A. V. Meshcheryakov. Stellar Mass—Halo Mass Relation and Star Formation Efficiency in High-Mass Halos. *Astronomy Letters*, 44(1): 8–34, January 2018.
- Andrey V. Kravtsov, Andreas A. Berlind, Risa H. Wechsler, Anatoly A. Klypin, Stefan Gottlöber, Brandon Allgood, and Joel R. Primack. The Dark Side of the Halo Occupation Distribution. , 609(1):35–49, July 2004.
- Mirko Krumpe, Takamitsu Miyaji, Alison L. Coil, and Hector Aceves. The Spatial Clustering of ROSAT All-Sky Survey Active Galactic Nuclei. III. Expanded Sample and Comparison with Optical Active Galactic Nuclei. , 746(1):1, February 2012. .
- Mirko Krumpe, Takamitsu Miyaji, Alison L. Coil, and Hector Aceves. Spatial clustering and halo occupation distribution modelling of local AGN via cross-correlation measurements with 2MASS galaxies. , 474(2):1773–1786, February 2018. .
- L. Kuhn, J. Shangguan, R. Davies, A. W. S. Man, Y. Cao, J. Dexter, F. Eisenhauer, N. M. Förster Schreiber, H. Feuchtgruber, R. Genzel, S. Gillessen, S. Hönig, D. Lutz, H. Netzer, T. Ott, S. Rabien, D. J. D. Santos, T. Shimizu, E. Sturm, and L. J. Tacconi. Broad-line region geometry from multiple emission lines in a single-epoch spectrum. , 684:A52, April 2024. .
- Ivo Labbe, Jenny E. Greene, Rachel Bezanson, Seiji Fujimoto, Lukas J. Furtak, Andy D. Goulding, Jorryt Matthee, Rohan P. Naidu, Pascal A. Oesch, Hakim Atek, Gabriel Brammer, Iryna Chemerynska, Dan Coe, Sam E. Cutler, Pratika Dayal, Robert Feldmann, Marijn Franx, Karl Glazebrook, Joel Leja, Danilo Marchesini, Michael Maseda, Themiya Nanayakkara, Erica J. Nelson, Richard Pan, Casey Papovich, Sedona H. Price, Katherine A. Suess, Bingjie Wang, Katherine E. Whitaker, Christina C. Williams, and

Adi Zitrin. UNCOVER: Candidate Red Active Galactic Nuclei at 3¡z¡7 with JWST and ALMA. *arXiv e-prints*, art. arXiv:2306.07320, June 2023. .

- Claudia del P. Lagos, Rodrigo J. Tobar, Aaron S. G. Robotham, Danail Obreschkow, Peter D. Mitchell, Chris Power, and Pascal J. Elahi. Shark: introducing an open source, free, and flexible semi-analytic model of galaxy formation. , 481(3):3573–3603, December 2018. .
- Claudia del P. Lagos, Aaron S. G. Robotham, James W. Trayford, Rodrigo Tobar, Matías Bravo, Sabine Bellstedt, Luke J. M. Davies, Simon P. Driver, Pascal J. Elahi, Danail Obreschkow, and Chris Power. From the far-ultraviolet to the far-infrared galaxy emission at $0 \le z \le 10$ in the SHARK semi-analytic model. , 489(3):4196–4216, November 2019. .
- Brivael Laloux, Antonis Georgakakis, Carolina Andonie, David M. Alexander, Angel Ruiz, David J. Rosario, James Aird, Johannes Buchner, Francisco J. Carrera, Andrea Lapi, Cristina Ramos Almeida, Mara Salvato, and Francesco Shankar. The demographics of obscured AGN from X-ray spectroscopy guided by multiwavelength information. , 518(2):2546–2566, January 2023.
- Brivael Laloux, Antonis Georgakakis, David M. Alexander, Johannes Buchner, Carolina Andonie, Nischal Acharya, James Aird, Alba V. Alonso-Tetilla, Angela Bongiorno, Ryan C. Hickox, Andrea Lapi, Blessing Musiimenta, Cristina Ramos Almeida, Carolin Villforth, and Francesco Shankar. Accretion properties of X-ray AGN: evidence for radiation-regulated obscuration with redshift-dependent host galaxy contribution. , 532(3):3459–3479, August 2024.
- A. Lamastra, N. Menci, R. Maiolino, F. Fiore, and A. Merloni. The building up of the black hole-stellar mass relation. , 405(1):29–40, June 2010. .
- G. Lanzuisi, P. Ranalli, I. Georgantopoulos, A. Georgakakis, I. Delvecchio, T. Akylas, S. Berta, A. Bongiorno, M. Brusa, N. Cappelluti, F. Civano, A. Comastri, R. Gilli, C. Gruppioni, G. Hasinger, K. Iwasawa, A. Koekemoer, E. Lusso, S. Marchesi, V. Mainieri, A. Merloni, M. Mignoli, E. Piconcelli, F. Pozzi, D. J. Rosario, M. Salvato, J. Silverman, B. Trakhtenbrot, C. Vignali, and G. Zamorani. Compton thick AGN in the XMM-COSMOS survey. , 573:A137, January 2015.
- A. Lapi, A. Cavaliere, and N. Menci. Intracluster and Intragroup Entropy from Quasar Activity., 619(1):60–72, January 2005.
- A. Lapi, F. Shankar, J. Mao, G. L. Granato, L. Silva, G. De Zotti, and L. Danese. Quasar Luminosity Functions from Joint Evolution of Black Holes and Host Galaxies., 650(1): 42–56, October 2006.
- A. Lapi, S. Raimundo, R. Aversa, Z. Y. Cai, M. Negrello, A. Celotti, G. De Zotti, and L. Danese. The Coevolution of Supermassive Black Holes and Massive Galaxies at High Redshift., 782(2):69, February 2014.

A. Lapi, C. Mancuso, A. Bressan, and L. Danese. Stellar Mass Function of Active and Quiescent Galaxies via the Continuity Equation. , 847(1):13, September 2017. .

- Sharon Lapiner, Avishai Dekel, Jonathan Freundlich, Omri Ginzburg, Fangzhou Jiang, Michael Kretschmer, Sandro Tacchella, Daniel Ceverino, and Joel Primack. Wet compaction to a blue nugget: a critical phase in galaxy evolution. , 522(3):4515–4547, July 2023. .
- A. Lawrence. The relative frequency of broad-lined and narrow-lined active galactic nuclei: implications for unified schemes., 252:586, October 1991.
- M. T. Leist, C. Packham, D. J. V. Rosario, D. A. Hope, A. Alonso-Herrero, E. K. S. Hicks, S. Hönig, L. Zhang, R. Davies, T. Díaz-Santos, O. Ganzález-Martín, E. Bellocchi, P. G. Boorman, F. Combes, I. García-Bernete, S. García-Burillo, B. García-Lorenzo, H. Haidar, K. Ichikawa, M. Imanishi, S. M. Jefferies, Á. Labiano, N. A. Levenson, R. Nikutta, M. Pereira-Santaella, C. Ramos Almeida, C. Ricci, D. Rigopoulou, W. Schaefer, M. Stalevski, M. J. Ward, L. Fuller, T. Izumi, D. Rouan, and T. Shimizu. Deconvolution of JWST/MIRI Images: Applications to an AGN Model and GATOS Observations of NGC 5728. arXiv e-prints, art. arXiv:2312.14307, December 2023. .
- Joel Leja, Joshua S. Speagle, Yuan-Sen Ting, Benjamin D. Johnson, Charlie Conroy, Katherine E. Whitaker, Erica J. Nelson, Pieter van Dokkum, and Marijn Franx. A New Census of the 0.2 ; z ; 3.0 Universe. II. The Star-forming Sequence. , 936(2):165, September 2022.
- Adam K. Leroy, Fabian Walter, Elias Brinks, Frank Bigiel, W. J. G. de Blok, Barry Madore, and M. D. Thornley. The Star Formation Efficiency in Nearby Galaxies: Measuring Where Gas Forms Stars Effectively. , 136(6):2782–2845, December 2008.
- Shihong Liao, Peter H. Johansson, Matias Mannerkoski, Dimitrios Irodotou, Francesco Paolo Rizzuto, Stuart McAlpine, Antti Rantala, Alexander Rawlings, and Till Sawala. Modelling the accretion and feedback of supermassive black hole binaries in gas-rich galaxy mergers. , 520(3):4463–4489, April 2023. .
- Chen-Fatt Lim, Wei-Hao Wang, Ian Smail, Douglas Scott, Chian-Chou Chen, Yu-Yen Chang, James M. Simpson, Yoshiki Toba, Xinwen Shu, Dave Clements, Josh Greenslade, YiPing Ao, Arif Babul, Jack Birkin, Scott C. Chapman, Tai-An Cheng, Brian S. Cho, Helmut Dannerbauer, Ugnė Dudzevičiūtė, James Dunlop, Yu Gao, Tomotsugu Goto, Luis C. Ho, Li-Ting Hsu, Ho Seong Hwang, Woong-Seob Jeong, Maciej Koprowski, Chien-Hsiu Lee, Ming-Yi Lin, Wei-Ching Lin, Michał J. Michałowski, Harriet Parsons, Marcin Sawicki, Raphael Shirley, Hyunjin Shim, Sheona Urquhart, Jianfa Wang, and Tao Wang. SCUBA-2 Ultra Deep Imaging EAO Survey (Studies). III. Multiwavelength Properties, Luminosity Functions, and Preliminary Source Catalog of 450 µm Selected Galaxies. , 889(2):80, February 2020.

Sean T. Linden and J. Christopher Mihos. A Dynamical Model of the M101/NGC 5474 Encounter. , 933(2):L33, July 2022. .

- U. Lisenfeld, K. Alatalo, C. Zucker, P. N. Appleton, S. Gallagher, P. Guillard, and K. Johnson. The role of molecular gas in galaxy transition in compact groups. , 607:A110, November 2017.
- Daizhong Liu, Emanuele Daddi, Eva Schinnerer, Toshiki Saito, Adam Leroy, John D. Silverman, Francesco Valentino, Georgios E. Magdis, Yu Gao, Shuowen Jin, Annagrazia Puglisi, and Brent Groves. CO Excitation, Molecular Gas Density, and Interstellar Radiation Field in Local and High-redshift Galaxies., 909(1):56, March 2021.
- Zhaoxuan Liu, John D. Silverman, Emanuele Daddi, Annagrazia Puglisi, Alvio Renzini, Boris S. Kalita, Jeyhan S. Kartaltepe, Daichi Kashino, Giulia Rodighiero, Wiphu Rujopakarn, Tomoko L. Suzuki, Takumi S. Tanaka, Francesco Valentino, Irham Taufik Andika, Caitlin M. Casey, Andreas Faisst, Maximilien Franco, Ghassem Gozaliasl, Steven Gillman, Christopher C. Hayward, Anton M. Koekemoer, Vasily Kokorev, Erini Lambrides, Minju M. Lee, Georgios E. Magdis, Santosh Harish, Henry Joy McCracken, Jason Rhodes, Marko Shuntov, and Xuheng Ding. JWST and ALMA Discern the Assembly of Structural and Obscured Components in a High-redshift Starburst Galaxy., 968(1):15, June 2024.

Malcolm S. Longair. High Energy Astrophysics. 2011.

- I. E. López, M. Brusa, S. Bonoli, F. Shankar, N. Acharya, B. Laloux, K. Dolag, A. Georgakakis, A. Lapi, C. Ramos Almeida, M. Salvato, J. Chaves-Montero, P. Coelho, L. A. Díaz-García, J. A. Fernández-Ontiveros, A. Hernán-Caballero, R. M. González Delgado, I. Marquez, M. Pović, R. Soria, C. Queiroz, P. T. Rahna, R. Abramo, J. Alcaniz, N. Benitez, S. Carneiro, J. Cenarro, D. Cristóbal-Hornillos, R. Dupke, A. Ederoclite, C. López-Sanjuan, A. Marín-Franch, C. Mendes de Oliveira, M. Moles, Jr. Sodré, L., K. Taylor, J. Varela, and H. V. Ramió. The miniJPAS survey: AGN and host galaxy coevolution of X-ray-selected sources., 672:A137, April 2023.
- E. Lusso and G. Risaliti. The Tight Relation between X-Ray and Ultraviolet Luminosity of Quasars. , 819(2):154, March 2016. .
- D. Lynden-Bell. Galactic Nuclei as Collapsed Old Quasars., 223(5207):690–694, August 1969.
- Jianwei Lyu, Stacey Alberts, George H. Rieke, Irene Shivaei, Pablo G. Perez-Gonzalez, Fengwu Sun, Kevin N. Hainline, Stefi Baum, Nina Bonaventura, Andrew J. Bunker, Eiichi Egami, Daniel J. Eisenstein, Michael Florian, Zhiyuan Ji, Benjamin D. Johnson, Jane Morrison, Marcia Rieke, Brant Robertson, Wiphu Rujopakarn, Sandro Tacchella, Jan Scholtz, and Christopher N. A. Willmer. AGN Selection and Demographics: A New Age with JWST/MIRI. arXiv e-prints, art. arXiv:2310.12330, October 2023.

Yipeng Lyu, Benjamin Magnelli, David Elbaz, Pablo G. Pérez-González, Camila Correa, Emanuele Daddi, Carlos Gómez-Guijarro, James S. Dunlop, Norman A. Grogin, Anton M. Koekemoer, Derek J. McLeod, and Shiying Lu. PRIMER: JWST/MIRI reveals the evolution of star-forming structures in galaxies at z;2.5. *arXiv e-prints*, art. arXiv:2406.11571, June 2024.

- Benjamin Magnelli, Carlos Gómez-Guijarro, David Elbaz, Emanuele Daddi, Casey Papovich, Lu Shen, Pablo Arrabal Haro, Micaela B. Bagley, Eric F. Bell, Véronique Buat, Luca Costantin, Mark Dickinson, Steven L. Finkelstein, Jonathan P. Gardner, Eric F. Jiménez-Andrade, Jeyhan S. Kartaltepe, Anton M. Koekemoer, Yipeng Lyu, Pablo G. Pérez-González, Nor Pirzkal, Sandro Tacchella, Alexander de la Vega, Stijn Wuyts, Guang Yang, L. Y. Aaron Yung, and Jorge Zavala. CEERS: MIRI deciphers the spatial distribution of dust-obscured star formation in galaxies at 0.1 ; z ; 2.5., 678:A83, October 2023.
- Roberto Maiolino, Guido Risaliti, Matilde Signorini, Bartolomeo Trefoloni, Ignas Juodzbalis, Jan Scholtz, Hannah Uebler, Francesco D'Eugenio, Stefano Carniani, Andy Fabian, Xihan Ji, Giovanni Mazzolari, Elena Bertola, Marcella Brusa, Andrew J. Bunker, Stephane Charlot, Andrea Comastri, Giovanni Cresci, Christa Noel DeCoursey, Eiichi Egami, Fabrizio Fiore, Roberto Gilli, Michele Perna, Sandro Tacchella, and Giacomo Venturi. JWST meets Chandra: a large population of Compton thick, feedback-free, and X-ray weak AGN, with a sprinkle of SNe. *arXiv e-prints*, art. arXiv:2405.00504, May 2024.
- Dan Maoz. Low-luminosity active galactic nuclei: are they UV faint and radio loud? , 377(4):1696–1710, June 2007. .
- Stefano Marchesi, Marco Ajello, Lea Marcotulli, Andrea Comastri, Giorgio Lanzuisi, and Cristian Vignali. Compton-thick agns in the nustar era. *The Astrophysical Journal*, 854 (1):49, 2018.
- A. Marconi, G. Risaliti, R. Gilli, L. K. Hunt, R. Maiolino, and M. Salvati. Local supermassive black holes, relics of active galactic nuclei and the X-ray background. , 351(1): 169–185, June 2004. .
- Paul Martini. QSO Lifetimes. In Luis C. Ho, editor, *Coevolution of Black Holes and Galaxies*, page 169, January 2004. .
- Federico Marulli, Silvia Bonoli, Enzo Branchini, Lauro Moscardini, and Volker Springel. Modelling the cosmological co-evolution of supermassive black holes and galaxies I. BH scaling relations and the AGN luminosity function. , 385(4):1846–1858, April 2008.
- Jorryt Matthee, Rohan P. Naidu, Gabriel Brammer, John Chisholm, Anna-Christina Eilers, Andy Goulding, Jenny Greene, Daichi Kashino, Ivo Labbe, Simon J. Lilly, Ruari

Mackenzie, Pascal A. Oesch, Andrea Weibel, Stijn Wuyts, Mengyuan Xiao, Rongmon Bordoloi, Rychard Bouwens, Pieter van Dokkum, Garth Illingworth, Ivan Kramarenko, Michael V. Maseda, Charlotte Mason, Romain A. Meyer, Erica J. Nelson, Naveen A. Reddy, Irene Shivaei, Robert A. Simcoe, and Minghao Yue. Little Red Dots: An Abundant Population of Faint Active Galactic Nuclei at $z\sim 5$ Revealed by the EIGER and FRESCO JWST Surveys. , 963(2):129, March 2024. .

- Ian M. McHardy. X-ray variability of active galactic nuclei. In J. Hunt and B. Battrick, editors, *Two Topics in X-Ray Astronomy, Volume 1: X Ray Binaries. Volume 2: AGN and the X Ray Background*, volume 296 of *ESA Special Publication*, pages 1111–1124, November 1989.
- N. Menci, A. Cavaliere, A. Fontana, E. Giallongo, and F. Poli. Binary Aggregations in Hierarchical Galaxy Formation: The Evolution of the Galaxy Luminosity Function. , 575(1):18–32, August 2002. .
- N. Menci, A. Cavaliere, A. Fontana, E. Giallongo, F. Poli, and V. Vittorini. Early Hierarchical Formation of Massive Galaxies Triggered by Interactions. , 604(1):12–17, March 2004. .
- N. Menci, A. Fontana, E. Giallongo, and S. Salimbeni. Bimodal Color Distribution in Hierarchical Galaxy Formation. , 632(1):49–57, October 2005. .
- N. Menci, F. Fiore, S. Puccetti, and A. Cavaliere. The Blast Wave Model for AGN Feedback: Effects on AGN Obscuration. , 686(1):219–229, October 2008.
- N. Menci, M. Gatti, F. Fiore, and A. Lamastra. Triggering active galactic nuclei in hierarchical galaxy formation: disk instability vs. interactions. , 569:A37, September 2014.
- N. Menci, A. Grazian, A. Lamastra, F. Calura, M. Castellano, and P. Santini. Galaxy Formation in Sterile Neutrino Dark Matter Models. , 854(1):1, February 2018. .
- N. Menci, F. Fiore, C. Feruglio, A. Lamastra, F. Shankar, E. Piconcelli, E. Giallongo, and A. Grazian. Outflows in the Disks of Active Galaxies. , 877(2):74, June 2019.
- N. Menci, F. Fiore, F. Shankar, L. Zanisi, and C. Feruglio. Outflows in the gaseous disks of active galaxies and their impact on black hole scaling relations., 674:A181, June 2023.
- Alexander J. Mendez, Alison L. Coil, James Aird, Ramin A. Skibba, Aleksandar M. Diamond-Stanic, John Moustakas, Michael R. Blanton, Richard J. Cool, Daniel J. Eisenstein, Kenneth C. Wong, and Guangtun Zhu. PRIMUS + DEEP2: Clustering of X-Ray, Radio, and IR-AGNs at z~0.7., 821(1):55, April 2016.
- Harshitha Menon, Lukasz Wesolowski, Gengbin Zheng, Pritish Jetley, Laxmikant Kale, Thomas Quinn, and Fabio Governato. Adaptive techniques for clustered N-body cosmological simulations. *Computational Astrophysics and Cosmology*, 2:1, March 2015.

A. Merloni, A. Bongiorno, M. Brusa, K. Iwasawa, V. Mainieri, B. Magnelli, M. Salvato, S. Berta, N. Cappelluti, A. Comastri, F. Fiore, R. Gilli, A. Koekemoer, E. Le Floc'h, E. Lusso, D. Lutz, T. Miyaji, F. Pozzi, L. Riguccini, D. J. Rosario, J. Silverman, M. Symeonidis, E. Treister, C. Vignali, and G. Zamorani. The incidence of obscuration in active galactic nuclei. , 437(4):3550–3567, February 2014.

- J. Christopher Mihos and Lars Hernquist. Gasdynamics and Starbursts in Major Mergers. , 464:641, June 1996. .
- S. Mineo, M. Gilfanov, and R. Sunyaev. X-ray emission from star-forming galaxies I. High-mass X-ray binaries. , 419(3):2095–2115, January 2012. .
- Juan Molina, Luis C. Ho, Ran Wang, Jinyi Shangguan, Franz E. Bauer, and Ezequiel Treister. Enhanced Star Formation Efficiency in the Central Regions of Nearby Quasar Hosts., 944(1):30, February 2023.
- Pierluigi Monaco, Fabio Fontanot, and Giuliano Taffoni. The MORGANA model for the rise of galaxies and active nuclei. , 375(4):1189–1219, March 2007. .
- J. J. Monaghan. Smoothed particle hydrodynamics., 30:543–574, January 1992...
- Jorge Moreno, Paul Torrey, Sara L. Ellison, David R. Patton, Asa F. L. Bluck, Gunjan Bansal, and Lars Hernquist. Mapping galaxy encounters in numerical simulations: the spatial extent of induced star formation. , 448(2):1107–1117, April 2015. .
- Jorge Moreno, Paul Torrey, Sara L. Ellison, David R. Patton, Philip F. Hopkins, Michael Bueno, Christopher C. Hayward, Desika Narayanan, Dušan Kereš, Asa F. L. Bluck, and Lars Hernquist. Interacting galaxies on FIRE-2: the connection between enhanced star formation and interstellar gas content. , 485(1):1320–1338, May 2019.
- Raffaella Morganti. The many routes to AGN feedback. *Frontiers in Astronomy and Space Sciences*, 4:42, November 2017. .
- G. Mountrichas and A. Georgakakis. The clustering of X-ray-selected active galactic nuclei at z= 0.1. , 420(1):514–525, February 2012. .
- G. Mountrichas, V. Buat, G. Yang, M. Boquien, Q. Ni, E. Pouliasis, D. Burgarella, P. Theule, and I. Georgantopoulos. Comparison of star formation histories of AGN and non-AGN galaxies., 667:A145, November 2022.
- G. Mountrichas, M. Siudek, and O. Cucciati. Probing star formation rates and histories in AGN and non-AGN galaxies across diverse cosmic environments and X-ray luminosity ranges., 686:A229, June 2024.
- George Mountrichas and Francesco Shankar. Testing the evolutionary pathways of galaxies and their supermassive black holes and the impact of feedback from active galactic nuclei via large multiwavelength data sets. , 518(2):2088–2101, January 2023. .

J. R. Mullaney, D. M. Alexander, J. Aird, E. Bernhard, E. Daddi, A. Del Moro, M. Dickinson, D. Elbaz, C. M. Harrison, S. Juneau, D. Liu, M. Pannella, D. Rosario, P. Santini, M. Sargent, C. Schreiber, J. Simpson, and F. Stanley. ALMA and Herschel reveal that X-ray-selected AGN and main-sequence galaxies have different star formation rate distributions. , 453(1):L83–L87, October 2015. .

- R. F. Mushotzky. The X-ray spectrum and time variability of narrow emission line galaxies. , 256:92–102, May 1982. .
- B. Musiimenta, M. Brusa, T. Liu, M. Salvato, J. Buchner, Z. Igo, S. G. H. Waddell, Y. Toba, R. Arcodia, J. Comparat, D. Alexander, F. Shankar, A. Lapi, C. Ramos Almeida, A. Georgakakis, A. Merloni, T. Urrutia, J. Li, Y. Terashima, Y. Shen, Q. Wu, T. Dwelly, K. Nandra, and J. Wolf. A new discovery space opened by eROSITA. Ionised AGN outflows from X-ray selected samples. , 679:A84, November 2023. .
- Ramesh Narayan and Insu Yi. Advection-dominated Accretion: A Self-similar Solution. , 428:L13, June 1994. .
- Ramesh Narayan and Insu Yi. Advection-dominated Accretion: Underfed Black Holes and Neutron Stars. , 452:710, October 1995. .
- Narendra Nath Patra. HI scale height in spiral galaxies. *arXiv e-prints*, art. arXiv:2009.11299, September 2020.
- Julio F. Navarro, Carlos S. Frenk, and Simon D. M. White. The Structure of Cold Dark Matter Halos. , 462:563, May 1996. .
- Erica June Nelson, Pieter G. van Dokkum, Natascha M. Förster Schreiber, Marijn Franx, Gabriel B. Brammer, Ivelina G. Momcheva, Stijn Wuyts, Katherine E. Whitaker, Rosalind E. Skelton, Mattia Fumagalli, Christopher C. Hayward, Mariska Kriek, Ivo Labbé, Joel Leja, Hans-Walter Rix, Linda J. Tacconi, Arjen van der Wel, Frank C. van den Bosch, Pascal A. Oesch, Claire Dickey, and Johannes Ulf Lange. Where Stars Form: Inside-out Growth and Coherent Star Formation from HST H α Maps of 3200 Galaxies across the Main Sequence at 0.7 ; z ; 1.5. , 828(1):27, September 2016.
- H. Netzer. AGN emission lines. In R. D. Blandford, H. Netzer, L. Woltjer, T. J. L. Courvoisier, and M. Mayor, editors, *Active Galactic Nuclei*, pages 57–160, January 1990.
- Hagai Netzer. The Physics and Evolution of Active Galactic Nuclei. 2013.
- Hagai Netzer. Revisiting the Unified Model of Active Galactic Nuclei. , 53:365–408, August 2015. .
- Shoji Ogawa, Yoshihiro Ueda, Atsushi Tanimoto, and Satoshi Yamada. Systematic Study of AGN Clumpy Tori with Broadband X-Ray Spectroscopy: Updated Unified Picture of AGN Structure., 906(2):84, January 2021.

D. K. Ojha. Radial scalelengths of the galactic thin and thick disc with 2MASS data. , 322 (2):426–432, April 2001. .

- D. E. Osterbrock. Seyfert galaxies with weak broad H alpha emission lines. , 249:462–470, October 1981. .
- Christopher Packham, James T. Radomski, Patrick F. Roche, David K. Aitken, Eric Perlman, Almudena Alonso-Herrero, Luis Colina, and Charles M. Telesco. The Extended Mid-Infrared Structure of the Circinus Galaxy., 618(1):L17–L20, January 2005.
- P. Padovani, N. Miller, K. I. Kellermann, V. Mainieri, P. Rosati, and P. Tozzi. The VLA Survey of Chandra Deep Field South. V. Evolution and Luminosity Functions of Submillijansky Radio Sources and the Issue of Radio Emission in Radio-quiet Active Galactic Nuclei. , 740(1):20, October 2011.
- P. Padovani, D. M. Alexander, R. J. Assef, B. De Marco, P. Giommi, R. C. Hickox, G. T. Richards, V. Smolčić, E. Hatziminaoglou, V. Mainieri, and M. Salvato. Active galactic nuclei: what's in a name? , 25(1):2, August 2017. .
- Don N. Page and Kip S. Thorne. Disk-Accretion onto a Black Hole. Time-Averaged Structure of Accretion Disk. , 191:499–506, July 1974. .
- Francesca Panessa, Xavier Barcons, Loredana Bassani, Massimo Cappi, Francisco J. Carrera, L. C. Ho, and S. Pellegrini. The x-ray and radio connection in low-luminosity active nuclei, 2007.
- Eleonora Parlanti, Stefano Carniani, Hannah Übler, Giacomo Venturi, Francesco D'Eugenio, Santiago Arribas, Andrew J. Bunker, Stéphane Charlot, Nora Lützgendorf, Roberto Maiolino, Michele Perna, Bruno Rodríguez Del Pino, Chris J. Willott, Torsten Böker, Alex J. Cameron, Jacopo Chevallard, Chiara Circosta, Giovanni Cresci, Gareth C. Jones, Nimisha Kumari, Isabella Lamperti, and Jan Scholtz. GA-NIFS: Early-stage feedback in a heavily obscured AGN at z=4.76. $arXiv\ e-prints$, art. arXiv:2309.05713, September 2023.
- F. Shirley Patterson. The Luminosity Gradient of Messier 33. *Harvard College Observatory Bulletin*, 914:9–10, December 1940.
- Alessandro Peca, Nico Cappelluti, C. Megan Urry, Stephanie LaMassa, Stefano Marchesi, Tonima Tasnim Ananna, Mislav Baloković, David Sanders, Connor Auge, Ezequiel Treister, Meredith Powell, Tracey Jane Turner, Allison Kirkpatrick, and Chuan Tian. On the Cosmic Evolution of AGN Obscuration and the X-Ray Luminosity Function: XMM-Newton and Chandra Spectral Analysis of the 31.3 deg² Stripe 82X., 943(2):162, February 2023.
- L. Peralta de Arriba, A. Alonso-Herrero, S. García-Burillo, I. García-Bernete, M. Villar-Martín, B. García-Lorenzo, R. Davies, D. J. Rosario, S. F. Hönig, N. A. Levenson,

C. Packham, C. Ramos Almeida, M. Pereira-Santaella, A. Audibert, E. Bellocchi, E. K. S. Hicks, A. Labiano, C. Ricci, and D. Rigopoulou. A radio-jet-driven outflow in the Seyfert 2 galaxy NGC 2110?, 675:A58, July 2023.

- Pablo G. Pérez-González, Guillermo Barro, George H. Rieke, Jianwei Lyu, Marcia Rieke, Stacey Alberts, Christina C. Williams, Kevin Hainline, Fengwu Sun, Dávid Puskás, Marianna Annunziatella, William M. Baker, Andrew J. Bunker, Eiichi Egami, Zhiyuan Ji, Benjamin D. Johnson, Brant Robertson, Bruno Rodríguez Del Pino, Wiphu Rujopakarn, Irene Shivaei, Sandro Tacchella, Christopher N. A. Willmer, and Chris Willott. What Is the Nature of Little Red Dots and what Is Not, MIRI SMILES Edition., 968(1): 4, June 2024.
- Serena Perrotta, Alison L. Coil, David S. N. Rupke, Christy A. Tremonti, Julie D. Davis, Aleksandar M. Diamond-Stanic, James E. Geach, Ryan C. Hickox, John Moustakas, Gregory H. Rudnick, Paul H. Sell, Cameren N. Swiggum, and Kelly E. Whalen. Kinematics, Structure, and Mass Outflow Rates of Extreme Starburst Galactic Outflows., 949(1):9, May 2023.
- M. Persic and Y. Rephaeli. Galactic star formation rates gauged by stellar end-products. , 463(2):481–492, February 2007. .
- Bradley M. Peterson. *An Introduction to Active Galactic Nuclei*. Cambridge University Press, 1997. .
- Grayson C. Petter, Ryan C. Hickox, David M. Alexander, Adam D. Myers, James E. Geach, Kelly E. Whalen, and Carolina P. Andonie. Host Dark Matter Halos of Wide-field Infrared Survey Explorer-selected Obscured and Unobscured Quasars: Evidence for Evolution. , 946(1):27, March 2023. .
- A. J. Pica and A. G. Smith. Optical variability, absolute luminosity, and the Hubble diagram for QSOs. , 272:11–25, September 1983. .
- J. C. S. Pierce, C. Tadhunter, C. Ramos Almeida, P. Bessiere, J. V. Heaton, S. L. Ellison, G. Speranza, Y. Gordon, C. O'Dea, L. Grimmett, and L. Makrygianni. Galaxy interactions are the dominant trigger for local type 2 quasars. , 522(2):1736–1751, June 2023.
- J. D. H. Pilkington and J. F. Scott. A survey of radio sources between declinations 20° and 40° . , 69:183, January 1965.
- Elia Pizzati, Joseph F. Hennawi, Joop Schaye, Matthieu Schaller, Anna-Christina Eilers, Feige Wang, Carlos S. Frenk, Willem Elbers, John C. Helly, Ruari Mackenzie, Jorryt Matthee, Rongmon Bordoloi, Daichi Kashino, Rohan P. Naidu, and Minghao Yue. A unified model for the clustering of quasars and galaxies at $z\approx 6$. $arXiv\ e-prints$, art. arXiv:2403.12140, March 2024.

M. Pohlen and I. Trujillo. The structure of galactic disks. Studying late-type spiral galaxies using SDSS. , 454(3):759–772, August 2006. .

- M. Polletta, A. Omont, S. Berta, J. Bergeron, C. S. Stalin, P. Petitjean, M. Giorgetti, G. Trinchieri, R. Srianand, H. J. McCracken, Y. Pei, and H. Dannerbauer. Obscured and powerful AGN and starburst activities at z ~3.5., 492(1):81–92, December 2008.
- M. Polletta, N. P. H. Nesvadba, R. Neri, A. Omont, S. Berta, and J. Bergeron. Disk, merger, or outflow? Molecular gas kinematics in two powerful obscured QSOs at $z \geq 3.4.$, 533: A20, September 2011.
- M. Polletta, B. L. Frye, N. Garuda, S. P. Willner, S. Berta, R. Kneissl, H. Dole, R. A. Jansen, M. D. Lehnert, S. H. Cohen, J. Summers, R. A. Windhorst, J. C. J. D'Silva, A. M. Koekemoer, D. Coe, C. J. Conselice, S. P. Driver, N. A. Grogin, M. A. Marshall, M. Nonino, III Ortiz, R., N. Pirzkal, A. Robotham, Jr. Ryan, R. E., C. N. A. Willmer, H. Yan, V. Arumugam, C. Cheng, H. B. Gim, N. P. Hathi, B. Holwerda, P. Kamieneski, W. C. Keel, J. Li, M. Pascale, H. Rottgering, B. M. Smith, and M. S. Yun. JWST's PEARLS: resolved study of the stellar and dust components in starburst galaxies at cosmic noon. arXiv e-prints, art. arXiv:2405.07986, May 2024.
- P. Popesso, A. Concas, G. Cresci, S. Belli, G. Rodighiero, H. Inami, M. Dickinson, O. Ilbert, M. Pannella, and D. Elbaz. The main sequence of star-forming galaxies across cosmic times. , 519(1):1526–1544, February 2023. .
- Gergö Popping, Rachel S. Somerville, and Scott C. Trager. Evolution of the atomic and molecular gas content of galaxies. , 442(3):2398–2418, August 2014. .
- E. Pouliasis, A. Ruiz, I. Georgantopoulos, F. Vito, R. Gilli, C. Vignali, Y. Ueda, E. Koulouridis, M. Akiyama, S. Marchesi, B. Laloux, T. Nagao, S. Paltani, M. Pierre, Y. Toba, M. Habouzit, B. Vijarnwannaluk, and C. Garrel. AGN X-ray luminosity function and absorption function in the Early Universe ($3 \le z \le 6$). *arXiv e-prints*, art. arXiv:2401.13515, January 2024.
- M. C. Powell, N. Cappelluti, C. M. Urry, M. Koss, A. Finoguenov, C. Ricci, B. Trakhtenbrot, V. Allevato, M. Ajello, K. Oh, K. Schawinski, and N. Secrest. The Swift/BAT AGN Spectroscopic Survey. IX. The Clustering Environments of an Unbiased Sample of Local AGNs., 858(2):110, May 2018.
- F. Pozzi, F. Calura, Q. D'Amato, M. Gavarente, M. Bethermin, M. Boquien, V. Casasola, A. Cimatti, R. Cochrane, M. Dessauges-Zavadsky, A. Enia, F. Esposito, A. L. Faisst, R. Gilli, M. Ginolfi, R. Gobat, C. Gruppioni, C. C. Hayward, E. Ibar, A. M. Koekemoer, B. C. Lemaux, G. E. Magdis, J. Molina, M. Romano, M. Talia, L. Vallini, D. Vergani, and G. Zamorani. The ALPINE-ALMA [CII] survey: Dust emission effective radius up to 3 kpc in the early Universe., 686:A187, June 2024.

A. Puglisi, E. Daddi, D. Liu, F. Bournaud, J. D. Silverman, C. Circosta, A. Calabrò, M. Aravena, A. Cibinel, H. Dannerbauer, I. Delvecchio, D. Elbaz, Y. Gao, R. Gobat, S. Jin, E. Le Floc'h, G. E. Magdis, C. Mancini, D. A. Riechers, G. Rodighiero, M. Sargent, F. Valentino, and L. Zanisi. The Main Sequence at z ~ 1.3 Contains a Sizable Fraction of Galaxies with Compact Star Formation Sizes: A New Population of Early Poststarbursts?, 877(2):L23, June 2019.

- Annagrazia Puglisi, Emanuele Daddi, Francesco Valentino, Georgios Magdis, Daizhong Liu, Vasily Kokorev, Chiara Circosta, David Elbaz, Frederic Bournaud, Carlos Gomez-Guijarro, Shuowen Jin, Suzanne Madden, Mark T. Sargent, and Mark Swinbank. Submillimetre compactness as a critical dimension to understand the main sequence of star-forming galaxies. , 508(4):5217–5238, December 2021.
- Eliot Quataert and Ramesh Narayan. Spectral Models of Advection-dominated Accretion Flows with Winds. , 520(1):298–315, July 1999. .
- M. Querejeta, E. Schinnerer, S. García-Burillo, F. Bigiel, G. A. Blanc, D. Colombo, A. Hughes, K. Kreckel, A. Leroy, S. E. Meidt, D. S. Meier, J. Pety, and K. Sliwa. AGN feedback in the nucleus of M 51 (Corrigendum). , 599:C1, March 2017. .
- M. Querejeta, E. Schinnerer, S. Meidt, J. Sun, A. K. Leroy, E. Emsellem, R. S. Klessen, J. C. Muñoz-Mateos, H. Salo, E. Laurikainen, I. Bešlić, G. A. Blanc, M. Chevance, D. A. Dale, C. Eibensteiner, C. Faesi, A. García-Rodríguez, S. C. O. Glover, K. Grasha, J. Henshaw, C. Herrera, A. Hughes, K. Kreckel, J. M. D. Kruijssen, D. Liu, E. J. Murphy, H. A. Pan, J. Pety, A. Razza, E. Rosolowsky, T. Saito, A. Schruba, A. Usero, E. J. Watkins, and T. G. Williams. Stellar structures, molecular gas, and star formation across the PHANGS sample of nearby galaxies. , 656:A133, December 2021.
- James T. Radomski, Christopher Packham, N. A. Levenson, Eric Perlman, Lerothodi L. Leeuw, Henry Matthews, Rachel Mason, James M. De Buizer, Charles M. Telesco, and Manuel Orduna. Gemini Imaging of Mid-Infrared Emission from the Nuclear Region of Centaurus A., 681(1):141–150, July 2008.
- Cristina Ramos Almeida and Claudio Ricci. Nuclear obscuration in active galactic nuclei. *Nature Astronomy*, 1:679–689, October 2017. .
- P. Ranalli, A. Comastri, and G. Setti. The 2-10 keV luminosity as a Star Formation Rate indicator., 399:39–50, February 2003.
- Amy E. Reines and Marta Volonteri. Relations between Central Black Hole Mass and Total Galaxy Stellar Mass in the Local Universe. , 813(2):82, November 2015. .
- F. Renaud, F. Bournaud, K. Kraljic, and P. A. Duc. Starbursts triggered by intergalactic tides and interstellar compressive turbulence., 442:L33–L37, July 2014.

F. Renaud, E. Athanassoula, P. Amram, A. Bosma, F. Bournaud, P. A. Duc, B. Epinat, J. Fensch, K. Kraljic, V. Perret, and C. Struck. Morphology and enhanced star formation in a Cartwheel-like ring galaxy. , 473(1):585–602, January 2018. .

- Florent Renaud, Álvaro Segovia Otero, and Oscar Agertz. The merger-starburst connection across cosmic times. , 516(4):4922–4931, November 2022. .
- C. Ricci, Y. Ueda, M. J. Koss, B. Trakhtenbrot, F. E. Bauer, and P. Gandhi. Compton-thick Accretion in the Local Universe. , 815(1):L13, December 2015. .
- C. Ricci, F. E. Bauer, E. Treister, K. Schawinski, G. C. Privon, L. Blecha, P. Arevalo, L. Armus, F. Harrison, L. C. Ho, K. Iwasawa, D. B. Sanders, and D. Stern. Growing supermassive black holes in the late stages of galaxy mergers are heavily obscured. , 468(2): 1273–1299, June 2017a. .
- C. Ricci, T. T. Ananna, M. J. Temple, C. M. Urry, M. J. Koss, B. Trakhtenbrot, Y. Ueda, D. Stern, F. E. Bauer, E. Treister, G. C. Privon, K. Oh, S. Paltani, M. Stalevski, L. C. Ho, A. C. Fabian, R. Mushotzky, C. S. Chang, F. Ricci, D. Kakkad, L. Sartori, R. Baer, T. Caglar, M. Powell, and F. Harrison. BASS XXXVII: The role of radiative feedback in the growth and obscuration properties of nearby supermassive black holes. *arXiv e-prints*, art. arXiv:2209.00014, August 2022a.
- Claudio Ricci. *Active galactic nuclei at hard X-ray energies: absorption, reflection and the unified model.* PhD thesis, University of Geneva, Switzerland, January 2011.
- Claudio Ricci and Benny Trakhtenbrot. Changing-look active galactic nuclei. *Nature Astronomy*, 7:1282–1294, November 2023. .
- Claudio Ricci, Benny Trakhtenbrot, Michael J. Koss, Yoshihiro Ueda, Kevin Schawinski, Kyuseok Oh, Isabella Lamperti, Richard Mushotzky, Ezequiel Treister, Luis C. Ho, Anna Weigel, Franz E. Bauer, Stephane Paltani, Andrew C. Fabian, Yanxia Xie, and Neil Gehrels. The close environments of accreting massive black holes are shaped by radiative feedback. , 549(7673):488–491, September 2017b. .
- Federica Ricci, Stefano Marchesi, Francesco Shankar, Fabio La Franca, and Francesca Civano. Constraining the UV emissivity of AGN throughout cosmic time via X-ray surveys., 465(2):1915–1925, February 2017c. .
- Federica Ricci, Ezequiel Treister, Franz E. Bauer, Julian E. Mejía-Restrepo, Michael J. Koss, Jakob S. den Brok, Mislav Baloković, Rudolf Bär, Patricia Bessiere, Turgay Caglar, Fiona Harrison, Kohei Ichikawa, Darshan Kakkad, Isabella Lamperti, Richard Mushotzky, Kyuseok Oh, Meredith C. Powell, George C. Privon, Claudio Ricci, Rogerio Riffel, Alejandra F. Rojas, Eleonora Sani, Krista L. Smith, Daniel Stern, Benny Trakhtenbrot, C. Megan Urry, and Sylvain Veilleux. BASS. XXIX. The Near-infrared View of the Broad-line Region (BLR): The Effects of Obscuration in BLR Characterization. , 261 (1):8, July 2022b. .

G. Riccio, G. Yang, K. Małek, M. Boquien, Junais, F. Pistis, M. Hamed, M. Grespan, M. Paolillo, and O. Torbaniuk. X-ray luminosity-star formation rate scaling relation: Constraints from the eROSITA Final Equatorial Depth Survey (eFEDS)., 678:A164, October 2023.

- D. Richstone, E. A. Ajhar, R. Bender, G. Bower, A. Dressler, S. M. Faber, A. V. Filippenko, K. Gebhardt, R. Green, L. C. Ho, J. Kormendy, T. R. Lauer, J. Magorrian, and S. Tremaine. Supermassive black holes and the evolution of galaxies. , 385(6701):A14, October 1998. .
- Dominik A. Riechers, C. M. Bradford, D. L. Clements, C. D. Dowell, I. Pérez-Fournon, R. J. Ivison, C. Bridge, A. Conley, Hai Fu, J. D. Vieira, J. Wardlow, J. Calanog, A. Cooray, P. Hurley, R. Neri, J. Kamenetzky, J. E. Aguirre, B. Altieri, V. Arumugam, D. J. Benford, M. Béthermin, J. Bock, D. Burgarella, A. Cabrera-Lavers, S. C. Chapman, P. Cox, J. S. Dunlop, L. Earle, D. Farrah, P. Ferrero, A. Franceschini, R. Gavazzi, J. Glenn, E. A. Gonzalez Solares, M. A. Gurwell, M. Halpern, E. Hatziminaoglou, A. Hyde, E. Ibar, A. Kovács, M. Krips, R. E. Lupu, P. R. Maloney, P. Martinez-Navajas, H. Matsuhara, E. J. Murphy, B. J. Naylor, H. T. Nguyen, S. J. Oliver, A. Omont, M. J. Page, G. Petitpas, N. Rangwala, I. G. Roseboom, D. Scott, A. J. Smith, J. G. Staguhn, A. Streblyanska, A. P. Thomson, I. Valtchanov, M. Viero, L. Wang, M. Zemcov, and J. Zmuidzinas. A dust-obscured massive maximum-starburst galaxy at a redshift of 6.34., 496 (7445):329–333, April 2013.
- G. Risaliti, R. Maiolino, and M. Salvati. The Distribution of Absorbing Column Densities among Seyfert 2 Galaxies. , 522(1):157–164, September 1999. .
- G. Rodighiero, M. Brusa, E. Daddi, M. Negrello, J. R. Mullaney, I. Delvecchio, D. Lutz,
 A. Renzini, A. Franceschini, I. Baronchelli, F. Pozzi, C. Gruppioni, V. Strazzullo,
 A. Cimatti, and J. Silverman. Relationship between Star Formation Rate and Black
 Hole Accretion At Z = 2: the Different Contributions in Quiescent, Normal, and Starburst Galaxies. , 800(1):L10, February 2015.
- Rodrigo Córdova Rosado, Andy D. Goulding, Jenny E. Greene, Grayson C. Petter, Ryan C. Hickox, Nickolas Kokron, Michael A. Strauss, Jahmour J. Givans, Yoshiki Toba, and Cassandra Starr Henderson. Cross-correlation of luminous red galaxies with mlselected agn in hsc-ssp: Unobscured agn residing in more massive halos, 2024. URL https://arxiv.org/abs/2409.08314.
- M. Ryle and Allan Sandage. The Optical Identification of Three New Radio Objects of the 3c 48 Class. , 139:419, January 1964. .
- Takayuki R. Saitoh, Hiroshi Daisaka, Eiichiro Kokubo, Junichiro Makino, Takashi Okamoto, Kohji Tomisaka, Keiichi Wada, and Naoki Yoshida. Toward First-Principle Simulations of Galaxy Formation: II. Shock-Induced Starburst at a Collision Interface during the First Encounter of Interacting Galaxies. , 61:481, June 2009.

Ariel G. Sánchez, C. M. Baugh, W. J. Percival, J. A. Peacock, N. D. Padilla, S. Cole, C. S. Frenk, and P. Norberg. Cosmological parameters from cosmic microwave background measurements and the final 2dF Galaxy Redshift Survey power spectrum. , 366(1): 189–207, February 2006. .

- Allan R. Sandage. Review Paper: A New ERA in Cosmology: The Use of Radio Galaxies, Quasi-Stellar Sources and Quasi-Stellar Galaxies as Probes. , 70:690, January 1965. .
- D. B. Sanders and I. F. Mirabel. Luminous Infrared Galaxies., 34:749, January 1996. .
- D. B. Sanders, B. T. Soifer, J. H. Elias, B. F. Madore, K. Matthews, G. Neugebauer, and N. Z. Scoville. Ultraluminous Infrared Galaxies and the Origin of Quasars., 325:74, February 1988.
- D. B. Sanders, E. S. Phinney, G. Neugebauer, B. T. Soifer, and K. Matthews. Continuum Energy Distributions of Quasars: Shapes and Origins. , 347:29, December 1989. .
- P. Santini, R. Maiolino, B. Magnelli, D. Lutz, A. Lamastra, G. Li Causi, S. Eales, P. Andreani, S. Berta, V. Buat, A. Cooray, G. Cresci, E. Daddi, D. Farrah, A. Fontana, A. Franceschini, R. Genzel, G. Granato, A. Grazian, E. Le Floc'h, G. Magdis, M. Magliocchetti, F. Mannucci, N. Menci, R. Nordon, S. Oliver, P. Popesso, F. Pozzi, L. Riguccini, G. Rodighiero, D. J. Rosario, M. Salvato, D. Scott, L. Silva, L. Tacconi, M. Viero, L. Wang, S. Wuyts, and K. Xu. The evolution of the dust and gas content in galaxies. , 562:A30, February 2014.
- Paola Santini, Adriano Fontana, Marco Castellano, Marcella Di Criscienzo, Emiliano Merlin, Ricardo Amorin, Fergus Cullen, Emanuele Daddi, Mark Dickinson, James S. Dunlop, Andrea Grazian, Alessandra Lamastra, Ross J. McLure, Michał. J. Michałowski, Laura Pentericci, and Xinwen Shu. The Star Formation Main Sequence in the Hubble Space Telescope Frontier Fields. , 847(1):76, September 2017.
- M. T. Sargent, E. Daddi, M. Béthermin, H. Aussel, G. Magdis, H. S. Hwang, S. Juneau, D. Elbaz, and E. da Cunha. Regularity Underlying Complexity: A Redshift-independent Description of the Continuous Variation of Galaxy-scale Molecular Gas Properties in the Mass-star Formation Rate Plane., 793(1):19, September 2014.
- M. Schmidt. 3C 273: A Star-Like Object with Large Red-Shift., 197(4872):1040, March 1963..
- M. Schmidt and R. F. Green. Quasar evolution derived from the Palomar bright quasar survey and other complete quasar surveys. , 269:352–374, June 1983. .
- Maarten Schmidt. Models of Quasi-stellar Sources. In *Quasars and high-energy astronomy*, page 55, January 1969.

N. Scoville, H. Aussel, M. Brusa, P. Capak, C. M. Carollo, M. Elvis, M. Giavalisco, L. Guzzo, G. Hasinger, C. Impey, J. P. Kneib, O. LeFevre, S. J. Lilly, B. Mobasher, A. Renzini, R. M. Rich, D. B. Sanders, E. Schinnerer, D. Schminovich, P. Shopbell, Y. Taniguchi, and N. D. Tyson. The Cosmic Evolution Survey (COSMOS): Overview. , 172(1):1–8, September 2007.

- D. Sengupta, S. Marchesi, C. Vignali, N. Torres-Albà, E. Bertola, A. Pizzetti, G. Lanzuisi, F. Salvestrini, X. Zhao, M. Gaspari, R. Gilli, A. Comastri, A. Traina, F. Tombesi, R. Silver, F. Pozzi, and M. Ajello. Compton-thick AGN in the NuSTAR Era X: Analysing seven local CT-AGN candidates., 676:A103, August 2023.
- Carl K. Seyfert. Nuclear Emission in Spiral Nebulae., 97:28, January 1943. .
- N. I. Shakura and R. A. Sunyaev. Black holes in binary systems. Observational appearance. , 24:337–355, January 1973.
- F. Shankar, P. Salucci, G. L. Granato, G. De Zotti, and L. Danese. Supermassive black hole demography: the match between the local and accreted mass functions. , 354(4): 1020–1030, November 2004. .
- F. Shankar, A. Lapi, P. Salucci, G. De Zotti, and L. Danese. New Relationships between Galaxy Properties and Host Halo Mass, and the Role of Feedbacks in Galaxy Formation. , 643(1):14–25, May 2006. .
- F. Shankar, F. Marulli, S. Mathur, M. Bernardi, and F. Bournaud. Black holes in pseudobulges: demography and models. , 540:A23, April 2012. .
- Francesco Shankar. Merger-Induced Quasars, Their Light Curves, and Their Host Halos. In Bradley M. Peterson, Rachel S. Somerville, and Thaisa Storchi-Bergmann, editors, *Co-Evolution of Central Black Holes and Galaxies*, volume 267 of *IAU Symposium*, pages 248–253, May 2010.
- Francesco Shankar, David H. Weinberg, and Jordi Miralda-Escudé. Self-Consistent Models of the AGN and Black Hole Populations: Duty Cycles, Accretion Rates, and the Mean Radiative Efficiency. , 690(1):20–41, January 2009.
- Francesco Shankar, David H. Weinberg, and Jordi Miralda-Escudé. Accretion-driven evolution of black holes: Eddington ratios, duty cycles and active galaxy fractions. , 428 (1):421–446, January 2013. .
- Francesco Shankar, Mariangela Bernardi, Ravi K. Sheth, Laura Ferrarese, Alister W. Graham, Giulia Savorgnan, Viola Allevato, Alessandro Marconi, Ronald Läsker, and Andrea Lapi. Selection bias in dynamically measured supermassive black hole samples: its consequences and the quest for the most fundamental relation. , 460(3):3119–3142, August 2016. .

Francesco Shankar, Mariangela Bernardi, Kayleigh Richardson, Christopher Marsden, Ravi K. Sheth, Viola Allevato, Luca Graziani, Mar Mezcua, Federica Ricci, Samantha J. Penny, Fabio La Franca, and Fabio Pacucci. Black hole scaling relations of active and quiescent galaxies: Addressing selection effects and constraining virial factors. , 485(1): 1278–1292, May 2019.

- Ray S. Sharma, Ena Choi, Rachel S. Somerville, Gregory F. Snyder, Hannah Jhee, Dale D. Kocevski, Michaela Hirschmann, Benjamin P. Moster, Thorsten Naab, Desika Narayanan, Jeremiah P. Ostriker, and David J. Rosario. The connection between mergers and AGN activity in simulated and observed massive galaxies. , 527(3):9461–9479, January 2024. .
- Lu Shen, Casey Papovich, Guang Yang, Jasleen Matharu, Xin Wang, Benjamin Magnelli, David Elbaz, Shardha Jogee, Anahita Alavi, Pablo Arrabal Haro, Bren E. Backhaus, Micaela B. Bagley, Eric F. Bell, Laura Bisigello, Antonello Calabrò, M. C. Cooper, Luca Costantin, Emanuele Daddi, Mark Dickinson, Steven L. Finkelstein, Seiji Fujimoto, Mauro Giavalisco, Norman A. Grogin, Yuchen Guo, Benne W. Holwerda, Jeyhan S. Kartaltepe, Anton M. Koekemoer, Peter Kurczynski, Ray A. Lucas, Pablo G. Pérez-González, Nor Pirzkal, Laura Prichard, Marc Rafelski, Kaila Ronayne, Raymond C. Simons, Ben Sunnquist, Harry I. Teplitz, Jonathan R. Trump, Benjamin J. Weiner, Rogier A. Windhorst, and L. Y. Aaron Yung. CEERS: Spatially Resolved UV and Midinfrared Star Formation in Galaxies at 0.2 ; z ; 2.5: The Picture from the Hubble and James Webb Space Telescopes. , 950(1):7, June 2023.
- Xuejian Shen, Philip F. Hopkins, Claude-André Faucher-Giguère, D. M. Alexander, Gordon T. Richards, Nicholas P. Ross, and R. C. Hickox. The bolometric quasar luminosity function at z=0.7., 495(3):3252–3275, January 2020.
- Yue Shen. Supermassive Black Holes in the Hierarchical Universe: A General Framework and Observational Tests. , 704(1):89–108, October 2009. .
- Matilde Signorini, Stefano Marchesi, Roberto Gilli, Marcella Brusa, Andrea Comastri, Quirino D'Amato, Kazushi Iwasawa, Giorgio Lanzuisi, Giovanni Mazzolari, Marco Mignoli, Alessandro Peca, Isabella Prandoni, Paolo Tozzi, Cristian Vignali, Fabio Vito, and Colin Norman. X-ray properties and obscured fraction of AGN in the J1030 Chandra field., 676:A49, August 2023.
- Joseph Silk and Adi Nusser. The Massive-black-hole-Velocity-dispersion Relation and the Halo Baryon Fraction: A Case for Positive Active Galactic Nucleus Feedback. , 725 (1):556–560, December 2010. .
- Joseph Silk and Martin J. Rees. Quasars and galaxy formation., 331:L1-L4, March 1998. .
- Andrea Silva, Danilo Marchesini, John D. Silverman, Nicholas Martis, Daisuke Iono, Daniel Espada, and Rosalind Skelton. Galaxy Mergers up to z; 2.5. II. AGN Incidence in Merging Galaxies at Separations of 3-15 kpc., 909(2):124, March 2021.

John D. Silverman, Vincenzo Mainieri, Xuheng Ding, Daizhong Liu, Knud Jahnke, Michaela Hirschmann, Jeyhan Kartaltepe, Erini Lambrides, Masafusa Onoue, Benny Trakhtenbrot, Eleni Vardoulaki, Angela Bongiorno, Caitlin Casey, Francesca Civano, Andreas Faisst, Maximilien Franco, Steven Gillman, Ghassem Gozaliasl, Christopher C. Hayward, Anton M. Koekemoer, Vasily Kokorev, Georgios Magdis, Stefano Marchesi, Robert Michael Rich, Martin Sparre, Hyewon Suh, Takumi Tanaka, and Francesco Valentino. Resolving Galactic-scale Obscuration of X-Ray AGNs at z ≥ 1 with COSMOS-Web., 951(2):L41, July 2023.

- Manodeep Sinha and Lehman H. Garrison. CORRFUNC a suite of blazing fast correlation functions on the CPU. , 491(2):3022–3041, Jan 2020. .
- Harlan J. Smith and Dorrit Hoffleit. Light Variations in the Superluminous Radio Galaxy 3C273. , 198(4881):650–651, May 1963. .
- Krista Lynne Smith, Richard F. Mushotzky, Patricia T. Boyd, Matt Malkan, Steve B. Howell, and Dawn M. Gelino. The Kepler Light Curves of AGN: A Detailed Analysis., 857 (2):141, April 2018.
- S. Soldi, V. Beckmann, W. H. Baumgartner, G. Ponti, C. R. Shrader, P. Lubiński, H. A. Krimm, F. Mattana, and J. Tueller. Long-term variability of AGN at hard X-rays. , 563: A57, March 2014. .
- Rachel S. Somerville and Romeel Davé. Physical Models of Galaxy Formation in a Cosmological Framework. , 53:51–113, August 2015. .
- Rachel S. Somerville, Philip F. Hopkins, Thomas J. Cox, Brant E. Robertson, and Lars Hernquist. A semi-analytic model for the co-evolution of galaxies, black holes and active galactic nuclei., 391(2):481–506, December 2008.
- G. Speranza, C. Ramos Almeida, J. A. Acosta-Pulido, A. Audibert, L. R. Holden, C. N. Tadhunter, A. Lapi, O. González-Martín, M. Brusa, I. E. López, B. Musiimenta, and F. Shankar. Multiphase characterization of AGN winds in five local type-2 quasars., 681:A63, January 2024.
- Volker Springel. The cosmological simulation code GADGET-2. , 364(4):1105–1134, December 2005. .
- Volker Springel. E pur si muove: Galilean-invariant cosmological hydrodynamical simulations on a moving mesh. , 401(2):791–851, January 2010. .
- Volker Springel and Lars Hernquist. Formation of a Spiral Galaxy in a Major Merger., 622(1):L9–L12, March 2005.
- Volker Springel, Simon D. M. White, Adrian Jenkins, Carlos S. Frenk, Naoki Yoshida, Liang Gao, Julio Navarro, Robert Thacker, Darren Croton, John Helly, John A. Peacock, Shaun Cole, Peter Thomas, Hugh Couchman, August Evrard, Jörg Colberg, and Frazer

Pearce. Simulations of the formation, evolution and clustering of galaxies and quasars. , 435(7042):629–636, June 2005. .

- A. T. Steffen, I. Strateva, W. N. Brandt, D. M. Alexander, A. M. Koekemoer, B. D. Lehmer, D. P. Schneider, and C. Vignali. The X-Ray-to-Optical Properties of Optically Selected Active Galaxies over Wide Luminosity and Redshift Ranges. , 131(6):2826–2842, June 2006. .
- Kyle R. Stewart, James S. Bullock, Risa H. Wechsler, and Ariyeh H. Maller. Gas-rich Mergers in LCDM: Disk Survivability and the Baryonic Assembly of Galaxies. , 702(1): 307–317, September 2009.
- Tomoko L. Suzuki, Masato Onodera, Tadayuki Kodama, Emanuele Daddi, Masao Hayashi, Yusei Koyama, Rhythm Shimakawa, Ian Smail, David Sobral, Sandro Tacchella, and Ichi Tanaka. Dust, Gas, and Metal Content in Star-forming Galaxies at z \sim 3.3 Revealed with ALMA and Near-IR Spectroscopy. , 908(1):15, February 2021. .
- A. M. Swinbank, C. M. Harrison, J. Trayford, M. Schaller, Ian Smail, J. Schaye, T. Theuns, R. Smit, D. M. Alexander, R. Bacon, R. G. Bower, T. Contini, R. A. Crain, C. de Breuck, R. Decarli, B. Epinat, M. Fumagalli, M. Furlong, A. Galametz, H. L. Johnson, C. Lagos, J. Richard, J. Vernet, R. M. Sharples, D. Sobral, and J. P. Stott. Angular momentum evolution of galaxies over the past 10 Gyr: a MUSE and KMOS dynamical survey of 400 star-forming galaxies from z = 0.3 to 1.7., 467(3):3140–3159, May 2017.
- S. Tacchella, P. Lang, C. M. Carollo, N. M. Förster Schreiber, A. Renzini, A. E. Shapley, S. Wuyts, G. Cresci, R. Genzel, S. J. Lilly, C. Mancini, S. F. Newman, L. J. Tacconi, G. Zamorani, R. I. Davies, J. Kurk, and L. Pozzetti. SINS/zC-SINF Survey of z \sim 2 Galaxy Kinematics: Rest-frame Morphology, Structure, and Colors from Near-infrared Hubble Space Telescope Imaging. , 802(2):101, April 2015.
- L. J. Tacconi, R. Genzel, A. Saintonge, F. Combes, S. García-Burillo, R. Neri, A. Bolatto, T. Contini, N. M. Förster Schreiber, S. Lilly, D. Lutz, S. Wuyts, G. Accurso, J. Boissier, F. Boone, N. Bouché, F. Bournaud, A. Burkert, M. Carollo, M. Cooper, P. Cox, C. Feruglio, J. Freundlich, R. Herrera-Camus, S. Juneau, M. Lippa, T. Naab, A. Renzini, P. Salome, A. Sternberg, K. Tadaki, H. Übler, F. Walter, B. Weiner, and A. Weiss. PHIBSS: Unified Scaling Relations of Gas Depletion Time and Molecular Gas Fractions., 853(2): 179, February 2018.
- D. Tamburro, H. W. Rix, F. Walter, E. Brinks, W. J. G. de Blok, R. C. Kennicutt, and M. M. Mac Low. Geometrically Derived Timescales for Star Formation in Spiral Galaxies., 136(6):2872–2885, December 2008.
- Qing-Hua Tan, Emanuele Daddi, Benjamin Magnelli, Camila A. Correa, Frédéric Bournaud, Sylvia Adscheid, Shao-Bo Zhang, David Elbaz, Carlos Gómez-Guijarro, Boris S. Kalita, Daizhong Liu, Zhaoxuan Liu, Jérôme Pety, Annagrazia Puglisi, Eva Schinnerer,

John D. Silverman, and Francesco Valentino. Unveiling In-Situ Spheroid Formation in Distant, Submillimeter-Bright Galaxies. *arXiv e-prints*, art. arXiv:2407.16578, July 2024.

- Atsushi Tanimoto, Yoshihiro Ueda, Hirokazu Odaka, Toshihiro Kawaguchi, Yasushi Fukazawa, and Taiki Kawamuro. XCLUMPY: X-Ray Spectral Model from Clumpy Torus and Its Application to the Circinus Galaxy., 877(2):95, June 2019.
- Atsushi Tanimoto, Yoshihiro Ueda, Hirokazu Odaka, Shoji Ogawa, Satoshi Yamada, Toshihiro Kawaguchi, and Kohei Ichikawa. Application of an X-Ray Clumpy Torus Model (XCLUMPY) to 10 Obscured Active Galactic Nuclei Observed with Suzaku and NuSTAR., 897(1):2, July 2020.
- Atsushi Tanimoto, Yoshihiro Ueda, Hirokazu Odaka, Satoshi Yamada, and Claudio Ricci. NuSTAR Observations of 52 Compton-thick Active Galactic Nuclei Selected by the Swift/Burst Alert Telescope All-sky Hard X-Ray Survey., 260(2):30, June 2022.
- R. Teyssier. Cosmological hydrodynamics with adaptive mesh refinement. A new high resolution code called RAMSES. , 385:337–364, April 2002. .
- Romain Teyssier, Damien Chapon, and Frédéric Bournaud. The Driving Mechanism of Starbursts in Galaxy Mergers. , 720(2):L149–L154, September 2010. .
- Kip S. Thorne. Disk-Accretion onto a Black Hole. II. Evolution of the Hole. , 191:507–520, July 1974. .
- Yoshiki Toba, Teng Liu, Tanya Urrutia, Mara Salvato, Junyao Li, Yoshihiro Ueda, Marcella Brusa, Naomichi Yutani, Keiichi Wada, Atsushi J. Nishizawa, Johannes Buchner, Tohru Nagao, Andrea Merloni, Masayuki Akiyama, Riccardo Arcodia, Bau-Ching Hsieh, Kohei Ichikawa, Masatoshi Imanishi, Kaiki T. Inoue, Toshihiro Kawaguchi, Georg Lamer, Kirpal Nandra, John D. Silverman, and Yuichi Terashima. The eROSITA Final Equatorial-Depth Survey (eFEDS). A multiwavelength view of WISE mid-infrared galaxies/active galactic nuclei., 661:A15, May 2022.
- E. Treister, C. Megan Urry, and Shanil Virani. The Space Density of Compton-Thick Active Galactic Nucleus and the X-Ray Background., 696(1):110–120, May 2009.
- Ezequiel Treister, Priyamvada Natarajan, David B. Sanders, C. Megan Urry, Kevin Schawinski, and Jeyhan Kartaltepe. Major Galaxy Mergers and the Growth of Supermassive Black Holes in Quasars. *Science*, 328(5978):600, April 2010.
- Ezequiel Treister, Claudia M. Urry, Kevin Schawinski, Brooke D. Simmons, Priyamvada Natarajan, and Marta Volonteri. The Multiwavelength AGN Population and the X-ray Background. In Areg M. Mickaelian and David B. Sanders, editors, *Multiwavelength AGN Surveys and Studies*, volume 304 of *IAU Symposium*, pages 188–194, July 2014.

J. Tueller, R. F. Mushotzky, S. Barthelmy, J. K. Cannizzo, N. Gehrels, C. B. Markwardt, G. K. Skinner, and L. M. Winter. Swift BAT Survey of AGNs. , 681(1):113–127, July 2008. .

- T. J. Turner, I. M. George, K. Nandra, and R. F. Mushotzky. Asca observations of type 2 seyfert galaxies. iii. orientation and x-ray absorption. *The Astrophysical Journal*, 493(1): 91, jan 1998. URL https://dx.doi.org/10.1086/305117.
- Y. Ueda, Y. Ishisaki, T. Takahashi, K. Makishima, and T. Ohashi. The ASCA Medium Sensitivity Survey (the GIS Catalog Project): Source Catalog., 133(1):1–52, March 2001.
- Yoshihiro Ueda, Tadayuki Takahashi, Hajime Inoue, Takeshi Tsuru, Masaaki Sakano, Yoshitaka Ishisaki, Yasushi Ogasaka, Kazuo Makishima, Toru Yamada, Masayuki Akiyama, and Kouji Ohta. LOG N-LOG S Relations and Spectral Properties of Sources from the ASCA Large Sky Survey: Their Implications for the Origin of the Cosmic X-Ray Background (CXB). , 518(2):656–671, June 1999. .
- Yoshihiro Ueda, Michael G. Watson, Ian M. Stewart, Masayuki Akiyama, Axel D. Schwope, Georg Lamer, Jacobo Ebrero, Francisco J. Carrera, Kazuhiro Sekiguchi, Tohru Yamada, Chris Simpson, Günther Hasinger, and Silvia Mateos. The Subaru/XMM-Newton Deep Survey (SXDS). III. X-Ray Data. , 179(1):124–141, November 2008.
- Yoshihiro Ueda, Kazuo Hiroi, Naoki Isobe, Masaaki Hayashida, Satoshi Eguchi, Mutsumi Sugizaki, Nobuyuki Kawai, Hiroshi Tsunemi, Tatehiro Mihara, Masaru Matsuoka, Masaki Ishikawa, Masashi Kimura, Hiroki Kitayama, Mitsuhiro Kohama, Takanori Matsumura, Mikio Morii, Yujin E. Nakagawa, Satoshi Nakahira, Motoki Nakajima, Hitoshi Negoro, Motoko Serino, Megumi Shidatsu, Tetsuya Sootome, Kousuke Sugimori, Fumitoshi Suwa, Takahiro Toizumi, Hiroshi Tomida, Yohko Tsuboi, Shiro Ueno, Ryuichi Usui, Takayuki Yamamoto, Kazutaka Yamaoka, Kyohei Yamazaki, and Atsumasa Yoshida. Revisit of Local X-Ray Luminosity Function of Active Galactic Nuclei with the MAXI Extragalactic Survey., 63:S937–S945, November 2011.
- Yoshihiro Ueda, Masayuki Akiyama, Günther Hasinger, Takamitsu Miyaji, and Michael G. Watson. Toward the Standard Population Synthesis Model of the X-Ray Background: Evolution of X-Ray Luminosity and Absorption Functions of Active Galactic Nuclei Including Compton-thick Populations. , 786(2):104, May 2014.
- C. Megan Urry and Paolo Padovani. Unified Schemes for Radio-Loud Active Galactic Nuclei., 107:803, September 1995. .
- Milena Valentini, Giuseppe Murante, Stefano Borgani, Pierluigi Monaco, Alessandro Bressan, and Alexander M. Beck. On the effect of galactic outflows in cosmological simulations of disc galaxies. , 470(3):3167–3193, September 2017. .

Milena Valentini, Giuseppe Murante, Stefano Borgani, Gian Luigi Granato, Pierluigi Monaco, Fabrizio Brighenti, Luca Tornatore, Alessandro Bressan, and Andrea Lapi. Impact of AGN feedback on galaxies and their multiphase ISM across cosmic time. , 491(2):2779–2807, January 2020. .

- Freeke van de Voort, Joop Schaye, C. M. Booth, Marcel R. Haas, and Claudio Dalla Vecchia. The rates and modes of gas accretion on to galaxies and their gaseous haloes., 414(3):2458–2478, July 2011.
- P. C. van der Kruit. Optical surface photometry of eight spiral galaxies studied in Westerbork. , 38:15–38, October 1979.
- A. van der Wel, M. Franx, P. G. van Dokkum, R. E. Skelton, I. G. Momcheva, K. E. Whitaker, G. B. Brammer, E. F. Bell, H. W. Rix, S. Wuyts, H. C. Ferguson, B. P. Holden, G. Barro, A. M. Koekemoer, Yu-Yen Chang, E. J. McGrath, B. Häussler, A. Dekel, P. Behroozi, M. Fumagalli, J. Leja, B. F. Lundgren, M. V. Maseda, E. J. Nelson, D. A. Wake, S. G. Patel, I. Labbé, S. M. Faber, N. A. Grogin, and D. D. Kocevski. 3D-HST+CANDELS: The Evolution of the Galaxy Size-Mass Distribution since z = 3., 788(1):28, June 2014.
- A. Viitanen, V. Allevato, A. Finoguenov, F. Shankar, R. Gilli, G. Lanzuisi, and F. Vito. Large-scale clustering of buried X-ray AGN: Trends in AGN obscuration and redshift evolution., 674:A214, June 2023.
- Bovornpratch Vijarnwannaluk, Masayuki Akiyama, Malte Schramm, Yoshihiro Ueda, Yoshiki Matsuoka, Yoshiki Toba, Naoki Matsumoto, Angel Ruiz, Ioannis Georgantopoulos, Ektoras Pouliasis, Elias Koulouridis, Kohei Ichikawa, Marcin Sawicki, and Stephen Gwyn. Observational properties of active galactic nucleus obscuration during the peak of accretion growth. , 529(4):3610–3629, April 2024.
- Carolin Villforth. A complete catalogue of merger fractions in AGN hosts: No evidence for an increase in detected merger fraction with AGN luminosity. *The Open Journal of Astrophysics*, 6:34, September 2023.
- Carolin Villforth, Anton M. Koekemoer, and Norman A. Grogin. A New Extensive Catalog of Optically Variable Active Galactic Nuclei in the GOODS Fields and a New Statistical Approach to Variability Selection. , 723(1):737–754, November 2010. .
- Marta Volonteri and Priyamvada Natarajan. Journey to the M_{BH} - σ relation: the fate of low-mass black holes in the Universe. , 400(4):1911–1918, December 2009. .
- Marta Volonteri, Priyamvada Natarajan, and Kayhan Gültekin. How Important is the Dark Matter Halo for Black Hole Growth? , 737(2):50, August 2011. .
- Keiichi Wada. Obscuring Fraction of Active Galactic Nuclei: Implications from Radiation-driven Fountain Models. , 812(1):82, October 2015. .

R P Walker. Synchrotron radiation. 1994. . URL https://cds.cern.ch/record/398429.

- Jing Wang, Jian Fu, Michael Aumer, Guinevere Kauffmann, Gyula I. G. Józsa, Paolo Serra, Mei-ling Huang, Jarle Brinchmann, Thijs van der Hulst, and Frank Bigiel. An observational and theoretical view of the radial distribution of H I gas in galaxies. , 441(3): 2159–2172, July 2014.
- Yunchong Wang, Mark Vogelsberger, Dandan Xu, Xuejian Shen, Shude Mao, David Barnes, Hui Li, Federico Marinacci, Paul Torrey, Volker Springel, and Lars Hernquist. Early-type galaxy density profiles from IllustrisTNG II. Evolutionary trend of the total density profile. , 490(4):5722–5738, October 2019.
- B. Louise Webster and Paul Murdin. Cygnus X-1-a Spectroscopic Binary with a Heavy Companion?, 235(5332):37–38, January 1972.
- D. B. Wijesinghe, A. M. Hopkins, R. Sharp, M. Gunawardhana, S. Brough, E. M. Sadler, S. Driver, I. Baldry, S. Bamford, J. Liske, J. Loveday, P. Norberg, J. Peacock, C. C. Popescu, R. J. Tuffs, J. Bland-Hawthorn, E. Cameron, S. Croom, C. Frenk, D. Hill, D. H. Jones, E. van Kampen, L. Kelvin, K. Kuijken, B. Madore, B. Nichol, H. Parkinson, K. A. Pimbblet, M. Prescott, A. S. G. Robotham, M. Seibert, E. Simmat, W. Sutherland, E. Taylor, and D. Thomas. Galaxy and mass assembly (GAMA): dust obscuration in galaxies and their recent star formation histories. , 410(4):2291–2301, February 2011.
- L. Woltjer. Emission Nuclei in Galaxies., 130:38, July 1959. .
- Mengyuan Xiao, Pascal Oesch, David Elbaz, Longji Bing, Erica Nelson, Andrea Weibel, Rohan Naidu, Emanuele Daddi, Rychard Bouwens, Jorryt Matthee, Stijn Wuyts, John Chisholm, Gabriel Brammer, Mark Dickinson, Benjamin Magnelli, Lucas Leroy, Pieter van Dokkum, Daniel Schaerer, Thomas Herard-Demanche, Laia Barrufet, Ryan Endsley, Yoshinobu Fudamoto, Carlos Gómez-Guijarro, Rashmi Gottumukkala, Garth Illingworth, Ivo Labbe, Daniel Magee, Danilo Marchesini, Michael Maseda, Yuxiang Qin, Naveen Reddy, Alice Shapley, Irene Shivaei, Marko Shuntov, Mauro Stefanon, Katherine Whitaker, and J. Stuart Wyithe. Massive Optically Dark Galaxies Unveiled by JWST Challenge Galaxy Formation Models. *arXiv e-prints*, art. arXiv:2309.02492, September 2023.
- Lizhi Xie, Gabriella De Lucia, Michaela Hirschmann, Fabio Fontanot, and Anna Zoldan. H_2 -based star formation laws in hierarchical models of galaxy formation. , 469(1):968–993, July 2017. .
- Lizhi Xie, Gabriella De Lucia, Michaela Hirschmann, and Fabio Fontanot. The influence of environment on satellite galaxies in the GAEA semi-analytic model. , 498(3):4327–4344, November 2020. .
- Cong Xu and Jack W. Sulentic. Infrared Emission in Paired Galaxies. II. Luminosity Functions and Far-Infrared Properties. , 374:407, June 1991. .

Y. Q. Xue, B. Luo, W. N. Brandt, F. E. Bauer, B. D. Lehmer, P. S. Broos, D. P. Schneider, D. M. Alexander, M. Brusa, A. Comastri, A. C. Fabian, R. Gilli, G. Hasinger, A. E. Hornschemeier, A. Koekemoer, T. Liu, V. Mainieri, M. Paolillo, D. A. Rafferty, P. Rosati, O. Shemmer, J. D. Silverman, I. Smail, P. Tozzi, and C. Vignali. The Chandra Deep Field-South Survey: 4 Ms Source Catalogs., 195(1):10, July 2011.

- Satoshi Yamada, Yoshihiro Ueda, Atsushi Tanimoto, Masatoshi Imanishi, Yoshiki Toba, Claudio Ricci, and George C. Privon. Comprehensive Broadband X-Ray and Multiwavelength Study of Active Galactic Nuclei in 57 Local Luminous and Ultraluminous Infrared Galaxies Observed with NuSTAR and/or Swift/BAT., 257(2):61, December 2021.
- Satoshi Yamada, Yoshihiro Ueda, Martín Herrera-Endoqui, Yoshiki Toba, Takamitsu Miyaji, Shoji Ogawa, Ryosuke Uematsu, Atsushi Tanimoto, Masatoshi Imanishi, and Claudio Ricci. Hard X-Ray to Radio Multiwavelength SED Analysis of Local U/LIRGs in the GOALS Sample with a Self-consistent AGN Model including a Polar-dust Component. , 265(2):37, April 2023. .
- Xiaolong Yang, Ravi Joshi, Gopal-Krishna, Tao An, Luis C. Ho, Paul J. Wiita, Xiang Liu, Jun Yang, Ran Wang, Xue-Bing Wu, and Xiaofeng Yang. Extended Catalog of Winged or X-shaped Radio Sources from the FIRST Survey., 245(1):17, November 2019.
- Robert M. Yates, David Hendriks, Aswin P. Vijayan, Robert G. Izzard, Peter A. Thomas, and Payel Das. The impact of binary stars on the dust and metal evolution of galaxies. , 527(3):6292–6311, January 2024. .
- Naomichi Yutani, Yoshiki Toba, Shunsuke Baba, and Keiichi Wada. Origin and Evolution of Dust-obscured Galaxies in Galaxy Mergers. , 936(2):118, September 2022. .
- Nadia L. Zakamska, Michael A. Strauss, Julian H. Krolik, Matthew J. Collinge, Patrick B. Hall, Lei Hao, Timothy M. Heckman, Željko Ivezić, Gordon T. Richards, David J. Schlegel, Donald P. Schneider, Iskra Strateva, Daniel E. Vanden Berk, Scott F. Anderson, and Jon Brinkmann. Candidate Type II Quasars from the Sloan Digital Sky Survey. I. Selection and Optical Properties of a Sample at 0.3¡Z¡0.83., 126(5):2125–2144, November 2003.
- Lorenzo Zanisi. Galaxy formation through the lens of galaxy structure with semi-empirical models and deep learning. PhD thesis, University of Southampton, United Kingdom, December 2021. URL https://eprints.soton.ac.uk/467307/.
- Ya. B. Zel'dovich and I. D. Novikov. The Radiation of Gravity Waves by Bodies Moving in the Field of a Collapsing Star. *Soviet Physics Doklady*, 9:246, October 1964.
- Dejene Zewdie, Mirjana Pović, Manuel Aravena, Roberto J. Assef, and Asrate Gaulle. AGN and star formation properties of inside-out assembled galaxy candidates at z; 0.1., 498(3):4345–4355, November 2020.

Haowen Zhang, Peter Behroozi, Marta Volonteri, Joseph Silk, Xiaohui Fan, Philip F. Hopkins, Jinyi Yang, and James Aird. TRINITY I: self-consistently modelling the dark matter halo-galaxy-supermassive black hole connection from z=0-10. , 518(2):2123–2163, January 2023. .

- Zhimin Zhou, Hong Wu, Xu Zhou, and Jun Ma. The Relation between H I Gas and Star Formation Properties in Nearby Galaxies. , 130(991):094101, September 2018. .
- Anna Zoldan, Gabriella De Lucia, Lizhi Xie, Fabio Fontanot, and Michaela Hirschmann. The evolution of sizes and specific angular momenta in hierarchical models of galaxy formation and evolution. , 487(4):5649–5665, August 2019.